Politecnico di Torino

ScuDo
Scuola di Dottorato ~ Doctoral School
WHAT YOU ARE, TAKES YOU FAR

Doctoral Dissertation

Doctoral Program in Electrical Electronics and Communication Engineering
(37^{th}cycle)

Enhancing the Electron Transfer at Electrochemical Interfaces by Spinel Oxide-Nanostructures

By

Mallikarjun Madagalam

******

Supervisors:
Mattia Bartoli, Co-Supervisor
Sandro Carrara, Co-Supervisor (EPFL)
Alberto Tagliaferro, Supervisor

Doctoral Examination Committee:
To be defined,

Politecnico di Torino
2025

Declaration

I hereby declare that, the contents and organization of this dissertation constitute my own original work and does not compromise in any way the rights of third parties, including those relating to the security of personal data.

Mallikarjun Madagalam
2025

* This dissertation is presented in partial fulfillment of the requirements for **Ph.D. degree** in the Graduate School of Politecnico di Torino (ScuDo).

In the end, it's not the years in your life that count, it's the life in your years.
— Abraham Lincoln

I dedicate this thesis to my family and friends

Abstract

Electrochemical interface can be influenced by several factors such as the type of sensing electrode material, size, shape and orientation of the particles, crystal structure, ionic radius, surface area, and material composition. It is very important to understand the effect of these different factors on the electron transfer at the electrochemcial interface for a proper, cost effective, robust design and fabrication of electrochemical sensors for biomedical applications. Therefore this work focuses on the fundamental understanding of the effects of crystal structure, electrode material composition, and ionic size on electron transfer rate constant 'k'. To study the effect of one parameter on 'k', all the other parameters should be kept constant. In the literature it is reported that spinel crystal structure-based nanomaterials are always produced in spherical form therefore spinel crystal structure-based multi-metal oxides are chosen in this study to avoid the importance particle orientation. Spinel crystal structure based-nanomaterials are synthesized by using simple auto combustion dry synthesis and the materials are characterized by field emission scanning electron microscopy (FESEM), X-ray diffraction (XRD), Raman, X-ray photoelectron (XPS), and ultra violet visible (UV-vis) spectroscopic techniques to understand the morphological and spectroscopic techniques to understand the morphological and structural properties of new materials. A single spinel phase for $Zn_xNi_{1-x}Fe_2O_4$ (x = 0, 0.2, 0.4, 0.6, 0.8, 1) and $ZnCr_xFe_{2-x}O_4$ (x = 0, 0.25, 0.5, 0.75, 1, 2) with spherical shaped nanoparticles of size varying between 20 and 70 nm is confirmed by XRD and FESEM images. While two separate spinel phases of $ZnFe_2O_4$ and $ZnBi_2O_4$ for $ZnBi_xFe_{2-x}O_4$ (x = 0, 0.25, 0.5, 0.75, 1, 2) are found with spherical and patch-like morphology particles at sub-micrometer scale. XRD also showed some secondary phases of ZnO, Fe_2O_3, and graphite for some materials. ZnO has hexagonal structure with pyramid shaped microparticles and ZnO/$ZnFe_2O_4$ has separate ZnO and $ZnFe_2O_4$ phases as expected with same morphology as $ZnFe_2O_4$ at nanoscale. Raman confirmed the molecular vibrations

with expected atomic bondings with respective Raman bands for each material. The elemental compositions and valence states of the elements in each material are verified by XPS full survey and high resolution spectra, respectively. The energy band gap (E_g) is estimated by diffuse reflectance UV-vis spectra and Tauc's plot method. E_g varies between 2 and 3 eV for different spinel nanomaterials, ZnO has an energy gap around 3.2 eV while ZnO/$ZnFe_2O_4$ has an E_g of 2.9 eV which is an average E_g of ZnO and $ZnFe_2O_4$. XPS valence band spectra are used to estimate the valence band maximum (E_V) and the conduction band minimum ($E_C = E_g + E_V$) is computed to construct energy band diagrams for each material.

Screen-printed carbon electrodes with carbon working electrode and counter electrode, and Ag/AgCl reference electrode are employed as reference electrochemical sensors. The carbon working electrode's surface is modified by spinel nanomaterials solution in 1-butanol by drop-casting. Cylic voltammetry is used to characterized the electrochemical sensors with paracetamol as a test molecule. It is found that all the surface-modified sensors with spinel nanomaterials have significantly enhanced the electrochemical sensing capability of the bare carbon sensor in detecting 1 mM paracetamol in 0.1 M phosphate buffer solution at pH 7. The kinetic rate constant of the sensors with three sets of spinel materials, no proper trend is observed but the rate constant of the bare carbon sensor is significantly enhanced. Among all the spinel-based sensors, $ZnFe_2O_4$ has the highest 'k' of 13.1 ± 2.8 ms^{-1} with a peak-to-peak separation of 386 ± 2 mV showing high electrochemical reversibility with faster reaction at the interface. The sensitivity of the normal spinel $ZnFe_2O_4$ is observed to be higher than the inverse spinel $NiFe_2O_4$. Zinc ferrite has improved the sensitivity of the bare carbon sensor by more than two times showing its excellent sensing capability towards paracetamol. The presence of Cr(III) in the composition of normal spinel zinc ferrite has degrading performance compared to $ZnFe_2O_4$. The inclusion of higher ionic sized Bi(III) in zinc ferrite has further decreased the sensitivity. The type of electron transfer mechanism is predicted by using the energy band edges of the nanomaterials and redox potentials of paracetamol. Only $ZnFe_2O_4$ has shown a possibility of direct electron transfer while the other materials are more prone to surface-mediated electron transfer. Since normal spinel $ZnFe_2O_4$ has shown the best performance, some of the potential applications are explored. $ZnFe_2O_4$, ZnO, and ZnO/$ZnFe_2O_4$ nanomaterials potential towards dissolved oxygen, and pH sensing is studied. Finally, $ZnFe_2O_4$ and $ZnCr_2O_4$ are used in the electrochemical sensing of anti-cancer drugs (5-Fluororacil and Etoposide).

Contents

List of Figures

List of Tables

Chapter 1

Introduction

1.1 Objective of the PhD Project

Understanding the fundamental processes happening at the electrode/electrolyte interface in electrochemical sensors is of prime importance to properly design the sensing materials with desired properties. One of the prime factors affecting the electrode/electrolyte interface is the electron transfer (ET), electron transfer can be by electron hopping or by tunneling depending on the energy barrier at the interface. Electron transfer gets affected by different parameters at the interface as clearly described different molecular models including Marcus model and modified Marcus model by Tachiya. According to Marcus theory the electron transfer rate depends on transfer integral (J), and reorganization energy (λ). J and λ depend on the radii 'a' and 'b' of donor and acceptor, and the distance 'R' between the donor and acceptor. The radii 'a' and 'b' change with size and morphology of the donor and acceptor ions/molecules. Oxidation state and crystallographic radius of the ion can affect the effective radius of the ion. Depending on the size of the donor/acceptor ions/molecules the distance 'R' changes affecting J and λ which eventually affect the electron transfer rate at the electrode. Crystal structure of the electrode material and composition can also affect the transfer integral and reorganization energy leading to different electron transfer rates. In order to understand the affect of different factors on the electron transfer at the electrode/electrolyte interface, it is necessary to keep some parameters constant and study the effect of other parameters.

To understand electron transfer rate at the electrode/electrolyte interface in electrochemical sensors, rational design and proper control of the electrode surface is necessary. The electrode parameters that affect the electrode reaction rate are the electrode material, surface area, geometry, and surface conditioning. In this work, in order to understand effect of electrode material on the electron transfer rate, the materials are designed and produced at nanoscale by maintaining a similar morphology (spherical shaped particles) so that it is possible to study the effect of other parameters on electron transfer rate at the electrochemical interface.

Spinel nanomaterials are chosen due to their flexibility in design and easily modifiable composition without disturbing too much the crystal structure of the spinel. It is reported in the literature that using auto combustion synthesis technique the spinel nanomaterials are produced always in spherical shaped particles. Hence, the auto combustion synthesis technique is used to synthesize spinel nanomaterials to produce the similar morphology of particles and the technique is cost effective and single step process (the method will be discussed with more details in chapter 2). Screen printed electrodes with carbon working electrode, carbon counter electrode, and Ag/AgCl as reference electrode are used as electrochemical sensors. The surface of the carbon working electrode is modified using different spinel-based nanomaterials to fabricate new spinel nanomaterials-based electrochemical sensors. The new sensors are characterized using paracetamol (an electroactive drug) as a model molecule to understand the effect of different factors of spinel nanomaterials on electron transfer at the elctrochemical interface between the spinel nanomaterials and paracetamol.

The whole research project is divided into four different parts, the first part of the study is about the effect of chemical composition and crystal structure on electron transfer at the elctrochemical interface. The second part describes about the effect of trivalent cation and the third part is about the effect of ionic size on electron transfer. The fourth part in chapter 6 presents some potentially possible applications of the best nanomaterials found in first three parts of this project.

The PhD thesis report is divided into seven chapters, the first chapter presents the basic theory of electrochemical sensors, fundamentals of electron transfer at the electrode/electrolyte interface, and the electrochemical characterization techniques used in this work. Chapter 2 discusses the crystal structure and different types of spinel nanomaterials, nanomaterial synthesis and characterization, preparation of dif-

ferent solutions, fabrication of electrochemical sensors, and different characterization methods and apparatus used in this research work.

Chapter 3 reports and discusses the main results of this work on the effect of the gradual transition of crystal structure from inverse spinel ($NiFe_2O_4$) to normal spinel ($ZnFe_2O_4$) on electron transfer at the electrochemical interface. Nanomaterials are characterized to understand the structural and morphological features, energy band gaps, conduction, and valence band edges are evaluated. Electrochemical performance of the new sensors is studied by cyclic voltammetry. Sensitivity, limit of detection, and kinetic parameters of seven different sensors ($Zn_xNi_{1-x}Fe_2O_4$ (x = 0, 0.2, 0.4, 0.6, 0.8, 1) and bare carbon) is presented and compared. Energy band diagrams of the nanomaterials are used to map with the redox potential of paracetamol to predict the type of electron transfer at the electrochemical interface. Similarly, chapter 4, and 5 present the effect of trivalent cation on electron transfer at the electrochemical interface between $ZnCr_xFe_{2-x}O_4$ (x = 0, 0.25, 0.5, 0.75, 1, 2) and paracetamol, and the effect of ionic size on electron transfer at the electrochemical interface between $ZnBi_xFe_{2-x}O_4$ (x = 0, 0.25, 0.5, 0.75, 1, 2) and paracetamol, respectively.

Chapter 6 exhibits some potential applications of $ZnFe_2O_4$ in combination with ZnO and $ZnCr_2O_4$ nanomaterials. Specifically in the first part of 6 ZnO, $ZnFe_2O_4$, and ZnO/$ZnFe_2O_4$ materials are used to electrochemically sense dissolved oxygen in buffer solution by chronoamperometry while ZnO and $ZnFe_2O_4$ performance as electrochemical pH sensors is compared and discussed by chronopotentiometric technique. Key challenges in pH sensing are scrutinized. In the second part of 6, $ZnFe_2O_4$ and $ZnCr_2O_4$ are used in electrochemical sensing of anti-cancer drugs namely 5-Fluorouracil (5-FU) and etoposide. Sensitivity and limit of detection of the three sensors are reported followed by conclusions and future outlook in chapter 7.

1.2 Electrochemical Sensors

Electrochemistry is a branch of chemistry that studies the relationship between electricity and chemical reactions. Electrochemical sensors harness the principles of electrochemistry to detect and quantify specific chemical substances. They operate by converting a chemical signal, often resulting from a target analyte's interaction with an electrode, into an electrical signal that can be measured and analyzed [1].

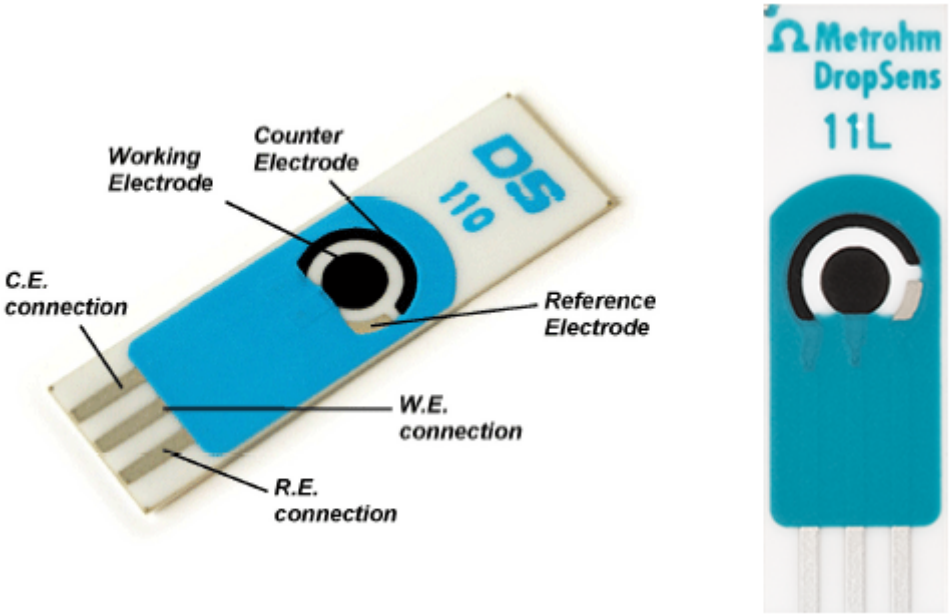

Fig. 1.1 Screen-printed three electrode electrochemical sensor from dropsense. 110 is the electrochemical sensor with carbon working electrode, carbon counter electrode, and pseudo Ag reference electrode where as 11L has Ag/AgCl as the reference electrode.

Typical electrochemical sensors are three electrode systems with working electrode, reference electrode, and counter electrode [2–4]. Working electrode is the primary site where the electrochemical reaction involving the target analyte occurs. It is usually made of materials such as platinum, gold, carbon, or modified conductive polymers. Reference electrode maintains a stable and known potential against which the working electrode's pontential can be measured. Common reference electrodes include the Ag/AgCl (silver/silver chloride) and saturated calomel electrode (SCE). Counter electrode balances the circuit allowing the current to flow. they are usually made of inert materials such as platinum or carbon, and the size should be much larger than the working electrode to ensure no current limitations [1].

Figure 1.1 shows the typical three electrodes electrochecmial sensor with carbon as a working electrode, Ag/AgCl as a reference electrode, and carbon as counter electrode fabricated by screen printing technique on a ceramic substrate. The sensor is used to quantify the presence of analytes in an electrolytic solution. Electrolytic solution is a solution with analyte/electrolyte of interest in a buffer solution typically Phosphate buffer (PB) or Phosphate buffer saline (PB with NaCl or/and KCl (PBS)) [1, 5].

Electrochemical sensors are characterized based on their sensing mechanism into four different types. 1) Potentiometric sensing measures the potential difference between the working and reference electrode in response to the concentration of an electrolyte. 2) Amperometric sensing detects current from the redox reactions of the target analyte at the surface of the working electrode when a potential is applied. 3) Conductometric sensing measures changes in the electrical conductivity of the solution caused by the interaction of the analyte with the sensor. 4) Impedometric sensing analyzes the impedance (resistance and reactance) of the system, providing information about the electrochemical processes and the properties of the interface [1, 6].

Electrochemical sensors are sophisticated analytical devices that leverage the principles of electron transfer (ET) at the electrode-electrolyte interface to detect and quantify chemical species. The fundamental theory underlying these sensors is deeply rooted in the study of electrochemistry, particularly the mechanisms by which electrons are transferred between electrodes and the reactive species in the electrolyte. Understanding these processes is crucial for the design and optimization of sensitive, selective, and reliable electrochemical sensors.

1.3 Fundamentals of Electron Transfer

Electron transfer at the electrode-electrolyte interface involves the movement of electrons between the electrode surface and the redox species in the electrolyte solution. This process is central to the operation of electrochemical sensors, where the detection of analytes is typically achieved through redox reactions. The electrode, immersed in the electrolyte, facilitates these reactions by providing a surface where electrons can be transferred [7].

1.3.1 Outer-Sphere Electron Transfer

Outer sphere electron transfer is a type of reaction where the electron transfer between the donor and acceptor occurs without any direct chemical bond formation between them [7–11]. This process involves the transfer of an electron through space or through the solvent molecules that separate the two redox partners, maintaining their individual coordination spheres intact as shown in Figure 1.2. The process is

usually governed by the overlap of the electronic wavefunctions of the donor and acceptor and the reorganization of their solvation shells. After the electron transfer, the products diffuse apart and the coordination spheres of the donor and acceptor remain unchanged throughout the process. A typical outer-sphere reaction process is the electron transfer process between hexacyanoferrate(III) and hexacyanoferrate(II):

$$[Fe(CN)_6]^{3-} + [Fe(CN)_6]^{4-} \rightarrow [Fe(CN)_6]^{4-} + [Fe(CN)_6]^{3-}$$

In this reaction, the electron transfer occurs between the iron centers, but the coordination spheres involving the cyanide ligands remain intact.

Several factors can influence the rate and efficiency of outer sphere electron transfer reactions. 1) Reorganization energy (λ): the energy required to reorganize the solvent and the internal structures of the donor and acceptor before the electron transfer can occur, lower reorganization energy typically leads to faster transfer rates. 2) Electronic coupling : The extent of overlap between the electronic wavefunctions of the donor and acceptor, stronger electronic coupling facilitates faster electron transfer. 3) Driving force: the difference in redox potentials between donor and acceptor. A larger driving force generally increases the rate of electron transfer, up to a certain limit. 4) Solvent effects: The polarity and dielectric constant of the solvent can affect the reorganization energy and the stabilization of the charged species. Solvents with high dielectric constants typically facilitate faster electron transfer. 5) Temperature: higher temperatures can increase the kinetic energy of the molecules. reducing the reaction energy barrier and enhancing the transfer rate [7, 12, 13].

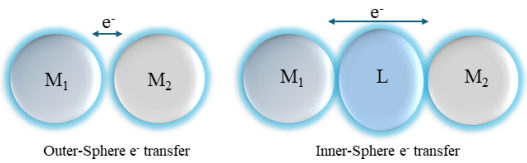

Fig. 1.2 Electron transfer mechanisms. Outer-Sphere e^- transfer: Electron transfer between two metal centers through electron cloud by tunneling process where two metal centers are loosely in contact. Inner-Sphere e^- transfer: Electron transfer between two metal centers through a common ligand bridge by forming a coordination complex. M1 and M2 are two metal centers and L is a ligand.

1.3.2 Tunnelling Process

Electron transfer by tunneling is a quantum mechanical phenomenon in which an electron moves between two sites (donor and acceptor) through a potential energy barrier that it would normally not have the energy to overcome. This process is significant in various physical, chemical, and biological systems, where it enables electron transfer over distances where classical hopping would be inefficient [8, 14].

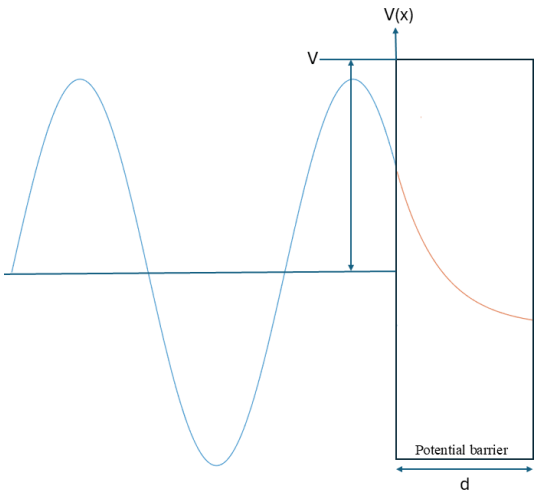

Fig. 1.3 Exponential decay of a wavefunction through a one-dimensional energy barrier with height 'V' and width 'd'.

Electron tunneling occurs when the wave function of an electron extends through a potential barrier as depicted in Figure 1.3, allowing a non-zero probability of finding the electron on the other side of the barrier without the electron having to overcome the barrier's potential energy peak. This phenomenon is described by the Schrödinger equation and is fundamentally a consequence of the wave-like nature of electrons [7, 8, 15].

In classical mechanics, a particle requires sufficient energy to overcome a potential barrier. However, in quantum mechanics, particles such as electrons have a nonzero probability of passing through a barrier. The probability (P) of an electron tunneling through a barrier depends exponentially on the barrier width (d) and height (V):

$$P \approx exp\left(-2\sqrt{\frac{2m(V-E_e)}{\hbar^2}}d\right) \tag{1.1}$$

where 'm' is the electron mass, 'E_e' is the energy of the electron, and $\hbar$ is the reduced Plank's constant. The probability of tunneling is affected by the electron coupling apart from the barrier width and height. Stronger electronic coupling between donor and acceptor can enhance the tunneling efficiency. Temperature can affect the energy distribution of electrons, indirectly influencing tunneling rates.

Tunneling plays a crucial role in biological processes such as photosynthesis and cellular respiration [16]. In molecular electronics and single molecule devices [15], tunneling is the primary mechanism for charge transport. Some enzymes use tunneling to transfer electrons rapidly between active sites.

1.3.3 Inner-Sphere Electron Transfer

Inner-sphere electron transfer is a mechanism in which an electron is transferred between a donor and an acceptor species via a direct coordination through a shared ligand or bridge as shown in Figure 1.2. The process involves the formation of a bridged complex, the oxidant and reductant form a coordination complex with a common ligand that bridges the two species. The bridging ligand temporarily binds to both metal centers, creating a pathway for the electron to move. This transfer is often associated with changes in the oxidation states of the involved metal centers. After the electron transfer, the bridged complex dissociates, resulting in the formation of the final products, often involving a change in the coordination environment of the metals and the release or migration of the bridging ligand [7, 17–19]. A general inner-sphere electron transfer reaction can be written as

$$[M_1(III)-L]+[M_2(II)-L'] \rightarrow [M_1(II)-L]+[M_2(III)-L'] \tag{1.2}$$

where M_1 and M_2 are the metal centers, and L and L' are the ligands forming the bridge. Common bridging ligands include halides, hydroxides, oxides, and other small anionic or neutral ligands that can coordinate to both the donor and acceptor metal centers. The nature of the bridging ligand significantly influences the rate and mechanism of the electron transfer process. The activation energy for the process depends on the bond formation and dissociation steps, as well as the

electronic properties of the bridge. The geometry and electronic structure of the donor, acceptor, and bridge influence the efficiency of electron transfer [7].

1.3.4 Marcus Theory of Electron Transfer

There are different models of electron transfer (ET) are proposed in the literature over the years such as elastic distortion model [20–22], the charge fluctuation model [23], and the solvent fluctuation model [12, 13, 24, 25]. The former two models proposed in the view of ET occurring at equilibrium or not too far from equilibrium whereas the latter model dealt with the processes occurring far from equilibrium. In the mid-1950s, Rudolph A. Marcus proposed this model and which is the widely accepted model for ET in the world. Marcus theory provides a comprehensive framework for understanding the rates of electron transfer reactions. This theory revolutionized the field of electrochemistry and earned Marcus the Nobel Prize in Chemistry in 1992. The theory explains how electron transfer occurs between two species and how the rate of this transfer depends on various factors, including the reorganization energy and the driving force of the reaction.

Marcus theory was based on an assumption that there is a slight overlap of electronic energy orbitals to facilitate a path for electron transfer between two molecules. An electron transfer reaction involves the transfer of an electron from a donor molecule (D) to an acceptor molecule (A). This can be represented as:

$$D + A \rightleftharpoons D^{+} + A^{-} \tag{1.3}$$

where D and A are the reactant species, and D^{+} and A^{-} are the product species after electron transfer.

Marcus was the first to study the dependence of rate of electron transfer on different factors. According to him the rate constant depends on so-called reorganization energy (λ) which can be defined as the energy required to reorganize the reactants and the surrounding solvent to a state that is conducive to electron transfer. Marcus theory was based on the dielectric continuum model which doesn't take into consideration the molecularity of the solvent. In 1992/93, Marcus theory was generalized by M.Tachiya [26–28] by taking into account the fluctuation of the local electrostatic potential produced by the fluctuating polar molecules in the solvent. The

transfer rate is described in terms of the distribution of the potential difference and it can be applied to any model of the solvent hence it is called generalized Marcus theory. According the Marcus theory and generalized Marcus theory by M.Tachiya the rate constant (k) for electron transfer between D and A which are separated by a distance 'R' is given by

$$k = \frac{2\pi}{\hbar}\frac{J^2}{(4\pi k_B T\lambda)^{1/2}} exp\left[-\frac{(\Delta G+\lambda)^2}{4k_B T\lambda}\right] \tag{1.4}$$

where $\hbar$ is the Plank constant divided by 2π. J is the transfer integral which can be determined by the initial state and the final state electronic wave functions, k_B is the Boltzmann constant, and T is the absolute temperature. λ is the reorganization energy, expressed as

$$\lambda = \frac{e^2}{2}(\varepsilon_{op}^{-1} - \varepsilon_s^{-1})\left(\frac{1}{a}+\frac{1}{b}-\frac{2}{R}\right) \tag{1.5}$$

where e is the electron charge, ε_{op} and ε_s are the orbital and static dielectric constants of the solvent, respectively. a and b are the radii of the donor and acceptor, respectively. ΔG is the gibbs free energy change of the reaction.

According to equation 1.4, the rate constant depends on the D-A distance R through the transfer integral J, λ, and ΔG. The transfer integral J is expressed as

$$J^2 = J_0^2 exp[-\beta\{R-(a+b)\}] \tag{1.6}$$

β is the overlap distance factor and the value of β is roughly 1 $Å^{-1}$. J_0 is the transfer integral when there is no overlap of wave functions. The free energy change of the reaction is expressed as

$$\Delta G = IP - EA - \Delta g_s - e^2/R \tag{1.7}$$

where IP is the ionization potential of the donor, EA is the electron affinity of the acceptor, Δg_s is the solvation energy of the produced ion pair and is given by

$$\Delta g_s = \frac{e^2}{2}(1-\varepsilon_s^{-1})\left(\frac{1}{a}+\frac{1}{b}-\frac{2}{R}\right) \tag{1.8}$$

and $-e^2/R$ is the Coulomb attractive energy between the produced ion pair. The electron transfer rate constant depends on the radius of the donor and acceptor, reorganization energy of the solvent, donor-acceptor distance, free energy change of the reaction which in turn depends on the solvation energy of the produced ion pair, polarity of the solvent, dynamic properties of the solvent, and temperature.

The electron transfer is homogeneous if the transfer is between two molecules and heterogeneous if it is between a molecule and an electrode. In electrochemical sensors, our interest is in the heterogeneous electron transfer since we study the electron transfer between an electrode surface and the analyte of interest in the electrolytic solution.

1.4 Electrode/electrolyte interface

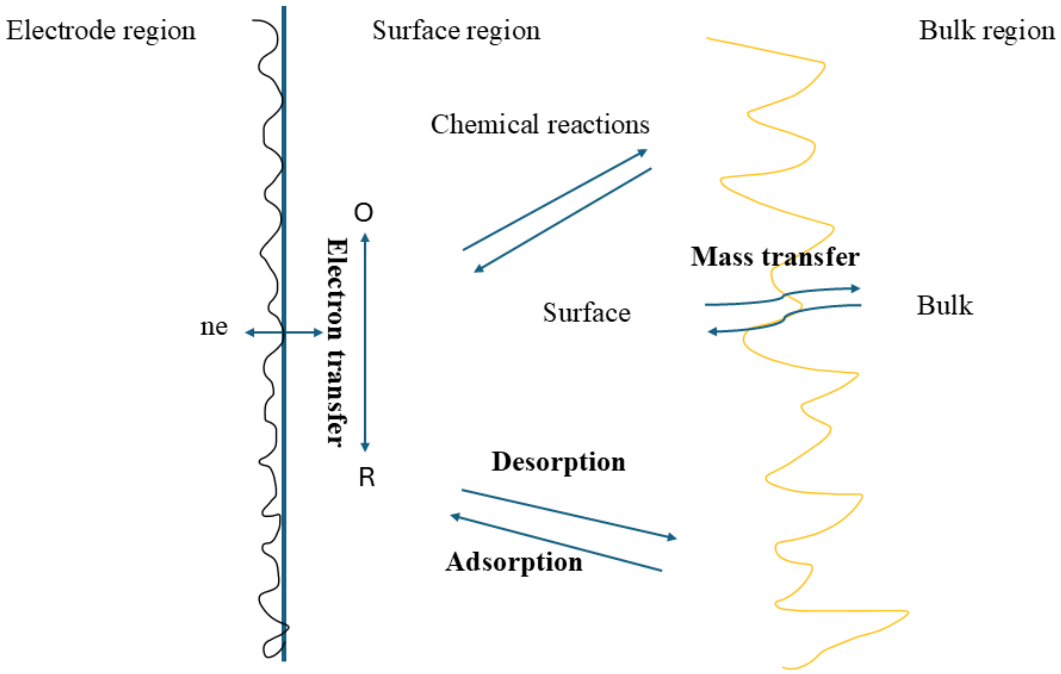

Fig. 1.4 Various processes occurring at the electrode/electrolyte interface.

The electrode-electrolyte interface is a dynamic region where various processes occur, including adsorption, desorption, mass transfer, and electron transfer. It is important to understand the various processes and factors that affect the electron transfer (or charge transfer) at the interface. We are concerned with the electrode/electrolyte

interface and the events that occur there when an electric potential is applied. Charge is transported through the electrode by the movement of electrons (and holes). The transition in electric potential crossing from one conducting phase to another usually occurs almost entirely at the interface. The sharpness of the transition implies that a very high electric field exists at the interface, and one can expect it to exert effects on the behavior of charge carriers (electrons or ions) in the interfacial region [1, 29].

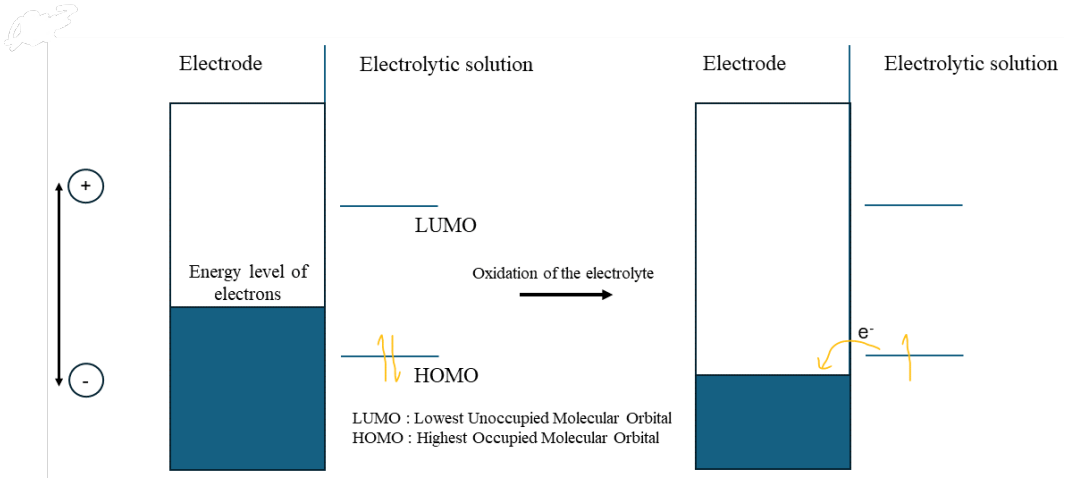

Fig. 1.5 Electron transfer process at the electrode/electrolyte during oxidation reaction. When a positive potential is applied to the electrode surface, the energy levels of the electrons on the surface of the electrode reached a lower energy level to facilitate a path to take an electron through the interface from the highest occupied molecular orbital (HOMO) of the electrolyte species.

As shown in Figures 1.5 and 1.6, by applying a negative potential to the electrode, we can rise the energy of the electrons, they can reach an energy level high enough to transfer electrons to the lowest unoccupied molecular orbital (LUMO) of the electrolyte. This is usually called as the reduction of the electrolyte as it gained an electron from the electrode surface through the interface. The current that passed due to the movement of electron from the electrode to the solution is called the reduction current. Similarly, by the application of the positive potential to the electrode surface, the energy of the electrons can be lowered and the electrons from the highest occupied molecular orbital (HOMO) of the electrolyte find a favorable path to move to the surface of the electrode. This process is called the oxidation of electrolyte as it loses an electron and the current is called the oxidation current. The whole process is called a redox (reduction + oxidation) process and the applied potentials are referred as redox potential and the current as redox current. The redox

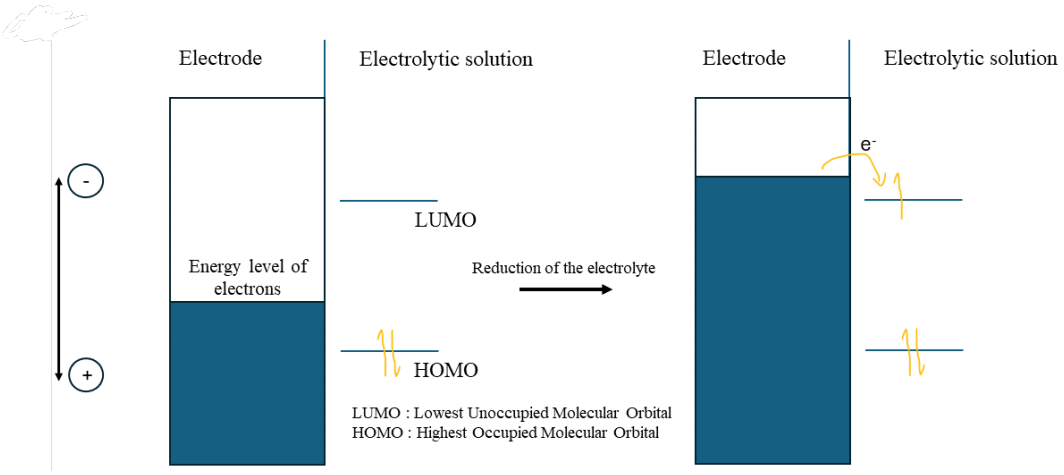

Fig. 1.6 Electron transfer process at the electrode/electrolyte during reduction reaction. Reduction process : When a negative potential is applied to the electrode surface, the energy levels of the electrons on the surface of the electrode reached a higher energy level to transfer an electron through the interface to the lowest unoccupied molecular orbital (LUMO) of the electrolyte species.

potentials at which these processes occur are related to the standard potentials, E^o, for the specific molecules or species in the system. The number of electrons that cross the electrode/electrolyte (electrochemical interface from now on referred as ECI) interface is explicitly related to the extent of the electrochemical reaction that is the amount of reactants used to generate products [1, 6, 29].

There are two types of process that occur at the electrode namely Faradaic and non-Faradaic processes. Faradaic process is usually when electrons transfer cause redox reaction of the electrolyte by passing a current and the current is called the Faradaic current. Apart from electron transfer other processes such as adsorption and desorption can occur at the ECI, the structure of the ECI varies with the application of the potential or change in the composition of the electrolytic solution. These processes are referred as non-Faradaic process where the movement of the electrons is not involved at the ECI. Though the charge (electrons) don't cross the ECI, current can flow due to the presence of the adsorbed or desorbed molecules/ions at the interface when there is a change in the potential, surface area of the electrode, or a change in the composition of the electrolytic solution. These effects must be taken into account in the interpretation of electrochemical data to get information about the charge transfer and related reactions [1].

1.4.1 Non-Faradaic Processes

An ideal polarized electrode (IPE) is defined as an electrode with no charge transfer across the electrode/electrolyte interface even when there is an external applied potential. In reality this is not happening over the whole potential range in the electrolytic solution. As there is no ET at the IPE interface with the potential change, it's behaviour can be interpreted as a capacitor [1]. A capacitor is a passive electrical component with two conductive sheets separated by a dielectric medium. The behaviour is seen as

$$C = \frac{q}{V} \tag{1.9}$$

where q is the charge stored by the capacitor in Coulombs, C and V is the potential across the capacitor in volts, V. When we apply a potential across the capacitor the charages will accumulate on the conductive metal plates of the capacitor. Our electrode/electrolyte interface behaves like a capacitor with a charge on the electrode (either positive or negative charge) and charge in the solution. The charge on the electrode and the charge in the electrolyte solution in the vicinity of the surface of the electrode made up at the interface is referred as an electrical double layer (EDL) [30, 31].

The EDL region consists of several layers where electric charges are distributed differently, affecting the electrochemical behavior of the system. The layers are differentiated into two different layers, the closest layer (up to few nanometers from the electrode surface) to the electrode surface, where ions specifically adsorb onto the electrode. This layer behaves like a parallel plate capacitor, it is termed as Helmholtz layer. The first layer of ions adsorbed onto the electrode surface, the locus of the centers of the adsorbed ions is called inner Helmholtz plane (IHP). Ions from the solvent can approach only to a certain distance from the electrode surface, the locus centers of these nearest solvated ions is called outer Helmholtz plane (OHP). Beyond the Helmholtz layer, the ions are more loosely associated and spread into the bulk electrolyte. This layer compensates for the charge on the electrode called as diffuse layer. The structure of the double layer can affect the rates of the electrode processes. Sometimes one can neglect EDL effects in considering reaction kinetics [1, 30, 31]. We can't neglect the existence of the double-layer capacitance or the presence of charging current in electrochemical experiments. When electrochemical reactiosn

involving very low concentrations of electroactive species, the charging current can be dominating the faradaic current for the reduction or oxidation reaction [1].

1.4.2 Faradaic Processes

Electrochemical cells with Faradaic processes can be either galvanic cells or electrolytic cells. Galvanic cells react immediately when brought in contact with a conductor while the electrolytic cells react upon the application of an external voltage greater than the open circuit potential (OCP). Our interest is more in electrolytic cells, these cells are widely employed to conduct desired chemical reactions to produce electrical energy. In electrochemical experiments, the behavior can be effected by various number of factors at the interface. It wise to keep some variables constant and study the effect of other variables on the electrochemical performance of a cell or a sensor. The rate of electrode reaction at the interface is affected by various factors 1) electrode variables : electrode material, surface area, geometry, surface condition, 2) external variables: temperature, pressure, time, 3) electrical variables : potential, current, resistance, 4) solution variables : concentration of the electroacitve species, pH, type of solvent, 5) mass transfer variables : diffusion, surface concentrations, adsorption. Faradaic electrode process is a heterogeneous process occurs at the electrode-electrolyte interface. The rate of reaction depends on the mass transfer to the electrode surface, and the surface effects apart from the kinetics [1, 32].

1.4.3 Mass Transfer

Mass transport involves the movement of electrolyte molecules from the bulk solution to the electrode surface, where they can participate in electrochemical reactions. Understanding the mechanisms of mass transport is essential for optimizing electrochemical performance. Mass transport in electrochemical systems can occur through three primary mechanisms: diffusion, migration, and convection. Diffusion is the movement of molecules from higher concentration to the lower concentration due to the concentration gradient [1].

Diffusion

Diffusion is generally govenrned by Fick's laws. The rate of diffusion can be mathematically described using Fick's laws of diffusion[33]. According to Fick's first law, the flux of the diffusing species is proportional to the concentration gradient. When a redox species is introduced into the solution, it creates a concentration gradient that drives mass diffusion. The flux ($\vec{J}$) of the species is given by:

$$\vec{J} = -D\vec{\nabla}C(\vec{x},t) \tag{1.10}$$

where D is the diffusion coefficient, and minus sign is due to the movement of species from high to low concentration, C is the concentration of the redox species, and $\vec{\nabla}C(\vec{x},t)$ is the concentration gradient at distance x from the electrode/electrode interface at a given time t. Fick's second law describes how the concentration of the diffusing species changes with time. It is derived from the first law and the principle of mass conservation. Mathematically Fick's second law is expressed as

$$\frac{\partial C(x,t)}{\partial t} = D\frac{\partial^2 C(x,t)}{\partial x^2} \tag{1.11}$$

where $\frac{\partial C(x,t)}{\partial t}$ is the rate of change of concentration with time and $\frac{\partial^2 C(x,t)}{\partial x^2}$ is the second derivative of concentration with respect to position.

Migration

Migration is termed as the movement of charged species in an electric field (potential gradient). Migration affects the distribution of ions near the electrode, impacting the electrochemical reactions at the interface. The migration is governed by Nernst-Planck equation [34, 35] as follows:

$$J(x) = -D\frac{\partial C(x)}{\partial x} - \frac{zF}{RT}DC\frac{\partial E}{\partial x} \tag{1.12}$$

where z is the charge (dimensionless) of the species, F is the Faraday constant, R is the universal gas constant, and $\frac{\partial E}{\partial x}$ is the potential gradient at distance x. By introducing an inert electrolyte at a higher concentration than the electroactive species the migration of ions can be minimized to negligible levels.

Convection

Convection is due to the bulk movement of the solution, which can be natural or forced convection the former is due to the density gradients while the latter is caused by stirring or flow. Convection enhances the mass transport by continually bringing fresh analyte to the electrode surface, reducing the diffusion layer thickness. Convection can be avoided by averting stirring and vibrations of the electrochemical system [36].

In practical scenarios, all three mechanisms often contribute to the mass transport of analytes. The relative importance of each mechanism depends on the specific conditions of the electrochemical sensor, such as the presence of an applied potential, stirring, or flow. The combined mass transport is governed by the generalized Nernst-Planck equation:

$$J(x) = -D\frac{\partial C(x)}{\partial x} - \frac{zF}{RT}DC\frac{\partial E}{\partial x} + vC \tag{1.13}$$

where v is the velocity of the solution.

Diffusion Layer and Limiting Current

The region near the electrode where the concentration of the analyte changes from the bulk value to the surface value is the diffusion layer. The thickness (δ) of the diffusion layer is crucial in determining the rate of mass transport. A thinner layer means faster transport of analytes to the surface [37].

The maximum current when the rate of the electrochemical reaction is controlled by the rate of mass transport is called the limiting current and the reaction is called diffusion controlled reaction. The limiting current is given by

$$I_{lim} = nFAC^*D/\delta \tag{1.14}$$

where I_{lim} is the limiting current, n is the number of electrons transferred, A is the electrode area, C^* is the bulk concentration, and δ is the diffusion layer thickness. The limiting current is directly proportional to the analyte concentration, making it a key parameter in the design and analysis of electrochemical sensors/systems. It is possible to enhance the mass transport by designing electrodes with micro or nano

features which can reduce the diffusion layer thickness or by employing stirring during the electrochemical measurements to mechanically agitate the solution in turn reduces the diffusion layer thickness.

Mass transport is a crucial factor in the performance of electrochemical sensors, determining the rate at which analytes reach the electrode surface and participate in electrochemical reactions. Understanding and optimizing the mechanisms of diffusion, migration, and convection can significantly enhance sensor sensitivity, selectivity, and response time. Advances in electrode design, stirring, and flow techniques continue to improve mass transport, driving the development of more efficient and effective electrochemical sensors [1, 32, 37].

1.4.4 Electrode Kinetics

The Nernst equation is the typical expression in electrochemistry that describes the equilibrium potential (also known as the Nernst potential) of an electrochemical cell as a function of the concentrations of the reactants and products involved in the redox reaction. It is essential for understanding and predicting the behavior of electrochemical cells under various conditions [1, 6]. In general, the overall reaction is

$$O + ne \underset{\overrightarrow{k_f}}{\overset{k_b}{\leftrightarrows}} R \tag{1.15}$$

where O is the oxidizing species and R is the reducing species with n nubmer of electrons participating in the redox reaction, k_f is the forward rate constant, and k_b is the backward reaction rate constant. The Nernst equation for the above overall reaction is

$$E = E^0 + \frac{RT}{nF} ln \frac{C_O^*}{C_R^*} \tag{1.16}$$

where C_O^* and C_R^* are the bulk concentrations, and E^0 is the standard potential. The Nernst equation includes a temperature term (T), indicating that the electrode potential depends on the temperature of the system. Higher temperatures typically increase the reaction rates and influence the equilibrium potential. Every valid

model of electrode kinetics must interpret the Nernst equation with the respective conditions.

In electrochemical kinetics, the logarithmic dependence of the overpotential (η) on the current density for an electrochemical reaction is described by the Tafel equation [1, 37], any successful model of electrode kinetics should explain the validity of their model with the Tafel equation. The Tafel equation is typically expressed in two forms, depending on whether the focus is on the anodic (oxidation) or cathodic (reduction) reaction.

$$\eta = a \pm blog(i) \tag{1.17}$$

where 'negative' sign is for the cathodic reaction while the 'positive' sign is for the anodic reaciton, a is the Tafel intercept, and b is the Tafel slope (V/decade), and i is the current. The Tafel slope b is given by

$$b = \frac{RT}{\alpha nF} \tag{1.18}$$

for the anodic reaction, and

$$b = \frac{RT}{(1-\alpha)nF} \tag{1.19}$$

for the cathodic reaction, where α is the electron transfer coefficient. It is possible to calculate the transfer rate coefficient α when we have the Tafel slopes for both anodic and cathodic reactions at the electrode [38].

Butler-Volmer Kinetics

The fundamental relationship in electrochemical kinetics that describes the current as a function of the potential at an electrode during an electrochemical reaction is the Butler-Volmer equation. It is used to model the rate of electron transfer reactions, accounting for both anodic and cathodic processes. Butler-Volmer equation [1, 37] is given by

$$i = FAk^0 \left[C_O(0,t)e^{-\alpha f(E-E^0)} - C_R(0,t)e^{(1-\alpha)f(E-E^0)} \right] \tag{1.20}$$

where k^0 is the standard rate constant, $f = F/RT$, $C_O(0,t)$ and $C_R(0,t)$ are the concentrations of the oxidized and reduced species at the interface at time 't', respectively. The transfer coefficient α reflects the symmetry of the energy barrier for the electron transfer reaction and it varies between '0' and '1'. At equilibrium conditions, the net current equals to zero and the electrodes adopts to a potential based on the bulk concentrations of the redox species. Then the Butler-Volmer equation become Nernst equation (equation 1.16) with surface concentration equalling to bulk concentration. The Butler-Volmer equation (1.20) is also expressed as current as a function of the overpotential 'η'

$$i = i_0 \left[\frac{C_O(0,t)}{C_O^*} e^{-\alpha f \eta} - \frac{C_R(0,t)}{C_R^*} e^{(1-\alpha) f \eta} \right] \tag{1.21}$$

where $\eta = E - E_{eq}$. Butler-Volmer equations are widely used in treating any problems related to heterogeneous electrode/electrolyte kinetics. For larger values of '$'eta$' we observe Tafel behaviour from the equation 1.21.

1.5 Electrochemical characterization techniques

Electrochemical sensors are a versatile and powerful system for detecting a wide range of analytes in various fields. Their potential for miniaturization makes them ideal for applications in healthcare [4, 32], environmental monitoring [39], and food safety [40, 41]. Ongoing research and development in materials science, fabrication techniques, and data integration will continue to advance the capabilities and applications of electrochemical sensors, paving the way for more efficient and accurate analytical devices. One of the key components in the fabrication of electrochemical sensors is the electrode material. In the literature, the most commonly used electrode material is carbon (graphite [3, 4], graphene, and carbon nanotubes [42]) due to their conductivity and chemical stability. Noble metals such as gold [43, 44], platinum [45, 46], and silver [47, 48] are used because of their high conductivity and catalytic properties and conductive polymers because of their flexibility and functionalization potential. Among all these materials, carbon is most widely used because of its low cost, fabrication flexibility, and ease of surface functionalization capabilities. Electrochemical sensors can be enzymatic with a specific enzyme to target a specific analyte with very high specificity or selective membranes for specific ions or

molecules [49, 50]. The other type is the non-enzymatic electrochemical sensors without the need of any enzyme [3–5]. Each type has their own advantages and disadvantages in specific applications.

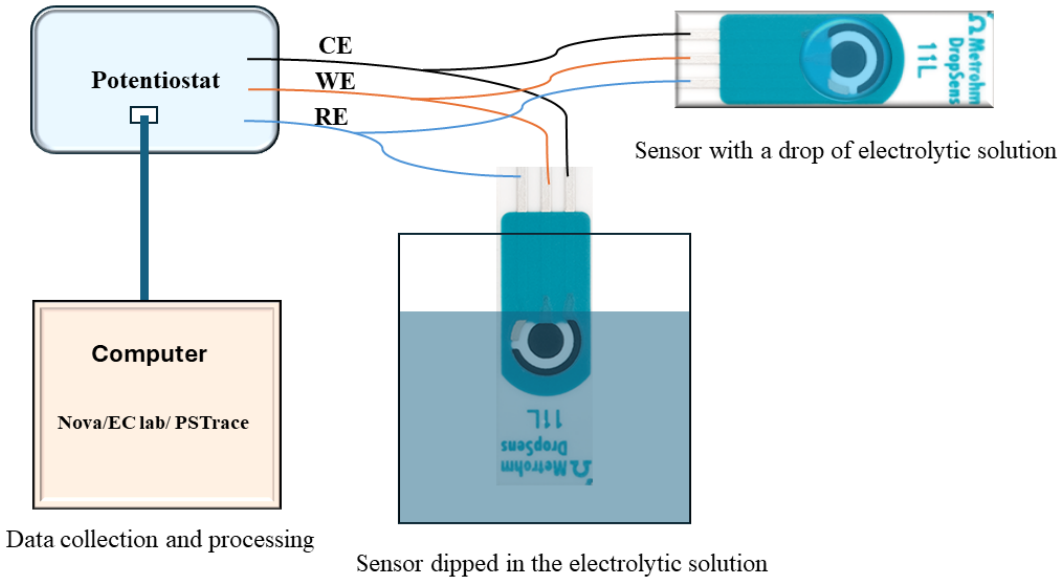

Fig. 1.7 Electrochemical sensor characterization in fully dipped condition and using a drop of the electrolytic solution on screen printed carbon working, carbon counter, and Ag/AgCl reference electrodes.

Screen-printed electrochemical sensors are a cost-effective class of sensors that have gained significant popularity for various applications. These sensors utilize screen printing technology to fabricate electrodes on various substrates like ceramics, glass, and flexible materials like paper and textiles [51–53]. Various types of screen printable inks (carbon, gold, graphite, silver, or platinum) can be used to fabricate the sensors. Screen printing is an economical method, allowing for mass production of sensors at a low cost, the technique is highly scalable, enabling the production of large batches of sensors with consistent quality. Easy to customize the design and composition of the electrodes to meet specific requirements of different applications. The compact and lightweight design makes these sensors portable and suitable for on-site and point-of-care testing. Screen printed electrode surface can be easily functionalized/immobilized with different nanomaterials or enzymes or selective ion membranes to enhance the electrochemical properties like sensitivity, selectivity, rate of reaction, and limit of detection. Screen printed carbon sensors are widely used in the research and the surface of the screen printed carbon is easily modifiable for

electrochemical peformance enhancement using novel metal nanoparticles [54, 55], or metal oxide-based nanoparticles [4, 56, 57].

As described in the introduction, an electrochemical sensor is typically made up of three electrodes with working, counter, and reference electrodes. In order to study the performance of the sensor, three electrodes of the sensor are either dipped inside an electrolytic solution (semi-infinite electrochemical cell) or a drop (limited diffusion condition, typically 100 μL) of the solution is dropped on the sensor to cover the surface of all the three electrodes as shown in Figure 1.7. There are amperometric, potentiometric, conductometric, and impedometric techniques to electrochemically characterize a sensor using . We focus on amperometric and potentiometric techniques in this work. In amperomteric techniques we apply a voltage between the working electrode and reference electrode and see the current behaviour between the working electrode and counter electrode. Voltammetric approaches are widely used in amperometric characterization of electrochemical sensors such cylic voltammetry (CV) and differential pulse voltammetry (DPV).

1.5.1 Cyclic Voltammetry

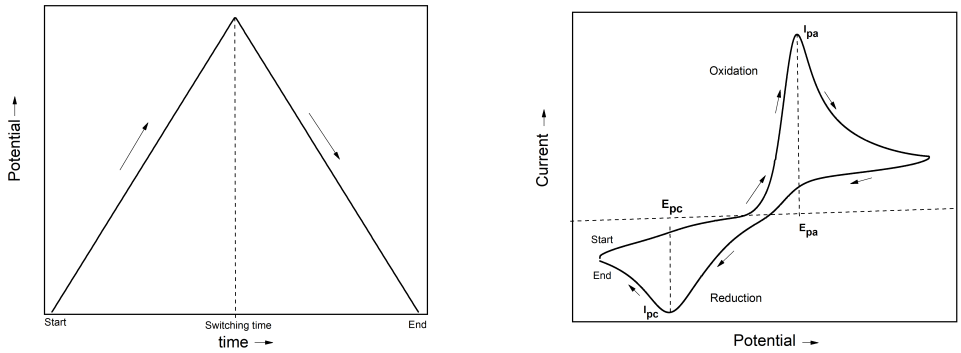

(a) (b)

Fig. 1.8 Cyclic voltammetry : (a) potential profile, (b) an example of a cyclic voltammogram.

Cylcic voltammetry is the widely used voltammetric technique to study an unknown electrochemical system [1, 29]. It can provide insights into the redox process, reaction kinetics, and stability of intermediates and products. Cyclic voltammetry is performed by applying a linearly varying potential to the working electrode in a triangluar waveform as shwon in Figure 1.8a while measuring the resulting

current between working and counter electrodes. The resulting current vs potential curve looks like a duck-shaped one commonly called as a cyclic voltammogram (an example is shown in Figure 1.8b) which provides information about the redox behaviour of the analyte.

In cyclic voltammetry, the potential is applied in the positive direction to reach a maximum applied potential and then reverses it's direction to the starting potential as shown in Figure 1.8a at a certain scan rate (scan rate is the speed at which the potential is varied with respect to time ($\nu = \frac{dE}{dt}$)). When the potential starts to increase in the positive direction the current starts to increase and reaches a maximum peak current (I_{pa}) due to the oxidation of the analyte at the oxidation peak potential (E_{pa}). In the negative direction, the analyte gets reduced and we get a maximum current (I_{pc}) at the reduction potential (E_{pc}) as shown in Figure 1.8. Two effects can be observed in the cyclic voltammetry, when the applied potential reaches the Nernst potential satisfying the Nernst equation 1.16, we observe the redox currents. Then we see that the current is not reaching zero due to the diffusion of the analytes towards the surface of the electrode after all the reactants at the surface are converted to products.

Two important parameters from the cyclic voltammogram are the ratio of the peak currents, I_{pa}/I_{pc} and the peak to peak separation, $\Delta E_p = E_{pa}\text{-}E_{pc}$. For a reversible electrochemical reaction I_{pa}/I_{pc}=1, and ΔE_p = 59/n mV at 25^oC irrespective of the scan rate. When these two conditions don't hold the reaction can be either quasireversible or irreversible.

Importance of scan rate

The scan rate defines how fast or slow the potential is applied to the surface of the working electrode. The scan rate can change the size of the diffusion layer this will effect the overall current observed in the reaction for example faster scan rates lower the diffusion layer leading to higher currents. From Randles-Sevcik's theory [1, 29, 37, 58], for a reversible ET process with freely diffusing species how the overall peak current I_p varies with scan rate can be described using the Randles-Sevcik's equation,

$$I_p = 0.446nFAC\left(\frac{nF\nu D}{RT}\right)^{\frac{1}{2}} \tag{1.22}$$

where D is the diffusion coefficient of the redox species, and C is the bulk concentration of the analyte, and A is the electroactive surface area of the electrode. For a reversible reaction the current varies linearly with the square root of the scan rate without affecting ΔE_p (at constant redox peak potentials). While for a quasireversible reaction the current varies linearly with the square root of the scan rate and the ΔE_p also changes as the scan rate changes (redox potentials shift with the scan rate). Another case is the electode-adsorbed species where the current I_p varies as follows

$$I_p = \frac{n^2F^2}{4RT}\nu A\Gamma^* \tag{1.23}$$

where Γ^* is the surface coverage of the adsorbed species. In this case, the current varies linearly with the scan rate and we should observe no variation of the peak potential with the scan rate.

If we observe these features in unknown electrochemical systems it is possible to distinguish between different reactions using Randles-Sevcik's theory. Using the equation 1.22, we can calculate the electroactive surface area of the working electrode, and diffusion coefficients of the analytes under study.

Calculation of kinetic parameters

In 1979, a method was proposed by E.Laviron [38] to calculate the kinetic rate constant for a diffusion less system meaning without any diffusion effects (Electrical double layer effects) when potential sweep voltammetric techniques are used. When the current is linearly varying with the square root of the scan rate and the redox peak potentials are varying linearly with the natural logarithm of the scan rate this model can be applied. In Laviron model, the cathodic peak potential

$$E_{pc} = E^0 - \left(\frac{RT}{\alpha nF}\right) ln\left[\frac{\alpha}{|m|}\right] \tag{1.24}$$

and the anodic peak potential

$$E_{pa} = E^0 + \left(\frac{RT}{(1-\alpha)nF}\right) ln\left[\frac{(1-\alpha)}{|m|}\right] \tag{1.25}$$

with α being the electron transfer rate coefficient and

$$m = \left(\frac{RT}{F}\right)\left(\frac{k}{n\nu}\right) \tag{1.26}$$

where k is the rate constant. Experimentally two conditions have been derived to calculate α and k by considering ΔE_p. If nΔE_p > 200 mV then equations 1.24 and 1.25 can be used to determine α by plotting the peak potentials with respect to ln(ν). Then the rate constant 'k' is calculated using the equation

$$logk = \alpha log(1-\alpha) + (1-\alpha)log\alpha - log\left(\frac{RT}{nF\nu}\right) - \alpha(1-\alpha)\frac{nF\Delta E_p}{2.3RT} \tag{1.27}$$

This is only valid for nΔE_p > 200 mV. If nΔE_p < 200 mV, then a different procedure has to be followed as described in [Laviron model paper]. In most of the cases, we usually find the first case so the equations 1.24, 1.25, and 1.27 are freely used in the literature to characterize different electrochemical systems. Note that these equations are only used by assuming no double layer effects without considering the diffusion layer effects. The EDL heavily effects the overall kinetic rate constant but only the first order effects are considered in the Laviron model to calculate the first order kinetic rate constant.

Throughout this work, cyclic voltammetry is mostly used to initially characterize all the electrochemical sensors in chapters 3, 4, 5, and 6. The sensors are calibrated from the oxidation peaks of cyclic voltammograms to obtain the sensitivity and limit of detection (LOD) is evaluated. Kinetic parameters such as electron transfer rate coefficient and kinetic rate constant are calculated using the Laviron model to compare the kinetic performance of different electrochemical sensors.

1.5.2 Chronoamperometry

Chronoamperometric technique is used to study the transient behaviour of the redox species with concentration, how the current changes with time and with concentration. The Cottrell equation [1, 6] is widely used to describe chronoamperometry, the equation describes the variation of current with respect to the change in concentration of the analyte as follows:

$$\Delta I = \frac{nFA\sqrt{D}}{\sqrt{\pi \Delta t_0}} \Delta C \tag{1.28}$$

where Δt_0 is the time interval between the analyte injection and the increment in current.

Chronoamperometry is done at a fixed potential (E_0) unlike cyclic voltammetry where a range of potential is applied. The fixed potential to be applied can be obtained from the intial CV measurements where we observe the redox peak currents and potentials depending on the type of the analyte and surface of the electrode under study. The usual trend of a chronoamperogram is shown in Figure 1.9, initially the current reaches a certain value depending on the concentration of the analyte and reaches a stable value as the diffusion of the analyte towards the surface of the electrode tends to reach null. When the concentration of the analyte changed then the current increases and reaches a stable current value, this repeats as the concentration of the analyte keeps changing. Calibration can be performed by plotting the change in current with respect to the change in concentration of the analyte. The slope of the calibration gives the sensitivity of the electrochemical sensor.

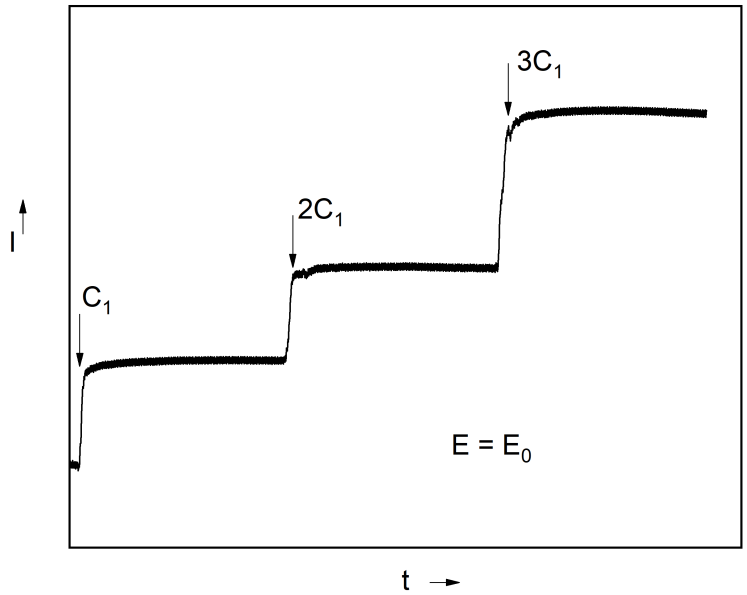

Fig. 1.9 An example of a chronoamperogram at a fixed potential.

Cyclic voltammetry can not be employed as it is difficult to observe the reduction current of oxygen in a phosphate buffer solution without any peaks. Therefore,

chronoamperometry is used to electrochemically sense dissolved oxygen (DO) in 10 mM phosphate buffer solution at pH 7.4 in the first part of chapter 6. Calibration of the sensors is performed by taking the average stable response of the reduction current of oxygen at each concentration of DO and the slope of the calibration is presented as the sensitivity of different sensors towards DO.

1.5.3 Potentiometric Sensing

Potentiometric sensing is based on the measurement of the potential difference between two electrodes namely reference electrode and working (or ion selective) electrode [1, 59, 60]. In chronoamperometry, a fixed potential between reference and working electrodes is applied and current is measured between working and counter electrodes while in potentiometry, the potential difference (open circuit potential (OCP)) is measured between reference and working electrodes. The working electrode can be replaced by a ion-selective electrode which is specific to the target ion of interest. In potentiometric sensing typically two electrode system is used instead of a three electrode system with reference and working or ion-selective electrode without counter electrode.

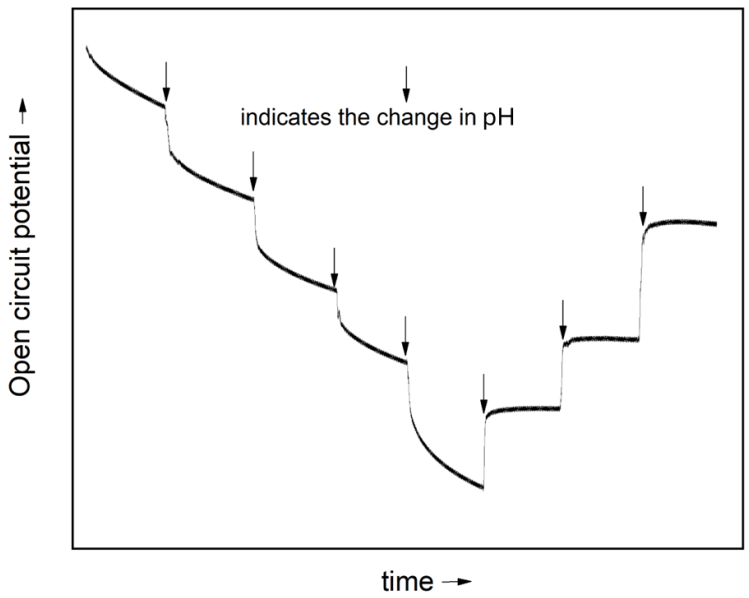

Fig. 1.10 An example of a chronopotentiometric graph

Potentiometric sensing is most widely used in pH measurements [61, 62], and ion concentration measurements [63–65]. As an example, measurement of open circuit potential with time in chronopotentiometry is shown in Figure 1.10 for a pH sensor. An average OCP in the stable region of the response for each pH value is taken and calibration is performed by plotting the average OCP with respect to the pH of the test solution. The slope gives the sensitivity of the sensor used, this method can be easily used to electrochemically characterize different materials (nanomaterials or composites) or interfaces between the surface of the working electrode and the analyte or ions containing solution. The calibration of a sensor's pH response is usually evaluated by comparing with the Nernst response (equation 1.29) showing the variation of potential (OCP) with respect to the pH of the solution [1]. The equation is written as:

$$E = E_0 - \frac{2.303RT}{nF} pH \tag{1.29}$$

At ambient conditions with T equal to 25^o C for single electron electrode reaction, the slope of the plot is 59 mV/pH. For a 'n' electron electrode process is 59/n mV/pH. Suppose three pH sensors show sensitivities below, close to, and above 59 mV/pH then the response is usually termed as non-Nernstian, Nernstian, and super-Nernstian behaviour, respectively. Nernstian reponse usually the gold standard for any electrochemical pH sensor.

In this work, chronopotentiometry is utilized in the first part of chapter 6 to study the electrochemical pH sensing capability of ZnO and $ZnFe_2O_4$-modified and unmodified screen-printed carbon sensors in universal buffer solution covering the pH range of 2-12.

1.5.4 Differential Pulse Voltammetry

Differential pulse voltammetry (DPV) is used to study redox processes, detect trace amounts of analytes, and characterize electrochemical properties of materials [1, 37]. The technique is particularly known for high sensitivity making the technique valuable in analytical chemistry. DPV is performed by superimposing a series of small amplitude potential pulses onto a linear potential sweep. The current is measured before and at the end of each pulse, and the difference in current is

plotted against the applied potential. Therefore the technique is called 'differential pulse voltammetry'. While performing DPV, attention should be paid to the pulse amplitude (the height of the potential pulse, typically between 10-100 mV), pulse width (the duration of the pulse (20 - 100 ms)), and the pulse interval (the time between successive pulses). an example of a potential pulse profile and differential pulse voltammogram is shown in Figure 1.11. The peak current can correspond to either oxidation or reduction event of the analyte and the position of the peak corresponds to the redox potential of the analyte.

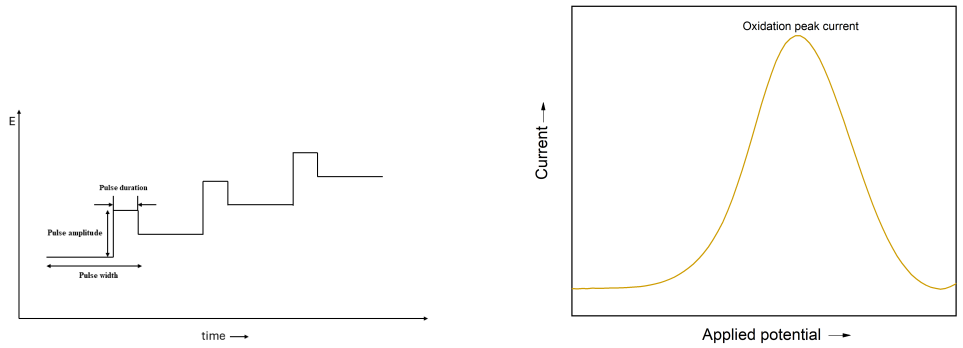

(a) (b)

Fig. 1.11 Differential pulse voltammetry : (a) potential pulse profile, (b) an example of a differential pulse voltammogram.

Calibration is easily performed to obtain the sensitivity when we have the redox peak currents. The technique is highly sensitive due to differential measurement, minimizing the background noise. and it can be applied to detect very low cocentration of analytes in the solution making it very useful in environmental monitoring and food safety. It is used to characterize the electrochemical properties of new materials, analysis of drugs, and studying drug interactions. Compared to CV which provides a comprehensive understanding of the electrochemical behaviour over a wide range of potential, DPV offers excellent sensitivity and resolution for detecting specific redox events at very low concentrations.

Cyclic voltmmetry is not very useful at low concentrations of the analytes as it is difficult to differentiate the redox peaks from the overall response. Since DPV technique is very effective at low concentrations, it is used to study the electrochemical sensing performance of three different sensors towards 5-Fluorouracil (an anti-cancer drug) in the second part of chapter 6 at low concentrations of the drug within the dosage range below 200 μM.

1.6 Conclusion

This chapter presented the main objective, motivation of the PhD research project, and summerized the whole thesis report chapter by chapter. Basic theory of electrochemical sensors, electron transfer fundamentals: inner sphere and outer sphere electron transfer, Marcus theory of electron transfer: effect of different parameters (reorganization energy and transfer integral) on electron transfer rate constant 'k', and the fundamental principles of different electrochemical characterization techniques used in this project and their significance in electrochemical sensing are discussed.

Chapter 2

Nanomaterials Synthesis and Characterization Methods

2.1 Spinel Nanomaterials

Transition multi-metal oxide nanomaterials hold significant promise for a variety of applications due to the extensive design flexibility they offer [66]. However, comprehending the diverse activities, particularly their electrocatalytic behavior, remains challenging because of the intricate nature of multi-metal compositions [67, 68]. This complexity is further amplified in materials with crystal structures that feature multiple metal occupancy sites, such as the cubic spinel system [67, 69, 70]. Grasping the origins of the electrochemical and catalytic activities in these materials is difficult due to the presence of multiple metals with varying oxidation/valence states. Nevertheless, spinel multi-metal oxides have demonstrated exceptional potential across numerous applications because of these characteristics.

Spinel oxides allow cation substitution at both bivalent and trivalent sites, enabling precise control over electronic and electrochemical properties [67, 3, 5]. This tunability enhances their electrocatalytic activity, bandgap engineering, and surface properties, which is more challenging in simple metal oxides. Spinel oxides offer a tunable bandgap (< 3 eV), allowing better control of charge transfer processes, making them ideal for electrochemical [71] and photocatalytic applications [72]. Spinel ferrites like $ZnFe_2O_4$, $NiFe_2O_4$ offer lower bandgap unlike single metal ZnO (3.2 eV) [73, 74] or TiO_2 (> 3 eV) [75, 76] making them more suitable in photocatalytic

applications [77–80]. Many metal oxides suffer from low electrical conductivity, limiting their electrochemical performance. In contrast, spinel oxides exhibit mixed electronic and ionic conductivity, facilitating better electron transfer at relatively low activation energy [81, 82]. Normal and inverse spinel configurations allow control over electron/hole conduction, making them highly adaptable for energy storage and electrochemical sensor applications [67, 83]. The presence of multiple valence states in spinel materials facilitates fast redox reactions, improving catalytic activity towards oxygen reduction reactions (ORR) [84] compared to single-metal oxides. The Fe^{3+}/Fe^{2+}, Co^{3+}/Co^{2+}, and Mn^{3+}/Mn^{2+} redox couples in spinel structures significantly enhance charge transfer efficiency, unlike conventional single metal oxides. Spinel oxides exhibit strong metal-oxygen bonding, which enhances their stability in harsh electrochemical environments where other oxides like ZnO show dissolution effects [85]. Compared to transition metal oxides like WO_3 [86] and MoO_3 [87], spinels resist phase transitions and maintain their structure under different conditions. Spinel nanomaterials have demonstrated superior performance in a variety of electrochemical applications compared to conventional metal oxides [67].

2.1.1 Spinel Crystal Structure

Spinel structure typically takes the AB_2X_4 form, if 'X' is oxygen (O) then it become spinel oxide with AB_2O_4 form with A as cation with '+2' oxidation state and B as a cation with '+3' oxidation state. The structure is typically a face centered cubic (FCC) structure with oxygen anions forming 32 tetrahedral 'Td' and 64 octahedral 'Oh' sites. In a spinel unit cell, 8 'Td' sites are occupied by A/B and 16 'Oh' sites are occupied by B/A forming a closely-packed electrically neutral system. Based on the occupancy A and B in 'Td' and 'Oh' sites the spinel is called normal, inverse, and mixed spinel. In normal spinel, 'Td' sites are occupied by A, and 'Oh' sites are occupied by B (example: $ZnFe_2O_4$ where Zn^{2+} in 'Td' sites and Fe^{3+} in 'Oh' sites) whereas in inverse spinel 'Td' sites are occupied by B by pushing A into 'Oh' sites hence, the 'Oh' sites are shared between A and B (example: $NiFe_2O_4$ where half of Fe^{3+} in 'Td' sites while remaining half of Fe^{3+} and Ni^{2+} occupy 'Oh' sites). In a mixed spinel structure, both 'Td' and 'Oh' sites are shared by A and B (example: $Ni_{0.5}Zn_{0.5}Fe_2O_4$, in this mixed spinel structure Zn^{2+} and half of Fe^{3+} occupy 'Td' sites and the remaining half of Fe^{3+} and Ni^{2+} occupy 'Oh' sites) [3, 5].

Spinel materials are called with different names based on the trivalent cation in the composition of the material. If the trivalent cation is Fe(III) then the spinel is referred as ferrite [3], cobaltite with Co(III) [70], manganite with Mn(III) [88], bismuthate with Bi(III) [5], and chromite with Cr(III) [89]. Due to spinel materials higher thermal, chemical stability, and electrical neutrality they are most widely studied as new catalytic materials in electrochemical sensors [3, 5], batteries [90, 91], supercapacitors [67, 92, 93], and fuel cells [67, 94].

Various synthesis methods have been proposed for spinels in the literature following dry and wet methods to get desired properties of the materials. Dry method follows the combustion-based synthesis [3, 95] where as wet method has different techniques to synthesize spinel nanomaterials. Hydrothermal/solvothermal method is most widely used following the wet route, then there are co-precipitation method, sol-gel, solvent deficient, and sonochemical methods. Based on the design and desired properties of the nanomaterials the synthesis method can be adopted [83].

By playing with the composition of the spinel it is possible to achieve interesting material properties by producing multi-metal spinel oxides with many degrees of freedom. The composition of the spinel can be easily modified by inserting different transition metal ions with different ionic sizes, oxidation states, different proportions of bivalent cations and trivalent cations by maintaining the structural neutrality. Different metal cations occupy different sites depending on their oxidation states and crystal field stabilization energies [96, 97].

2.1.2 Crystal Field Stabilization Energy (CFSE)

Crystal field (CF) theory was implemented by Hans Bethe as a model for understanding the optical and magnetic properties of metal complexes. Main importance is to achieve results essentially on the basis of the molecular symmetry consideration. In this theory, the effects of the presence of ligands which lower the symmetry around the metal ion on the energy levels of the metal ion are modelled. The metal ion is supposed to behave as a free ion which is surrounded by the ligands. Ligands are negatively charged points which interact electrostatically with the metal ion [96, 97]. The interaction (CF interaction) between the ligands and the d-orbitals removes the degeneracy of the d-orbitals leading to the orbitals splitting. To understand better first we have a look into the five d-orbital lobes namely d_{xy} (lobes in-between x and

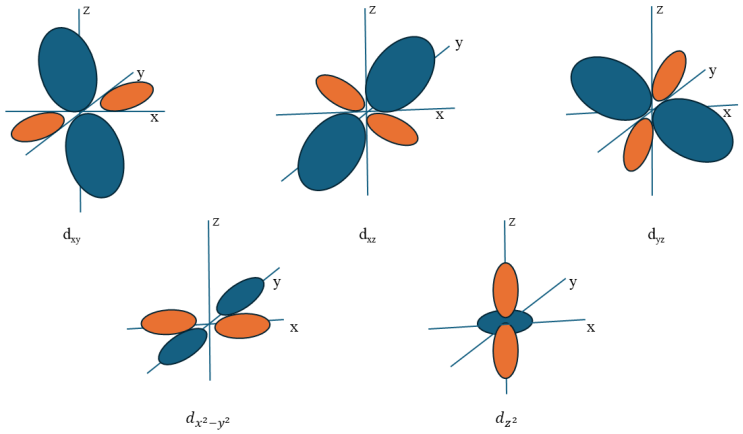

Fig. 2.1 Five different d-orbital lobes.

y axes), d_{xz} (lobes in-between x and z axes), d_{yz} (lobes in-between y and z axes), $d_{x^2-y^2}$ (lobes on x and y axes), and d_z^2 (two lobes on z axis and a donut on xy plane) as illustrated in Figure 2.1.

The d-orbital spiltting depends on the type of metal-ligand complexes, we will look into two types of metal-ligand complexes namely octahedral and tetrahedral complexes.

Octahedral Complexes

In an octahedral metal-ligand complex, the metal ion is in the center (at the origin) of the axes while 6 ligands are on the axes (x, y, and z) as shown in Figure 2.2. Due to the presence of ligands points on the axis the on axis d-orbital lobes experience very high repulsion from the ligand electrons and the orbital lobes get split. The off-axis lobes experience a very low repulsion hence the on axis lobes pushed to high energy levels and off-axis lobes to low energy levels (get more stabilized) compared to the original degenerated d-orbital energy level as depicted in Figure 2.2. This splitting of d-orbital energy levels is known as crystal field splitting and Δ_o or Δ_{Oh} is the octahedral crystal field splitting energy.

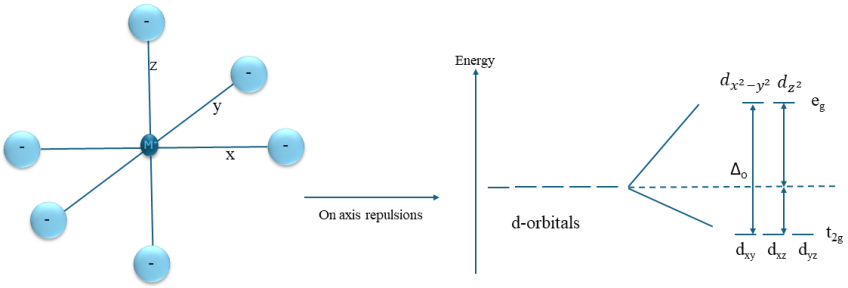

Fig. 2.2 Octahedral metal-ligand complex and d-orbital splitting due to very high on axis repulsion between the ligand electrons and d-orbital lobes.

In general, electrons get filled from lower energy to higher energy level orbitals. In the case of octahedral complexes, first d_{xy}, d_{xz}, and d_{yz} should be filled (t_{2g} level) with one electron and then to pair an electron with the filled electron an energy is required, this energy is called as the pairing energy (PE). If this energy is higher than Δ_o then the electron would move to higher energy levels (e_g level: $d_{x^2-y^2}$ and d_z^2), this situation is called the weak field situation ($\Delta_o <$ PE). If PE is lower than Δ_o then the electron gets paired with the first filled electron and the situation is termed as strong field as Δ_o is much higher than the pairing energy. Octahedral complexes are termed as low spin as the electrons have high chance of getting paired with low energy electrons due to low pairing energy lower than Δ_o.

Crystal field spiltting depends on the oxidation state of the metal and strength of the ligand [96, 97]. If the ligand is a strong field ligand the separation between the orbitals is higher (large Δ_o) and if the ligand is a weak field ligand the separation between the orbitals is lower (small Δ_o). In the spectrochemical series, the weak field ligands are usually halides with this order

$$I^- < Br^- < Cl^- < F^- < OH^- < H_2O < NH_3 < CO < CN^-$$

where I^- is the very weak ligand while CN^- is the very strong ligand.

Tetrahedral Complexes

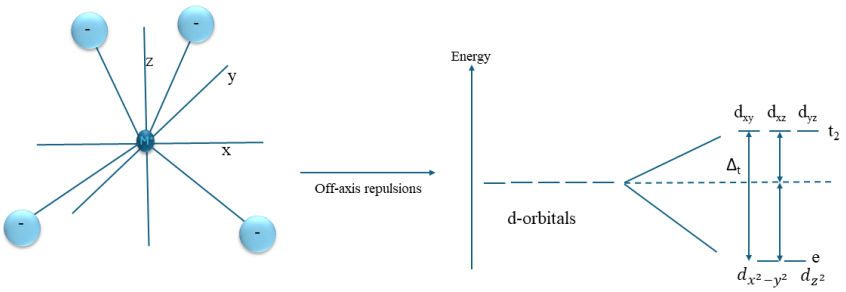

Fig. 2.3 Tetrahedral metal-ligand complex and d-orbital splitting due to off-axis repulsion between the ligand electrons and d-orbital lobes.

Tetrahedral complexes have four ligands off-axis with metal ion at the origin as shown in Figure 2.3. This case the off-axis lobes experience a repulsion from the off-axis ligand electrons and the d-orbital lobes get spilt as presented in Figure 2.3 but the repulsions are not that strong as in the case of octahedral complex hence the tetrahedral splitting energy Δ_t is lower than the octahedral splitting energy (Δ_o). This is due to poor overlap of ligand and metal orbitals. The pairing energy is higher than Δ_t hence tetrahedral complexes in general are high spin as the electrons can easily move to high energy levels without getting paired with the low energy electrons [96, 97].

Crystal field stabilization energy (CFSE) is the energy difference between ligand field and isotropic field or spherical field when there is no splitting of d-orbitals. For an octahedral complex CFSE is given by

$$CFSE_{Oh} = nt_{2g} \times \frac{3}{5}\Delta_o - ne_g \times \frac{2}{5}\Delta_o + PE \tag{2.1}$$

where nt_{2g} and ne_g are the number of electrons in t_{2g} and e_g energy levels, respectively. For a tetrahedral complex CFSE is calculated as

$$CFSE_{Td} = ne \times \frac{2}{5}\Delta_t - nt_2 \times \frac{3}{5}\Delta_t + PE \tag{2.2}$$

where ne and nt_2 are the number of electrons in e and t_2 energy levels, respectively.

CFSE depends on the type of d-orbital splitting, number of d-orbital electrons (oxidation state of the metal), spin pairing energy, type of spin either high or low spin (type of ligand: strong or weak) [96].

2.1.3 Application of Spinel Nanomaterials: State of the Art

Among different classes of spinel nanomaterials, ferrites are studied by several authors with different bivalent cations due to their excellent magnetic, optical, electrical, and chemical properties. Carbon-based electrochemical sensors (carbon paste, glassy carbon, screen-printed carbon) modified with ferrite-based nanomaterials is a well performing approach in achieving high sensitivity and selectivity towards different molecules/drugs [83] crucial in biomedical applications. In the class of ferrite nanomaterials, $NiFe_2O_4$ (nickel ferrite) nanomaterials are very interesting as sensing materials in electrochemical sensors. Nickel ferrite posses an inverse spinel structure with $(Fe^{3+})_{Td}(Ni^{2+}Fe^{3+})_{Oh}O_4$ distribution in the crystal lattice structure. It is reported in the literature that nickel ferrite acts as a p-type semiconductor with hole hopping in the lattice sites [3, 98, 99]. Nickel ferrite or nickel ferrite-based composites are most widely used in last few years as a sensing material to improve the electrochemical sensing performance in detecting different analytes in biomedical applications.

Table 2.1 Electrochemical sensing performance of $NiFe_2O_4$ in last few years.

Analyte	Technique	Linear range (μM)	LOD (μM)	Reference
Nitrite	CA	0.1-1000	0.1236	[100]
H_2O_2	AMP	4.5×10^{-3}-1320	12.4×10^{-6}	[101]
Bisphenol A	DPV	0.02-12.5	0.006	[102]
Ascorbic acid	DPV	0.5-100	0.1	[103]
Folic acid	DPV	0.1-500	0.034	[104]
Serotonin	DPV	0.1-300	0.07	[105]
Acetaminophen	DPV	1-90	0.49	[106]
Uric acid	DPV	0.398-6.761	0.15	[107]

$NiFe_2O_4$ nanomaterials are used in sensing nitrite in water samples, ascorbic acid and folic acid, H_2O_2, and many other drugs and molecules. The table 2.1

shows the electrochemical sensing performance of nickel ferrite alone with different structure/morphology based on the synthesis method used towards different analytes. Nickel ferrite is also used in combination with other materials to form composites to enhance the electrochemical sensing performance of nickel ferrite towards different analytes. Based on the type of electrochemical technique used the nickel ferrite-based sensors performed very well in different linear ranges achieving very low limit of detection (LOD) towards different analytes.

The other interesting ferrite material is $ZnFe_2O_4$ (zinc ferrite) with normal spinel having $(Zn^{2+})_{Td}(Fe^{3+})_{Oh}O_4$ cation distribution in the lattice structure [3]. Zinc ferrite acts as a n-type material with electron transfer due to its ion distribution in 'Td' and 'Oh' sites unlike nickel ferrite [3, 99, 108]. Zinc ferrite is also very well performing spinel ferrite in electrochemical sensing applications. Zinc ferrite is used as an excellent sensing material on carbon-based electrochemical sensing platforms in the literature. Table 2.2 shows the electrochemical performance of zinc ferrite on carbon-based electrochemical sensors in crucial analytes/drug detection.

Table 2.2 Electrochemical sensing performance of $ZnFe_2O_4$ in previous works.

Analyte	Technique	Linear range (μM)	LOD (μM)	Reference
Dopamine	AMP	0.002-0.6	0.0004	[109]
Glucose	DPV	10-100	0.8	[110]
Sertraline	DPV	0.07-300	0.02	[111]
Acetylcholine	DPV	0.08-500	0.024	[112]
Acetaminophen	DPV	0-500	0.29	[113]
Sudan I	DPV	1-500	0.03	[114]

The properties of nickel ferrite/zinc ferrite can be enhanced/modified by changing the composition of the bivalent cations or trivalent cations with other suitable cations. Depending on the ionic size and possible oxidation states the cation can have, and the crystal field stabilization energy, the spinel structure maintains the same crystal structure or the spinel can be modified into another type possesing different properties which will lead to different electrochemical activity.

2.2 Material Synthesis and Characterization

Nanomaterials synthesis method plays a crucial role in obtaining the desired properties. There are several methods reported for the synthesis of spinel metal-oxide nanomaterials in the literature namely hydrothermal, co-precipitation, sol-gel, solvothermal, auto combustion, and electrospinning [115, 95, 116–118]. Hydrothermal or solvothermal methods can produce highly crystalline, ultra-fine material, and environmentally friendly methods but require extreme experimental conditions [119–121]. Co-precipitation technique offers low cost, homogeneous, high purity materials but there is a possibility of impurities and higher reaction process time [121]. Sol-gel synthesis is known for its control over particle size, homogeneous ultra-fine particles whereas its high cost and toxic reagents is a problem [122, 121, 123]. Electrospinning method can provide particles with high surface area and porosity while the use of toxic reagents and the number of parameters that must be controlled lead to avoid this method as a first choice of synthesis for spinel oxides [124]. Due to its simplicity, cost effectiveness, purity, faster reaction time, and no requirement any organic, aqueous, or toxic solvents, in this work we used the combustion synthesis method proposed in the literature [95] to synthesize different types of spinel metal oxide nanomaterials.

2.2.1 Combustion Synthesis

Combustion synthesis follows principles similar to those of propellant chemistry, where the propellant is a chemical mixture burned to produce thrust in rockets and consists of a fuel and an oxidizer [125, 126]. A fuel is a substance that combusts when combined with oxygen, producing gas for propulsion. An oxidizer is an agent that releases oxygen to react with the fuel. The ratio of oxidizer to fuel is known as the mixture ratio. Propellants are classified according to their physical state: solid, liquid, or hybrid. Combustion reactions can become explosive if the mixture ratio is not controlled or if the reaction occurs in a closed vessel [127, 128].

Combustion of a suitable combination of an oxidizer and a fuel can generate the exothermicity required for the simultaneous synthesis of oxide ceramic powders. Oxidizers commonly used include metal nitrates, ammonium nitrate, and ammonium perchlorate, while successful fuels encompass urea, carbohydrazide, glycine, among others. Typically, metal nitrates such as $M(NO_3)_2$ x$\cdot$ H_2O (where M can be Mg,

Mn, Fe, Co, Ni, Cu, Zn, Se, Ca, Ba) and $M(NO_3)_3$ x· H_2O (where M can be Al, La, Nd, Fe, Y, Cr, Bi) serve as effective oxidizers, though metal perchlorates are considered hazardous due to their potential to form explosive metal azides. Fuels are usually organic compounds, particularly those containing nitrogen, which also act as complexing agents in the precursor, preventing inhomogeneous precipitation before combustion. Nitrogen-rich fuels are especially effective at preventing complexation, ensuring that when a fuel is added to a metal nitrate solution, it forms a clear liquid without precipitation. Hydrazides ($RNHNH_2$) are excellent fuels, with urea (NH_2-CO-NH_2) being the simplest. Upon oxidative decomposition, urea can either produce NH_3 and CO_2 or N_2, H_2, and CO_2; complete combustion leaves no residue, ensuring purity. Combustion methods are particularly well-suited for producing multicomponent metal oxides, resulting in compositionally homogeneous, fine particles with low impurity content. The exothermic redox decomposition of these oxidizer-fuel mixtures is initiated at relatively low temperatures, typically between 250°C and 500°C. The properties of the resulting products are influenced by the nature of the fuel and the oxidizer/fuel ratio. Many technologically significant ceramics have been synthesized using these methods [129, 130].

The combustion chemical reaction can be generalized as follows with a single metal nitrate as an oxidizer and a fuel:

$A(NO_3)_x$ + Fuel $\rightarrow$ AO_y + H_2O + Gases(N_2, NH_3, CO_2, CO)
where $A(NO_3)_x$ represents the metal nitrate, and AO_y is the metal oxide product. In the typical case of spinel metal oxides, there are two metal nitrates and a fuel therefore the reaction is written as follows:

$A(NO_3)_2$ + $B(NO_3)_3$ + Fuel $\rightarrow$ AB_2O_4 + H_2O + Gases(N_2, NH_3, CO_2, CO)
where $A(NO_3)_2$ and $B(NO_3)_3$ are two different metal nitrates, and AB_2O_4 is the resulting spinel metal oxide.

The auto-combustion process undergoes 5 different steps in a very short time upon heating at low temperatures (250 to 500°C). 1) *Dehydration*: removal of water content from the redox mixture, 2) *decomposition*: metal nitrates and fuel molecules breakdown, 3) *ignition*: initiation of combustion reaction due to exothermic interactions, 4) *propagation*: rapid propagation of the combustion through the reaction mixture, resulting in the formation of metal oxide particles, and 5) *cooling*: the reaction product cools down to room temperature (RT), yielding fine metal oxide powders.

In this work, 17 different spinel-based materials and ZnO are synthesized using auto-combustion synthesis.

2.2.2 Synthesis Procedure

Chemicals

$Zn(NO_3)_2{\cdot}6H_2O$ (Zinc nitrate hexahydrate), $Ni(NO_3)_2{\cdot}6H_2O$ (Nickel nitrate hexahydrate), $Fe(NO_3)_3{\cdot}9H_2O$ (Iron nitrate nonahydrate), $Cr(NO_3)_3{\cdot}9H_2O$ (Chromium nitrate nonahydrate), and $Bi(NO_3)_3{\cdot}9H_2O$ (Bismuth nitrate nonahydrate) are purschased from Sigma-Aldrich and used without any further modification as oxidizers, and $C(NH_2)_2O$ (Urea) is the fuel. Molecular weights of metal nitrates and urea are listed in table 2.3.

Table 2.3 Molecular weight of different reactants

Reactant	Molecular weight (g/mol)
$Ni(NO_3)_2{\cdot}6H_2O$	290.795
$Zn(NO_3)_2{\cdot}6H_2O$	297.482
$Fe(NO_3)_3{\cdot}9H_2O$	403.997
$Cr(NO_3)_3{\cdot}9H_2O$	400.15
$Bi(NO_3)_3{\cdot}9H_2O$	485.07
$C(NH_2)_2O$	60.055

Auto-combustion Synthesis

The synthesis is performed to yield 1g of final product. The number of moles required for each reactant is calculated using the below formula:

$$n_m = \frac{Y}{MW} \tag{2.3}$$

where n_m is the number of moles, Y is the yield, and MW is the molecular weight of the reactant. The number of moles (n_m) is adopted based on the final composition of the product. For example, if the final product is $NiFe_2O_4$, then n_m moles of nickel nitrate, 2 times n_m moles of iron nitrate, and n_m moles of urea are used in the redox

mixture. Stochiometric proportion of 1:1 mole ratio is always maintained between the respective bivalent cation nitrate and the fuel urea.

Table 2.4 Amount of reactants used in the auto combustion synthesis

Material	N.n (g)	Z.n (g)	I.n (g)	C.n (g)	B.n (g)	Urea (g)
$NiFe_2O_4$	1.251	-	3.474	-	-	0.258
$Zn_{0.2}Ni_{0.8}Fe_2O_4$	0.977	0.249	3.394	-	-	0.252
$Zn_{0.4}Ni_{0.6}Fe_2O_4$	0.733	0.499	3.394	-	-	0.252
$Zn_{0.6}Ni_{0.4}Fe_2O_4$	0.489	0.749	3.394	-	-	0.252
$Zn_{0.8}Ni_{0.2}Fe_2O_4$	0.244	0.999	3.394	-	-	0.252
$ZnFe_2O_4$	-	1.249	3.394	-	-	0.252
$ZnCr_{0.25}Fe_{1.75}O_4$	-	1.238	2.941	0.416	-	0.249
$ZnCr_{0.5}Fe_{1.5}O_4$	-	1.243	2.533	0.836	-	0.251
$ZnCr_{0.75}Fe_{1.25}O_4$	-	1.246	2.116	1.258	-	0.252
$ZnCrFeO_4$	-	1.249	1.697	1.681	-	0.252
$ZnCr_2O_4$	-	1.279	-	3.441	-	0.258
$ZnBi_{0.25}Fe_{1.75}O_4$	-	1.065	2.531	-	0.434	0.215
$ZnBi_{0.5}Fe_{1.5}O_4$	-	0.937	1.909	-	0.764	0.189
$ZnBi_{0.75}Fe_{1.25}O_4$	-	0.836	1.419	-	1.022	0.169
$ZnBiFeO_4$	-	0.744	1.009	-	1.213	0.151
$ZnBi_2O_4$	-	0.544	-	-	1.775	0.109
ZnO	-	3.659	-	-	-	0.739
$ZnO/ZnFe_2O_4$	-	2.499	3.394	-	-	0.252

As a first set, six different spinel ferrite materials are synthesized using nickel nitrate, zinc nitrate, and iron nitrate as oxidizers to produce $Zn_xNi_{1-x}O_4$ (x = 0, 0.2, 0.4, 0.6, 0.8, 1) nanomaterials.

Second set of the synthesis is to introduce Cr^{3+} ions into the crystal structure of $ZnFe_2O_4$ nanomaterial. Hence, zinc nitrate, chromium nitrate, and iron nitrate are used as oxidizers in producing $ZnCr_xFe_{2-x}O_4$ (x = 0, 0.25, 0.5, 0.75, 1, 2) nanomaterials.

In the third set, a larger ionic sized Bi^{3+} ions are introduced into $ZnFe_2O_4$ nanomaterial, therefore bismuth nitrate, iron nitrate, and zinc nitrate are used as

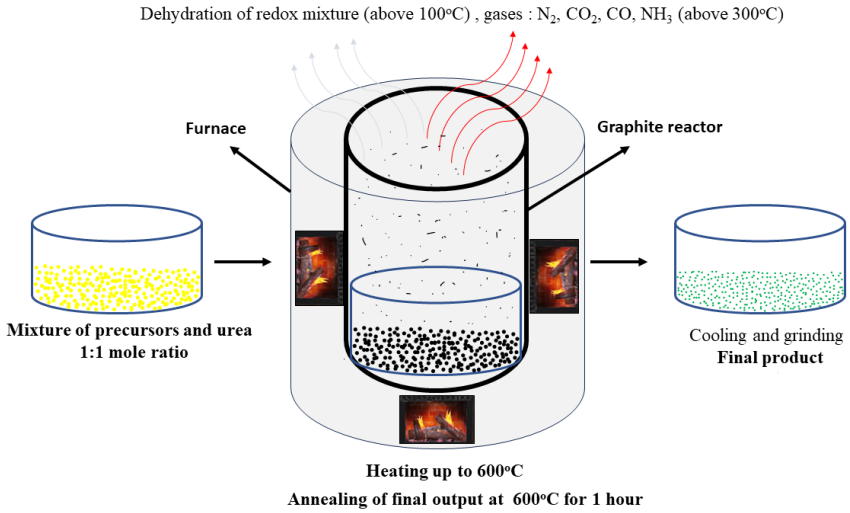

Fig. 2.4 Auto combustion synthesis.

oxidizers in preparing the redox mixture with urea to produce $ZnBi_xFe_{2-x}O_4$ (x = 0, 0.25, 0.5, 0.75, 1, 2) nanomaterials.

The fourth and final set of the synthesis, ZnO interfaced with $ZnFe_2O_4$ is produced. ZnO is synthesized using zinc nitrate and urea, and ZnO/$ZnFe_2O_4$ is synthesized using zinc nitrate and iron nitrate but double the number of moles of zinc nitrate is used in the redox mixture different from the synthesis of zinc ferrite.

The synthesis of different materials in four parts described above is performed by following the same procedure inspired from the literature [95]. The auto-combustion synthesis scheme is shown in Figure 2.4. The amount of each reactant used in the synthesis of each material is reported in table 2.2. As a first step in the synthesis, based on the composition of the final material, metal nitrates and urea are weighed according to table 2.4 using a balance. Then the oxidizing and reducing agents are mixed in a crucible to make a redox mixture. The crucible with the redox mixture is kept inside a graphite reactor, and the graphite reactor is placed in a furnace. The graphite reactor is heated inside the furnace up to 600°C. The dehydration of the mixture starts when the temperature inside the reactor reaches above 100°C. When the temperature reaches around 300°C we observe the release of gases (N_2, NH_3, CO_2, CO) upon breaking of reactant molecules [129] and exothermic reaction makes the reaction propagates faster and the temperature inside the reactor reaches 600°C in a matter of few minutes. The final output is annealed at 600°C for 1 hour to remove

any residues and the product after annealing is cooled down to RT. The final product is grounded to obtain the fine powders of different spinel-based materials.

2.2.3 Physicochemical Characterization

Synthesized materials are characterized using various techniques to investigate and understand their physical and chemical properties. Field Emission Scanning Electron Microscopy (FESEM) images are collected using the Zeiss SupraTM 50 (Oberkochen, Germany) to analyze the morphological and size features of the materials. The average particle size of different materials is estimated from FESEM images using ImageJ software (version 1.54d).

X-ray diffraction (XRD) is employed to examine the crystallographic phases, crystallite size of the particles. XRD experiments are performed on powder samples using a Panalytical Empyrean diffractometer (Malvern Panalytical, Malvern, UK). These experiments cover a 2θ range from 10° to 80° with a time step of 60 seconds (step of 0.013°/s) in Bragg-Brentano configuration, utilizing Cu Kα radiation (λ = 1.5418 Å) at 40 kV and 40 mA. The collected XRD patterns are analyzed using X'pert HighScore software to compare with different powder diffraction patterns, identifying various phases related to the material compositions and detecting any contamination. Scherrer's method is used to calculate the crystallite size of the powder samples [3, 5].

Spectroscopic characterization of materials is performed to better understand their internal features. Micro-Raman spectroscopy is first utilized using a Renishaw inVia Raman microscope to obtain information about different molecular bonds and vibrational modes. To understand the optical absorption characteristics and calculate the energy band gap of the materials—an important feature for understanding their electronic transitions, ultraviolet-visible (UV-Vis) spectroscopic measurements are conducted. A Cary 5000 ultraviolet-visible-near-infrared (UV-Vis-NIR) spectrophotometer (Varian Instruments, Mulgrave, Australia) equipped with a diffuse reflectance (DR) system is employed for UV-Vis investigations. The Tauc plot method is used to calculate the energy band gap (E_g) from the diffuse reflectance UV-Vis spectra.

Finally, surface oxidation states of the elements in different compositions of the materials and any possible contamination with elements other than those in

the composition are studied using X-ray photoelectron spectroscopy (XPS). XPS experiments are carried out with a PHI 5000 Versaprobe spectrometer equipped with a monochromatic Al Kα (1486.6 eV) X-ray source. An Ar ion gun and an electron gun are used for charge compensation. Binding energy calibration is performed by setting the adventitious C sp^3 component at 284.8 eV. Pass energies are set at 187.85 and 23.5 eV for acquiring survey and high-resolution scans, respectively. XPS full survey, high-resolution (HR) spectra, and valence band (VB) spectra are recorded to study the elemental composition, oxidation states of the elements, and to calculate the valence band minimum (E_V) of the materials, respectively. XPS spectra are processed using CasaXPS software (v2.3.23, Casa Software Ltd). All data are plotted and presented using Origin 8.5 software, all the features of the materials using the above techniques will be discussed in their respective chapters.

2.3 Electrochemical Characterization

2.3.1 Electrochemical Sensors Preparation

In order to prepare the new sensors based on spinel-based materials, firstly material solutions are prepared. Material solutions are prepared using three different solvents namely, water, methanol, and 1-butanol. From our previous knowledge [4], 3:1 material to solvent ratio is sustained in preparing the particle solutions. First to optimize the sensor performance, 2, 5, 7, 10 μL material solutions are utilized. As a reference electrochemical sensor, a three electrode electrochemical system with carbon working electrode (WE), carbon counter electrode (CE), and Ag/AgCl reference electrode is used. The newly prepared material solution is dropped on the surface of the working electrode and dried for 24 hours at 27°C. This technique of surface modification is usually referred as 'drop casting' technique. The sensors are stored in petri dishes under normal atmospheric conditions.

2.3.2 Preparation of Buffer Solution

To prepare electrolytic solution, phosphate buffer (PB) solution is used as a solvent. Phosphate buffer solution is prepared by using sodium monobasic phosphate (NaH_2PO_4) and sodium dibasic phosphate (Na_2HPO_4). The calculations for the

preparation of 0.1 molar PB at pH 7 are made by using the typical pH calculation equation of a base and acid.

$$pH = Pka + log\frac{B}{A} \tag{2.4}$$

where B and A are the concentrations of base and acid, and *Pka* value for sodium monobasic phosphate is taken as 7.21.

- The number of moles of sodium monobasic and dibasic are found to be 0.062, and 0.038.
- Then the amount is calculated by multiplying with the molecular weight of NaH_2PO_4 (119.98 g/mol) and Na_2HPO_4 (141.96 g/mol) which is equal to 7.438 g and 5.394 g, respectively.

The materials are weighed using a balance and mixed with 1 liter of deionized (DI) water in a volumetric flask and the mixture is kept in an ultrasonic bath for 30 minutes to dissolve all the phosphate in the solution to finally achieve 0.1 M PB at pH 7. The solution is stored under normal atmospheric conditions and used whenever is required for the electrochemical sensing experiments.

2.3.3 Preparation of Electrolytic Solution

For the first three parts of the work, paracetamol is used as a model/test molecule to study the performance of new sensors based on spinel materials. Electrolytic solution of paracetamol is prepared in 0.1 M PB at pH 7 at different concentration of paracetamol. As a base solution 1 mM paracetamol in 0.1 M PB at pH 7 is prepared. To calculate the amount of paracetamol required to prepare the solution, below equation is used.

$$Weight(grams) = Cocentration(moles/liter) \times Volume(liters) \times MW \tag{2.5}$$

For the dilution of electrolytic solution,

$$M_1V_1 = M_2V_2 \tag{2.6}$$

is used, where M_1 is the molarity (concentration) of the initial solution, V_1 is the volume required to make the solution with M_2 molarity (concentration of the final solution) and V_2 (final volume) volume. For the calibration studies of the sensors, 0.5 - 3 mM (steps of 0.5 mM) concentrations of paracetamol in 0.1 M PB at pH 7 are prepared. The molecular weight of paracetamol is taken as 151.163 g/mol.

Preparation anti-cancer drug solutions

In this work, as a potential application of the pure spinel-based nanomaterials, the electrochemical sensing performance towards three anti-cancer drugs such as 5-fluorouracil (5-FU), etoposide, and methotrexate is studied. 5-FU solutions are directly prepared in 0.1 M PB at pH 7 as 5-FU is easily dissolved in PB solution. Firstly 500 μM solution is prepared as a base solution for preliminary study and then for calibration 10 - 200 μM (in steps of 30 μM) solutions are prepared to stay in the pharmological concentration range of 5-FU.

It is difficult to dissolve etoposide and methotrexate directly in PB solution hence, the initial solution with 1 mM concentration is prepared in DMSO (dimethyl-sulfoxide) for each drug and then the solution is diluted to achieve 10 - 100 μM concentrations in PB solution.

2.3.4 Preparation of Universal Buffer Solution

Universal buffer solution (UBS) is used for pH sensing measurements of the sensors to cover the pH range from 2 - 12. Acetic acid (CH_3COOH), potassium nitrate (KNO_3), boric acid (H_3BO_3), and phosphoric acid (H_3PO_4) are used to prepare the base UBS solution. Potassium hydroxide (KOH) and nitric acid (HNO_3) (65% concentration) are used as base and acid stock solutions to control the pH of the UBS solution.

Table 2.5 Molarity and amount of chemicals used for UBS solution

Chemical	Molarity (M)	Amount
CH_3COOH	0.01	0.3 mL
KNO_3	0.1	5.05 g
H_3BO_3	0.01	0.31 g
H_3PO_4	0.01	0.58 mL
KOH	1	5.611 g
HNO_3	1	9.69 mL

The molarity and the amount of each chemical used are reported in table 2.5. The measured amounts are mixed in 0.5 L DI water in a glass container and put under ultrasonic bath to dissolve all the chemical inside DI water to have the final base UBS solution. The KOH and HNO_3 stock solutions are prepared in 100 mL of DI water and they are used to increase and decrease the pH of the UBS solution.

2.3.5 Sensor Characterization Techniques

For the first three parts of the work, electrochemical sensor characterization is performed by using cyclic voltammetry with the help of a Bio-Logic SP300 potentiostat. New electrochemical sensors based on spinel materials and bare carbon are characterized using paracetamol as a model/test molecule. 100 μL of 1 mM paracetamol in 0.1 M PB at pH 7 is dropped using a micro pipette to cover the whole surface of the electrochemical sensor. A cyclic potential between -0.6 to +0.8 V (vs Ag/AgCl) at a scan rate of 100 mV/s is applied to the working electrode of the sensor. Cyclic voltammograms (current vs potential plots) are recorded and oxidation and reduction currents are assesed after baseline correction by using the peak analysis option in EC-lab software (software used to control the Bio-Logic potentiostat).

Cyclic voltammetry is performed by changing the scan rate from 50 mV/s to 300 mV/s (step size = 50 mV/s) to understand the nature of the electrochemical interface between the surface of the working electrode and paracetamol. Using the scan rate analysis kinetic parameters (electron transfer rate coefficient α, kinetic rate constant 'k') of the sensors are calculated. Sensors calibration is performed by doing CV at different concentrations (0.5 mM - 3 mM in steps of 0.5 mM) of

paracetamol and taking the average of the oxidation current over 3 measurements at each concentration of paracetamol. The average oxidation current is plotted against the concentration of paracetamol and a linear fitting is performed. The slope of the linear fit is the sensitivity of the sensor. Limit of detection (LOD) is calculated with the help of blank measurements (D) and the sensitivity (S) using the below formula:

$$LOD = \frac{lD}{S} \tag{2.7}$$

where l is the statistical confidence level (K = 1, 2, and 3 corresponding to 68.2 %, 95.4 %, and 99.6 % of statistical confidence, respectively) taken as '3'. Other important parameters such as repeatability and reproducibility are assessed by performing 5 measurements with the same sensor and on three different sensors of the same type at the same concentration of paracetamol.

Dissolved oxygen (DO) sensing measurements are performed to study the performance of the spinel-based sensors as a potential application. 100 mL of 10 mM PBS solution (commercial solution) at pH 7.4 is used to perform the DO sensing measurements. Initially CV is performed to get a reference voltage to perform chronoamperometric measurements. -0.5 V is used as the fixed potential for chronoamperometric measurements to sense DO.

The experimental setup of DO sensing is presented in Figure 2.5. The setup involves covering the solution with parafilm, with a small tube inserted through a hole in the parafilm to allow nitrogen bubbling, which is used to adjust the concentration of dissolved oxygen (DO) in the solution. An external Ag/AgCl reference electrode is inserted through another hole, and nitrogen is bubbled into the solution for 30 minutes at a flow rate of 2L/min. The oxygen is vented through a separate small hole in the parafilm. Once the desired DO concentration in the PBS solution is reached, the probe with the screen-printed electrode is inserted into the solution through an additional hole. Initially, the probe is kept out of the solution to protect its connections from potential damage during the nitrogen bubbling process.

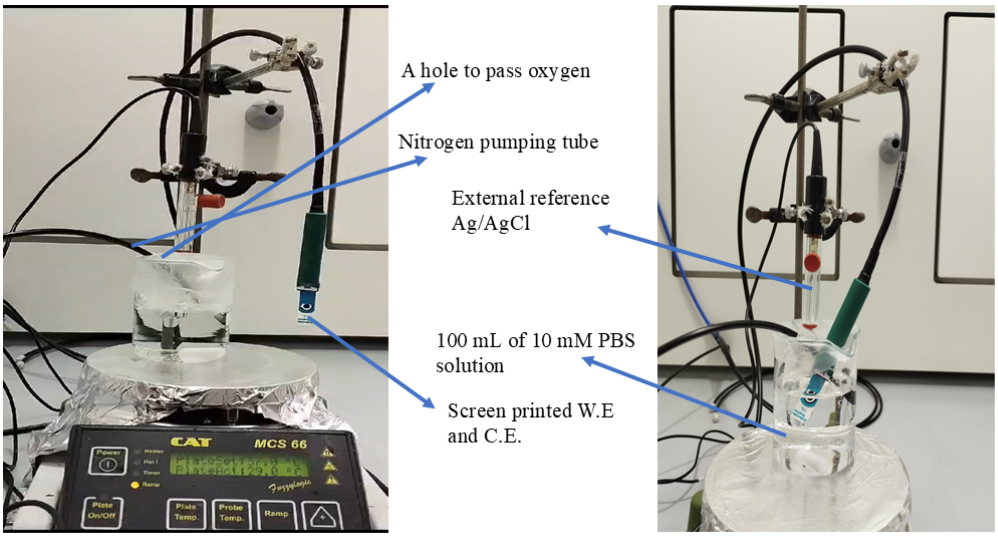

Fig. 2.5 Electrochemical sensing setup of dissolved oxygen (DO).

After completing the setup procedure, an initial chronoamperometric measurement is conducted for 3 minutes using a Metrohm Autolab (NOVA 2.1). The solution is then stirred for 5 minutes with a small stirrer set at 100 rpm (revolutions per minute) to alter the DO concentration near the surface of the working electrode, allowing oxygen to enter through the small hole in the parafilm. This process is repeated five times to calibrate the sensor. For each DO concentration, the current is averaged over a stable 60-second period from the 3-minute chronoamperogram. The averaged current is plotted against the DO concentration, and the slope of the resulting linear fit is reported as the sensor's sensitivity for electrochemical sensing of dissolved oxygen.

As a potential application of the spinel ferrite sensors, pH sensing measurements are performed by using chronopotentiometric technique. 75 mL of the freshly prepared UBS solution is taken in a beaker and the pH calibration of the UBS solution (pH changed using KOH and HNO_3 stock solutions to cover 2 - 12 pH range) is performed using consort pH probe. Potentiometric sensing is usually done using two electrode system hence the CE and RE probes of the potentiostat are coupled together and the screen printed electrode and external Ag/AgCl reference electrode are dipped in 75 mL of UBS solution with a pH 1.98. The solution is continuously stirred at 500 rpm during the measurement using a small stirrer. Open circuit potential (OCP) is recorded by running a chronopotentiometric scan for two

minutes and last 60 seconds of the measurement is averaged for each pH value and the sensors are calibrated by plotting the OCP with respect to the pH of the solution. Similar to the previous cases the slope of the linear fit is reported as the sensitivity of the sensors in pH sensing. The sensors are characterized by potentiometry in the physiological pH range of 4 - 8.5 similar to the initial measurements, as the main goal is to use these sensors in biomedical applications. The stability of the sensors is checked by doing the measurement at each pH for longer times (5, 10, 15, 20 minutes). Finally, interference tests are performed by using 30 mM KCl, and 5 mM NaCl as possible interferences.

In the last part of the work, spinel based sensors are used to sense anti-cancer drugs as another potential application of these sensors. As a preliminary measurements, 0.5 mM 5-FU in 0.1 M PB at pH 7 is detected by using cyclic voltammetry. The potential is scanned between 0.5 and 1.2 at a scan rate of 100 mV/s and a clear oxidation of 5-FU around 0.9 V is observed. Since the pharmaceutical concentration of the drug is low, DPV technique is employed. It is the best technique to study the electrochemical sensor performance at low concentrations as it is very sensitive technique. DPV is performed using 100 mV of modulation amplitude, 0.1 s of interval time, and 0.025 s of modulation time. Calibration of the sensors is performed in the concentration range of 5-FU from 10 - 200 μM in steps of 30 μM.

Etoposide is detected through CV as the drug is very electroactive compound even at low concentrations. CV is performed in the potential range from -0.4 to +0.8 V at a scan rate of 20 mV/s and the two oxidation peaks of the etoposide are assessed and the sensors are calibrated in the concentration range from 10 - 100 μM in steps of 20 μM.

2.4 Conclusion

This chapter presented the advantages and significance of spinel nanomaterials over single metal oxides, crystal structure of spinel oxides, and some of the applications of spinel ferrites in biomedical applications. Advantages and use of combustion technique in spinel oxides synthesis is discussed, apparatus for physicochemical characterization of nanomaterials, preparation of buffer and electrolytic solutions, and instruments used for electrochemical characterization of new electrochemical sensors is presented.

Chapter 3

Effect of Crystal Structure on Electron Transfer

The reorganization energy 'λ' and transfer integral 'J' can get affected by the changes in the composition of the electrode material, size of the particles, and the crystal structure. This can eventually effect the wavefunctions of the electrons participating the electron transfer between the acceptor and donor leading to different transfer integrals (overlap of wavefunctions) and reorganization energies. This leads to a significant change in the final kinetic rate constant 'k' of the electron transfer. Therefore it is important to understand the affects of these parameters on electron transfer and eventually 'k'. Hence in this work, the effect of crystal structure on electron transfer at the electrochemical interface is studied. In order to study the effect of crystallographic features on electron transfer an inverse spinel-oxide, $NiFe_2O_4$ is considered. Ni^{2+} ions in the crystal structure of the $NiFe_2O_4$ are gradually substituted by Zn^{2+} (very similar ionic radius compared to Ni^{2+}) in steps of 0.2 mole fraction (x) to gradually change the crystal structure of the inverse spinel ($NiFe_2O_4$) to a normal spinel ($ZnFe_2O_4$). To do so, $Zn_xNi_{1-x}Fe_2O_4$ (x = 0, 0.2, 0.4, 0.6, 0.8, 1) nanomaterials are synthesized using the auto combustion synthesis method as described in chapter 2.2.2. Synthesized nanomaterials are characterized using different material characterization methods in order to study the morphological, crystallographic, structural, electronic, and optical features of the materials.

The surface of the screen-printed carbon working electrode is modified using the newly synthesized spinel nanomaterials by following the procedure described in

section 2.3.1. Bare carbon and modified sensors are electrochemically characterized by cyclic voltammetry technique using paracetamol as a test/model molecule since paracetamol is an electroactive drug, it can be easily studied for direct comparison among different electrochemical sensors in terms of sensitivity and electron transfer rate constant. To predict the type of electron transfer at the electrochemical interface between the working electrode surface and paracetamol, band energies of the nanomaterials are estimated and mapped with the experimental redox potentials of paracetamol, the role of surface states/defects on electron transfer at the ECI is discussed.

3.1 Material Characterization

3.1.1 Structural Characterization

Firstly, the synthesis method is tested with different annealing times and processes. $NiFe_2O_4$ material is synthesized without annealing initially and then annealed the following day. Another batch is synthesized and annealed using a single-step procedure as described in section 2.2.2. The XRD patterns of these two materials are compared in Figure 3.1. A shift of +0.24 degrees in 2θ is observed, along with improved crystallinity, as evidenced by the reduced peak broadening in the single-step synthesis (red pattern) compared to the material annealed the next day (black pattern). To assess the effect of annealing time, $NiFe_2O_4$ is synthesized with annealing durations of 1 hour and 2 hours at 600°C. The powder diffraction patterns of $NiFe_2O_4$ for both annealing times are shown in Figure 3.2. It is noted that the annealing time of either 1 or 2 hours did not affect the XRD pattern of the material at a constant temperature. Consequently, a single-step synthesis with a 1-hour annealing time is selected as the standard procedure throughout this work.

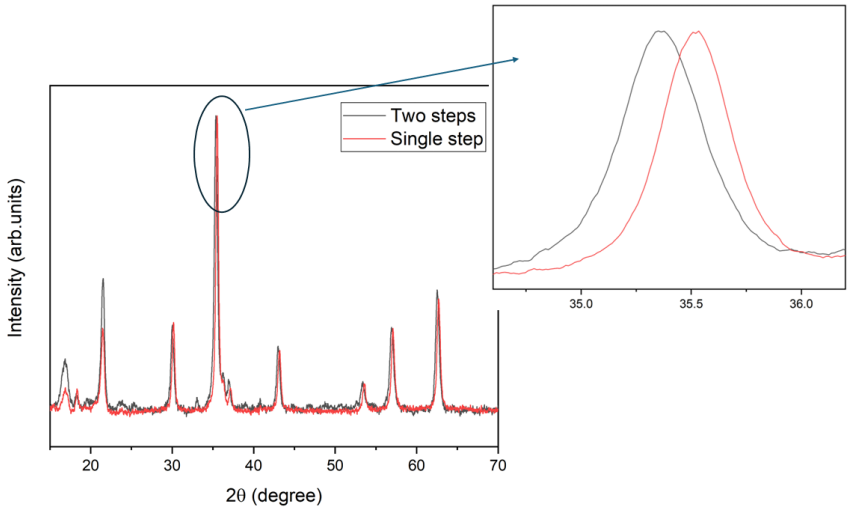

Fig. 3.1 Effect of annealing on two ways of synthesis on XRD pattern of $NiFe_2O_4$ nanomaterial.

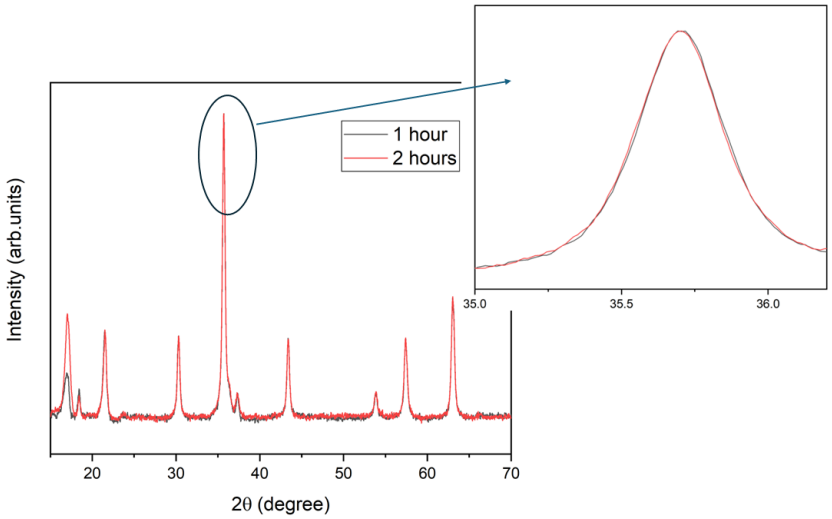

Fig. 3.2 Effect of annealing time on XRD pattern of $NiFe_2O_4$ nanomaterial in single step synthesis.

The XRD patterns of powder $Zn_xNi_{1-x}Fe_2O_4$ (x = 0, 0.2, 0.4, 0.6, 0.8, 1) samples are displayed in Figure 3.3. The XRD results confirm that the primary crystalline phase of the $Zn_xNi_{1-x}Fe_2O_4$ nanomaterials is the cubic (FCC - face centered cubic) spinel crystal phase belonging to the cubic Fd-3m space group. Notably, for x = 0 and x = 1, the experimental patterns align perfectly with the inverse spinel Trevorite ($NiFe_2O_4$, ref. code 01-086-2267, ICSD-040040 (ICSD release 1997)) and the

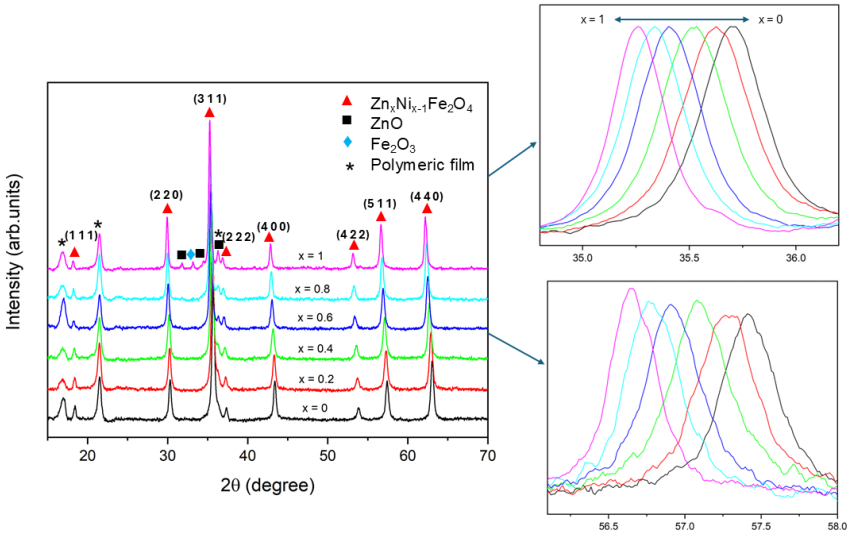

Fig. 3.3 XRD patterns of $Zn_xNi_{1-x}Fe_2O_4$ nanomaterials showing the different phases and illustrating the clear crystal phase transition from inverse spinel to normal spinel with too different phases.

normal spinel Franklinite ($ZnFe_2O_4$, ref. code 01-074-2397, ICSD-028511 (ICSD release 1997)), respectively.

For intermediate compositions, an increase in Zn content results in a gradual shift of the peaks towards lower 2θ angles, as shown in Figure 3.3, which illustrates this shift for the most intense peak and another less intense peak of the spinel structure. This shift in peaks indicates a gradual expansion of the lattice volume, which is attributed to the smaller ionic radius of Ni(II) (69 pm) compared to Zn(II) (74 pm). This gradual shift confirms that the synthesized materials exhibit a crystal structure transitioning between the normal and inverse spinel forms, as expected. This proves the successful synthesis of materials with different spinel phases from inverse to normal spinel and then the mixed phases in between.

In addition to the expected spinel phase, the XRD patterns display three additional peaks at 2θ values of 16.8°, 21.4°, and 36.3°. The last of these peaks, in spectra with low Zn content (x = 0, 0.2, 0.4), partially overlaps with the main peak of the spinel, but becomes more prominent at higher Zn content (x = 0.6, 0.8, and 1) due to the shift of the main peak towards lower angles. During the XRD analysis, a polymeric sealing was used as a safety precaution because of the nanometric size of the spinel powders. To determine the origin of these three unknown peaks, XRD patterns are collected with and without the polymeric sealing. The three peaks mentioned above

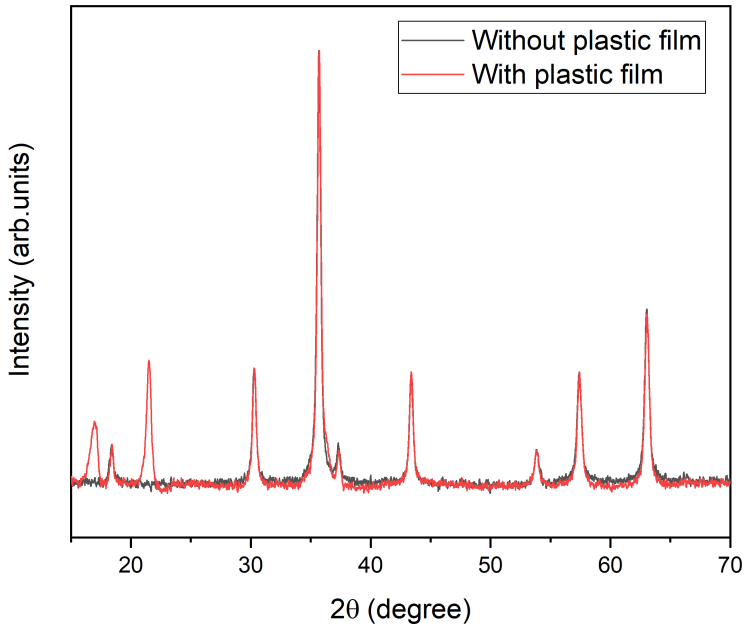

Fig. 3.4 XRD patterns of $NiFe_2O_4$ nanomaterial with and without a polymeric plastic film.

are not present in the diffractogram of the unsealed sample, as shown in Figure 3.4, but they are observed in the sealed samples, as mentioned. Therefore, these three peaks are attributed to the presence of the polymeric film used during the analysis.

Additionally, the XRD pattern of $ZnFe_2O_4$ shows four low-intensity peaks between 30° and 36°. The positions of these peaks correspond to the most intense peaks of ZnO and Fe_2O_3, respectively as expected due to the adopted synthesis method and reactants used.

Table 3.1 The average crystallite size of $Zn_xNi_{1-x}Fe_2O_4$ materials

Material	Average crystallite size (nm)
$NiFe_2O_4$	27.5 ± 0.9
$Zn_{0.2}Ni_{0.8}Fe_2O_4$	24.1 ± 0.4
$Zn_{0.4}Ni_{0.6}Fe_2O_4$	23.8 ± 0.9
$Zn_{0.6}Ni_{0.4}Fe_2O_4$	26.5 ± 0.3
$Zn_{0.8}Ni_{0.2}Fe_2O_4$	27.4 ± 0.9
$ZnFe_2O_4$	36.2 ± 1.4

The average crystallite size of the particles was calculated using Scherrer's method. For the Scherrer equation, seven high intense peaks are used. The size of the crystallites is calculated using the equation:

$$D = \frac{m\lambda}{\beta_{hkl} cos\theta} \tag{3.1}$$

where'D' is the crystallite size, m = 0.9 is a dimensionless shape factor assuming spherical shape, β is the FWHM (full width half maximum) of the XRD peak and θ is the Bragg angle of the peak center. The instrumental broadening β is corrected using the equation,

$$\beta_{hkl} = \sqrt{(\beta_{hkl})^2_{measured} - (\beta_{hkl})^2_{standard}} \tag{3.2}$$

As shown in Table 3.1, the average crystallite size ranges from 24 to 35 nm. The crystallite size varies irregularly between materials, likely due to the synthesis method used. Autocombustion synthesis allows a weak control over crystallite growth, leading to this variation.

3.1.2 Morphological Characterization

FESEM technique is used to examine the size and morphology of the synthesized $Zn_xNi_{1-x}Fe_2O_4$ materials. As shown in Figure 3.5, the particles exhibit a spherical shape and are aggregated into clusters. This aggregation is likely due to the auto-combustion synthesis method employed. The observed morphology of the nanoparticles is consistent with that of ferrite materials reported in the literature [95, 131]. Particle sizes are estimated from Figure 3.5 by analyzing the particles of each material using ImageJ software. The average particle sizes, which range between 30 and 70 nm, are summarized in Table 3.2.

Table 3.2 The average particle size of $Zn_xNi_{1-x}Fe_2O_4$ materials

Material	Average particle size (nm)
$NiFe_2O_4$	35 ± 6
$Zn_{0.2}Ni_{0.8}Fe_2O_4$	39 ± 8
$Zn_{0.4}Ni_{0.6}Fe_2O_4$	31 ± 7
$Zn_{0.6}Ni_{0.4}Fe_2O_4$	66 ± 18
$Zn_{0.8}Ni_{0.2}Fe_2O_4$	36 ± 9
$ZnFe_2O_4$	44 ± 17

Variations in particle size with the addition of Zn into the $NiFe_2O_4$ structure are noticed. As seen in the SEM images (Figure 3.5), the particles are aggregated, making it challenging to determine the exact size. A part of the image is chosen where the particles seem less aggregated and the average size is estimated. Particularly in Figures 3.5d and 3.5f, the particles appear larger compared to those in Figures 3.5a–3.5c and 3.5e. This suggests that some particles may have formed from multiple crystallites, as the synthesis method used does not allow precise control over particle size and shape. It is plausible that $Zn_{0.6}Ni_{0.4}Fe_2O_4$ and $ZnFe_2O_4$ consist of more crystallites compared to the $Zn_xNi_{1-x}Fe_2O_4$ (x = 0, 0.8, 0.4, 0.2) nanomaterials due to the control over the particle growth kinetics.

Figure 3.6 presents the FESEM images of the surface of the $ZnFe_2O_4$-modified carbon working electrode (WE). In Figure 3.6a, $ZnFe_2O_4$ particles are shown dispersed on the carbon WE, clearly illustrating that these dispersed particles are nanoparticles with some degree of aggregation. To determine the particle size, a less aggregated region of the image in Figure 3.6b is selected and analyzed using ImageJ software. The image was scaled to visualize the particles at the nanoscale, and a line tool was used to measure the diameters of 30 different particles. The average particle size was calculated to be 41 ± 8 nm.

3.1.3 Spectroscopic Characterization

Pure and mixed ferrites crystallize in a spinel structure belonging to the Fd-3m space group, which, according to group theory, exhibits five active Raman bands (A_{1g}, E_g, and $3T_{2g}$) [132–134]. A well-known example of the (inverse) spinel structure

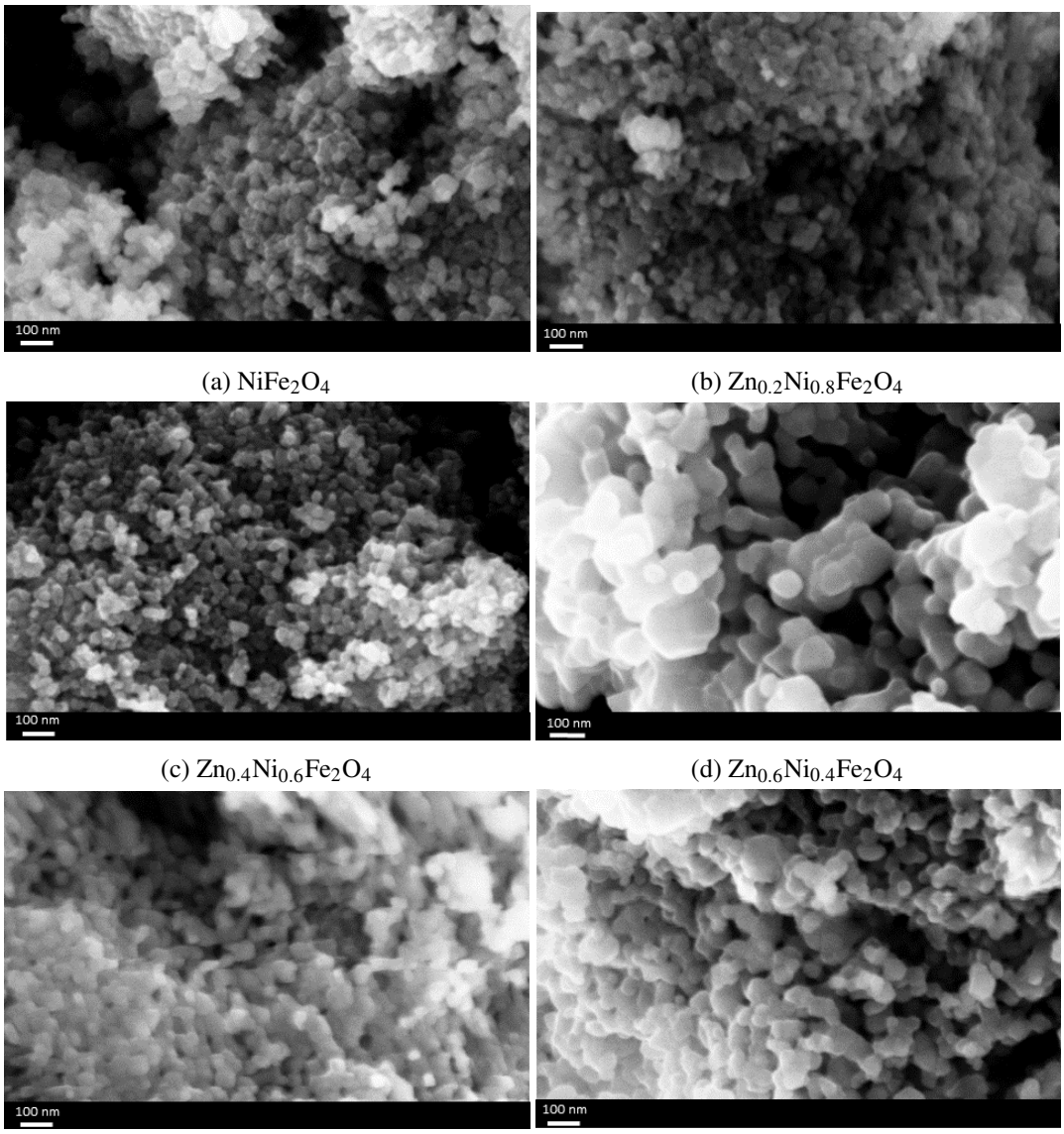

(a) $NiFe_2O_4$ (b) $Zn_{0.2}Ni_{0.8}Fe_2O_4$

(c) $Zn_{0.4}Ni_{0.6}Fe_2O_4$ (d) $Zn_{0.6}Ni_{0.4}Fe_2O_4$

(e) $Zn_{0.8}Ni_{0.2}Fe_2O_4$ (f) $ZnFe_2O_4$

Fig. 3.5 FESEM images of $Zn_xNi_{1-x}Fe_2O_4$ nanomaterials at 250kX.

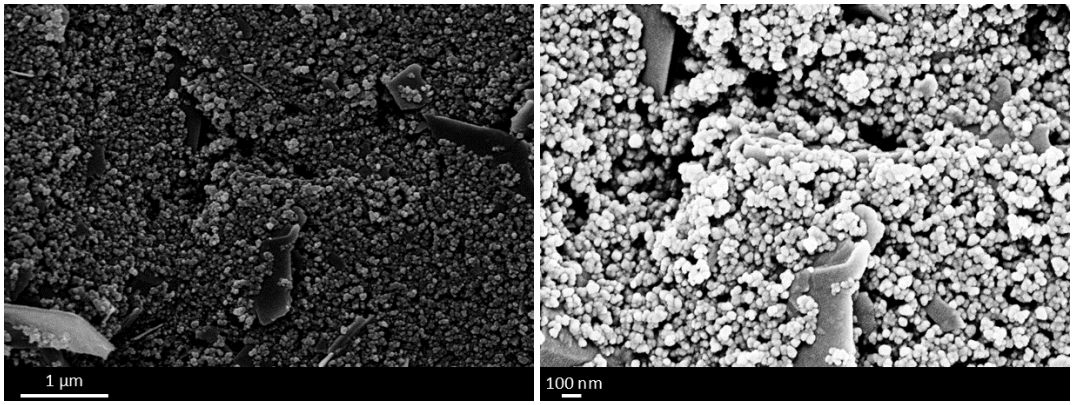

(a) Scale: 1 μm (b) Scale: 100 nm

Fig. 3.6 FESEM images of $ZnFe_2O_4$-modified carbon surface at different scales.

is magnetite (Fe_3O_4), where Fe^{3+} ions occupy both the 'Td' and 'Oh' sites. In $NiFe_2O_4$, however, only half of the Fe^{3+} ions occupy the 'Td' sites, while the 'Oh' sites are shared between Ni^{2+} and Fe^{3+} ions. This difference suggests that in Fe_3O_4, the Fe-O bond distances are uniform, whereas in $NiFe_2O_4$, some distortion in bond distances may occur due to the differing ionic radii of Ni^{2+} and Fe^{3+} ions. Raman spectroscopy, being highly sensitive to local structural changes, can detect such disturbances in the local structure. Thus, similar structural changes can be anticipated in $Zn_xNi_{1-x}Fe_2O_4$ nanomaterials as the composition varies from x = 0 to 1.

The Raman spectra for all six materials are shown in Figure 3.7. As the composition changes, the spectra reveal clear variations, reflecting local changes in the crystal structure. The spectra closely resemble those of Fe_3O_4 reported in the literature [134]; however, a key difference is that the Fe_3O_4 bands are sharp and well-defined, while in Zn–Ni mixed ferrites, the bands exhibit shoulder or doublet-like behavior (with two cations) and triplet-like behavior (with three cations). These changes are attributed to variations in ionic radii, which affect bond distances.

For the inverse spinel $NiFe_2O_4$, five Raman peaks are identified at 703 cm^{-1} (A_{1g} band), 573 cm^{-1} ($T_{2g}(3)$ band), 482 cm^{-1} ($T_{2g}(2)$ band), 333 cm^{-1} (E_g band), and 211 cm^{-1} ($T_{2g}(1)$ band). The Fe-related AA_{1g} mode is observed at 703 cm^{-1}. Upon incorporating Ni into the ferrite structure, an additional prominent mode appears at ≈ 670, attributed to the Ni-related A_{1g} mode [133]. These peaks closely align with those reported in the literature [98, 134]. In the spectrum of $Ni_{0.6}Zn_{0.4}Fe_2O_4$, in

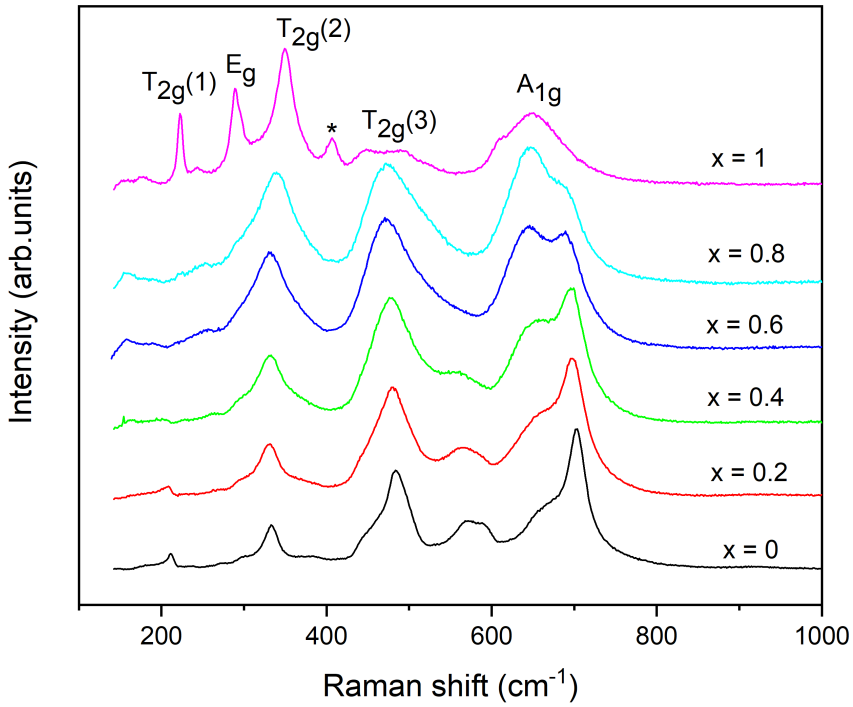

Fig. 3.7 Raman spectra of $Zn_xNi_{1-x}Fe_2O_4$ nanomaterials.

addition to the Fe and Ni-related peaks at 698 and 667 cm^{-1}, respectively, a strong peak at 644 cm^{-1} is observed, which is associated with Zn within the A_{1g} band and is attributed to Zn–O vibrations at the Td sites, as previously noted [135, 136]. Similarly, in the normal spinel $ZnFe_2O_4$, the Fe-related peak at 646 cm^{-1} and the Zn-related peak at 612 cm^{-1} within the A_{1g} band are identified. Besides the five typical Raman bands, an additional band marked as "*" around 400 cm^{-1} is attributed to the Zn-O bonding as in ZnO [137]. The peak positions of the other four Raman bands—$T_{2g}(3)$, $_{2g}(2)$, E_g, and $T_{2g}(1)$ are also identified in the Raman spectra as indicated in Figure 3.7.

The Kubelka–Munk function, $F(R_\infty)$ of diffuse reflectance (DR) UV–vis spectra of powder samples is reported in Figure 3.8. The function $F(R_\infty)$ is expressed as:

$$F(R_\infty) = \frac{(1-R_\infty)^2}{2R_\infty} = \frac{K}{s} \tag{3.3}$$

where 'R_∞' represents the fraction of incident UV–vis light reflected by a sample considered infinitely thick, 's' is the scattering coefficient, and K denotes the molar absorption coefficient.

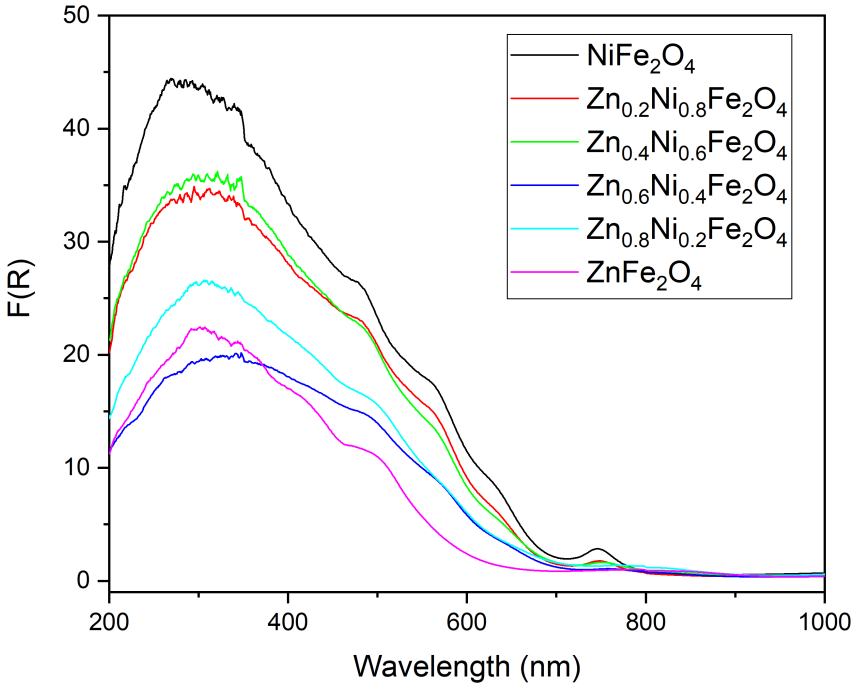

Fig. 3.8 Diffuse reflectance (DR) UV-vis spectra of $Zn_xNi_{1-x}Fe_2O_4$ nanomaterials.

The $Zn_xNi_{1-x}Fe_2O_4$ nanomaterials exhibit varying Kubelka–Munk curves, as shown in Figure 3.8. These spectra display distinct absorption onsets and different bands, which are likely linked to localized electronic levels.

The energy gap (E_g) of the synthesized materials is determined using Tauc's plot, as illustrated in Figure 3.9. Direct electronic transitions are assumed for this analysis, and the calculated E_g values for the nanomaterials are presented in Table 3.4. The E_g values obtained for $NiFe_2O_4$ (2.41 $\pm$ 0.05 eV) and $ZnFe_2O_4$ (2.58 $\pm$ 0.06 eV) are consistent with previously reported values [138–141]. The incorporation of Zn into the $NiFe_2O_4$ lattice leads to changes in the energy gap of the nanomaterials.

As shown in Figure 3.8, the $Zn_xNi_{1-x}Fe_2O_4$ nanomaterials exhibit distinct absorption spectra, characterized by different absorption onsets and other spectroscopic features attributed to surface electronic states. However, when it comes to the corresponding bandgap energy values (Table 3.4), no clear trend could be established in relation to the nanoparticle size. It is well recognized that the size and shape of nanoparticles significantly influence the energy of electronic levels within a material [142–144]. The shape, in particular, can have a substantial impact on light absorption, leading to variations in bandgap energy. For simplicity, the nanoparticles are

assumed to be spherical, but a closer examination of SEM images reveals that the nanomaterials possess some irregular shapes. Additionally, it should be noted that the DR UV–vis spectra in Figure 3.8 indicate the presence of surface energy levels, which can significantly influence the bandgap calculation. These surface energy levels may be associated with surface states or defects, contributing to the observed spectral tailing and complicating a more precise determination of the nanomaterials' bandgap.

The composition and valence states of the elements in the $Zn_xNi_{1-x}Fe_2O_4$ nanomaterials are analyzed using XPS. The full survey scan spectra, presented in Figure 3.10, revealed peaks corresponding to Ni, Zn, Fe, and O, as well as adventitious carbon (C), confirming their presence in the nanomaterial composition. High-resolution (HR) core-level spectra are recorded for Fe 2p, Ni 2p, Zn $2p_{3/2}$, and O 1s, and the resulting data are fitted, as illustrated in Figure 3.11. The binding energies for Zn, Ni, Fe, and O within the $Zn_xNi_{1-x}Fe_2O_4$ nanomaterials are detailed in Table 3.3.

Table 3.3 The binding energies of different elements in $Zn_xNi_{1-x}Fe_2O_4$ nanomaterials

Material	Binding energy (eV)			
	Fe^{3+}	Ni^{2+}	Zn^{2+}	O^{2-}
$NiFe_2O_4$	Fe $2p_{3/2}$ - 710.1 Fe $2p_{1/2}$ - 723.7	Ni $2p_{3/2}$ - 854.6 Ni $2p_{1/2}$- 872.2	-	O 1s - 529.6
$Zn_{0.2}Ni_{0.8}Fe_2O_4$	Fe $2p_{3/2}$ - 710.5 Fe $2p_{1/2}$ - 724.1	Ni $2p_{3/2}$ - 854.6 Ni $2p_{1/2}$ - 872.2	Zn $2p_{3/2}$ - 1021.1	O 1s - 529.6
$Zn_{0.4}Ni_{0.6}Fe_2O_4$	Fe $2p_{3/2}$ - 710.4 Fe $2p_{1/2}$ - 724.1	Ni $2p_{3/2}$ - 854.6 Ni $2p_{1/2}$ - 872.4	Zn $2p_{3/2}$ - 1021.2	O 1s - 529.7
$Zn_{0.6}Ni_{0.4}Fe_2O_4$	Fe $2p_{3/2}$ - 710.5 Fe $2p_{1/2}$ - 724.5	Ni $2p_{3/2}$ - 854.7 Ni $2p_{1/2}$ - 872.3	Zn $2p_{3/2}$ - 1021.2	O 1s - 529.8
$Zn_{0.8}Ni_{0.2}Fe_2O_4$	Fe $2p_{3/2}$ - 710.7 Fe $2p_{1/2}$ - 724.5	Ni $2p_{3/2}$ - 854.8 Ni $2p_{1/2}$ - 872.5	Zn $2p_{3/2}$ - 1021.3	O 1s - 529.7
$ZnFe_2O_4$	Fe $2p_{3/2}$ - 710.6 Fe $2p_{1/2}$ - 724.5		Zn $2p_{3/2}$ - 1021.4	O 1s - 529.7

The Fe 2p region showed two primary peaks at 711–710 eV (Fe $2p_{3/2}$) and 724.5–723.5 eV (Fe $2p_{1/2}$), along with two broad shake-up peaks at higher binding energies, which are indicative of Fe(III) [141, 91]. The HR spectra for Ni 2p

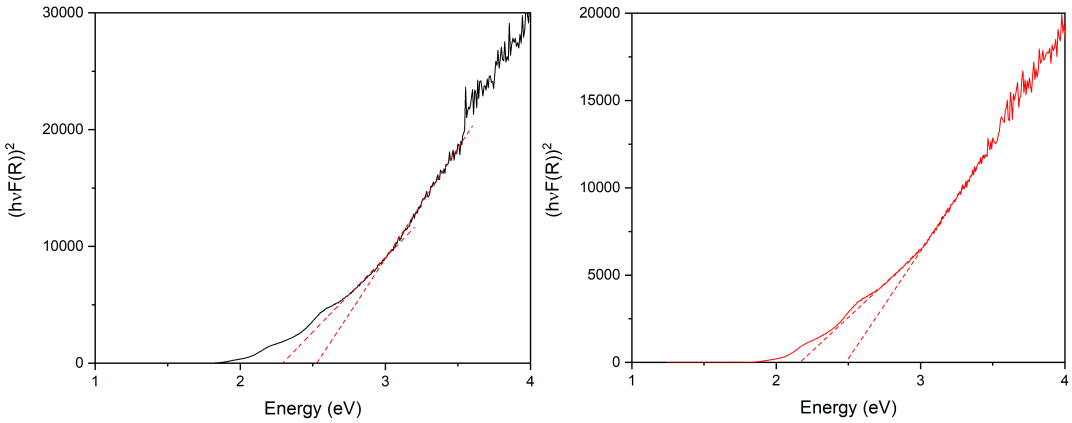

(a) $NiFe_2O_4$

(b) $Zn_{0.2}Ni_{0.8}Fe_2O_4$

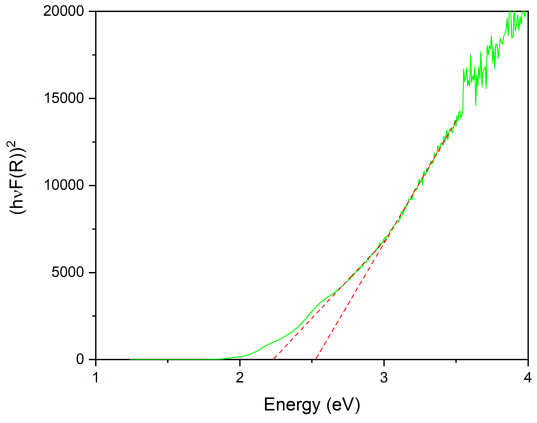

(c) $Zn_{0.4}Ni_{0.6}Fe_2O_4$

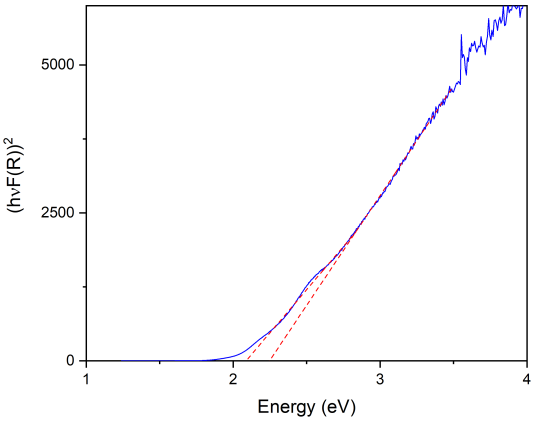

(d) $Zn_{0.6}Ni_{0.4}Fe_2O_4$

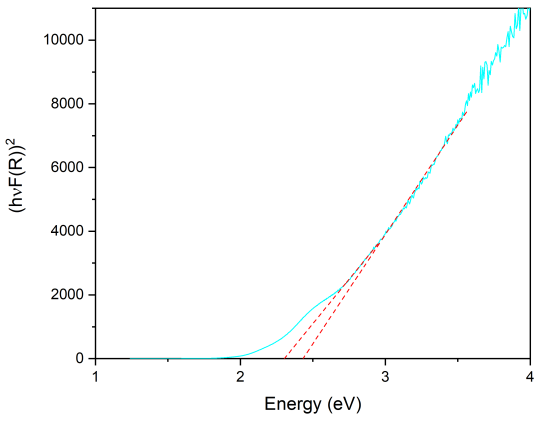

(e) $Zn_{0.8}Ni_{0.2}Fe_2O_4$

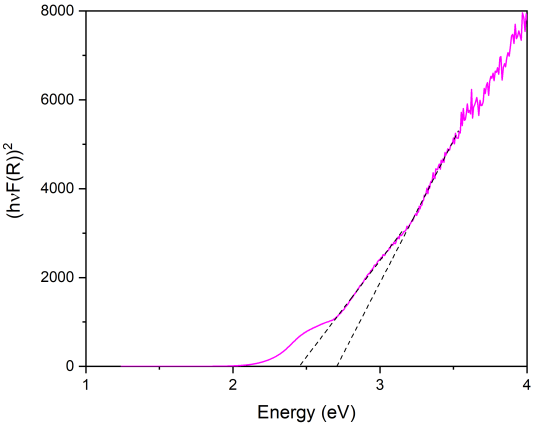

(f) $ZnFe_2O_4$

Fig. 3.9 Tauc plot method to determine the energy gap (E_g) of $Zn_xNi_{1-x}Fe_2O_4$ nanomaterials.

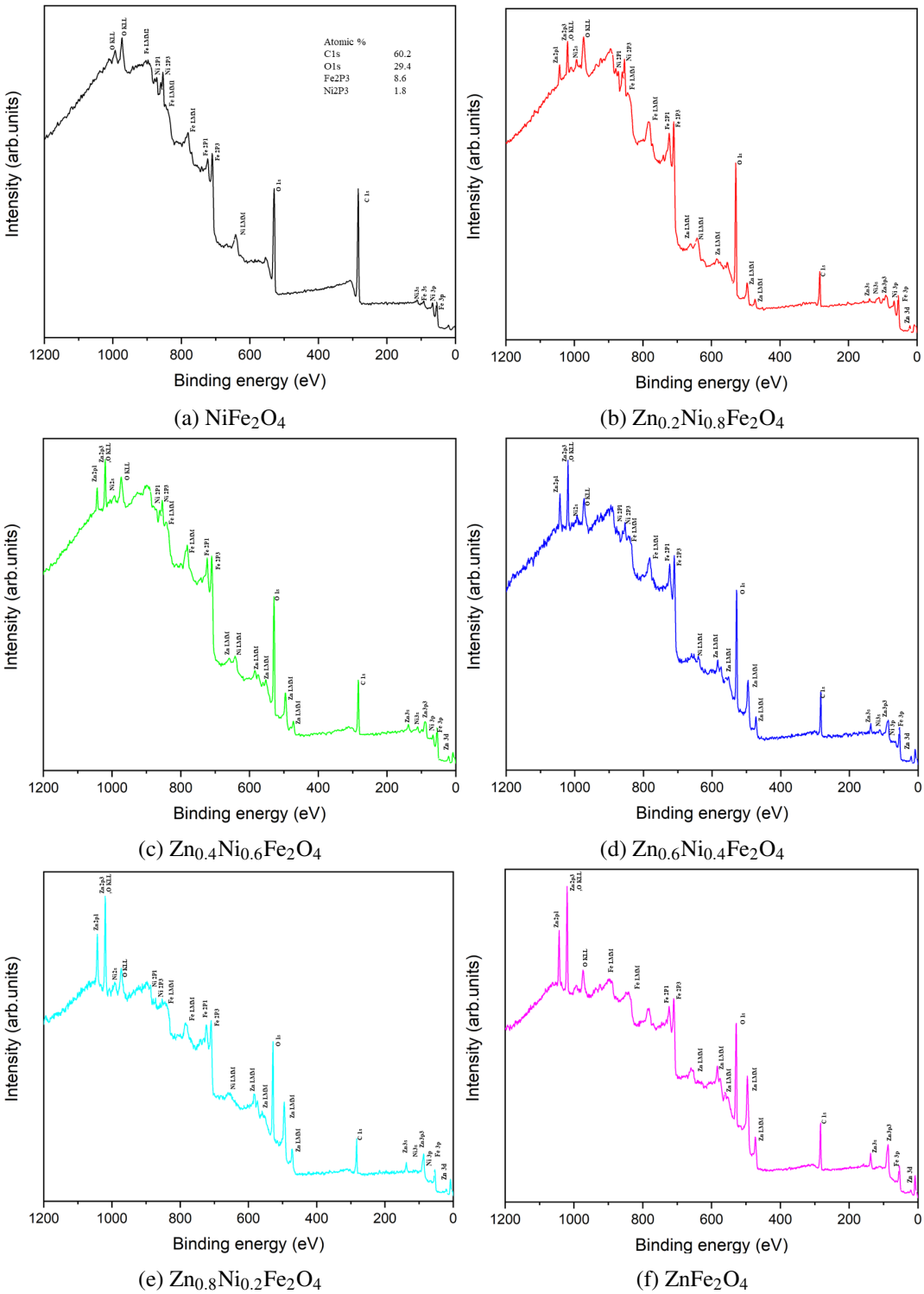

(a) $NiFe_2O_4$ (b) $Zn_{0.2}Ni_{0.8}Fe_2O_4$

(c) $Zn_{0.4}Ni_{0.6}Fe_2O_4$ (d) $Zn_{0.6}Ni_{0.4}Fe_2O_4$

(e) $Zn_{0.8}Ni_{0.2}Fe_2O_4$ (f) $ZnFe_2O_4$

Fig. 3.10 XPS full survey spectra of $Zn_xNi_{1-x}Fe_2O_4$ nanomaterials.

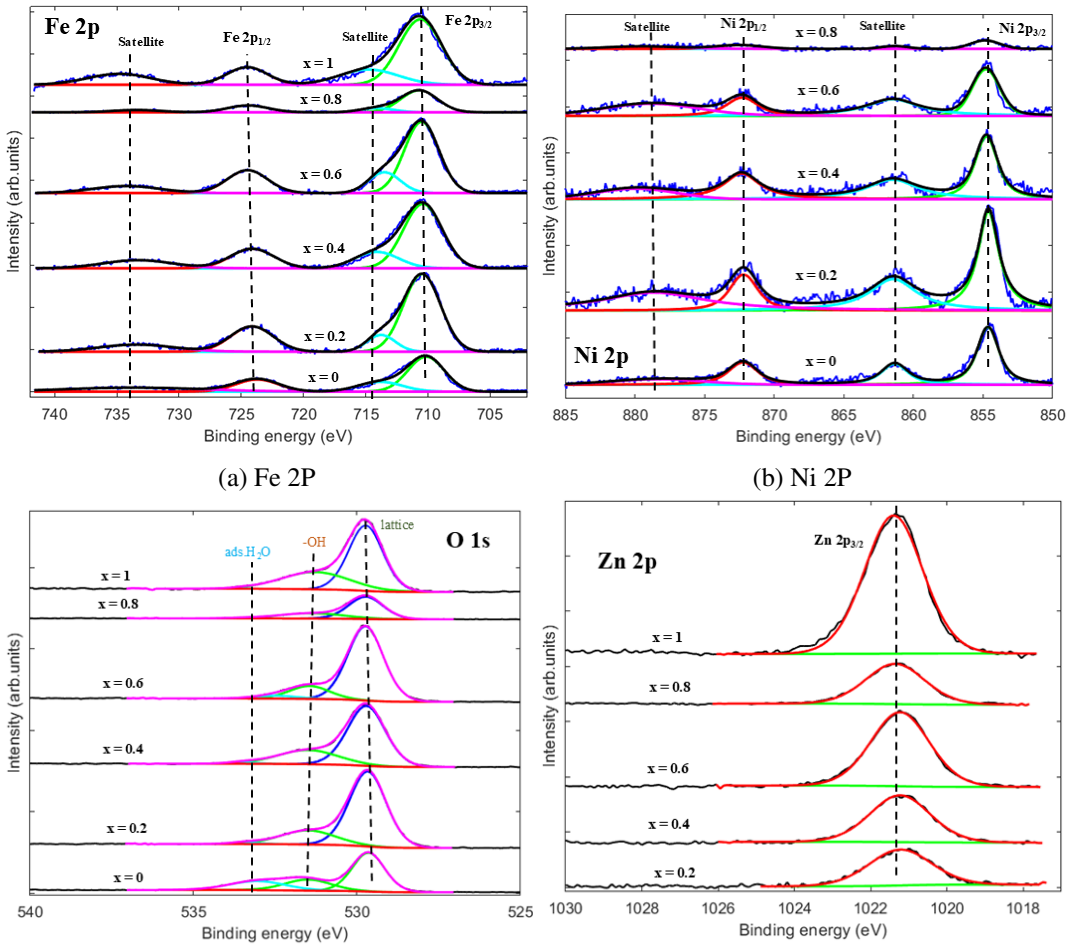

(a) Fe 2P (b) Ni 2P

(c) O 1s (d) Zn 2P

Fig. 3.11 XPS high resolution (HR) spectra of different elements in the composition of $Zn_xNi_{1-x}Fe_2O_4$ nanomaterials.

displayed two major peaks around 854.7 eV and 872.2 eV, corresponding to the Ni $2p_{3/2}$ and Ni $2p_{1/2}$ peaks, respectively [145]. Additionally, shake-up satellite peaks characteristic of Ni(II) species were observed at higher binding energies [146]. For Zn $2p_{3/2}$, the HR spectra showed main peaks between 1021.1 eV and 1021.4 eV, which are associated with Zn(II) [141, 91]. The O 1s spectra are deconvoluted into two main components at approximately 529.7 eV and 531.4 eV, corresponding to O^{2-} in the lattice and O^{2-} in hydroxyl groups, respectively, with an additional shoulder above 532 eV attributed to adsorbed water [146, 147]. XPS analysis confirmed that the valence states of Zn, Ni, Fe, and O in the $Zn_xNi_{1-x}Fe_2O_4$ nanomaterials are '+2', '+2', '+3', and '-2', respectively.

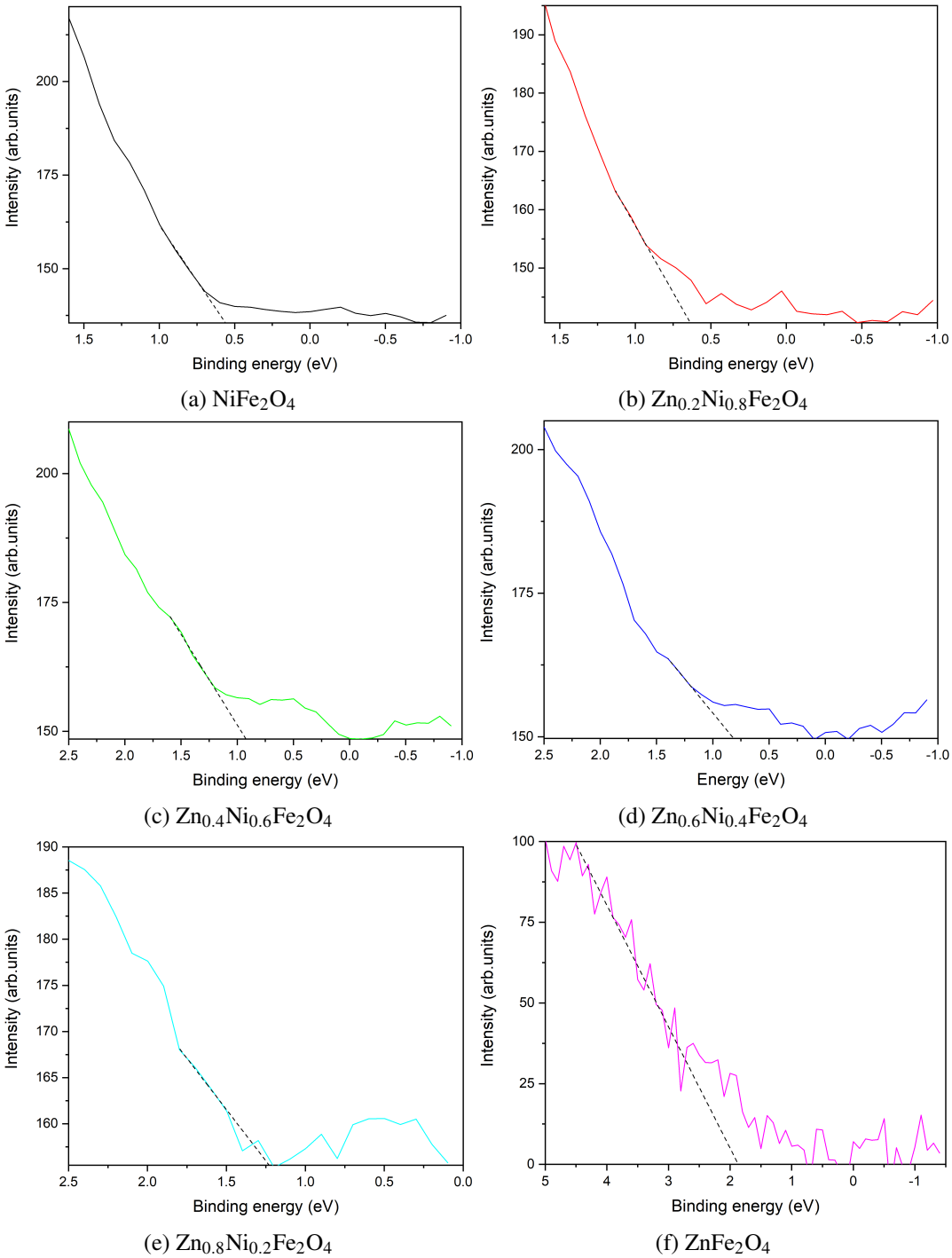

(a) $NiFe_2O_4$ (b) $Zn_{0.2}Ni_{0.8}Fe_2O_4$

(c) $Zn_{0.4}Ni_{0.6}Fe_2O_4$ (d) $Zn_{0.6}Ni_{0.4}Fe_2O_4$

(e) $Zn_{0.8}Ni_{0.2}Fe_2O_4$ (f) $ZnFe_2O_4$

Fig. 3.12 Estimation of the valence band maximum (E_V) of $Zn_xNi_{1-x}Fe_2O_4$ nanomaterials using XPS valence band spectra.

Table 3.4 The energy gap and band edges of $Zn_xNi_{1-x}Fe_2O_4$ materials

Material	E_g (eV)	E_V (eV)	E_C (eV)
$NiFe_2O_4$	2.41 ± 0.05	-0.56 ± 0.01	1.85 ± 0.06
$Zn_{0.2}Ni_{0.8}Fe_2O_4$	2.32 ± 0.04	-0.64 ± 0.01	1.68 ± 0.05
$Zn_{0.4}Ni_{0.6}Fe_2O_4$	2.38 ± 0.04	-0.92 ± 0.02	1.41 ± 0.06
$Zn_{0.6}Ni_{0.4}Fe_2O_4$	2.17 ± 0.05	-0.81 ± 0.01	1.36 ± 0.06
$Zn_{0.8}Ni_{0.2}Fe_2O_4$	2.37 ± 0.04	-1.23 ± 0.01	1.14 ± 0.05
$ZnFe_2O_4$	2.58 ± 0.06	-1.87 ± 0.13	0.71 ± 0.19

The valence band maximum (E_V) of the nanomaterials is determined using XPS valence band spectra following the procedure outlined in reference [148]. This method involves extrapolating the leading edge of the peak observed in the XPS valence band spectrum to meet the baseline of the flat region, as depicted in Figure 3.12. The point where this extrapolation intersects the baseline corresponds to the valence band maximum (E_V). With the Fermi energy level (E_f) assumed to be at 0 eV, the calculated E_v values are presented as negative energy values. By adding the energy gap (E_g) to the valence band maximum (E_V), the minimum energy of the conduction band (E_C) is obtained. The computed E_g, E_V, and E_C values for the $Zn_xNi_{1-x}Fe_2O_4$ nanomaterials are summarized in Table 3.4.

3.2 Electrochemical Characterization

Initially, $NiFe_2O_4$ and $ZnFe_2O_4$ solution in methanol modified carbon (WE) sensors are characterized with paracetamol (APAP) as a test analyte in 0.1 M PB at pH 7. Figure 3.13a shows the cyclic voltammograms of Bare, $NiFe_2O_4$ and $ZnFe_2O_4$ modified sensors with 1 mM APAP in 0.1 M PBS at pH 7. It is clear that the modified sensors with spinel nanomaterials have enhanced the oxidation peak current and redox potential has been decreased compared to the unmodified or bare carbon sensor.

To investigate the impact of varying nanoparticle deposition amounts on the WE surface, the surface was modified by applying 2, 5, 7, and 10 μL of $NiFe_2O_4$ in methanol solution. The corresponding cyclic voltammograms are presented in Figure 3.13b. As the deposition volume increased from 2 to 5 μL, the performance of the electrode improved. However, further increases to 7 and 10 μL resulted in a

significant decrease in the oxidation peak current. This suggests that a higher deposition volume on the WE surface increases the interface resistance, thereby reducing the electrode's surface electrochemical activity. Based on these observations, 5 μL was selected as the optimal deposition amount for subsequent sensor performance studies.

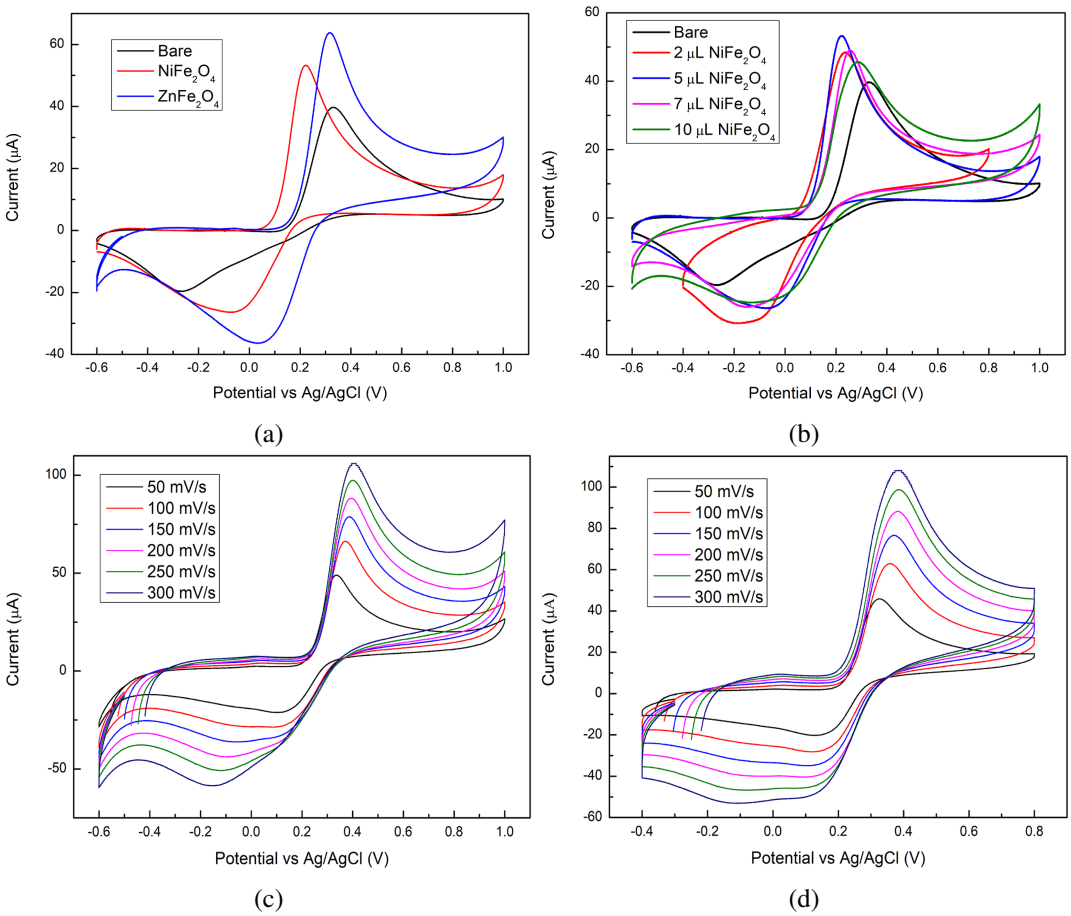

Fig. 3.13 Cyclic voltammograms of spinel nanomaterials in methanol solution modified sensors while detecting 1 mM APAP in 0.1 M PB at pH 7. (a) Comparison of $NiFe_2O_4$ and $ZnFe_2O_4$ sensors with bare carbon sensor, (b) effect of the amount of $NiFe_2O_4$ deposition. Effect on cyclic voltammograms due to the spreading of naonmaterial onto the CE and RE surface of (c) $NiFe_2O_4$ and (d) $ZnFe_2O_4$ sensors.

As proceeded further in the characterization of the sensors, it is realized that the performance of the sensors is affected by the spreading of the solution onto the RE and CE surfaces since the surface modification is performed manually by the drop-casting technique as seen in the cyclic voltammograms as reported in Figures 3.13c and 3.13d. To tackle this issue the solvent is changed from methanol to 1-butanol and

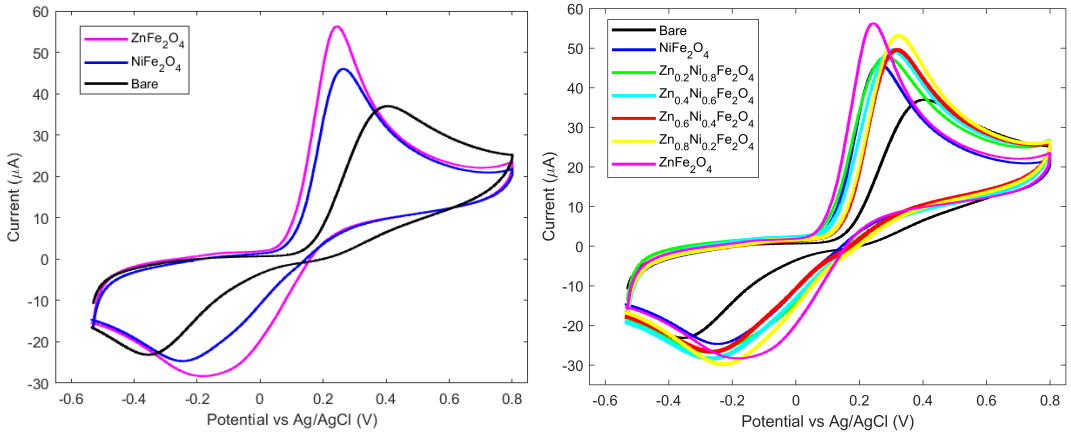

(a) (b)

Fig. 3.14 Cyclic voltammograms of bare and $Zn_xNi_{1-x}Fe_2O_4$ nanomaterials-modified sensors while detecting 1 mM APAP in 0.1 M PB at pH 7. (a) Comparison of $NiFe_2O_4$ and $ZnFe_2O_4$ sensors with bare carbon sensor, (b) comparison of $Zn_xNi_{1-x}Fe_2O_4$ (x = 0, 0.2, 0.4, 0.6, 0.8, 1) sensors with bare carbon sensor.

solutions prepared in 1-butanol are used for the surface modification as the progress of spreading is slower than in methanol.

Figure 3.14a shows the cyclic voltammograms of the $ZnFe_2O_4$, Ni_2O_4, and bare sensors (where the nanoparticles are dispersed in butanol) with 1 mM APAP in 0.1 M PB at pH 7, (ν = 100 mV/s). When comparing the cyclic voltammograms of the bare sensor and the $NiFe_2O_4$ sensor, it is clear that the $NiFe_2O_4$ sensor outperforms the bare sensor, producing an oxidation peak current of 40.4 $\pm$ 0.2 μA (with all errors reported as standard error of the mean, SEM (unless specified)) at a potential of 282 $\pm$ 1 mV, whereas the bare sensor achieves an oxidation peak current of 34.5 $\pm$ 0.2 μA at a potential of 396 $\pm$ 2 mV. The $ZnFe_2O_4$ sensor demonstrates an oxidation peak current of 52.14 $\pm$ 0.56 μA at a potential of 244 $\pm$ 1 mV. This represents an increase of 6 μA and a reduction of 114 mV for the $NiFe_2O_4$ sensor, and an increase of 18 μA and a reduction of 152 mV for the $ZnFe_2O_4$ sensor, compared to the bare sensor.

Figure 3.14b presents a comparison of the CVs for $Zn_xNi_{1-x}Fe_2O_4$ (x = 0, 0.2, 0.4, 0.6, 0.8, 1) and the bare sensors. As the percentage of Zn in $Zn_xNi_{1-x}Fe_2O_4$ increases, the oxidation current rises gradually, due to the effect of the transition from inverse spinel to normal spinel. The conductivity of $NiFe_2O_4$ is lower than that of $ZnFe_2O_4$ due to the occupancy of Ni and Zn in the “Oh” and “Td” sites, respectively,

in their respective spinel structures. The gradual addition of Zn alters the crystal structure from inverse to normal spinel (as evidenced by the XRD results), resulting in an increase in the material's conductivity. This change explains the increase in oxidation current as the Zn percentage in the composition of $Zn_xNi_{1-x}Fe_2O_4$ is raised.

For the bare sensor, the oxidation peak of APAP is observed at 396 $\pm$ 2 mV. However, when Zn–Ni ferrites are immobilized on the SPCE surface, the peaks shift to lower potentials. Specifically, the oxidation peaks occur at 282 $\pm$ 2 mV for $NiFe_2O_4$ and 244 $\pm$ 1 mV for $ZnFe_2O_4$ in a 1 mM APAP solution. The use of $ZnFe_2O_4$ nanoparticles results in a significant reduction of oxidation peak potential up to 152 mV. This reduction implies that less energy is required for ET, which in turn allows for a more efficient electronics design with lower voltage requirements for driving the ECI. This shift to lower potentials is a clear indication of the well-known Nernst effect (equation 1.16). However, this can't be accounted based on the semi-infinite planar diffusion model in the case of thin-layer effects [1].

The more effective equation considering the nano-structured thin layers is the modified Nernst equation which is proposed initially for an irreversible system [149] as follows:

$$E = E_{Nernst} + \frac{ET}{\alpha F} ln\left(\frac{\alpha F \nu}{RTlk_0}\right) \tag{3.4}$$

where E_{Nernst} is the standard Nernst potential given by equation 1.16, 'l' is the the thickness of the thin layer, k_0 is the standard heterogeneous rate constant [150]. This shows that the presence of nanostructured layers at the ECI influences the Nernst potential leading to different redox potentials of the analyte.

3.2.1 Effect of Scan rate

Figure 3.15 shows the CVs of bare and $Zn_xNi_{1-x}Fe_2O_4$ (x = 0, 0.2, 0.4, 0.6, 0.8, 1) sensors with varying scan rate from 50 to 300 mV/s (steps of 50 mV/s) and inset plots show the reduction and oxidation peak currents variation with respect to $\sqrt{\nu}$. It is observed that the redox potential peak positions shift with (ν), and both the oxidation current (I_{pa}) and reduction current (I_{pc}) vary linearly with respect to $\sqrt{\nu}$. The linear

regression equations and corresponding regression coefficients are presented in Table 3.5.

Table 3.5 I_{pa} and I_{pc} linear regression equations for bare and $Zn_xNi_{1-x}Fe_2O_4$ sensors.

Sensor	I_{pa}	R^2	I_{pc}	R^2
Bare	$2.82\sqrt{\nu} + 6.35$	0.998	$-2.26\sqrt{\nu} + 8.93$	0.999
$NiFe_2O_4$	$4.25\sqrt{\nu} + 3.17$	0.997	$-2.47\sqrt{\nu} + 0.83$	0.987
$Zn_{0.2}Ni_{0.8}Fe_2O_4$	$4.15\sqrt{\nu} + 3.69$	0.996	$-2.67\sqrt{\nu} + 3.33$	0.981
$Zn_{0.4}Ni_{0.6}Fe_2O_4$	$5.69\sqrt{\nu} - 1.92$	0.998	$-3.66\sqrt{\nu} + 5.23$	0.989
$Zn_{0.6}Ni_{0.4}Fe_2O_4$	$4.95\sqrt{\nu} + 2.77$	0.999	$-2.86\sqrt{\nu} + 2.17$	0.992
$Zn_{0.8}Ni_{0.2}Fe_2O_4$	$5.28\sqrt{\nu} - 0.04$	0.996	$-2.97\sqrt{\nu} + 1.67$	0.996
$ZnFe_2O_4$	$5.86\sqrt{\nu} + 0.87$	0.999	$-3.27\sqrt{\nu} + 4.35$	0.991

As the scan rate (ν) increases, the redox currents shows a linear increase with $\sqrt{\nu}$. This increase in ν accelerates the rate at which the potential is applied to the sensor, resulting in a reduction in the diffusion layer thickness (d). This reduction leads to higher currents due to the addition of a capacitive current ($I_C = C\nu$, where $\nu = \frac{dE}{dt}$, and 'C' is the capacitance at the interface) to the faradaic current [1, 151]. Our results clearly demonstrate this effect, with the peak position shifting as ν changes. These two concurrent effects indicate that the electrochemical interface behaves as a freely diffusing quasi-reversible system [29].

3.2.2 Kinetic Parameters

Figures 3.16 illustrate that the anodic peak position (E_{pa}) and cathodic peak position (E_{pc}) vary linearly with $\ln(\nu)$, with the corresponding linear regression equations provided in Table 3.6. Additionally, the insets in Figure 3.16 show that the peak separation, ΔE_p, also varies linearly as a function of $\ln(\nu)$, with the regression equations listed in Table 3.7. Notably, all $Zn_xNi_{1-x}Fe_2O_4$ sensors exhibit a lower ΔE_p compared to the bare carbon sensor, indicating a greater potential for reversibility. Given that the redox peak currents vary linearly with $\sqrt{\nu}$ and the redox peak positions vary linearly with $\ln(\nu)$, we applied the Laviron model to calculate the electron transfer rate coefficient (α) and the electron transfer rate constant (k) as described in chapter 1 section 1.5.1.

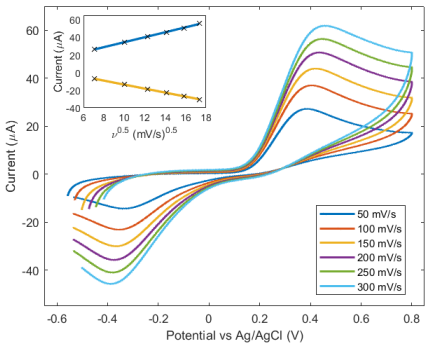

(a) Bare

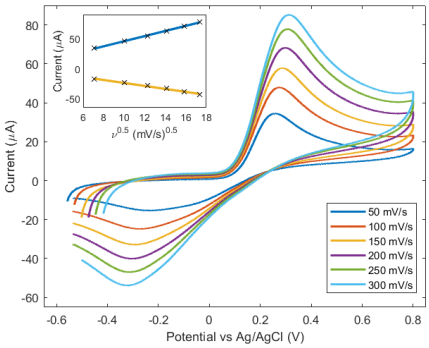

(b) $NiFe_2O_4$

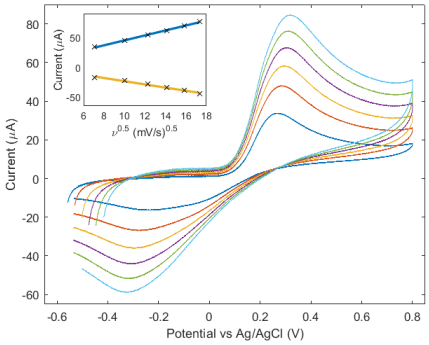

(c) $Zn_{0.2}Ni_{0.8}Fe_2O_4$

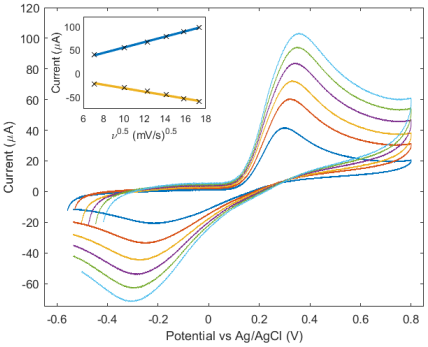

(d) $Zn_{0.4}Ni_{0.6}Fe_2O_4$

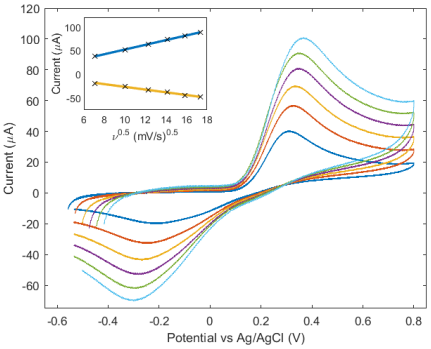

(e) $Zn_{0.6}Ni_{0.4}Fe_2O_4$

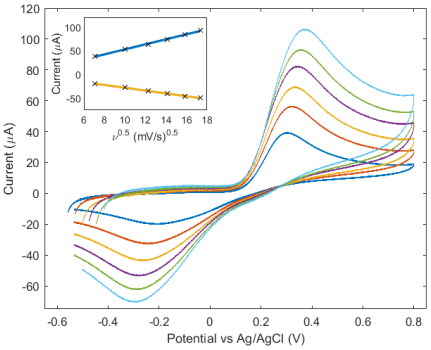

(f) $Zn_{0.8}Ni_{0.2}Fe_2O_4$

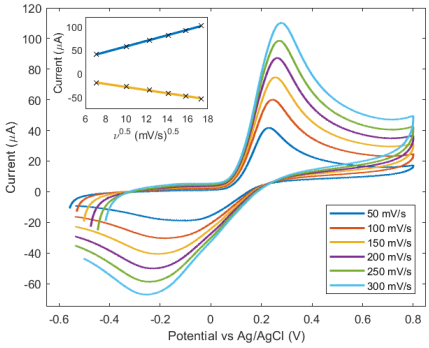

(g) $ZnFe_2O_4$

Fig. 3.15 Cyclic voltammograms with varying scan rate from 50 to 300 mV/s (step 50 mV/s). a) bare, b) $NiFe_2O_4$, c) $Zn_{0.2}Ni_{0.8}Fe_2O_4$, d) $Zn_{0.4}Ni_{0.6}Fe_2O_4$, e) $Zn_{0.6}Ni_{0.4}Fe_2O_4$, f) $Zn_{0.8}Ni_{0.2}Fe_2O_4$, and g) $ZnFe_2O_4$ sensors, respectively. Inset shows the redox peak currents versus $\sqrt{\nu}$.

The electron transfer coefficient "α" is calculated using the slopes of the plots of E_{pa} and E_{pc} versus ln(ν). Knowing that the redox process of paracetamol involves two electrons [4], the peak-to-peak separation ΔE_p is determined at ν = 100 mV s^{-1}. For a reversible electrochemical system, the redox positions don't change as we increase 'ν' hence ΔE_p don't change with 'ν' [1]. For a reversible electrochemical process involving 'n' electrons, ΔE_p = 59/n mV, so for a '2' electron process is 29.5 mV [29]. Following this, another big advantage we have obtained is that all the $Zn_xNi_{1-x}Fe_2O_4$ sensors have a lower ΔE_p which have the higher possibility of reversibility compared to the bare sensor. From Randles-Sevčik's theory it is found that the electrochemical interface is not reversible hence the redox positions differ with 'ν' so does the ΔE_p. Therefore, we have considered ΔE_p at a specific 'ν' while calculating 'k'.

The rate constant (k) is then calculated by substituting the known values into the equation 1.27. Table 3.8 presents the values of α, ΔE_p, and k for all sensors. The bare sensor exhibits a higher ΔE_p (746 $\pm$ 5 mV) and a lower k value ((2.22 $\pm$ 0.19) $\times 10^{-3}$ ms^{-1}), while the $ZnFe_2O_4$ sensor shows a lower ΔE_p (386 $\pm$ 2 mV) and a higher k (13.1 $\pm$ 2.8 ms^{-1}), which is four orders of magnitude higher than the bare carbon sensor proving its superior performance. All $Zn_xNi_{1-x}Fe_2O_4$ sensors exhibit higher k values, with $ZnFe_2O_4$ demonstrating the highest k, leading to faster electrochemical reactions compared to the bare carbon sensor.

Table 3.6 E_{pa} and E_{pc} linear regression equations for bare and $Zn_xNi_{1-x}Fe_2O_4$ sensors.

Sensor	E_{pa}	R^2	E_{pc}	R^2
Bare	41.49 ln(ν) + 216.1	0.973	-33.3 ln(ν) - 189.3	0.996
$NiFe_2O_4$	28.6 ln(ν) + 151.3	0.989	-49.1 ln(ν) - 20.9	0.997
$Zn_{0.2}Ni_{0.8}Fe_2O_4$	26.6 ln(ν) + 160.8	0.992	-53.1 ln(ν) - 4.9	0.996
$Zn_{0.4}Ni_{0.6}Fe_2O_4$	21.8 ln(ν) + 196.7	0.985	-51.5 ln(ν) + 15.1	0.989
$Zn_{0.6}Ni_{0.4}Fe_2O_4$	28.3 ln(ν) + 199.6	0.975	-50.9 ln(ν) + 1.2	0.991
$Zn_{0.8}Ni_{0.2}Fe_2O_4$	29.8 ln(ν) + 189.9	0.959	-45.6 ln(ν) - 20.2	0.999
$ZnFe_2O_4$	26.39 ln(ν) + 127.3	0.975	-90.2 ln(ν) - 278.3	0.996

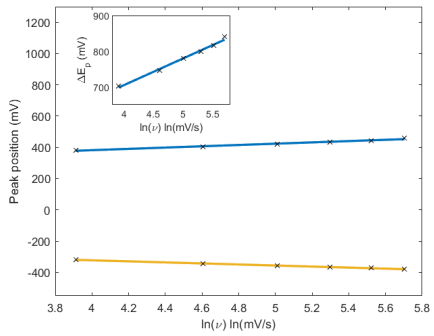

(a) Bare

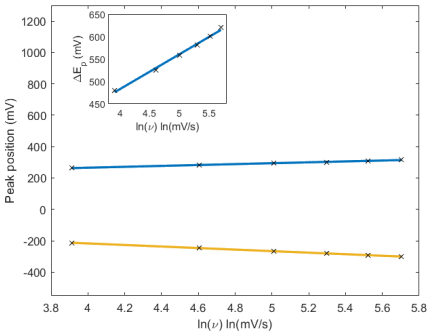

(b) $NiFe_2O_4$

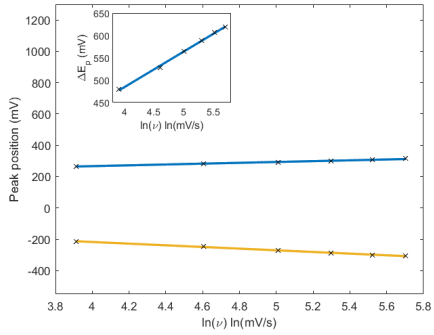

(c) $Zn_{0.2}Ni_{0.8}Fe_2O_4$

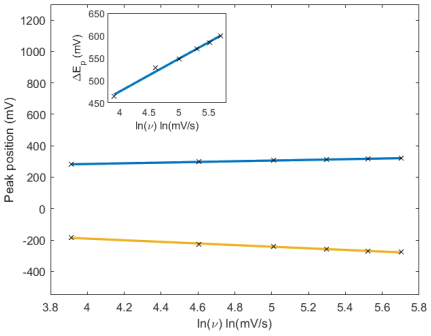

(d) $Zn_{0.4}Ni_{0.6}Fe_2O_4$

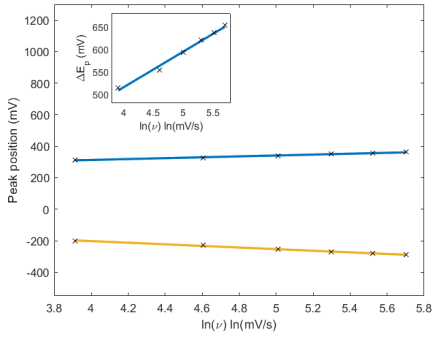

(e) $Zn_{0.6}Ni_{0.4}Fe_2O_4$

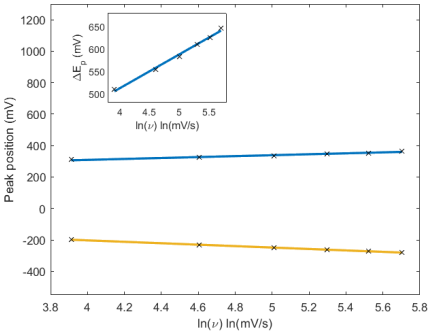

(f) $Zn_{0.8}Ni_{0.2}Fe_2O_4$

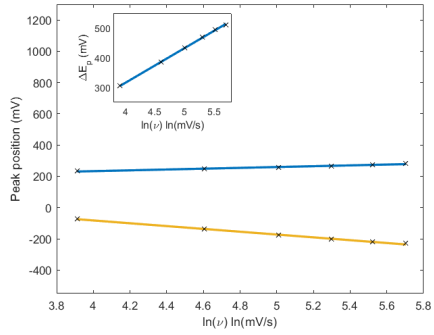

(g) $ZnFe_2O_4$

Fig. 3.16 Redox peak potentials with $\ln(\nu)$. a) bare, b) $NiFe_2O_4$, c) $Zn_{0.2}Ni_{0.8}Fe_2O_4$, d) $Zn_{0.4}Ni_{0.6}Fe_2O_4$, e) $Zn_{0.6}Ni_{0.4}Fe_2O_4$, f) $Zn_{0.8}Ni_{0.2}Fe_2O_4$, and g) $ZnFe_2O_4$ sensors, respectively. Inset shows the ΔE_p versus $\ln(\nu)$.

Table 3.7 ΔE_p linear regression equations for bare and $Zn_xNi_{1-x}Fe_2O_4$ sensors.

Sensor	ΔE_p	R^2
Bare	74.8 ln(ν) + 405.47	0.991
$NiFe_2O_4$	77.6 ln(ν) + 172.13	0.995
$Zn_{0.2}Ni_{0.8}Fe_2O_4$	79.6 ln(ν) + 165.7	0.998
$Zn_{0.4}Ni_{0.6}Fe_2O_4$	73.3 ln(ν) + 181.6	0.991
$Zn_{0.6}Ni_{0.4}Fe_2O_4$	79.2 ln(ν) + 198.4	0.989
$Zn_{0.8}Ni_{0.2}Fe_2O_4$	75.4 ln(ν) + 210.1	0.992
$ZnFe_2O_4$	116.6 ln(ν) - 151.1	0.999

Table 3.8 α, ΔE_p, and k of bare and $Zn_xNi_{1-x}Fe_2O_4$ sensors.

Sensor	α	ΔE_p (mV)	k (ms^{-1})
Bare	0.536 ± 0.004	746 ± 5	$(2.22 \pm 0.19) \times 10^{-3}$
$NiFe_2O_4$	0.367 ± 0.004	526 ± 6	0.27 ± 0.02
$Zn_{0.2}Ni_{0.8}Fe_2O_4$	0.333 ± 0.015	528 ± 4	0.39 ± 0.07
$Zn_{0.4}Ni_{0.6}Fe_2O_4$	0.296 ± 0.023	528 ± 7	0.62 ± 0.10
$Zn_{0.6}Ni_{0.4}Fe_2O_4$	0.340 ± 0.021	550 ± 6	0.25 ± 0.04
$Zn_{0.8}Ni_{0.2}Fe_2O_4$	0.391 ± 0.023	554 ± 8	0.14 ± 0.01
$ZnFe_2O_4$	0.226 ± 0.017	386 ± 2	13.1 ± 2.8

3.2.3 Sensitivity and limit of detection

CVs are recorded three times for each type of sensor, the average of the three oxidation peak currents at each concentration of APAP is used to calibrate the sensors as shown in Figure 3.17. The sensitivities (S) of all the sensors with fitting coefficient R^2 and standard error mean (SEM) are reported in Table 3.9 are evaluated by taking the slope of the calibration plots. And the limit of detection (LOD), which is the lowest concentration of the analyte detectable by the sensor, is calculated as described in chapter 1 and reported in Table 3.9.

According to Table 3.9, the bare sensor has a sensitivity of 16.68 ± 0.93 μA/mM, while the $Zn_xNi_{1-x}Fe_2O_4$ sensors with x = 0, 0.2, 0.4, 0.6, and 0.8 exhibit sensitivities close to 30 μA/mM, significantly higher than the bare carbon sensor. The $ZnFe_2O_4$

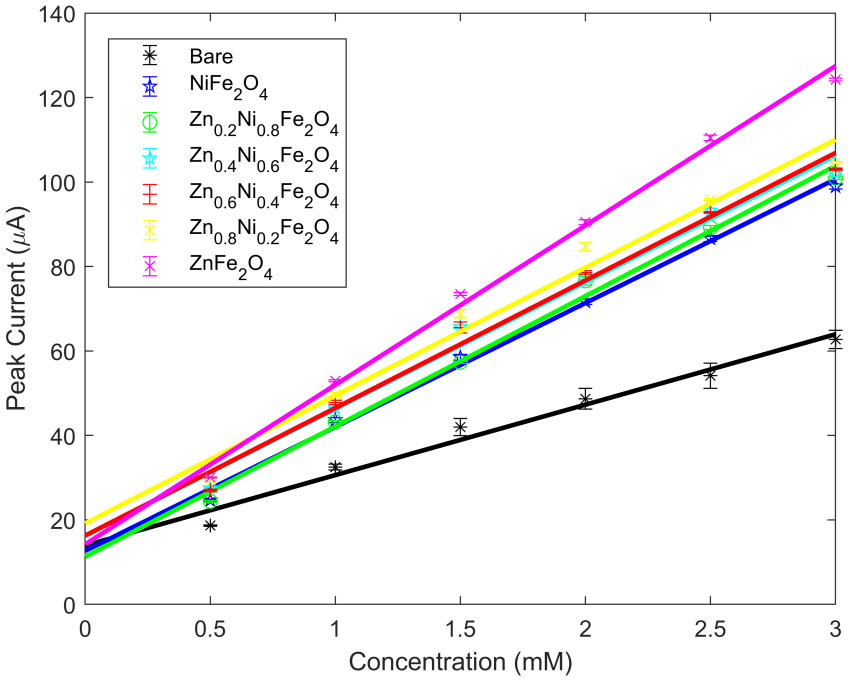

Fig. 3.17 Calibration of bare and $Zn_xNi_{1-x}Fe_2O_4$ sensors with paracetamol.

sensor is the most sensitive, with a sensitivity of 37.75 ± 0.17 μA/mM, which is more than two times higher than the bare carbon sensor. The Randles-Sevčik's effect is observed in the oxidation current with the change in concentration during the calibration process. This indicates that the enhancement in "S" is due to the nanostructured thin layers present at the electrochemical interface (ECI). The two-fold increase in sensitivity of the $ZnFe_2O_4$ sensor compared to the bare sensor represents a significant advancement using ferrite nanomaterials.

Table 3.9 Sensitivity and limit of detection of bare and $Zn_xNi_{1-x}Fe_2O_4$ sensors.

Sensor	Sensitivity (μA/mM)	R^2	LOD (μM)
Bare	16.7 ± 0.9	0.975	3.26 ± 0.17
$NiFe_2O_4$	29.4 ± 0.4	0.996	6.93 ± 0.08
$Zn_{0.2}Ni_{0.8}Fe_2O_4$	30.9 ± 0.2	0.994	13.08 ± 0.05
$Zn_{0.4}Ni_{0.6}Fe_2O_4$	30.0 ± 0.2	0.986	16.41 ± 0.09
$Zn_{0.6}Ni_{0.4}Fe_2O_4$	30.2 ± 0.3	0.986	26.96 ± 0.24
$Zn_{0.8}Ni_{0.2}Fe_2O_4$	30.3 ± 0.2	0.976	42.94 ± 0.22
$ZnFe_2O_4$	37.8 ± 0.2	0.995	7.94 ± 0.04

When developing an electrochemical sensor, repeatability and reproducibility are crucial parameters. To assess repeatability, CV is conducted five times on the same sensor under identical conditions. The relative standard error of the mean (RSem) is found to be 0.57% for $NiFe_2O_4$ sensor and 1.07% for $ZnFe_2O_4$ sensors. Reproducibility is tested by performing CV on three different sensors, yielding RSem values of 1.84% and 1.58% for $NiFe_2O_4$ and for $ZnFe_2O_4$ sensors, respectively.

3.3 Effect of Material Properties on Electrochemical Sensing

The particles' surfaces and sides are not fully exposed, limiting their participation in the electrochemical reaction at the interface. This limitation is due to the aggregation of particles on the surface, which can lead to varying levels of reactivity among individual nanoparticles during the electrochemical process. This could be one of the reasons for the similar sensitivities of $Zn_xNi_{1-x}Fe_2O_4$ (x = 0, 0.2, 0.4, 0.6, 0.8) sensors. To verify the effect of the degree of aggregation and exposure of particles' surface in electrochemical reaction, a controlled study by varying the degree of aggregation and particle exposure is required. As the thickness of the nanoparticle layer increased, we observed a reduction in the oxidation current, likely caused by greater particle aggregation increasing the resistance between electrode surface and the electrolytic solution, which in turn reduced the reactivity of the nanoparticles and hindered the electron transfer rate. However, we managed to achieve a consistent shape of nanomaterials where the orientation of the particles does not impact their electrochemical activity. This uniformity enabled a direct comparison of the electrochemical performance across different ferrite-based sensors.

XRD confirmed that $NiFe_2O_4$ has an inverse spinel structure, where half of the Fe(III) occupies the 'Td' sites, while Ni(II) and the remaining half of Fe(III) shares the 'Oh' sites. When Zn(II) is introduced into $NiFe_2O_4$, it gradually transforms the inverse spinel into a normal spinel by removing Ni(II) from the structure by pushing Fe(III) into the 'Oh' sites from 'Td' sites. In this normal spinel configuration, Zn(II) occupies the 'Td' sites, while all the Fe(III) go into the 'Oh' sites. The electrochemical data indicate that as the percentage of Zn(II) in the crystal structure increases, the sensor performance, in terms of sensitivity (S) and electron transfer rate

(k), increases. This enhancement is attributed to the changes in electronic transitions within the crystal structure from inverse to normal spinel.

Research into the electronic properties of $NiFe_2O_4$ and $ZnFe_2O_4$ has shown that $NiFe_2O_4$ has lower conductivity compared to ZnFe2O4, largely due to differences in site occupancy and charge transfer between cations [138]. In spinel structures, conductivity is explained by the "small polaron-hopping" model, where charge transfer between cations in "Oh" sites with different valency electrons occurs [152]. In ferrites, conductivity is primarily driven by electron exchange between Fe(III) and Fe(II) in "Oh" sites, with conductivity varying based on the Fe ion concentration in these sites. In inverse spinel structures, the "Oh" sites are shared between Ni(II) and Fe(III), and as the Ni(II) content decreases with the addition of Zn(II), which prefers "Td" sites, the Fe(III) concentration in "Oh" sites increases. This shift towards a normal spinel structure enhances electron hopping between Fe(III) and Fe(II) in "Oh" sites, thereby increasing conductivity.

Inverse spinel $NiFe_2O_4$ is widely recognized as a p-type semiconductor [98, 99, 153–155] due to hole hopping between Ni(III)/Ni(II) states, whereas normal spinel $ZnFe_2O_4$ is considered an n-type semiconductor [99, 156, 108, 157] due to electron hopping between Fe(III)/Fe(II) states. Generally, p-type semiconductors have lower conductivity than n-type semiconductors because holes, the majority carriers in p-type materials, have lower mobility than electrons. Additionally, inverse spinels exhibit a higher dielectric constant at low frequencies compared to normal spinels. Since materials with higher dielectric constants tend to have lower electrical conductivity, this dielectric property further supports the lower conductivity observed in inverse spinels [98]. These characteristics, along with higher resistivity observed in inverse spinels compared to normal spinels, align with the electrochemical behavior of $Zn_xNi_{1-x}Fe_2O_4$ sensors.

3.4 Type of Electron Transfer at the Electrochemical Interface

Burello and Worth's proposed a theoretical predictive model [158, 159], by which the electron transfer mechanism between biological molecules and metal oxide nanoparticles can be understood. The model correlates the HOMO and LUMO of

biological molecules with the conduction band minimum (E_C) and valence band maximum (E_V) of metal oxide semiconductors. The prediction is that the electron transfer is enhanced when the E_C of the metal oxide semiconductor is below or overlaps with the standard redox potential of the biological molecule. However, this enhancement occurs only if an energy level within the conduction band of the metal oxide semiconductor aligns with one of the filled energy levels of the biological molecule. This model assumes the absence of surface states within the bandgap of the metal oxide semiconductor nanomaterials.

A similar methodology was previously applied to examine the oxidative stress and toxic effects of 24 different metal oxides on biological molecules [66], combining experimental and theoretical models to map the E_C and E_V levels with the standard redox potentials of biological molecules. Following these approaches, this work demonstrates the significance of E_g, E_C, and E_V levels as crucial semiconductor properties in electrochemical sensing applications. In this context, E_C represents the LUMO of metal oxide nanoparticles involved in electron transfer with the sensing material, while states below E_V (the valence band) are occupied. For oxidation to occur, the oxidation potential (E_{pa}) of APAP must be higher than the E_C of the ferrite nanomaterial, allowing direct electron hopping/tunneling from APAP to the ferrite surface and subsequently to electron acceptors until the system reaches a steady state. Similarly, for reduction, the reduction potential (E_{pc}) of APAP should be lower than the E_C of the ferrite nanomaterial, enabling electron transfer from the nanomaterials' surface to APAP.

According to this prediction, the energy levels of ferrite nanoparticles are determined using the band gap (E_g) from UV–vis spectroscopy, the valence band maximum (E_V) from XPS, and the conduction band minimum (E_C), calculated as $E_C = E_g + E_v$. The experimentally obtained redox potentials E_{pa} and E_{pc} of APAP are then mapped onto the energy levels of the ferrites, as illustrated in Figure 3.18. The Figure 3.18 shows that only the E_C of $ZnFe_2O_4$ overlaps with the E_{pa} of APAP, while the E_C levels of materials with x = 0 to 0.8 are higher than the E_{pa} of APAP. This overlap accounts for the superior electrochemical performance of the $ZnFe_2O_4$ sensor, which exhibits the lowest E_{pa}, the highest sensitivity, and the fastest electron transfer rate.

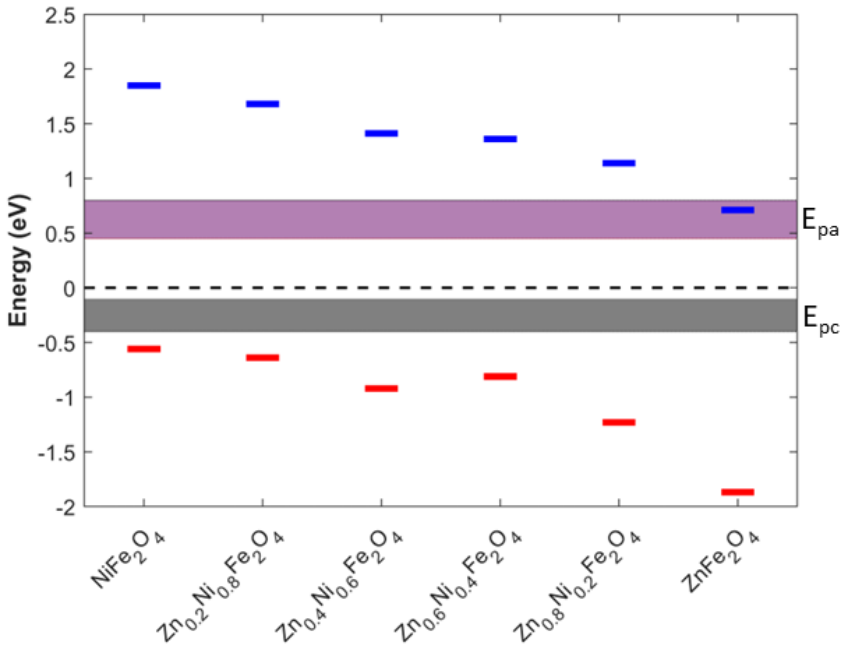

Fig. 3.18 Conduction (E_C) band minimum (blue) and valence (E_V) (red) band maximum of $Zn_xNi_{1-x}Fe_2O_4$ nanomaterials constructed by using E_g (the energy gap between E_C and E_V). Electron transfer prediction from/to paracetamol to/from the surface of the WE by mapping the E_C of the WE with the experimental E_{pa} and E_{pc} of paracetamol. The black dotted lines represent the fermi energy level 'E_f' at '0' eV.

The overlap between $ZnFe_2O_4$'s E_C and APAP's E_{pa} means that the sensor requires less energy for efficient electron transfer with APAP. As a result, the peak-to-peak separation (ΔE_p) is reduced, leading to faster kinetics, a higher rate constant (k), and a greater likelihood of a reversible electrochemical reaction.

Electron transfers are more likely to occur when the energy of the orbitals of the semiconducting materials align with the energy levels of the redox couples. By applying a potential through a potentiostat, we can induce the orbitals of the nanomaterials to match the energy levels of the molecular orbitals of the analyte molecules. The potential required for this alignment depends on the proximity of the sensor material's energy bands to the HOMO levels of the analyte. The closer these levels are, the less potential is needed to facilitate electron transfer, as demonstrated by the $ZnFe_2O_4$ sensor

This electron transfer process involves either the acceptance of an electron into an unoccupied energy level or the removal of an electron from an occupied level. When the sensor is introduced into the analyte solution, electron transfer occurs at the

electrochemical interface (ECI) until chemical potential equilibrium is reached. In the case of a bare sensor, this transfer is direct, occurring between the carbon surface and the analyte, APAP. However, in ferrite-based sensors, the transfer involves two steps: first from APAP to the ferrite nanomaterials and then from the ferrite to the carbon material during oxidation of APAP, or from carbon to ferrite and then to APAP during reduction. This approach provides a valuable framework for identifying the electron transfer phenomena at the ECI between the sensor surface and the analyte of interest.

Additionally, as the Zn content in $NiFe_2O_4$ increases, a trend emerges in the energy bands: the E_C gradually moves towards the APAP's E_{pa}. This shift means that sensors with more nickel require higher voltage to provide sufficient energy for direct electron transfer, which could explain their much lower 'k' values compared to the $ZnFe_2O_4$ sensor. The sensitivity of the sensors also decreases as the E_C level moves further from the E_{pa} level, particularly for sensors with x = 0.8 to 0. Despite the lack of overlap or proximity between E_C and E_{pa}, electron transfer still occurs at the interface, as confirmed by the electrochemical data. This suggests that while the predictive energy band framework offers valuable insights, it may not fully account for electron transfer mechanisms in all cases.

DR UV–vis spectroscopy results suggest the presence of surface states, which is consistent with literature reports on metal oxides like ZnO, and Fe_2O_3 on the surface [160, 161], as confirmed by XRD spectra in Figure 3.3. Since electrochemical sensing is fundamentally a surface phenomenon, these surface states likely play a critical role in the electron transfer process. According to the literature, the energy levels of surface states typically fall within the bandgap of semiconducting materials. As shown in Figure 3.18, the E_{pa} and E_{pc} levels of APAP are within the bandgap of the ferrite nanomaterials. Therefore, the energy levels of these surface states may be positioned below or overlapping with the redox potentials of APAP, facilitating the subsequent electron transfer steps.

This could explain the observed electron transfer in cases with x = 0 to 0.8, where despite the lack of overlap between E_C and E_{pa}, electron transfer still occurred, suggesting that surface state levels could enhance electron transfer at the electrochemical interface (ECI). For instance, during the oxidation of APAP, the complete electron transfer pathway might involve an initial transfer from the HOMO of APAP to the conduction band of the ferrite nanomaterial, followed by a transfer

to the surface state oxide, and finally to the LUMO of the carbon material, achieving chemical potential equilibrium. Alternatively, electrons might transfer directly from the HOMO of APAP to the surface state energy level and then to the LUMO of the carbon material to maintain equilibrium.

Each step in this electron transfer pathway has its own electron transfer rate constant, 'k'. Since these steps occur sequentially, the overall rate constant of the process is determined by the step with the lowest 'k' value. Generally, lower 'k' values are associated with tunneling processes, while higher values correspond to direct transfer processes. This rationale supports the higher 'k' value observed for the $ZnFe_2O_4$ sensor, where there is an overlap between E_C and E_{pa}, indicating a high likelihood of direct electron transfer. In contrast, in cases with x = 0 to 0.8, where no overlap occurs and 'k' values are lower, the electron transfer might involve tunneling through an energy barrier at electrode/electrolyte interface.

In addition to the role of ferrite surface states in electrochemical sensing, it is crucial to consider the impact of metal oxide dissolution in the surrounding environment. The dissolution process depends on the metal's solubility and the difference between the nanoparticle surface and the bulk solution phase [162]. For instance, in the case of ZnO, even without an overlap between the conduction band minimum (E_C) and the standard redox potentials of biological molecules, ZnO nanoparticles have been shown to exhibit toxic effects [66]. These effects have been attributed to the dissolution of ZnO into Zn(II) and $Zn(OH)^+$ ions in water [85], particularly in environments with moderate alkalinity and neutral pH.

Research has demonstrated that a reduction in dissolution decreases these toxic effects. For less soluble materials, the observed effects are a combination of catalytic surface activity and ion release into the environment [163, 85]. Given these considerations, fully understanding electron transfer at the ECI requires comprehensive knowledge of the material's energy levels, surface state energy levels, and the effects of metal dissolution.

3.5 Original Contribution I

This work presents the fundamental investigation of the effect of crystal structure from normal spinel ($ZnFe_2O_4$) to inverse spinel ($NiFe_2O_4$) nanomaterials with a

uniform spherical size particles on electron transfer at the electrochemical interface using paracetamol as a test probe molecule. The electrochemical performance of the spinel oxide nanomaterials by autocombustion synthesis is presented in terms of sensitivity and rate constant. The electrochemical parameters are correlated with crystal structure of the ferrite nanomaterials and type of electron transfer is predicted based on nanomaterials enery bands.

A part of the work has been presented as a poster at the 'Nano innovation' conference in Rome, Italy in September, 2022.

A full manuscript of the work has been successfully published in "Small Structures" journal by Wiley publications as "Unraveling the Effect of the Chemical and Structural Composition of $Zn_xNi_{1-x}Fe_2O_4$ on the Electron Transfer at the Electrochemical Interface". The paper can be found at the following url:
https://onlinelibrary.wiley.com/doi/10.1002/sstr.202300163

Chapter 4

Effect of Trivalent Cation on Electron Transfer

Chapter 3 showed that normal spinel $ZnFe_2O_4$ has higher sensitivity and rate constant in detecting paracetamol with direct electron transfer compared to inverse or mixed spinel nanomaterials. Therefore, normal spinel $ZnFe_2O_4$ is chosen to be the reference material to continue further. In this work, the effect of trivalent cations on electron transfer at the electrochemical interface is studied by substituting Fe^{3+} ions with Cr^{3+} ions which have similar ionic radius. For direct comparison to previous work (chapter 3) and further work (chapter 5), the sensors are always studied in electrochemical detection of paracetamol.

Normal spinel $ZnFe_2O_4$ is synthesized by substituting Fe^{3+} ions with Cr^{3+} ions with different mole fractions to understand the effect of Cr^{3+} (trivalent cation) ions on the electrochemical activity of $ZnFe_2O_4$ nanomaterial. $ZnCr_xFe_{2-x}O_4$ (x = 0, 0.25, 0.5, 0.75, 1, 2) materials are synthesized by auto combustion and the materials are characterized as in chapter 3. Electrochemical performance with paracetamol is studied by comparing the sensitivity and rate constant of different sensors with Cr^{3+} substituted materials. Insights on electron transfer at the ECI are presented and discussed in this chapter.

4.1 Material Characterization

4.1.1 Morphological Characterization

Figure 4.1, illustrates the SEM captures of $ZnCr_xFe_{2-x}O_4$ (x = 0, 0.25, 0.5, 0.75, 1, 2) materials. The images reveal that the nanostructured particles exhibit a similar morphology across all samples (Figure 4.1a - 4.1f). Aggregation of particles is evident in the images and consistent with previous images in chapter 3 due to the auto-combustion synthesis method. Particle size estimation is carried out using ImageJ software by selecting a region of the image with minimal aggregation and the results presented in Table 4.1. $ZnCr_xFe_{2-x}O_4$ (x = 0.25, 0.5, 0.75, 1, 2) displayed particle sizes comparable to those of zinc ferrite (x = 0), which had a slightly larger size (as seen in Figure 4.1a). This difference in size could be due to the formation of particles from a greater number of crystallites in the case of x = 0, which is expected based on the synthesis method used.

Table 4.1 The average particle size of $ZnCr_xFe_{2-x}O_4$ materials

Material	Average particle size (nm)
$ZnFe_2O_4$	44 ± 17
$ZnCr_{0.25}Ni_{1.75}Fe_2O_4$	29 ± 6
$ZnCr_{0.5}Ni_{1.5}Fe_2O_4$	25 ± 5
$ZnCr_{0.75}Fe_{1.25}Fe_2O_4$	26 ± 5
$ZnCrFeO_4$	26 ± 7
$ZnCr_2O_4$	20 ± 3

4.1.2 Structural Characterization

The XRD patterns for $ZnCr_xFe_{2-x}O_4$ (x = 0, 0.25, 0.5, 0.75, 1, 2) are displayed in Figure 4.2. For the samples with x = 0 and x = 2, the diffraction patterns align completely with those of the normal spinel structures Franklinite (ZnFe2O4, ref. code 01-089-4926, ICSD-076178) and Zincochromite (ZnCr2O4, ref. code 00-022-1107). Even in the intermediate compositions, the $ZnCr_xFe_{2-x}O_4$ spinel phase remains the predominant crystalline phase, although the patterns are shifted relative to both Franklinite and Zincochromite. Specifically, for x values between 0.25 and 1,

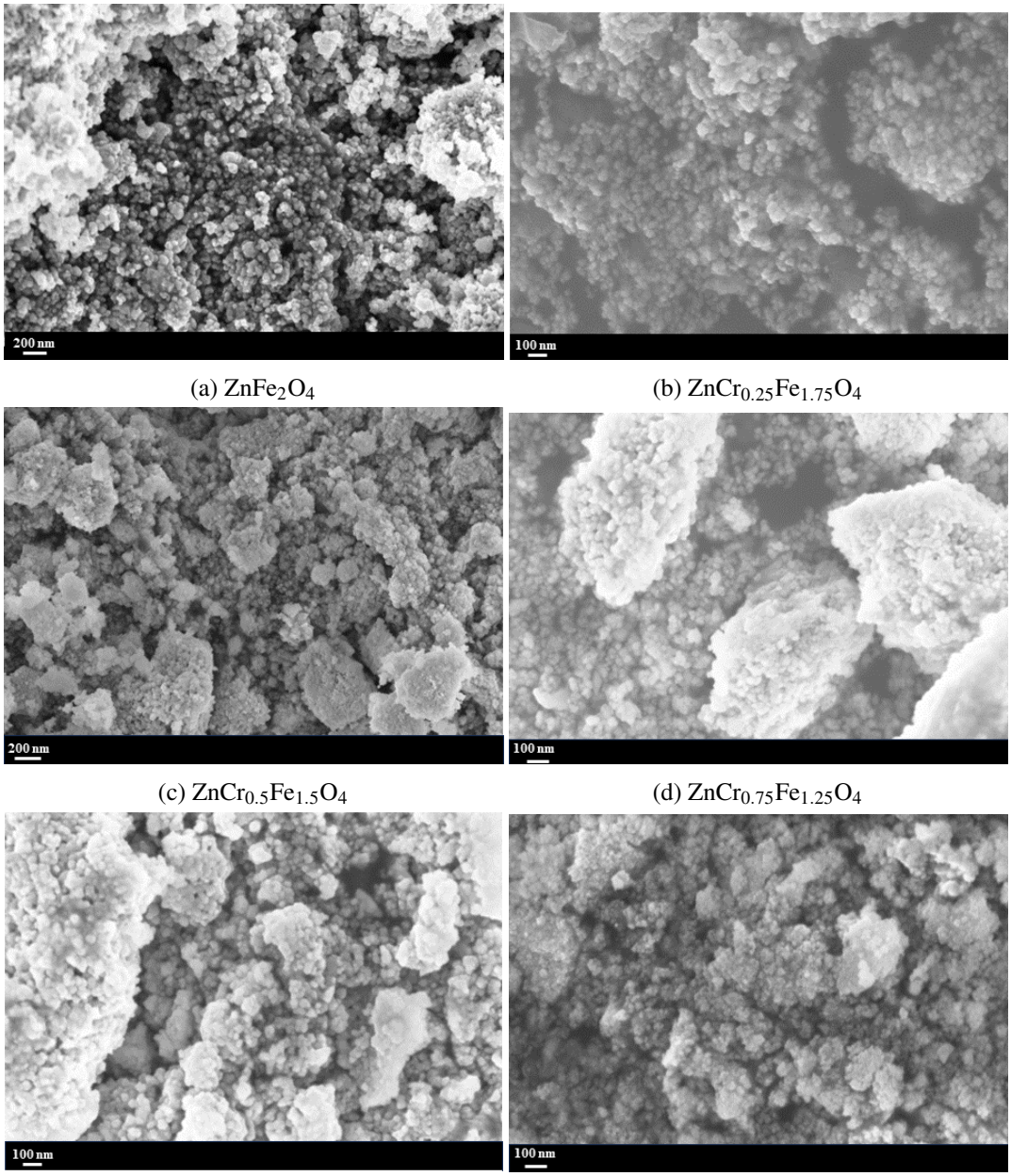

(a) $ZnFe_2O_4$ (b) $ZnCr_{0.25}Fe_{1.75}O_4$

(c) $ZnCr_{0.5}Fe_{1.5}O_4$ (d) $ZnCr_{0.75}Fe_{1.25}O_4$

(e) $ZnCrFeO_4$ (f) $ZnCr_2O_4$

Fig. 4.1 FESEM images of $ZnCr_xFe_{2-x}O_4$ nanomaterials.

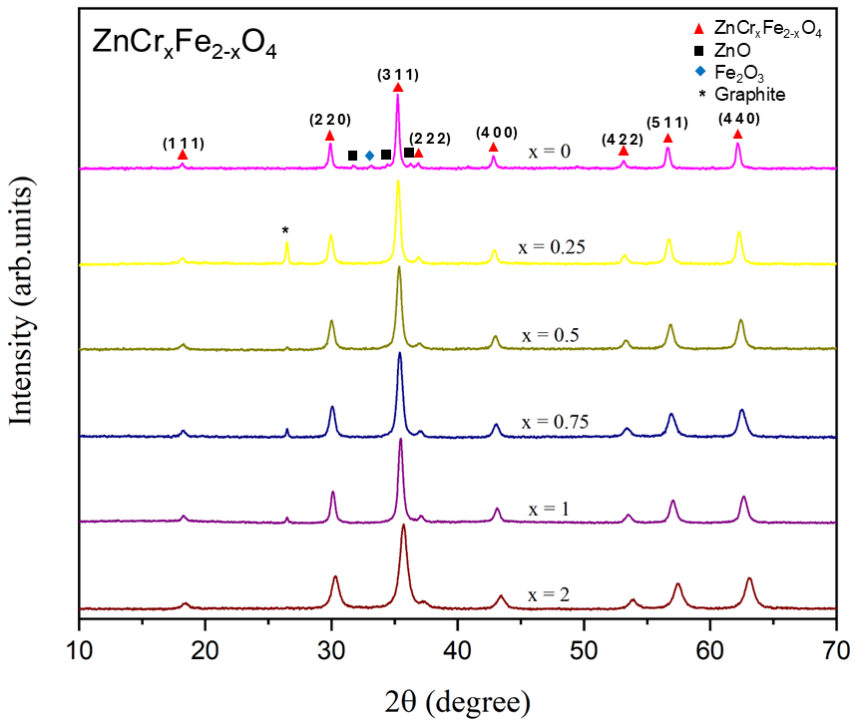

Fig. 4.2 XRD patterns of $ZnCr_xFe_{2-x}O_4$ nanomaterials showing different crystal phases.

the spinel XRD peaks progressively shift towards lower 2θ values as the Cr content increases. This intermediate positioning of diffraction peaks between Franklinite and Zincochromite suggests that materials with intermediate compositions may possess a structure that is between those of $ZnFe_2O_4$ and $ZnCr_2O_4$, similar to observations in our previous study on $Zn_xNi_{1-x}Fe_2O_4$ nanomaterials in chapter 3.

This behavior can be explained by considering the cation distribution within spinel oxides, which is influenced by factors such as ionic radii, electrostatic forces, and crystal field stabilization energy (CFSE) [164]. Cr^{3+} ions typically form d^3 (high spin) complexes with a significant octahedral crystal field stabilization energy (CFSE) of -6/5Δ_O (octahedral d-orbital splitting energy), leading to a very high octahedral site preference energy (OSPE), as depicted in Figure 4.3. Fe^{3+} ions, on the other hand, form d^5 high spin complexes (due to the weak ligand (O^{2-}), resulting in a lower Δ_O), with zero CFSE and zero OSPE [165] indicating that Fe^{3+} has no specific site preference. In contrast, Zn^{2+} ions have a strong preference for tetrahedral sites as discussed in chapter 3, causing Fe^{3+} to occupy octahedral sites. These factors suggest that $ZnCr_2O_4$ and $ZnFe_2O_4$ are normal spinels, as mixing Zn^{2+} with Cr^{3+} or Fe^{3+} in tetrahedral or octahedral sites is not feasible. The progressive shift in the

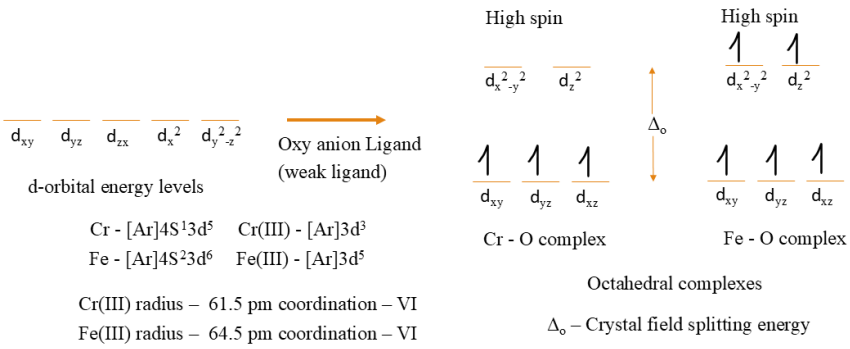

Fig. 4.3 Cr, Fe octahedral complexes with high spin crystal field stabilization energy.

XRD peaks as the composition changes could be attributed to the slightly different ionic radii of Cr^{3+} (61.5 pm) and Fe^{3+} (64.5 pm) [166] ions in the octahedral sites.

The XRD patterns for the intermediate compositions (x = 0.25, 0.5, 0.75, and 1) reveal a small peak at a 2θ value of 26.5°, corresponding to the most intense peak of graphite. The presence of this crystalline phase can be attributed to the synthesis process, which utilized a graphite reactor. However, the weaker peaks of graphite are not detected, likely due to the limited quantity of this phase. Additionally, four small peaks are observed in the XRD pattern of $ZnFe_2O_4$ within the 2θ range of 30° to 36° as discussed in chapter 3.

The Debye-Scherrer method is applied to calculate the average crystallite size of the spinel oxides, using a shape factor of 0.9, which assumes a spherical shape. Seven high-intensity peaks corresponding to the diffraction from the (111), (220), (311), (400), (422), (511), and (440) planes are analyzed. Table 4.2 presents the average crystallite size of $ZnCr_xFe_{2-x}O_4$ nanomaterials. The crystallite sizes derived from XRD align well with the particle sizes estimated from SEM. An irregular variation in crystallite size is observed as the composition of $ZnCr_2O_4$ changed with the substitution of Fe^{3+} by Cr^{3+}. Such irregularities are common in auto-combustion synthesis due to the limited control over crystallite growth kinetics as observed in chapter 3. Since the synthesis is due to self sustained reaction the growth kinetics could be different due to the variation in the total weight of the reaction mixture and the amount of oxygen present during the reaction as the synthesis is performed at ambient conditions. This can be verified by performing the in-situ synthesis in a controlled environment.

Table 4.2 The average crystallite size of $ZnCr_xFe_{2-x}O_4$ materials

Material	Average crystallite size (nm)
$ZnFe_2O_4$	36.2 ± 1.4
$ZnCr_{0.25}Fe_{1.75}O_4$	22.9 ± 1.1
$ZnCr_{0.5}Fe_{1.5}O_4$	18.7 ± 0.6
$ZnCr_{0.75}Fe_{1.25}O_4$	16.6 ± 0.7
$ZnCrFeO_4$	20.1 ± 1.2
$ZnCr_2O_4$	12.3 ± 0.2

4.1.3 Spectroscopic Characterization

Figure 4.4a shows the Raman spectrum of $ZnCr_2O_4$. According to previous studies [167], the $ZnCr_2O_4$ spinel exhibits five Raman active modes. The modes at 180, 510, and 589 cm^{-1} correspond to the $F_{2g}(3)$, $F_{2g}(2)$, and $F_{2g}(1)$ symmetries of the spinel structure, respectively. The prominent mode around 730 cm^{-1} is associated with the Cr-O symmetric stretching vibration of A_{1g} symmetry in CrO_6 octahedra. The mode at 420 cm^{-1} corresponds to the E_g symmetry of the spinel, while the peak at 340 cm^{-1} is attributed to the multi-phonon vibration of ZnO [168], likely due to the surface ZnO present on the $ZnCr_2O_4$ spinel. The band near 820 cm^{-1} is assigned to O-Cr^{3+}-O symmetric stretching, which is attributed to the presence of surface chromium hydroxide. Meanwhile, the bands between 900 and 1000 cm^{-1} are ascribed to Cr^{6+}-O vibrations, resulting from the over-oxidation of Cr to form CrO_3 on the spinel surface [169].

The Raman spectra of $ZnCr_xFe_{2-x}O_4$ (x = 0, 0.25, 0.5, 0.75, 1) nanomaterials are shown in Figure 4.4b. As Fe is introduced into the $ZnCr_2O_4$ spinel structure, the bands between 900 and 1000 cm^{-1} disappear, suggesting that the over-oxidation of Cr is prevented. However, the bands around 820 cm^{-1} persist, indicating the presence of surface chromium hydroxide. The other Raman bands of the spinel can be similarly assigned to the Zn-Cr-Fe spinel nanomaterials. The interpretation of the Raman spectrum for pure zinc ferrite (x = 0) is discussed in section 3.1.3.

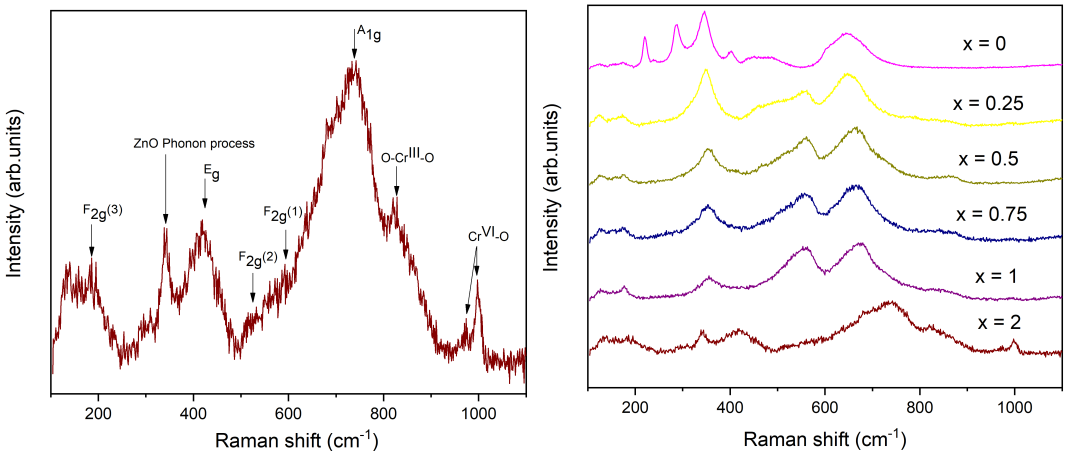

Fig. 4.4 Raman spectra of a) $ZnCr_2O_4$ and b) $ZnCr_xFe_{2-x}O_4$ nanomaterials.

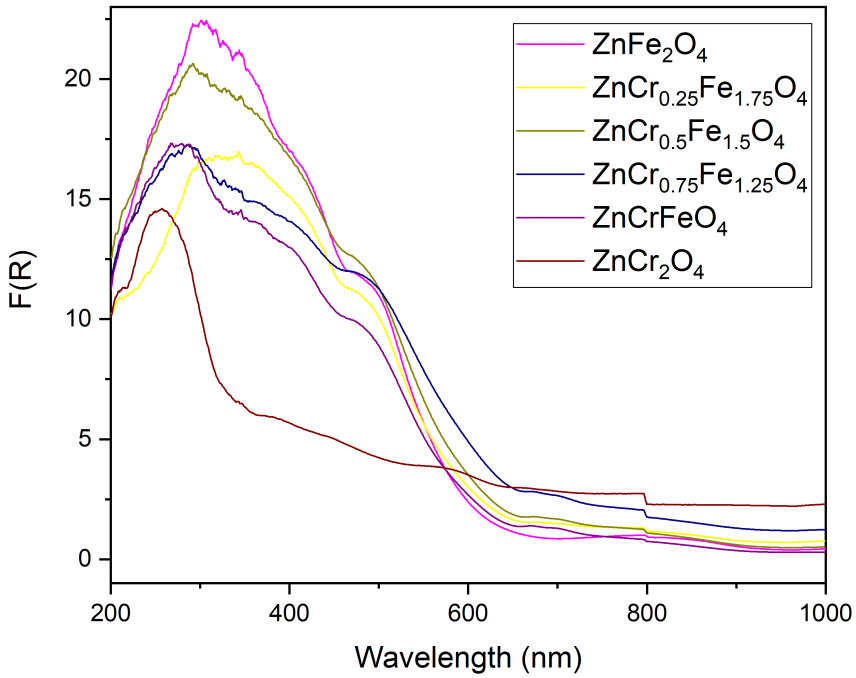

Fig. 4.5 Diffuse reflectance (DR) UV-vis spectra of $ZnCr_xFe_{2-x}O_4$ nanomaterials.

The Diffuse Reflectance (DR) UV-Vis spectra of $ZnCrxFe_{2-x}O_4$ nanomaterials are presented as the Kubelka-Munk function in Figure 4.5. The spike around 800 nm is due to the optical filter change during the measurement. E_g is determined using Tauc plot method, assuming direct electron transitions. The Tauc plot extrapolation accounted for the band tailing effect caused by surface states (confirmed by XRD,

Raman, and XPS) as shown in Figure 4.6. The band gap values, reported in Table 4.3, reflect an average energy due to these surface oxides or hydroxides on the $ZnCr_xFe_{2-x}O_4$ spinel nanomaterials. As Cr^{3+} ions are introduced into the $ZnFe_2O_4$ spinel, the band gap initially decreased, reaching its lowest point at a Cr^{3+} ion content of x = 0.5. However, with further increases in Cr(III) content, the band gap began to rise, continuing to increase as Fe^{3+} ions are fully replaced by Cr^{3+} ions in the spinel.

The full XPS survey of $ZnCr_xFe_{2-x}O_4$ (x = 1, 2) nanomaterials, shown in Figure 4.7, confirmed the presence of only the expected elements in the spinels, along with adventitious carbon, and ruled out the presence of nitrates. High-resolution (HR) XPS spectra (Figure 4.8) are analyzed to determine the oxidation states of Zn, Fe, Cr, and O in $ZnCr_xFe_{2-x}O_4$ nanomaterials. The HR spectrum of O 1s (Figure 4.8d) is decomposed into three components: lattice oxygen O^{2-} (Zn-O, Fe-O, and Cr-O) at a binding energy (BE) of approximately 529.9 eV, hydroxyl groups at around 531 eV, and adsorbed water at about 533 eV [147]. In Figure 4.8a, the Zn 2p spectrum exhibits splitting into Zn $2p_{1/2}$ and Zn $2p_{3/2}$ peaks at 1044.1 eV and 1021.1 eV (ΔBE = 23 eV), respectively, which are indicative of tetrahedral Zn^{2+} in the spinel structure. The Fe 2p spectrum (Figure 4.8c) shows Fe $2p_{1/2}$ and Fe $2p_{3/2}$ peaks at approximately 725.6 eV and 711.5 eV (ΔBE = 14.3 eV), along with two shake-up satellites at 733.8 eV and 718.4 eV, confirming the presence of octahedral Fe^{3+} in the spinel ferrites. The Cr $2p_{1/2}$ and Cr $2p_{3/2}$ peaks (Figure 4.8b) are resolved into three components. The peaks at 588 eV and 578.1 eV (ΔBE = 10.1 eV) are attributed to Cr^{3+} bonding with hydroxyl groups, as confirmed by the O 1s spectrum, indicating the formation of Cr^{3+} hydroxide [170]. The components at 588 eV and 586.4 eV of Cr $2p_{1/2}$, 578.1 eV and 576.7 of Cr $2p_{3/2}$ are assigned to Cr^{3+} species present in the octahedral sites of the spinel and/or as Cr_2O_3 at the surface [167].

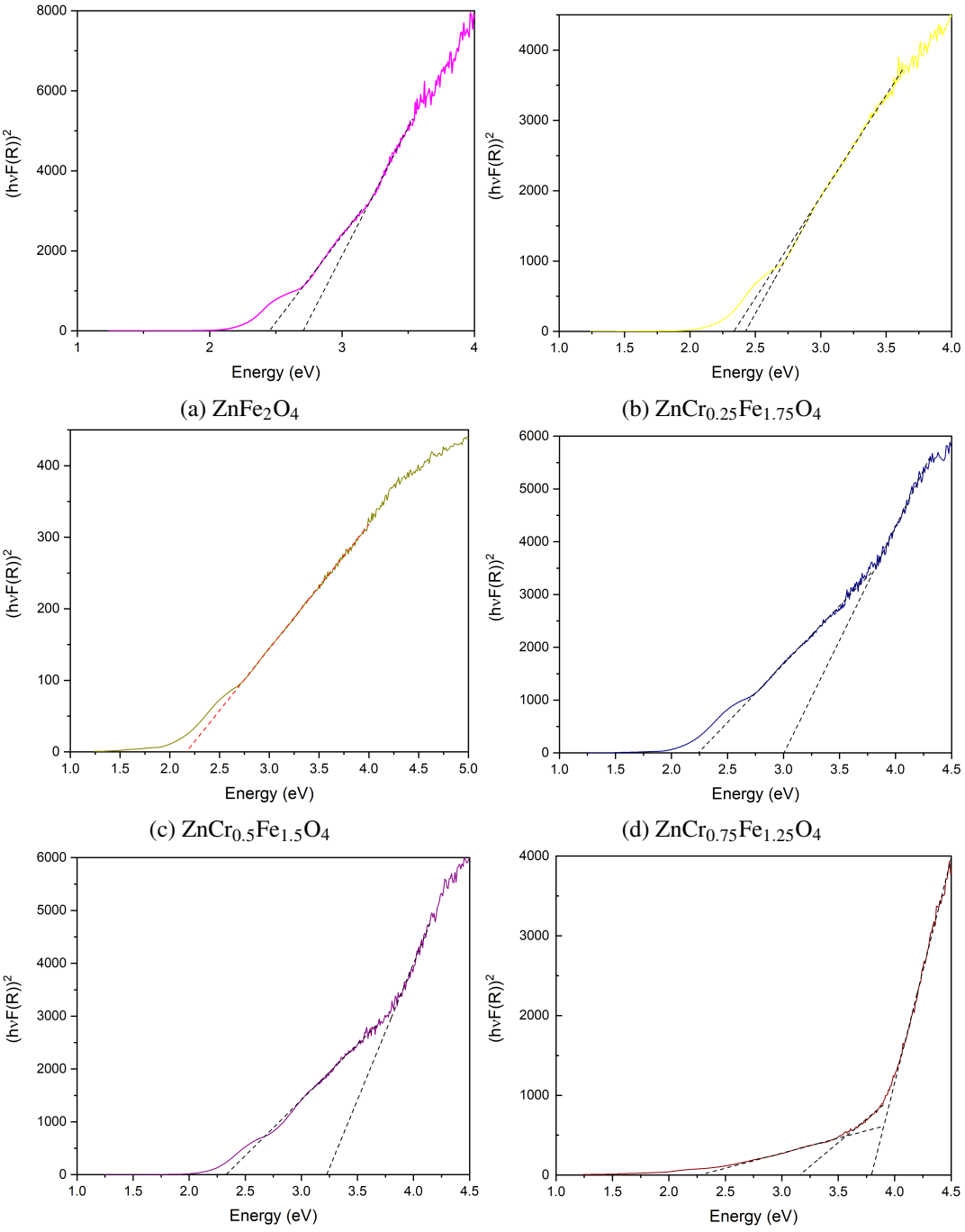

(a) $ZnFe_2O_4$ (b) $ZnCr_{0.25}Fe_{1.75}O_4$

(c) $ZnCr_{0.5}Fe_{1.5}O_4$ (d) $ZnCr_{0.75}Fe_{1.25}O_4$

(e) $ZnCrFeO_4$ (f) $ZnCr_2O_4$

Fig. 4.6 Tauc plot method to determine the energy gap (E_g) of $ZnCr_xFe_{2-x}O_4$ nanomaterials.

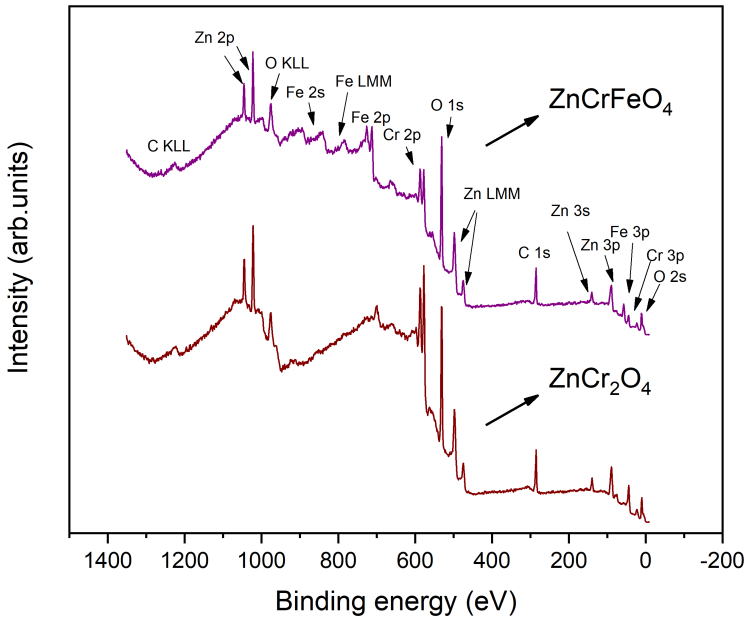

Fig. 4.7 XPS full survery spectra of $ZnCr_xFe_{2-x}O_4$ (x = 1, 2) nanomaterials.

The energy of the valence band maximum (E_V) of $ZnCr_xFe_{2-x}O_4$ (x = 0, 0.25, 0.5, 0.75, 1, 2) nanomaterials is determined from the XPS valence band spectrum similarly as in chapter 3. The E_V was determined by extrapolating the initial rising edge of the valence band spectrum to the x-axis after baseline correction, with the x-intercept representing the valence band maximum energy of the nanomaterial as illustrated in Figure 4.9. The energy level of the conduction band minimum (E_C), calculated as $E_C = E_g + E_V$, the values for E_g, E_V, and E_C, are presented in Table 4.3. The Fermi energy level (E_F) for these nanomaterials is considered to be at '0' eV, therefore the E_V values are reported with a negative sign.

Table 4.3 The energy gap and band edges of $ZnCr_xFe_{2-x}O_4$ nanomaterials

Material	E_g (eV)	E_V (eV)	E_C (eV)
$ZnFe_2O_4$	2.58 ± 0.06	-1.87 ± 0.13	0.71 ± 0.19
$ZnCr_{0.25}Fe_{1.75}Fe_2O_4$	2.38 ± 0.06	-1.32 ± 0.43	1.06 ± 0.49
$ZnCr_{0.5}Fe_{1.5}Fe_2O_4$	2.17 ± 0.01	-0.89 ± 0.27	1.28 ± 0.28
$ZnCr_{0.75}Fe_{1.25}Fe_2O_4$	2.61 ± 0.12	-0.64 ± 0.21	1.97 ± 0.09
$ZnCrFeO_4$	2.78 ± 0.13	-0.94 ± 0.28	1.84 ± 0.15
$ZnCr_2O_4$	3.07 ± 0.11	-0.33 ± 0.09	2.74 ± 0.20

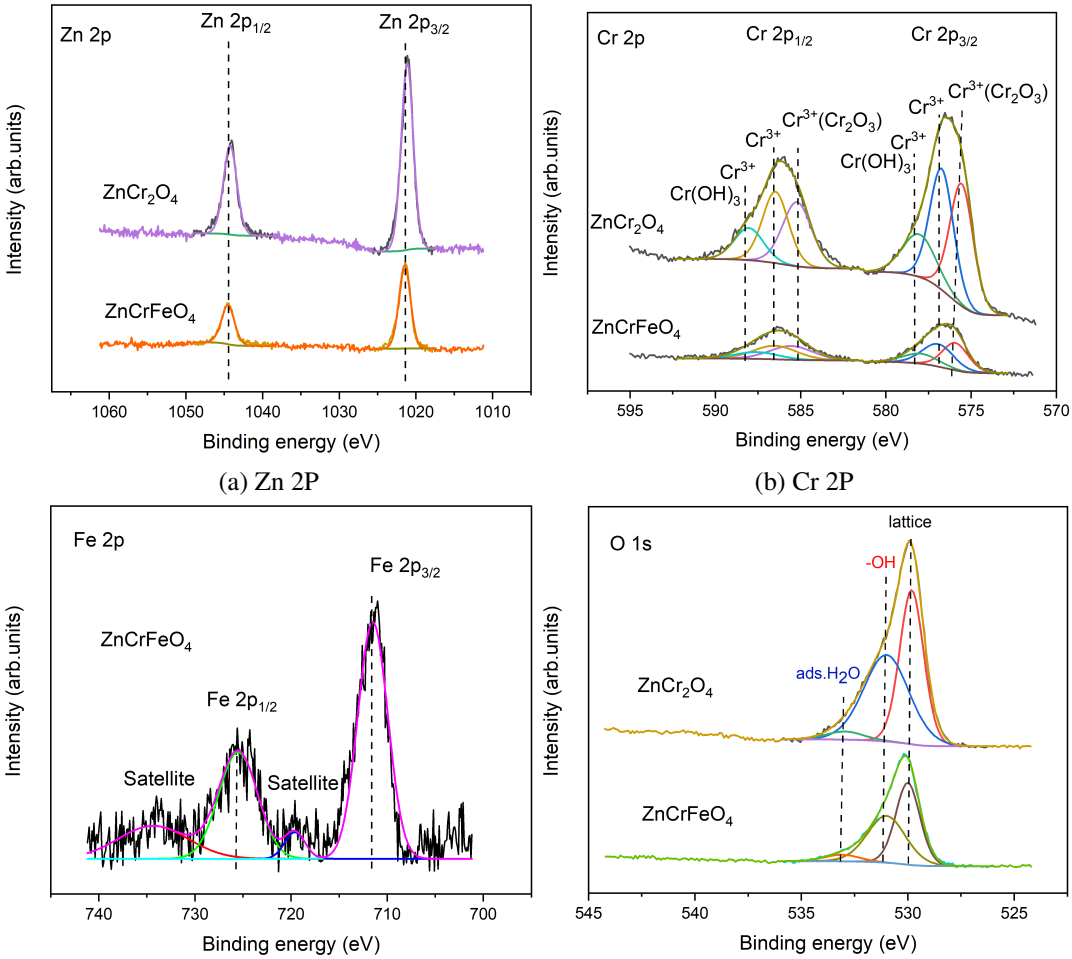

(a) Zn 2P (b) Cr 2P

(c) Fe 2P (d) O 1s

Fig. 4.8 XPS high resolution (HR) spectra of different elements in the composition of $ZnCr_xFe_{2-x}O_4$ nanomaterials.

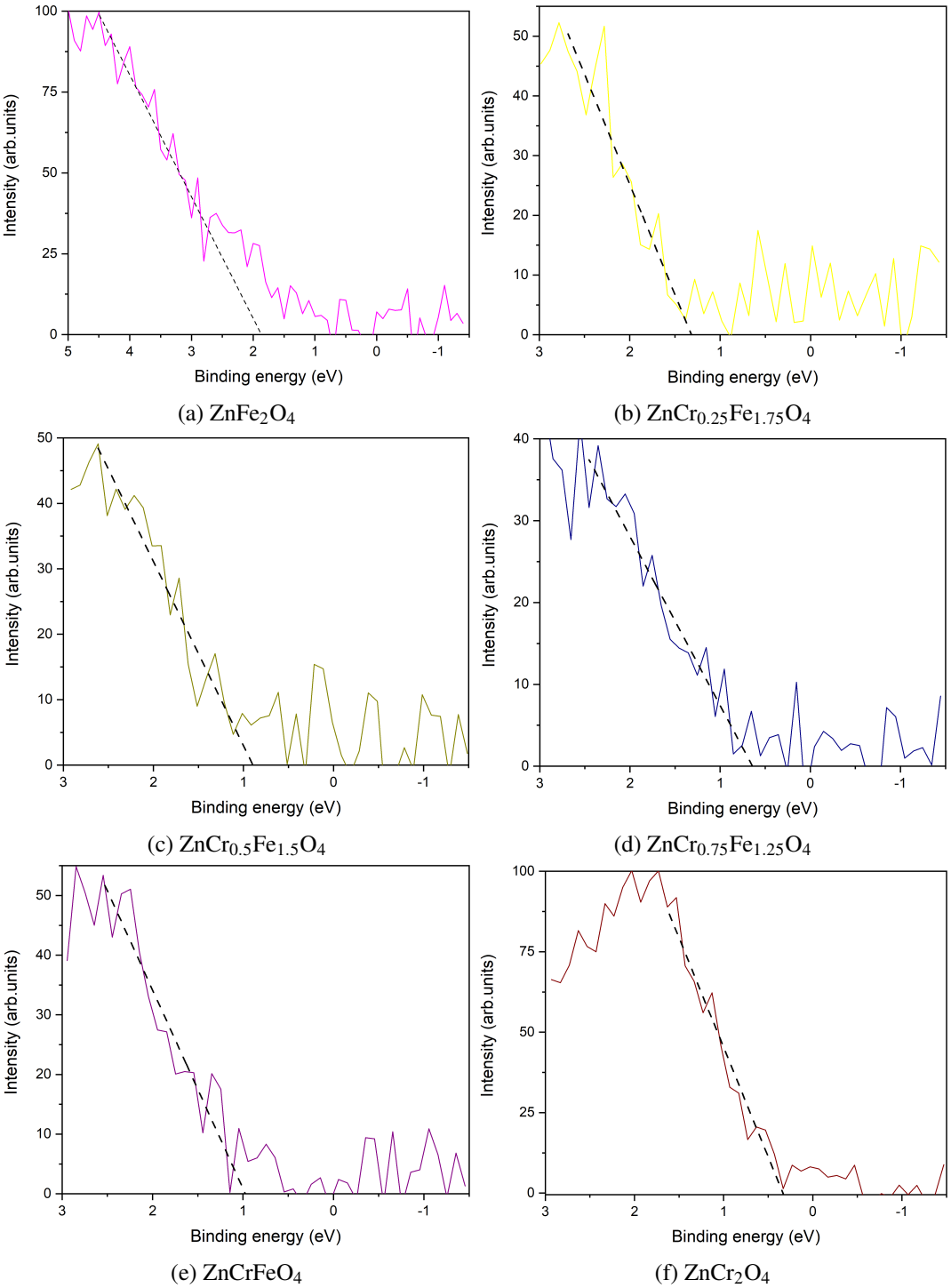

(a) $ZnFe_2O_4$ (b) $ZnCr_{0.25}Fe_{1.75}O_4$

(c) $ZnCr_{0.5}Fe_{1.5}O_4$ (d) $ZnCr_{0.75}Fe_{1.25}O_4$

(e) $ZnCrFeO_4$ (f) $ZnCr_2O_4$

Fig. 4.9 Estimation of the valence band maximum (E_V) of $ZnCr_xFe_{2-x}O_4$ nanomaterials using XPS valence band spectra.

4.2 Electrochemical Characterization

Figure 4.10 presents the cyclic voltammograms for bare and $ZnCr_xFe_{2-x}O_4$ sensors tested with 1 mM paracetamol in 0.1 M PB at pH 7, scanned at 100 mV/s. Initial observations indicate that $ZnCr_xFe_{2-x}O_4$ (x = 0, 0.25, 0.5, 0.75, 1, 2) sensors outperform the bare carbon sensor, showing higher current and lower peak potential, making them electrochemically more effective. Among the $ZnCr_xFe_{2-x}O_4$ sensors, the pure $ZnFe_2O_4$ sensor exhibits the highest oxidation current and the lowest oxidation potential when compared to the pure $ZnCr_2O_4$ sensor and mixed Cr-Fe sensors. The $ZnCr_2O_4$ sensor delivers a 13.21 μA higher current at a 104 mV lower peak potential compared to the bare sensor, Substituting 50% of Fe with Cr (x = 1) in the $ZnFe_2O_4$ lattice results in a 7 mV reduction in oxidation peak potential and a similar oxidation current compared to the pure chromite sensor. As the Cr percentage decreases in the $ZnCr_xFe_{2-x}O_4$ (x = 0.75, 0.5, 0.25) structure, comparable oxidation currents and potentials are observed, indicating that lower Cr content in $ZnFe_2O_4$ structure does not significantly affects electrochemical performance. It was reported in chapter 3 that the pure ferrite sensor (x = 0) shows a 152 mV reduction in oxidation potential and a 17.9 μA increase in oxidation current compared to the bare carbon sensor. This indicates that the introduction of a trivalent cation with similar ionic radii didn't actually enhance the electrochemical performance of $ZnFe_2O_4$ nanoparticles even if the performance is very effective compared to the bare carbon sensor due to the presence of nanolayers at the electrode-paracetamol interface.

4.2.1 Effect of scan rate

Figure 4.11 displays the cyclic voltammograms for $ZnCr_xFe_{2-x}O_4$ (x = 0.25, 0.5, 0.75, 1, 2) sensors tested with 1 mM paracetamol in 0.1 M PB at pH 7 at different scan rates. The inset of Figure 4.11 shows the plots of redox currents as a function of $\sqrt{\nu}$. For bare and $ZnFe_2O_4$ (x = 0) sensors are presented in chapter 3. Both oxidation (I_{pa}) and reduction (I_{pc}) currents increase linearly with $\sqrt{\nu}$, while the peak potential shifts to higher values as 'ν' increases. The linear regression equations for the redox currents, along with their regression coefficients for the bare and $ZnCr_xFe_{2-x}O_4$ sensors, are presented in Table 4.4. Since the peak position shifts with 'ν' and the current varies linearly with $\sqrt{\nu}$, this indicates that the electrochemical system

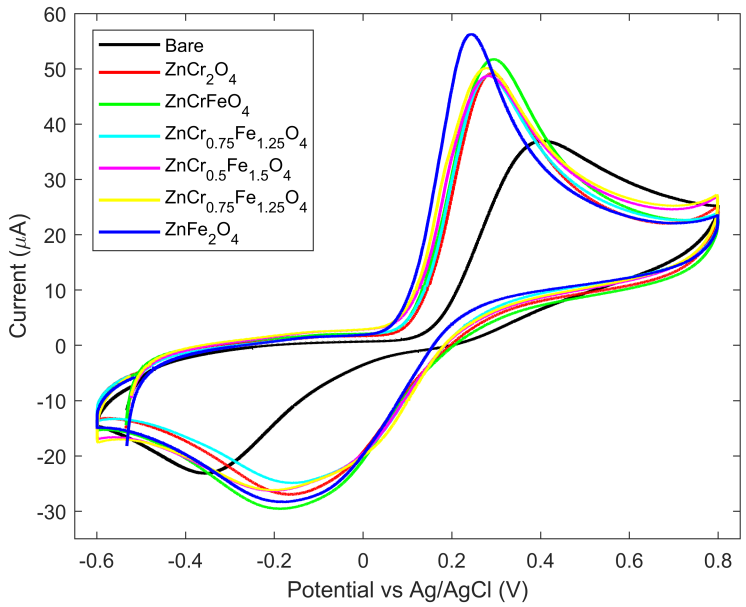

Fig. 4.10 Cyclic voltammograms of bare and $ZnCr_xFe_{2-x}O_4$ nanomaterials-modified sensors while detecting 1 mM APAP in 0.1 M PB at pH 7.

operates as a freely diffusing quasi-reversible system according to Randles-Sevčik theory [1, 29].

Table 4.4 I_{pa} and I_{pc} linear regression equations for bare and $ZnCr_xFe_{2-x}O_4$ sensors.

Sensor	I_{pa}	R^2	I_{pc}	R^2
Bare	$2.82\sqrt{\nu} + 6.35$	0.998	$-2.26\sqrt{\nu} + 8.93$	0.999
$ZnFe_2O_4$	$5.86\sqrt{\nu} + 0.87$	0.999	$-3.27\sqrt{\nu} + 4.35$	0.991
$ZnCr_{0.25}Fe_{1.75}O_4$	$6.69\sqrt{\nu} - 8.82$	0.999	$-3.92\sqrt{\nu} + 7.04$	0.998
$ZnCr_{0.5}Fe_{1.5}O_4$	$5.74\sqrt{\nu} - 5.86$	0.997	$-3.38\sqrt{\nu} + 4.89$	0.995
$ZnCr_{0.75}Fe_{1.25}O_4$	$4.31\sqrt{\nu} - 3.25$	0.998	$-2.43\sqrt{\nu} + 1.08$	0.993
$ZnCrFeO_4$	$5.96\sqrt{\nu} - 8.90$	0.999	$-3.71\sqrt{\nu} - 7.21$	0.997
$ZnCr_2O_4$	$4.91\sqrt{\nu} - 1.70$	0.999	$-3.32\sqrt{\nu} + 4.74$	0.998

4.2.2 Kinetic Parameters

The potential values of the anodic (E_{pa}) and cathodic (E_{pc}) peaks, along with the peak-to-peak separation (ΔE_p) plotted against $\ln(\nu)$ for $ZnCr_xFe_{2-x}O_4$ (x = 0.25, 0.5, 0.75, 1, 2) sensors are shown in Figure 4.12 (Bare and $ZnFe_2O_4$ (x = 0) in chapter

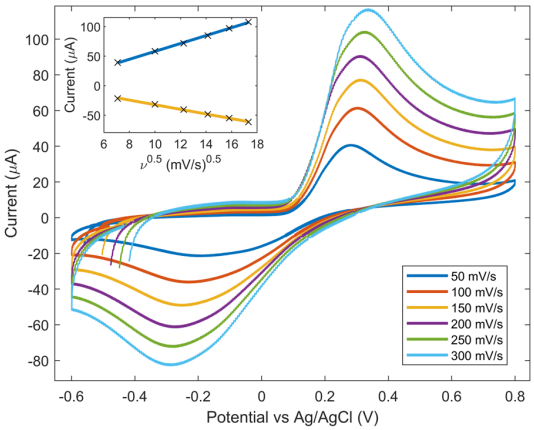

(a) $ZnCr_{0.25}Fe_{1.75}O_4$

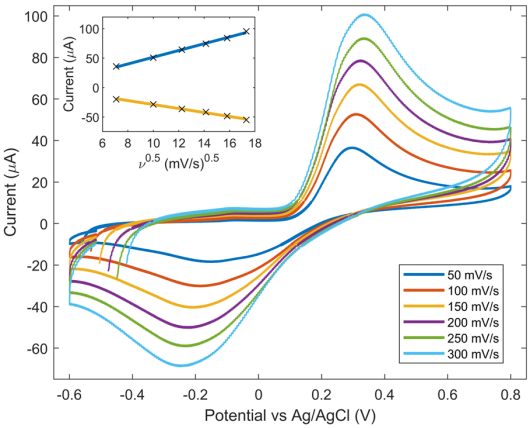

(b) $ZnCr_{0.5}Fe_{1.5}O_4$

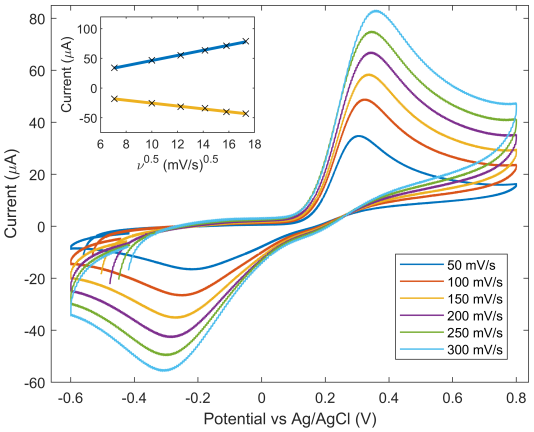

(c) $ZnCr_{0.75}Fe_{1.25}O_4$

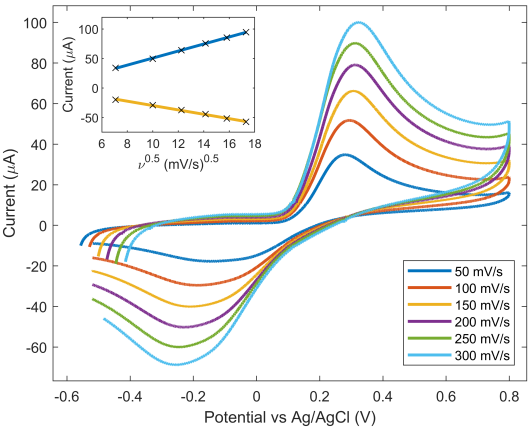

(d) $ZnCr_{0.25}Fe_{1.75}O_4$

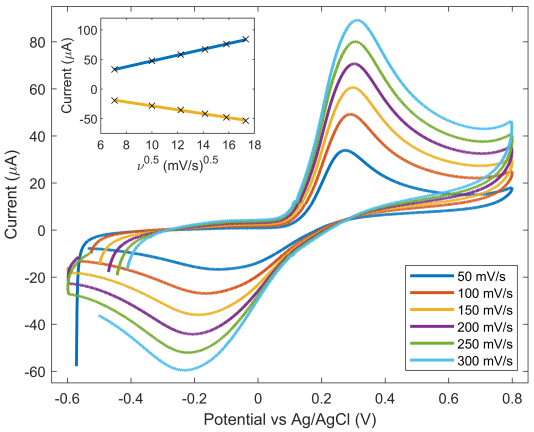

(e) $ZnCrFe_2O_4$

Fig. 4.11 Cyclic voltammograms with varying scan rate from 50 to 300 mV/s (step 50 mV/s). a) $ZnCr_{0.25}Fe_{1.75}O_4$, b) $ZnCr_{0.5}Fe_{1.5}O_4$, c) $ZnCr_{0.75}Fe_{1.25}O_4$, d) $ZnCr_{0.25}Fe_{1.75}O_4$, e) $ZnCrFe_2O_4$ sensors, respectively. Inset shows the redox peak currents versus $\sqrt{\nu}$.

3.16). E_{pa}, E_{pc}, and ΔE_p exhibit a linear relationship with $\ln(\nu)$, with the linear regression parameters provided in Table 4.5 and 4.6. After confirming the linearity of the redox currents with $\sqrt{\nu}$ and the linearity of E_{pa}, E_{pc}, and ΔE_p with $\ln(\nu)$, Laviron model is applied to calculate the electron transfer rate coefficient (α) and the kinetic rate constant (k), following an approach similar to chapter 3.

Table 4.5 E_{pa} and E_{pc} linear regression equations for bare and $ZnCr_xFe_{2-x}O_4$ sensors.

Sensor	E_{pa}	R^2	E_{pc}	R^2
Bare	41.5 $\ln(\nu)$ + 216.1	0.973	-33.3 $\ln(\nu)$ - 189.3	0.996
$ZnFe_2O_4$	26.4 $\ln(\nu)$ + 127.3	0.975	-90.2 $\ln(\nu)$ - 278.3	0.996
$ZnCr_{0.25}Fe_{1.75}O_4$	28.6 $\ln(\nu)$ + 168.5	0.934	-59.8 $\ln(\nu)$ - 82.1	0.986
$ZnCr_{0.5}Fe_{1.5}O_4$	23.4 $\ln(\nu)$ + 202.6	0.968	-46.9 $\ln(\nu)$ + 52.4	0.967
$ZnCr_{0.75}Fe_{1.25}O_4$	26.8 $\ln(\nu)$ + 202.6	0.974	-48.6 $\ln(\nu)$ - 10.3	0.978
$ZnCrFeO_4$	22.6 $\ln(\nu)$ + 189.3	0.963	-64.7 $\ln(\nu)$ + 144.5	0.989
$ZnCr_2O_4$	21.1 $\ln(\nu)$ + 190.8	0.995	-63.2 $\ln(\nu)$ + 150.4	0.981

Table 4.6 ΔE_p linear regression equations for bare and $ZnCr_xFe_{2-x}O_4$ sensors.

Sensor	ΔE_p	R^2
Bare	74.8 $\ln(\nu)$ + 405.5	0.991
$ZnFe_2O_4$	116.6 $\ln(\nu)$ - 151.1	0.999
$ZnCr_{0.25}Fe_{1.75}O_4$	88.4 $\ln(\nu)$ + 86.5	0.997
$ZnCr_{0.5}Fe_{1.5}O_4$	70.3 $\ln(\nu)$ + 150.2	0.979
$ZnCr_{0.75}Fe_{1.25}Fe_2O_4$	75.5 $\ln(\nu)$ + 212.9	0.992
$ZnCrFe_2O_4$	87.3 $\ln(\nu)$ + 44.9	0.997
$ZnCr_2O_4$	84.3 $\ln(\nu)$ + 40.4	0.989

The values of α, ΔE_p, and k for the bare and $ZnCr_xFe_{2-x}O_4$ sensors are presented in Table 4.7. Compared to the bare sensor, the $ZnCr_xFe_{2-x}O_4$ sensors exhibit lower electron transfer rate coefficients (α) and reduced ΔE_p values. Since ΔE_p is lower for the $ZnCr_xFe_{2-x}O_4$ sensors, they possess higher k values, which correspond to faster electrochemical reactions at the sensor-paracetamol interface. The k value, often referred to as the first-order kinetic rate constant, is calculated using the Laviron model, which does not account for double layer and diffusion effects at the interface.

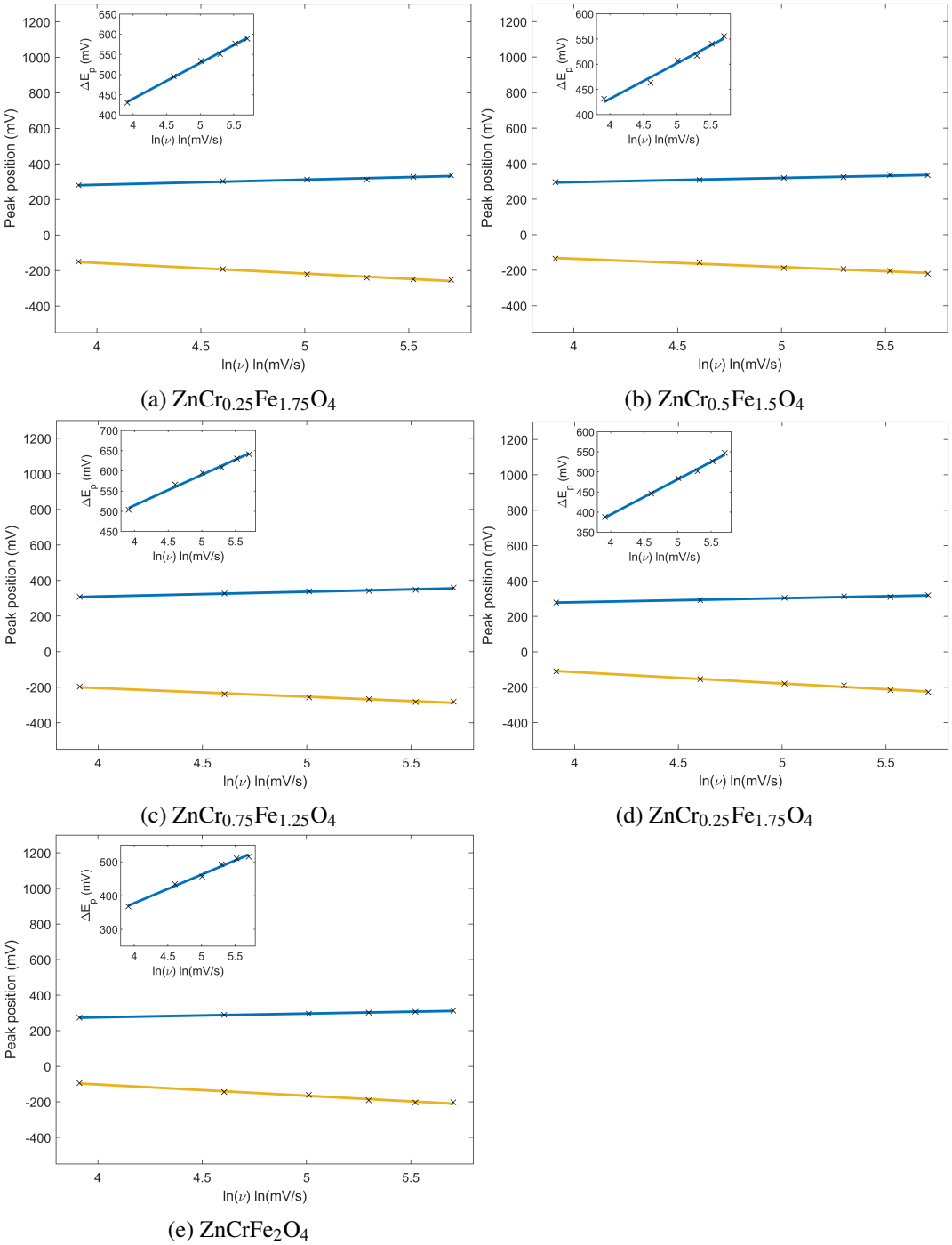

(a) $ZnCr_{0.25}Fe_{1.75}O_4$

(b) $ZnCr_{0.5}Fe_{1.5}O_4$

(c) $ZnCr_{0.75}Fe_{1.25}O_4$

(d) $ZnCr_{0.25}Fe_{1.75}O_4$

(e) $ZnCrFe_2O_4$

Fig. 4.12 Redox peak potentials with ln(ν).a) $ZnCr_{0.25}Fe_{1.75}O_4$, b) $ZnCr_{0.5}Fe_{1.5}O_4$, c) $ZnCr_{0.75}Fe_{1.25}O_4$, d) $ZnCr_{0.25}Fe_{1.75}O_4$, e) $ZnCrFe_2O_4$ sensors, respectively. Inset shows the ΔE_p versus ln(ν).

Table 4.7 shows that the k values for the $ZnCr_2O_4$, $ZnCrFeO_4$, and $ZnFe_2O_4$ sensors are 3.73 ± 0.55, 4.53 ± 0.54, and 13.1 ± 2.8 ms^{-1}, respectively. As the Fe content in $ZnCr_2O_4$ increases from 0 to 50%, the k value initially increases of approximately 0.8 ms^{-1}, then slightly decreases, and finally shows a significant increase when Cr is completely replaced by Fe. As a matter of fact, the pure ferrite sensor stands out as the best performer in terms of kinetic performance among all the sensors studied in this work.

Table 4.7 α, ΔE_p, and k of bare and $ZnCr_xFe_{2-x}O_4$ sensors.

Sensor	α	ΔE_p (mV)	k (ms^{-1})
Bare	0.536 ± 0.004	746 ± 5	$(2.22 \pm 0.19) \times 10^{-3}$
$ZnFe_2O_4$	0.23 ± 0.02	386 ± 2	13.1 ± 2.8
$ZnCr_{0.25}Fe_{1.75}O_4$	0.32 ± 0.01	488 ± 4	0.88 ± 0.16
$ZnCr_{0.5}Fe_{1.5}O_4$	0.35 ± 0.01	455 ± 4	1.11 ± 0.06
$ZnCr_{0.75}Fe_{1.25}O_4$	0.355 ± 0.003	564 ± 7	0.18 ± 0.03
$ZnCrFeO_4$	0.24 ± 0.01	446 ± 2	4.53 ± 0.54
$ZnCr_2O_4$	0.258 ± 0.004	444 ± 6	3.73 ± 0.55

4.2.3 Sensitivity and limit of detection

Cyclic voltammograms are recorded at various concentrations of paracetamol at a fixed scan rate of 100 mV/s. The oxidation current is measured and averaged over three trials at each concentration to produce a calibration curve for each sensor, as shown in Figure 4.13.

The slope of each calibration curve represents the sensor's sensitivity with R^2 and standard error mean are detailed in Table 4.8. The $ZnCr_xFe_{2-x}O_4$ sensors exhibit more than a two-fold increase in sensitivity (> 32 μA/mM) compared to the bare sensor, which has a sensitivity of 16.7 ± 0.9 μA/mM. The $ZnFe_2O_4$ sensor demonstrates the highest sensitivity at 37.8 ± 0.2 μA/mM, with the $ZnCrFeO_4$ sensor following closely behind. The limit of detection (LOD) for each sensor is also listed in Table 4.8, with the $ZnCrFeO_4$ sensor showing the lowest LOD at 1.94 ± 0.01 μM, while the $ZnFe_2O_4$ sensor has the highest LOD at 7.94 ± 0.04 μM among those tested in this study. LOD can get affected by the background noise of the instrument used during the measurement since the blank standard deviation is based on the

background or instrumental noise. The other factor is the signal level (oxidation peak level) compared to the noise level, to improve the LOD the signal to noise level ratio should be as high as possible.

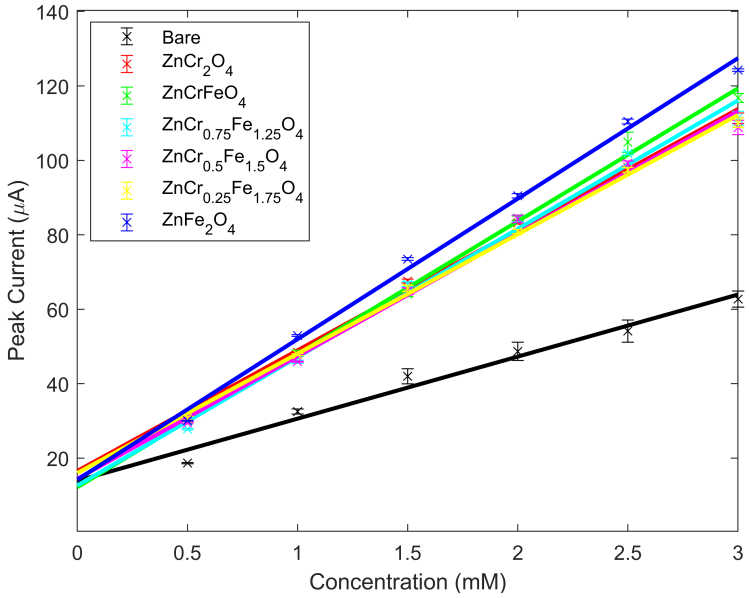

Fig. 4.13 Calibration of bare and $ZnCr_xFe_{2-x}O_4$ sensors with paracetamol.

Table 4.8 Sensitivity and limit of detection of bare and $ZnCr_xFe_{2-x}O_4$ sensors.

Sensor	Sensitivity (μA/mM)	R^2	LOD (μM)
Bare	16.7 ± 0.9	0.975	3.26 ± 0.17
$ZnFe_2O_4$	37.8 ± 0.2	0.995	7.94 ± 0.04
$ZnCr_{0.25}Fe_{1.75}O_4$	32.1 ± 0.3	0.998	7.57 ± 0.08
$ZnCr_{0.5}Fe_{1.5}O_4$	33.3 ± 0.6	0.990	2.21 ± 0.04
$ZnCr_{0.75}Fe_{1.25}O_4$	34.5 ± 0.5	0.990	2.29 ± 0.03
$ZnCrFeO_4$	35.7 ± 0.1	0.996	1.94 ± 0.01
$ZnCr_2O_4$	32.4 ± 0.5	0.996	2.99 ± 0.05

4.3 Effect of Cr(III) on Electrochemical Performance

XRD analysis confirmed that both $ZnFe_2O_4$ and $ZnCr_2O_4$ nanomaterials possess a normal spinel structure. The conduction in spinel materials is described by the

'small polaron hopping' model, as detailed in section 3.3. In both zinc ferrite and zinc chromite, which have normal spinel structures, Fe(III) and Cr(III) occupy the 'Oh' sites. In other $ZnCr_xFe_{2-x}O_4$ (x = 0.25, 0.5, 0.75, 1) nanomaterials, Fe(III) and Cr(III) ions share these 'Oh' sites. In $ZnCr_2O_4$ and $ZnFe_2O_4$, conduction occurs through electron hopping between Cr^{3+}/Cr^{4+} and Fe^3+/Fe^{2+}, respectively. However, conductivity is not solely dependent on the hopping of electrons in the spinel structure. It also depends on the electron hopping rate (jumps per second), with a higher hopping rate leading to greater conductivity in the spinel nanomaterials [171]. The magnetic properties of the spinel structure also influence conductivity due to electron spin and scattering effects, as chromites typically exhibit antiferromagnetic behavior [172], while ferrites display ferromagnetic behavior [173].

The increase in sensitivity and rate constant from x = 2 to x = 1 could be attributed to the equal proportion of Cr and Fe ions in the spinel, which enhances conductivity compared to pure chromite. However, as the composition shifts from x = 1 to x = 0.25, both sensitivity and rate constant decrease, possibly due to stoichiometric mismatches in the spinel system affecting conductivity. The pure ferrite (x = 0) exhibits the highest sensitivity and rate constant, likely due to its ferromagnetic nature and higher conductivity relative to the other nanomaterials studied [171]. A normal spinel is typically an n-type semiconductor, conduction occuring by electron hopping, while an inverse spinel is p-type, conducting through hole hopping. Consequently, a normal spinel generally exhibits better conductivity than an inverse spinel. Comparing these results with those reported in Table 3.9, we noticed that the sensitivity and rate constant of the normal spinel nanomaterials are higher than those of inverse spinel $NiFe_2O_4$, demonstrating superior performance in electrochemical sensing of paracetamol.

Another significant factor to consider is the difference in ionic radii between Cr^{3+} (61.5 pm) and Fe^{3+} (64.5 pm). Although the difference is only 3 pm (2.4%), it results in a 0.5 eV change in the energy band gap. This variation in band gap has a substantial impact on sensitivity and kinetic rate constant, leading to different electron transfer mechanisms at the electrochemical interface. It also highlights how sensitive electrochemical processes are at this interface, where even a slight modification to the sensor's surface can significantly affects the performance.

The possible valence states of Cr^{3+} compared to Fe^{3+} suggest that intermediate reactions may occur between chromites and paracetamol, due to the differing reactiv-

ities of Cr^{3+} valence states. These intermediate reactions could slow down the final reaction, leading to a lower kinetic rate constant. This explanation also accounts for the higher kinetic rate constant and greater sensitivity observed in the $ZnFe_2O_4$ sensor compared to the other sensors.

4.4 Type of Electron Transfer at the Electrochemical Interface

The nature of electron transfer can be predicted using the energy band gap of the nanomaterials. Similar to the previous research in section 3.4, Burello and Worth's theoretical predictive model [158, 159] is employed to forecast the type of electron transfer between the sensor surface and the target molecule. The energy band edges (EC and EV) of the nanomaterials are estimated using UV-vis spectroscopy and XPS techniques, while the experimental redox potentials (E_{pa} and E_{pc} of paracetamol are utilized. Figure 4.14 illustrates the mapping of E_C and E_V against E_{pa} and E_{pc}. Electron transfer is predicted by comparing the E_C of the nanomaterial with the E_{pa} of paracetamol.

From 4.14, it is evident that only $ZnFe_2O_4$ shows an overlap between its E_C and the E_{pa} of paracetamol, indicating a direct electron transfer mechanism between the sensor material and paracetamol. As the Cr^{3+} ion content decreases from x = 2 to 0.25 in $ZnCr_xFe_{2-x}O_4$, the E_C shifts closer to the E_{pa} of paracetamol, but there is no overlap, making it difficult to predict direct electron transfer. Despite this, electron transfer and the redox mechanism of paracetamol are still observed at the sensor surface. This difficulty in predicting electron transfer using Burello and Worth's model arises because the model does not account for surface states.

For $ZnCr_xFe_{2-x}O_4$ nanomaterials with x ranging from 0.25 to 2, surface states or defects confirmed by XRD, Raman, and XPS could be involved. The presence of these energy states within the band gap leads to band tailing due to surface defects. These energy states within the band gap could overlap with the E_{pa} of paracetamol, creating a pathway for electrons from the HOMO of paracetamol to the nanomaterial, resulting in surface-state-mediated electron transfer. This mechanism might explain why the $ZnFe_2O_4$ sensor operates at a lower E_{pa} compared to the other sensors,

leading to a smaller ΔE_p and a faster reaction at the interface, with a higher rate constant.

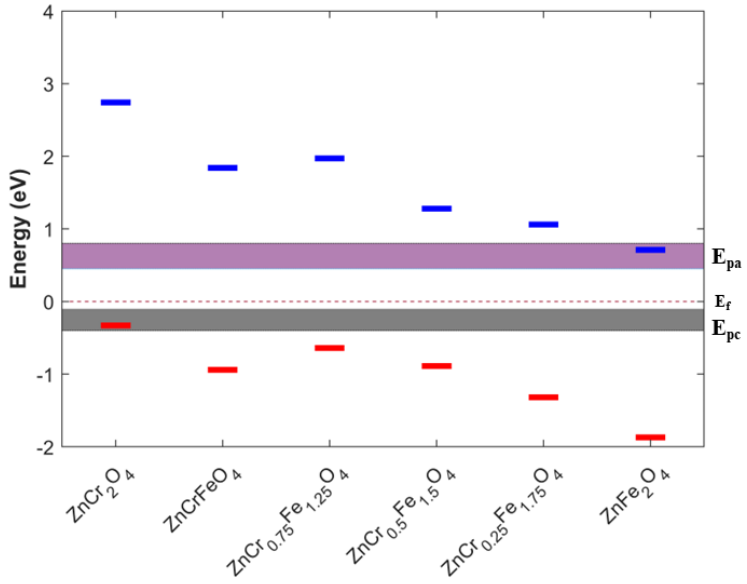

Fig. 4.14 Conduction (E_C) band minimum (blue) and valence (E_V) (red) band maximum of $ZnCr_xFe_{2-x}O_4$ nanomaterials constructed by using E_g (the energy gap between E_C and E_V). Electron transfer prediction from/to paracetamol to/from the surface of the WE by mapping the E_C of the WE with the experimental E_{pa} and E_{pc} of paracetamol. The black dotted lines represent the fermi energy level 'E_f' at '0' eV.

4.5 Original Contribution II

In this work, the effect of similar ionic size trivalent cations of Cr^{3+} in the crystal structure of $ZnFe_2O_4$ is investigated in electrochemical sensing of paracetamol. Sensitivity and rate constant of sensors are presented and discussed with respect to the amount of Cr^{3+} ions in $ZnCr_xFe_{2-x}O_4$. The type of electron transfer at the electrochemical interface is predicted using the nanomaterials energy bands and redox potential of paracetamol.

A part of this work has been presented as a poster at the 1st IEEE Biosensors conference in London, UK, in July 2023. The paper can be found with title "$ZnM_xFe_{2-x}O_4$ (M = Cr, Bi) Nanoparticles-modified electrochemical sensors: Effect on sensitivity and first-order kinetic rate constant" at the url:

https://ieeexplore.ieee.org/abstract/document/10280910

A part of this work has been presented as an oral presentation at the 25th IEEE Sensors conference in Vienna, Austria, in October 2023. The paper is available with title "$ZnCr_{2-x}Fe_xO_4$ Nanoparticles-Modified Electrochemical Sensors: A Comparative Study" at the below url:

https://ieeexplore.ieee.org/abstract/document/10325135

A full manuscript titled "Effect of Cr substitution in $ZnFe_2O_4$ nanoparticles on the electron transfer at the electrochemical interface" has been published in "Materials Research Bulletin" journal by Elsevier publications. The paper can be found at the following url:

https://www.sciencedirect.com/science/article/pii/S002554082400521X

Chapter 5

Effect of Ionic Size on Electron Transfer

In chapter 4, the work was focused on the effect of trivalent cations with very similar ionic size in $ZnFe_2O_4$ nanomaterials on electrochemical performance. This chapter focuses on the effect of bigger ionic sized Bi^{3+} ions in the crystal structure of $ZnFe_2O_4$ nanomaterials on electron transfer at the electrochemical interface. Bi^{3+} ions are introduced into the $ZnFe_2O_4$ structure with mole fractions of x = 0.25, 0.5, 0.75, 1, 2 by auto combustion. Different materials properties are discussed and electrochemical performance is studied, and the type of electron transfer at the ECI is reported similar to chapter 4.

5.1 Material Characterization

5.1.1 Morphological Characterization

FESEM images of $ZnBi_xFe_{2-x}O_4$ (x = 0, 0.25, 0.5, 0.75, 1, 2) materials are presented in Figure 5.1. In Figure 5.1a, the pure $ZnFe_2O_4$ sample (x = 0) shows highly nanostructured particles with a predominantly spherical shape. As the Bi content increases from x = 0.25 to 2, shown in Figures 5.1b to 5.1f, two distinct particle morphologies emerge. Some particles grow larger, and their shape shifts from quasi-spherical to a more patch-like morphology. The level of nanostructuring decreases as Fe(III) is fully replaced by Bi(III) in the material composition. The FESEM images

also reveal that most particles are sub-micrometric in size (>100 nm and <1 μm), while some retain their spherical, nanometer-scale dimensions as the Bi 'x' content increases from 0 to 2.

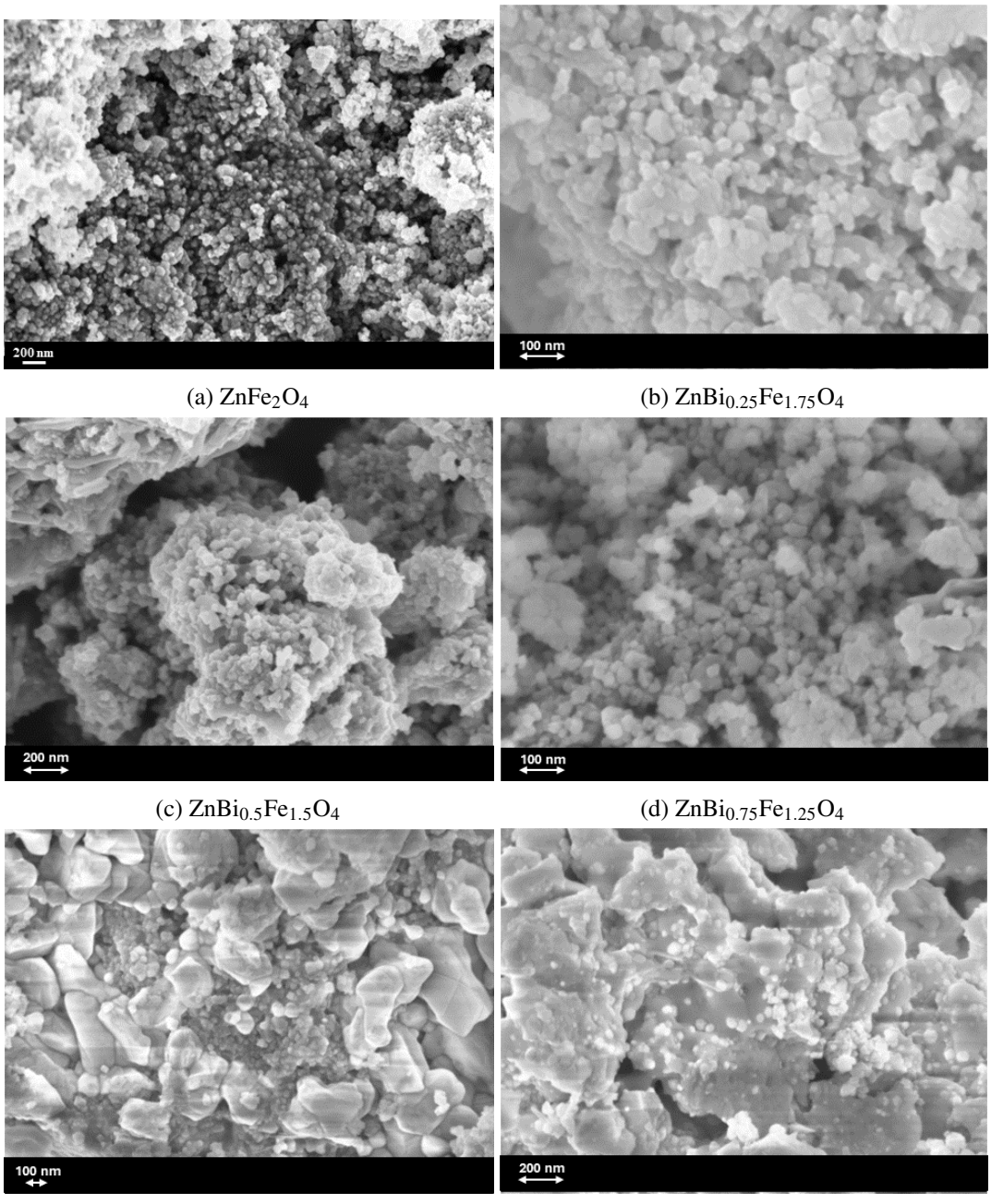

(a) $ZnFe_2O_4$ (b) $ZnBi_{0.25}Fe_{1.75}O_4$

(c) $ZnBi_{0.5}Fe_{1.5}O_4$ (d) $ZnBi_{0.75}Fe_{1.25}O_4$

(e) $ZnBiFeO_4$ (f) $ZnBi_2O_4$

Fig. 5.1 FESEM images of $ZnBi_xFe_{2-x}O_4$ nanomaterials.

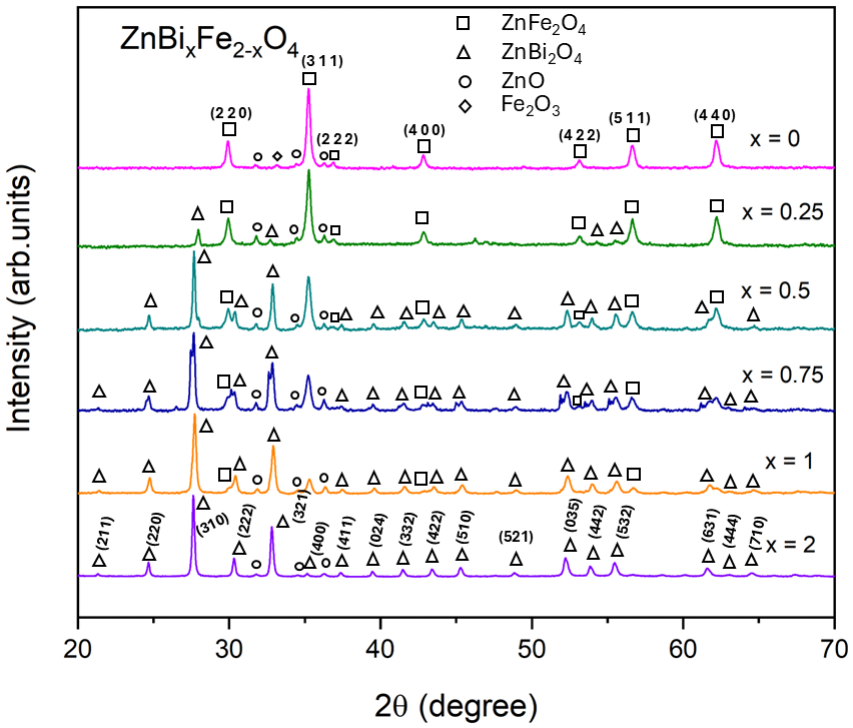

Fig. 5.2 XRD patterns of $ZnBi_xFe_{2-x}O_4$ nanomaterials showing different crystal phases.

5.1.2 Structural Characterization

The XRD patterns for $ZnBi_xFe_{2-x}O_4$ (x = 0, 0.25, 0.5, 0.75, 1, 2) are presented in Figure 5.2. The diffraction pattern for x = 0 aligns with the normal spinel structure of Franklinite (zinc iron oxide) (ICDD reference code 01-089-4926). In contrast, the pattern for x = 2 corresponds well with cubic bismuth zinc oxide (ICDD reference code 01-077-0569). For the intermediate compositions (x = 0.5, 1), the XRD patterns display a combination of peaks, reflecting contributions from both zinc-iron oxide and bismuth-zinc oxide, as illustrated in Figure 5.2.

In all XRD patterns, minor peaks are detected between 30° and 37°, which are attributed to zinc oxide (ICDD ref. code 01-080-0075) and iron oxide (ICDD ref. code 01-085-0987), as their positions align with the most prominent peaks of these phases similar to the XRD patterns in chapter 3 and 4.

Scherrer's method [3] is used to calculate the crystallite size based on seven prominent peaks. The crystallite sizes are presented in Table 5.1, showing variation across different materials as their composition changes with the introduction of Bi^{3+} in $ZnFe_2O_4$.

Table 5.1 The average crystallite size of $ZnBi_xFe_{2-x}O_4$ materials

Material	Average crystallite size (nm)
$ZnFe_2O_4$	36.2 ± 1.4
$ZnBi_{0.25}Fe_{1.75}O_4$	31 ± 9
$ZnBi_{0.5}Fe_{1.5}O_4$	40 ± 20
$ZnBi_{0.75}Fe_{1.25}O_4$	54 ± 26
$ZnBiFeO_4$	31 ± 5
$ZnBi_2O_4$	49 ± 12

5.1.3 Spectroscopic Characterization

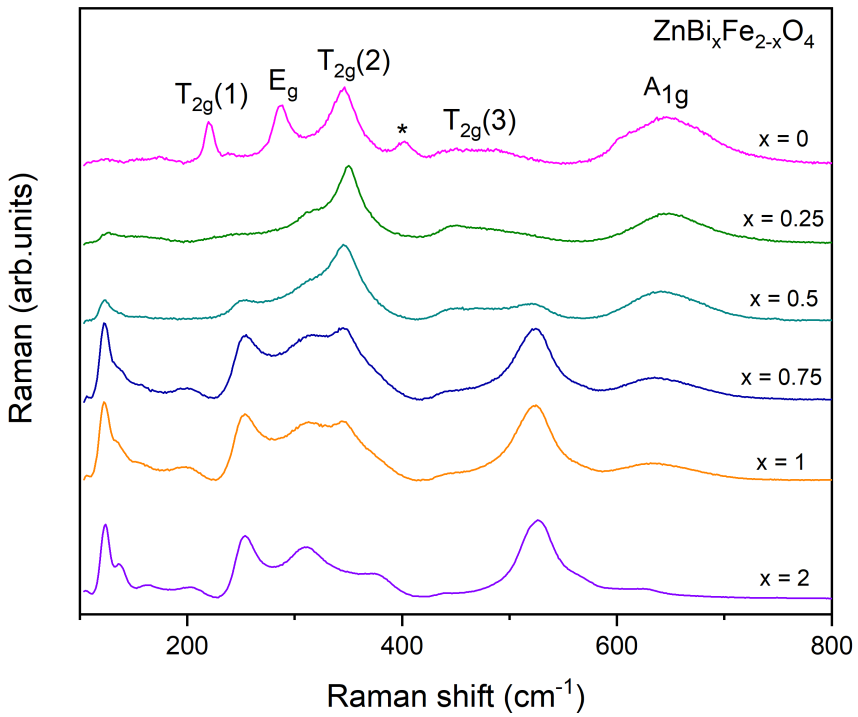

Fig. 5.3 Raman spectra of $ZnBi_xFe_{2-x}O_4$ nanomaterials.

Figure 5.3 presents the Raman spectra of $ZnBi_xFe_{2-x}O_4$ (x = 0.25, 0.5, 0.75, 1, 2) materials. As illustrated in Figure 5.3, all bands below 220 cm^{-1} for $ZnBi_xFe_{2-x}O_4$ (x = 0.25, 0.5, 0.75, 1, 2) are attributed to the Bi-O framework, similar to that in cubic Bi_2O_3 [174]. The band above 600 cm^{-1} corresponds to the A_{1g} symmetry of the

spinel structure, while the band around 445 cm^{-1} is assigned to the $T_{2g}(3)$ symmetry of the spinel. Raman bands observed around 310 and 520 cm^{-1} for materials with x = 0.5, 1, and 2 are also linked to Bi-O bonds characteristic of the cubic Bi_2O_3 phase. Another band at approximately 345 cm^{-1} is attributed to the $T_{2g}(2)$ mode of the spinel for x = 0.5 and 1, though this mode is absent for x = 2. The band around 250 cm^{-1} may be assigned to a shifted E_g mode of the spinel, potentially caused by local variations (bond length, angle, and molecular vibrations) due to the coexistence of Fe and Bi in the crystal structure. Alternatively, it could represent another band related to cubic Bi_2O_3, as the E_g mode in the spinel with x = 0 exhibits only a 30 cm^{-1} difference, as previously shown [3]. For the x = 0 material, the band around 375 cm^{-1} is associated with Zn-O bonding, as seen in ZnO [137].

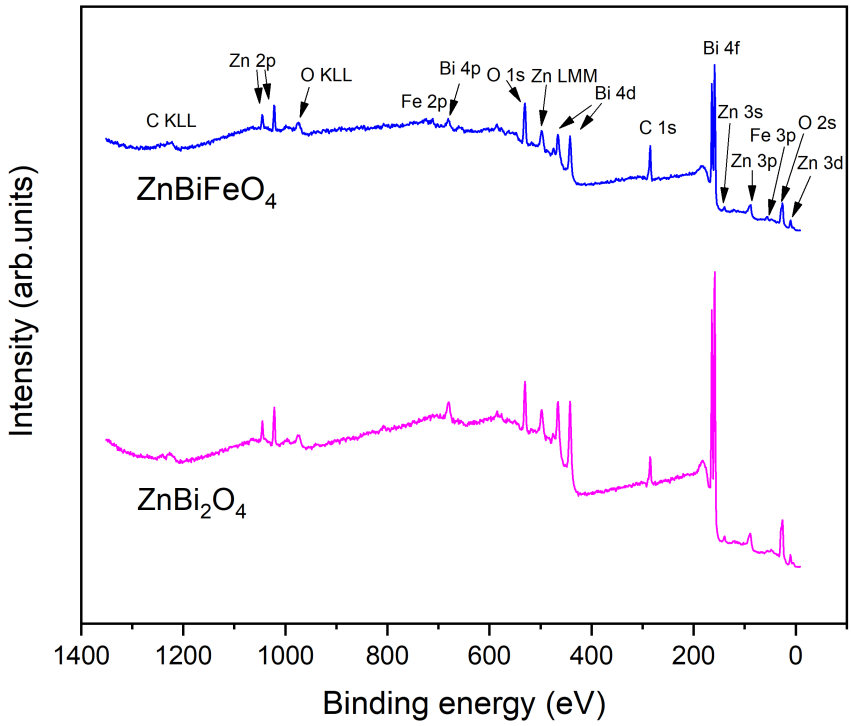

Fig. 5.4 XPS full survery spectra of $ZnBi_xFe_{2-x}O_4$ (x = 1, 2) nanomaterials.

The oxidation states of the elements in $ZnBi_2O_4$ and $ZnBiFeO_4$ materials are investigated by XPS, high-resolution (HR) XPS spectra are recorded for each element. Figure 5.5a presents the HR spectrum of Zn 2p, showing peaks at binding energies of 1021.5 eV and 1044.6 eV, corresponding to Zn $2p_{3/2}$ and Zn $2p_{1/2}$ states. These peak positions confirm the presence of Zn^{2+} ions [3]. In Figure 5.5b, the HR spectrum of the Bi 4f region reveals the splitting of the Bi 4f orbital into Bi $4f_{7/2}$ and Bi $4f_{5/2}$.

Peaks at 158.5 eV and 163.9 eV are attributed to octahedral Bi^{3+}, while peaks at 160 eV and 165 eV correspond to tetrahedral Bi^{3+}, confirming that Bi^{3+} occupies two different sites in the main spinel phase [175, 176].

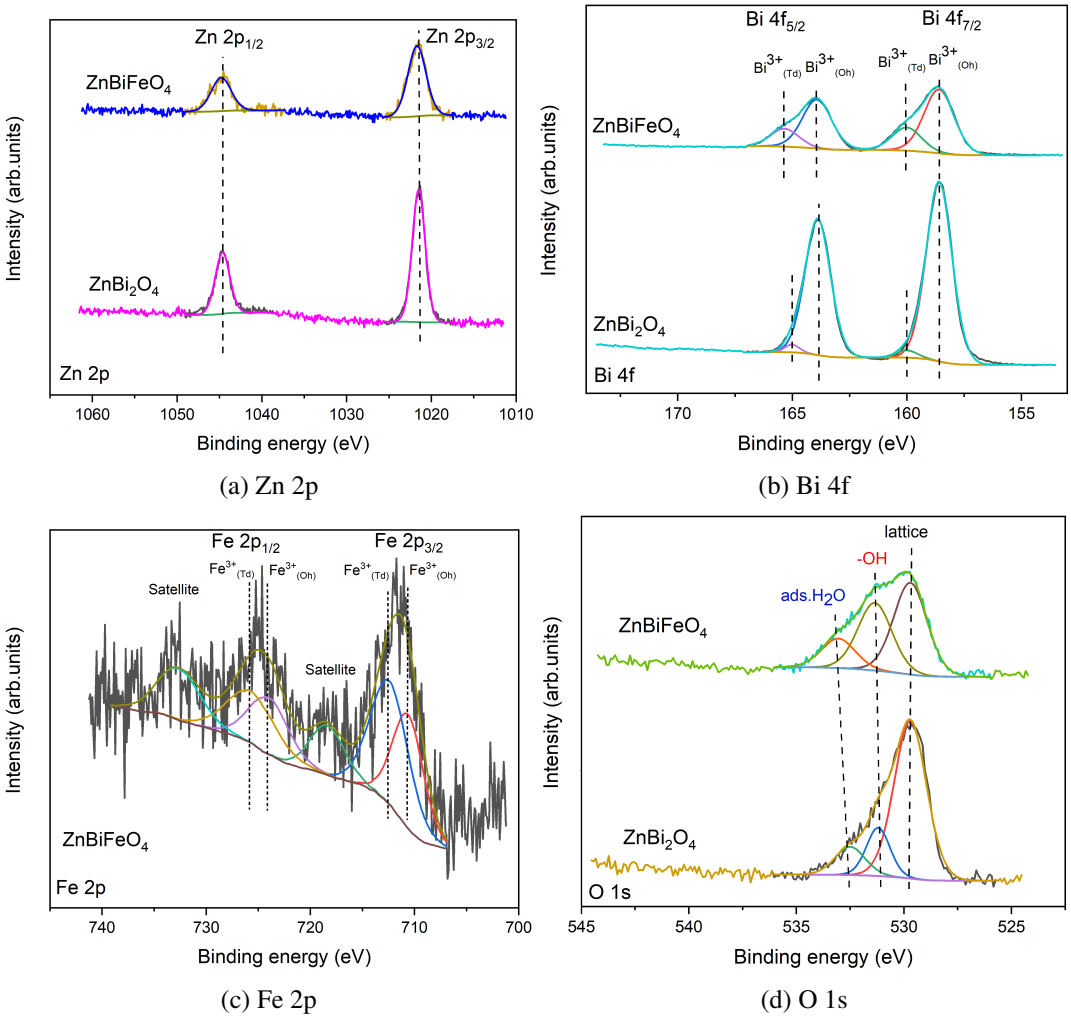

(a) Zn 2p (b) Bi 4f

(c) Fe 2p (d) O 1s

Fig. 5.5 XPS high resolution (HR) spectra of different elements in the composition of $ZnBi_xFe_{2-x}O_4$ nanomaterials.

Figure 5.5c shows the core level spectrum of the Fe 2p orbital, with a doublet at 711.5 eV and 725.1 eV corresponding to Fe $2p_{3/2}$ and Fe $2p_{1/2}$, respectively, along with shake-up satellites at 718.5 eV and 732.8 eV. The Fe $2p_{3/2}$ and Fe $2p_{1/2}$ peaks are deconvoluted into two components, representing Fe^{3+} in octahedral (710.8 eV and 724.1 eV) and tetrahedral (712.6 eV and 725.9 eV) sites within the spinel structure [175].

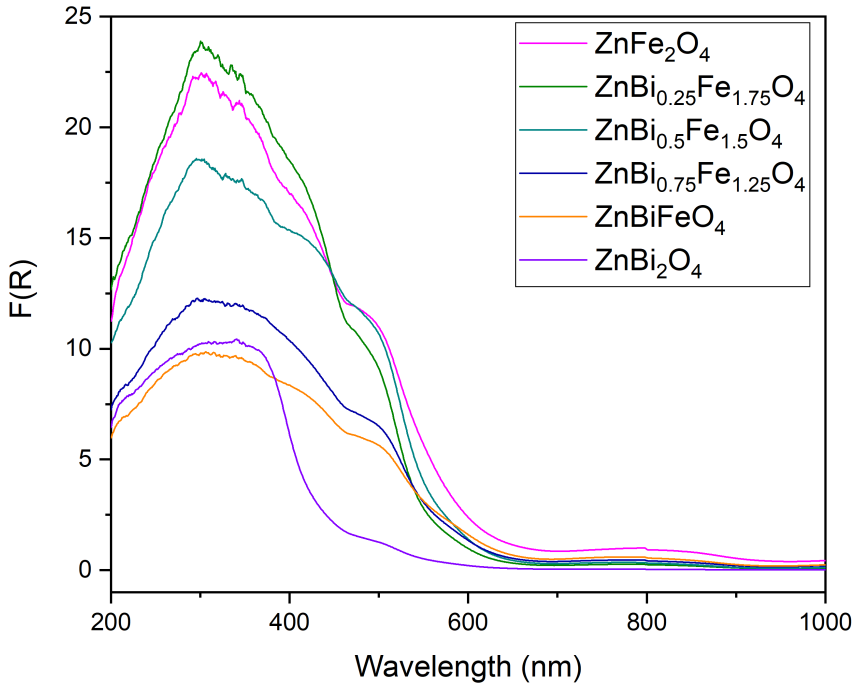

Fig. 5.6 Diffuse reflectance (DR) UV-vis spectra of $ZnBi_xFe_{2-x}O_4$ nanomaterials.

Figure 5.5d presents the O 1s HR XPS spectrum, where three components are identified: lattice oxygen (∼529.6 eV), hydroxyl groups (∼531.3 eV), and adsorbed water (∼533.1 eV) [3, 147, 177]. As indicated in Figure 5.4, besides the expected elements, only adventitious carbon is detected on the surface.

Diffuse reflectance UV visible (DR UV-vis) spectra of $ZnBi_xFe_{2-x}O_4$ (x= 0, 0.25, 0.5, 0.75, 1, 2) materials are reported (F(R) Kubelka-Munk function versus wavelength) in Figure 5.6.

The Tauc's plot method is employed to estimate the energy gap (Eg) of the $ZnBi_xFe_{2-x}O_4$ (x = 0, 0.25, 0.5, 0.75, 1, 2) materials, assuming a direct electronic transition process similar to the procedure followed in chapter 3 and 4. The Tauc's plot is extrapolated by considering the band edges in a manner that accounts for the band tailing effect due to surface states or defects as shown in Figure 5.7. The average energy gap values for these materials are summarized in Table 5.2. Upon the introduction of Bi^{3+} ions into the $ZnFe_2O_4$ spinel structure, the E_g decreases for x = 0.25, 0.5, 0.75 and 1 , but then increases for $ZnBi_2O_4$ (x = 2), aligning with literature values for $ZnBi_2O_4$, which range between 2.90 and 3.00 eV [178].

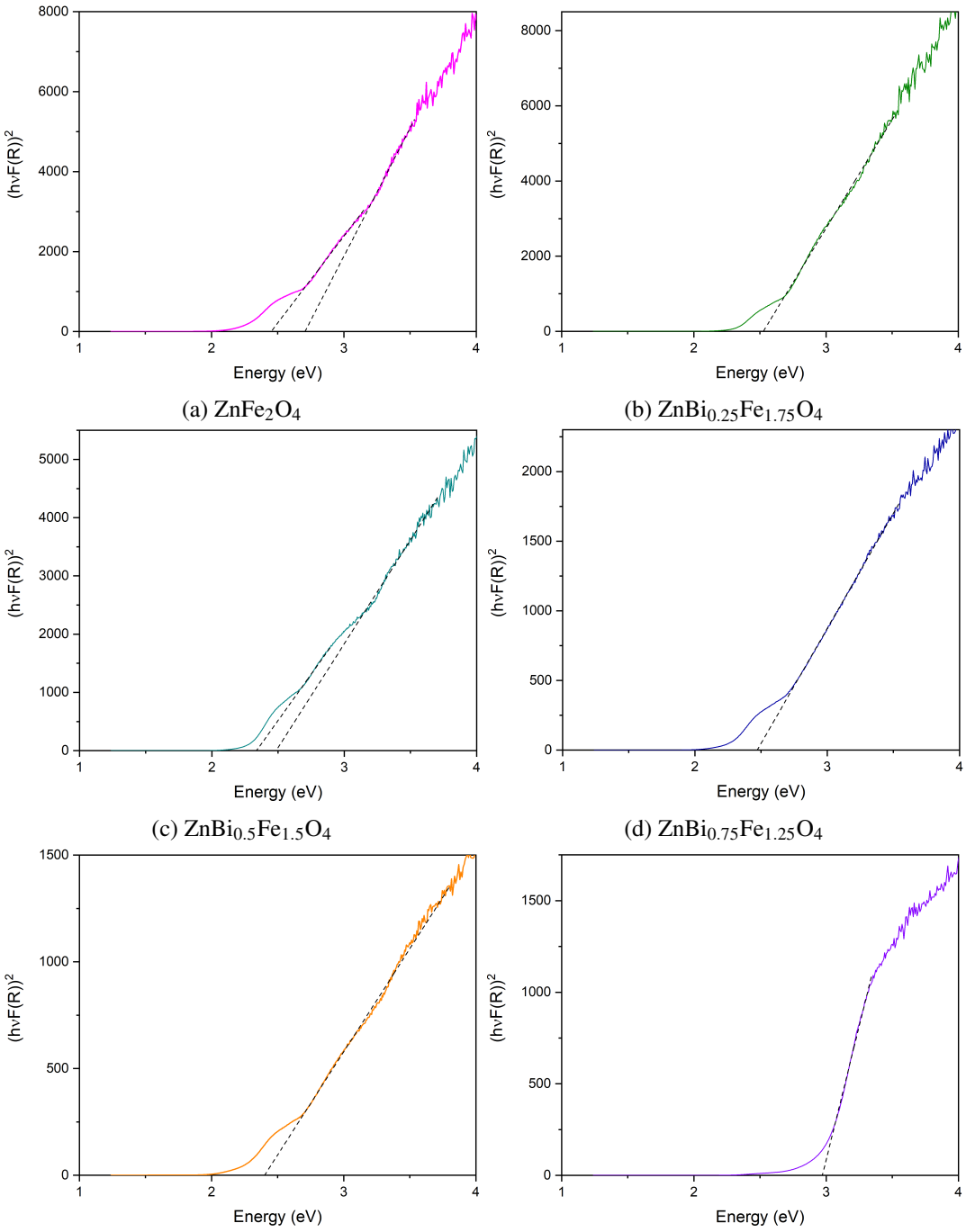

(a) $ZnFe_2O_4$ (b) $ZnBi_{0.25}Fe_{1.75}O_4$

(c) $ZnBi_{0.5}Fe_{1.5}O_4$ (d) $ZnBi_{0.75}Fe_{1.25}O_4$

(e) $ZnBiFeO_4$ (f) $ZnBi_2O_4$

Fig. 5.7 Tauc's plot method to determine the energy gap (E_g) of $ZnBi_xFe_{2-x}O_4$ nanomaterials.

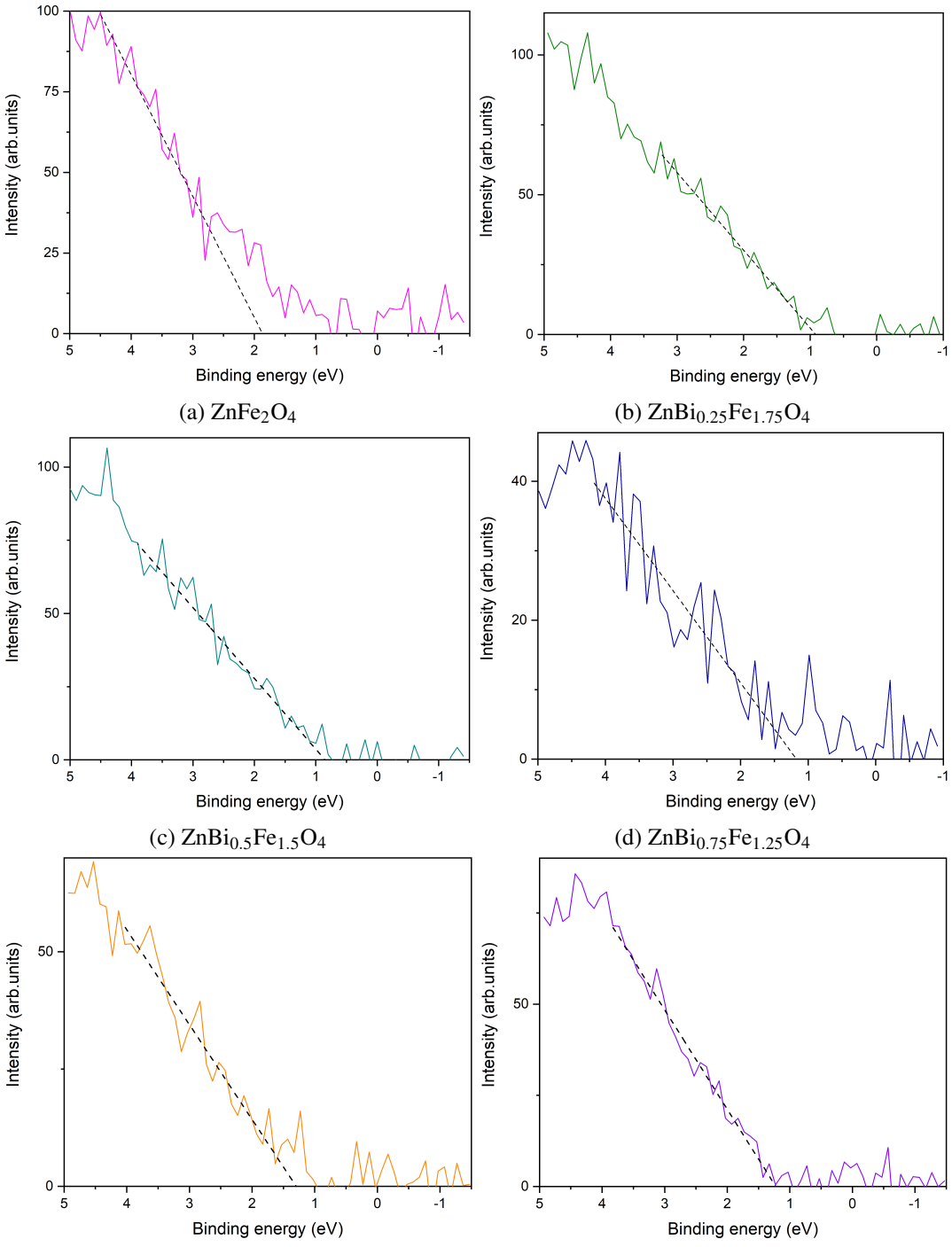

(a) $ZnFe_2O_4$ (b) $ZnBi_{0.25}Fe_{1.75}O_4$

(c) $ZnBi_{0.5}Fe_{1.5}O_4$ (d) $ZnBi_{0.75}Fe_{1.25}O_4$

(e) $ZnBiFeO_4$ (f) $ZnBi_2O_4$

Fig. 5.8 Estimation of the valence band maximum (E_V) of $ZnBi_xFe_{2-x}O_4$ nanomaterials using XPS valence band spectra.

Table 5.2 The energy gap and band edges of $ZnBi_xFe_{2-x}O_4$ nanomaterials

Material	E_g (eV)	E_V (eV)	E_C (eV)
$ZnFe_2O_4$	2.58 ± 0.06	-1.87 ± 0.13	0.71 ± 0.19
$ZnBi_{0.25}Fe_{1.75}Fe_2O_4$	2.52 ± 0.02	-0.92 ± 0.16	1.60 ± 0.18
$ZnBi_{0.5}Fe_{1.5}Fe_2O_4$	2.43 ± 0.08	-0.85 ± 0.25	1.58 ± 0.33
$ZnBi_{0.75}Fe_{1.25}Fe_2O_4$	2.47 ± 0.01	-1.17 ± 0.36	1.30 ± 0.37
$ZnBiFeO_4$	2.40 ± 0.02	-1.29 ± 0.10	1.11 ± 0.12
$ZnBi_2O_4$	2.97 ± 0.04	-1.22 ± 0.14	1.75 ± 0.18

The valence band maximum (E_V) of $ZnBi_xFe_{2-x}O_4$ (x = 0, 0.25, 0.5, 0.75, 1, 2) materials is determined from the XPS valence band spectra, with the detailed method provided in Figure 5.8. Table 5.2 lists the values for E_V, along with the calculated conduction band minimum (E_C). Since the Fermi energy (E_F) is set at '0' eV, the E_V values are reported with a negative sign.

5.2 Electrochemical Characterization

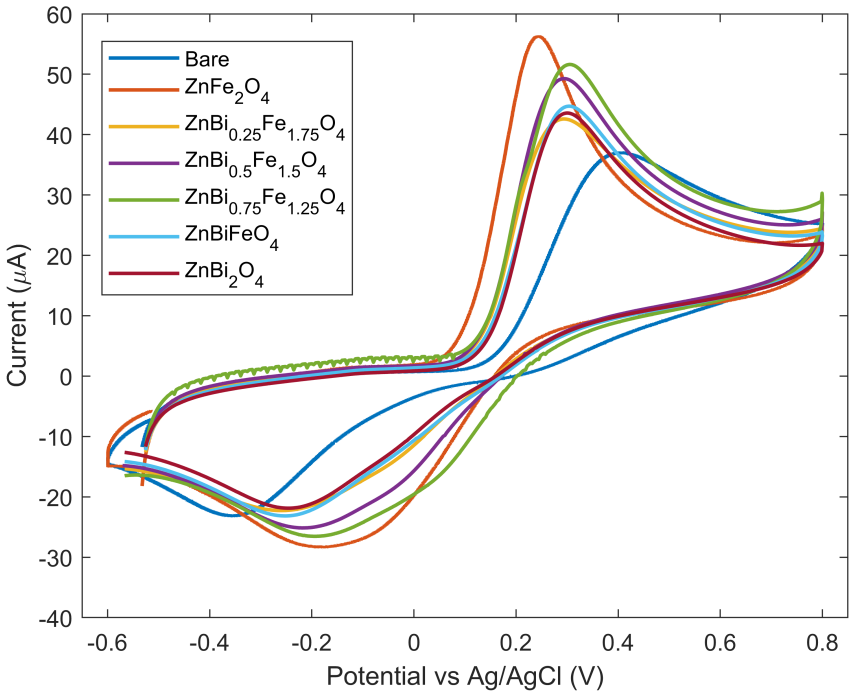

Fig. 5.9 Cyclic voltammograms of bare and $ZnBi_xFe_{2-x}O_4$ nanomaterials-modified sensors while detecting 1 mM APAP in 0.1 M PB at pH 7.

Figure 5.9 presents the cyclic voltammograms for bare and $ZnBi_xFe_{2-x}O_4$ (x = 0, 0.25, 0.5, 0.75, 1, 2) sensors in the presence of 1 mM paracetamol in 0.1 M PB at pH 7, with a scan rate of 100 mV/s. The Figure clearly demonstrates that the $ZnBi_xFe_{2-x}O_4$-modified sensors significantly enhance the electrochemical detection of paracetamol compared to the bare carbon sensor. In fact, the oxidation current decreases as Bi(III) is introduced into the $ZnFe_2O_4$ structure, and it drops further when Bi(III) fully replaces Fe(III). Additionally, the oxidation potential increases with Bi(III) incorporation. Although the introduction of Bi(III) into zinc ferrite reduces performance, it still surpasses the bare carbon sensor, showing an increase in oxidation current (> 8 μA) and a decrease in potential (> 100 mV).

5.2.1 Effect of scan rate

Similarly as in chapter 3 and 4, the nature of the electrochemical interface is investigated by performing cyclic voltammetry at different scan rates from 50 mV/s to 300 mV/s in 50 mV/s increments. Figure 5.10 displays the cyclic voltammograms of $ZnCr_xFe_{2-x}O_4$ (x = 0.25, 0.5, 0.75, 1, 2) at different scan rates. The insets in these Figures show the anodic (I_{pa}) and cathodic (I_{pc}) peak currents plotted with respect to '$\sqrt{\nu}$' while prior work in 3 provides for the bare and zinc ferrite sensors. Table 5.3 lists the linear regression equations and fitting coefficients for each sensor. The redox peak currents exhibit strong linearity with '$\sqrt{\nu}$', and the position of the redox peaks shifts with changes in scan rate. Like previous EC systems in chapters 3 and 4, this ECI is also classified as a freely diffusing quasi-reversible electrochemical system.

Table 5.3 I_{pa} and I_{pc} linear regression equations for bare and $ZnBi_xFe_{2-x}O_4$ sensors.

Sensor	I_{pa}	R^2	I_{pc}	R^2
Bare	$2.82\sqrt{\nu} + 6.35$	0.998	$-2.26\sqrt{\nu} + 8.93$	0.999
$ZnFe_2O_4$	$5.86\sqrt{\nu} + 0.87$	0.999	$-3.27\sqrt{\nu} + 4.35$	0.991
$ZnBi_{0.25}Fe_{1.75}O_4$	$4.34\sqrt{\nu} + 4.18$	0.997	$-2.78\sqrt{\nu} + 8.26$	0.959
$ZnBi_{0.5}Fe_{1.5}O_4$	$4.93\sqrt{\nu} + 1.17$	0.995	$-3.35\sqrt{\nu} + 9.24$	0.958
$ZnBi_{0.75}Fe_{1.25}O_4$	$4.08\sqrt{\nu} + 3.74$	0.992	$-2.62\sqrt{\nu} + 5.89$	0.979
$ZnBiFeO_4$	$4.48\sqrt{\nu}$ - 0.32	0.985	$-2.71\sqrt{\nu} + 6.43$	0.978
$ZnBi_2O_4$	$3.69\sqrt{\nu} + 5.28$	0.997	$-1.82\sqrt{\nu} + 1.98$	0.987

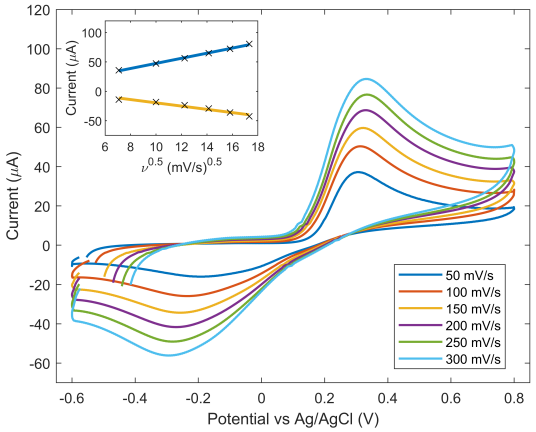

(a) $ZnBi_{0.25}Fe_{1.75}O_4$

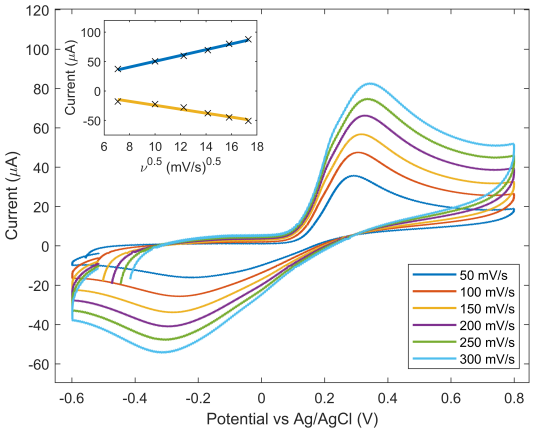

(b) $ZnBi_{0.5}Fe_{1.5}O_4$

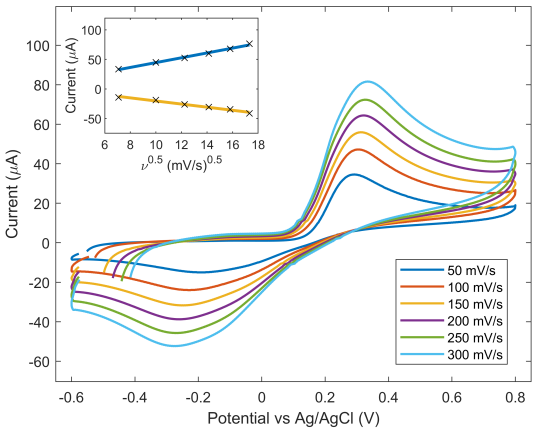

(c) $ZnBi_{0.75}Fe_{1.25}O_4$

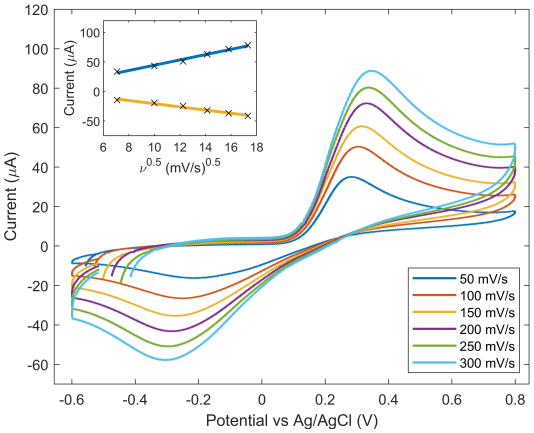

(d) $ZnBiFeO_4$

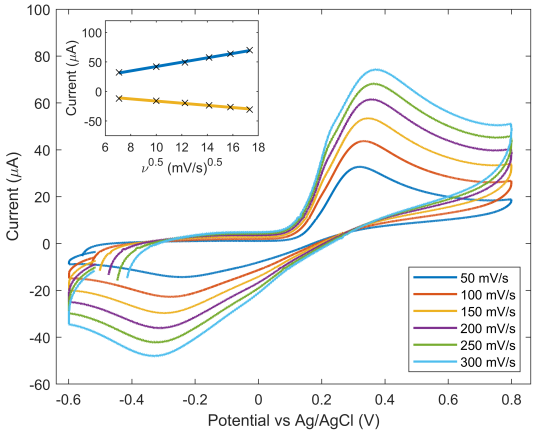

(e) $ZnBi_2O_4$

Fig. 5.10 Cyclic voltammograms with varying scan rate from 50 to 300 mV/s (step 50 mV/s) for $ZnBi_xFe_{2-x}O_4$ (x = 0.25, 0.5, 0.75, 1, 2) sensors. Inset shows the redox peak currents versus $\sqrt{\nu}$.

5.2.2 Kinetic Parameters

The anodic E_{pa} and cathodic E_{pc} peak positions are determined at varying scan rates and plotted against $\ln(\nu)$, as shown in Figures 5.11 for the $ZnBi_xFe_{2-x}O_4$ (x = 0.25, 0.5, 0.75, 1, 2) sensors. Similarly, ΔE_p values are calculated and plotted against $\ln(\nu)$ as inset Figures in Figure 5.11, and for bare and zinc ferrite sensors were presented in Figure 3.16.

A linear relationship between the redox peak positions and ΔE_p with respect to $\ln(\nu)$ is identified. The corresponding linear regression equations and coefficients are reported in Table 5.4 and 5.5, respectively. Since the redox peak currents and positions exhibit a linear dependence on '$\sqrt{\nu}$' and $\ln(\nu)$, respectively, the Laviron model is employed to calculate 'α' and rate constant 'k'.

The calculated 'α', ΔE_p, and 'k' for bare and $ZnBi_xFe_{2-x}O_4$ (x = 0, 0.25, 0.5, 0.75, 1, 2) sensors are listed in Table 5.6. It is observed that 'α') decreased from the bare sensor to the zinc ferrite sensor but increased as the Bi(III) content in the zinc ferrite composition is raised. A similar trend is noted for ΔE_p values. In contrast, 'k' significantly increased from the bare sensor to the zinc ferrite sensor as seen previously in chapters 3 and 4 but decreased as the Bi(III) content is further increased. This analysis demonstrates that the modified sensors offer a substantial improvement in reaction rates at the interface compared to the bare carbon sensor, with zinc ferrite proving to be the most effective sensor without any presence of Bi(III). Nevertheless, the addition of Bi(III) had a notable impact on the sensor's performance, particularly in terms of the reaction speed at the interface.

Table 5.4 E_{pa} and E_{pc} linear regression equations for bare and $ZnBi_xFe_{2-x}O_4$ sensors.

Sensor	E_{pa}	R^2	E_{pc}	R^2
Bare	41.5 $\ln(\nu)$ + 216.1	0.973	-33.3 $\ln(\nu)$ - 189.3	0.996
$ZnFe_2O_4$	26.4 $\ln(\nu)$ + 127.3	0.975	-90.2 $\ln(\nu)$ - 278.3	0.996
$ZnBi_{0.25}Fe_{1.75}O_4$	22.7 $\ln(\nu)$ + 192.9	0.977	-59.6 $\ln(\nu)$ + 86.3	0.999
$ZnBi_{0.5}Fe_{1.5}O_4$	18.5 $\ln(\nu)$ + 218.5	0.962	-65.7 $\ln(\nu)$ + 155.6	0.987
$ZnBi_{0.75}Fe_{1.25}O_4$	21.9 $\ln(\nu)$ + 204.6	0.993	-43.8 $\ln(\nu)$ + 15.9	0.973
$ZnBiFeO_4$	28.9 $\ln(\nu)$ + 160	0.951	-57.5 $\ln(\nu)$ + 82.3	0.993
$ZnBi_2O_4$	20.3 $\ln(\nu)$ + 216.8	0.988	-47.3 $\ln(\nu)$ + 18.2	0.992

Table 5.5 ΔE_p linear regression equations for bare and $ZnBi_xFe_{2-x}O_4$ sensors.

Sensor	ΔE_p	R^2
Bare	74.8 ln(ν) + 405.5	0.991
$ZnFe_2O_4$	116.6 ln(ν) - 151.1	0.999
$ZnBi_{0.25}Fe_{1.75}O_4$	82.3 ln(ν) + 106.6	0.998
$ZnBi_{0.5}Fe_{1.5}O_4$	84.2 ln(ν) + 62.8	0.987
$ZnBi_{0.75}Fe_{1.25}Fe_2O_4$	65.8 ln(ν) + 188.6	0.987
$ZnBiFe_2O_4$	86.5 ln(ν) + 77.7	0.989
$ZnBi_2O_4$	67.6 ln(ν) + 198.6	0.996

Table 5.6 α, ΔE_p, and k of bare and $ZnBi_xFe_{2-x}O_4$ sensors.

Sensor	α	ΔE_p (mV)	k (ms^{-1})
Bare	0.536 ± 0.004	746 ± 5	$(2.22 \pm 0.19) \times 10^{-3}$
$ZnFe_2O_4$	0.23 ± 0.02	386 ± 2	13.1 ± 2.8
$ZnBi_{0.25}Fe_{1.75}O_4$	0.27 ± 0.01	485 ± 3	1.8 ± 0.1
$ZnBi_{0.5}Fe_{1.5}O_4$	0.24 ± 0.01	438 ± 4	5.6 ± 0.6
$ZnBi_{0.75}Fe_{1.25}O_4$	0.31 ± 0.01	486 ± 3	0.99 ± 0.21
$ZnBiFeO_4$	0.30 ± 0.02	479 ± 3	1.3 ± 0.2
$ZnBi_2O_4$	0.32 ± 0.01	532 ± 12	0.45 ± 0.16

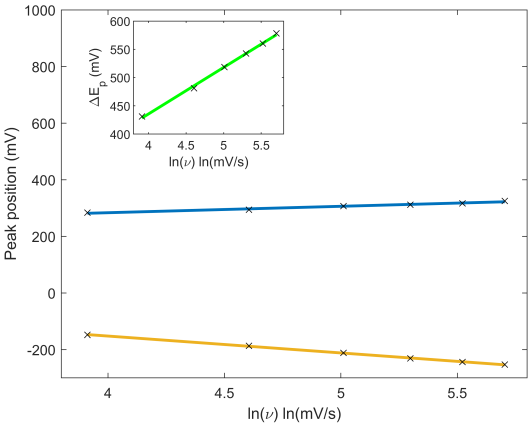

(a) $ZnBi_{0.25}Fe_{1.75}O_4$

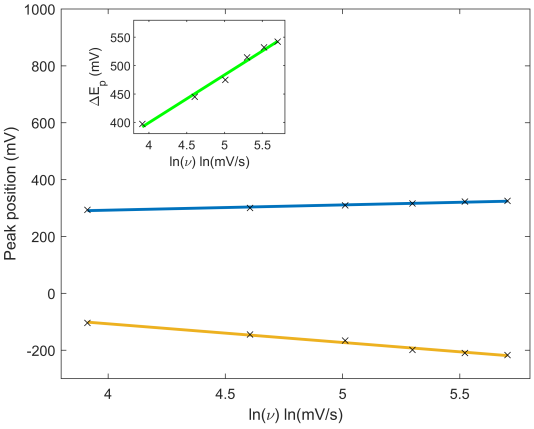

(b) $ZnBi_{0.5}Fe_{1.5}O_4$

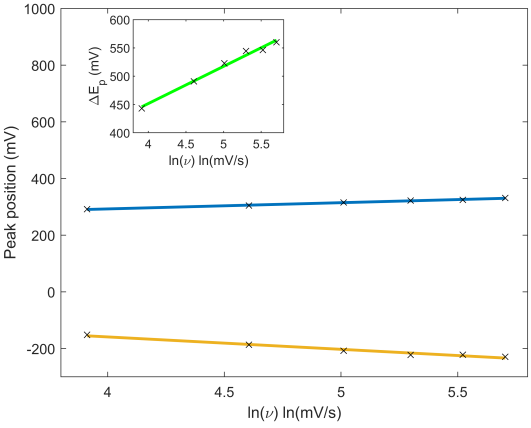

(c) $ZnBi_{0.75}Fe_{1.25}O_4$

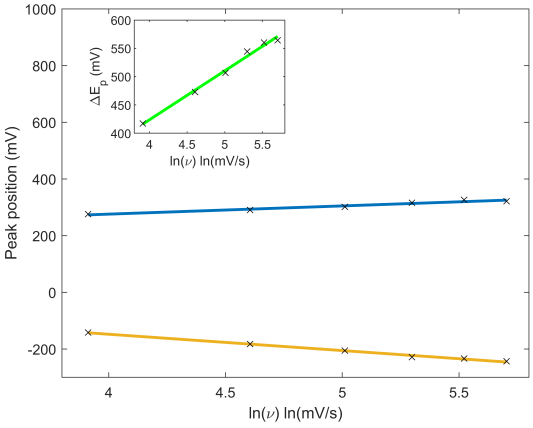

(d) $ZnBiFeO_4$

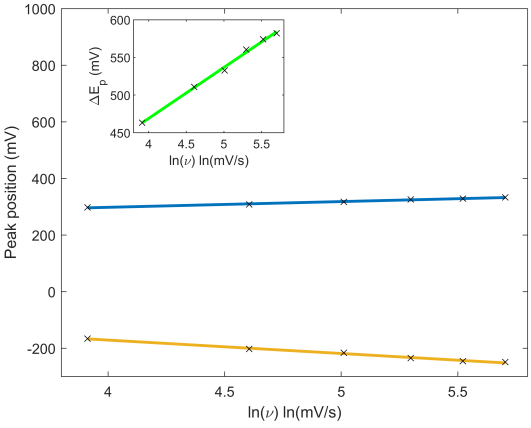

(e) $ZnBi_2O_4$

Fig. 5.11 Redox peak potentials with $\ln(\nu)$ for $ZnBi_xFe_{2-x}O_4$ (x = 0.25, 0.5, 0.75, 1, 2) sensors. Inset shows the ΔE_p versus $\ln(\nu)$.

5.2.3 Sensitivity and limit of detection

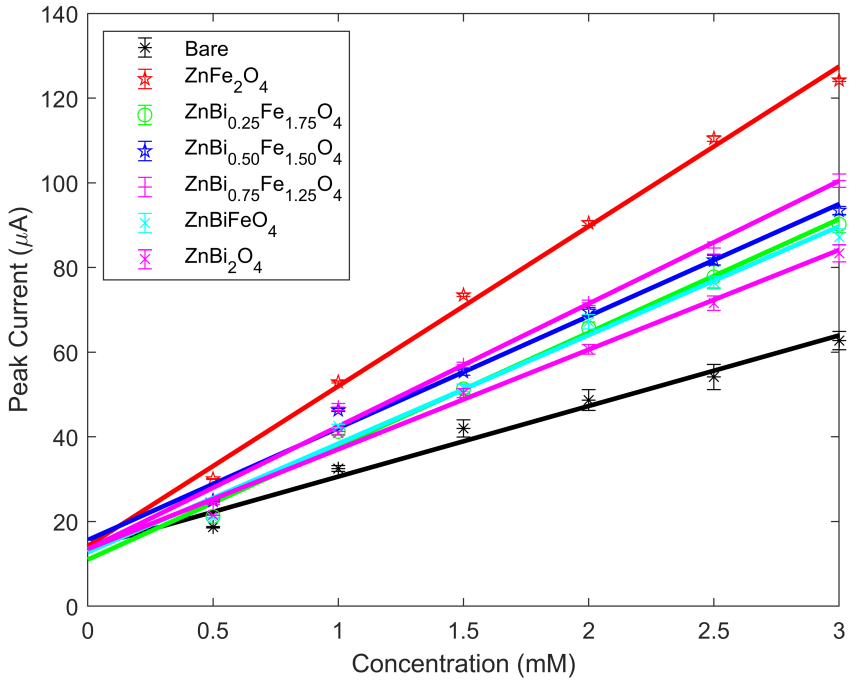

Fig. 5.12 Calibration of bare and $ZnBi_xFe_{2-x}O_4$ sensors with paracetamol.

Each sensor is calibrated by averaging the oxidation current over three measurements for each concentration, with the calibration curves for the different sensors displayed in Figure 5.12. The sensitivity of each sensor, determined from the slope of its respective calibration curve with R^2, and standard error, are reported in Table 5.7. The zinc ferrite sensor exhibited a substantial increase in sensitivity, more than doubling that of the bare sensor, with the values being 37.8 ± 0.2 μA/mM and 16.7 ± 0.9 μA/mM, respectively. However, the introduction of Bi^{3+} ions into the $ZnFe_2O_4$ structure significantly reduced the sensitivity of the sensors and further decreased as the Bi^{3+} content increased and completely replaced the Fe^{3+} ions. The calculated LOD for each sensor is reported in Table 5.7. It is observed that the LOD has a non monotonic variation with the increase of Bi^{3+} in $ZnFe_2O_4$.

Table 5.7 Sensitivity and limit of detection of bare and $ZnBi_xFe_{2-x}O_4$ sensors.

Sensor	Sensitivity (μA/mM)	R^2	LOD (μM)
Bare	16.7 ± 0.9	0.975	3.26 ± 0.17
$ZnFe_2O_4$	37.8 ± 0.2	0.995	7.94 ± 0.04
$ZnBi_{0.25}Fe_{1.75}O_4$	26.8 ± 0.9	0.976	3.2 ± 0.1
$ZnBi_{0.5}Fe_{1.5}O_4$	26.5 ± 0.4	0.988	2.36 ± 0.04
$ZnBi_{0.75}Fe_{1.25}O_4$	28.7 ± 0.6	0.986	5.4 ± 0.1
$ZnBiFeO_4$	25.6 ± 0.8	0.980	2.26 ± 0.07
$ZnBi_2O_4$	23.5 ± 0.6	0.986	7.35 ± 0.02

5.3 Effect of Bi(III) on Electrochemcial Performance

The XRD analysis (Figure 5.2) revealed the presence of two distinct phases: zinc ferrite and zinc bismuthate, along with secondary phases such as ZnO and Fe_2O_3. Unlike in our previous studies in chapter 3 and 4, where a solid solution of two spinel materials with a single phase is achieved, this work produced a dual spinel phase. This could explain the two morphologies observed in the SEM images (Figure 5.1), where the spherical particles are likely ferrite (as seen in SEM images of ferrites previously) and the patch-like structures (new morphology observed in this work) are bismuthate. The presence of these two distinct phases impacts the electrochemical behavior, as we are observing the combined effect of two materials rather than a single-phase material when both Bi(III) and Fe(III) are present.

This indicates that rather than integrating Bi(III) into the zinc ferrite crystal structure, the synthesis process results in the formation of two distinct materials. Each of these materials interacts with and influences the electrochemical interface in a unique manner. Zinc ferrite exhibited higher sensitivity, while zinc bismuthate showed lower sensitivity. The combination of both resulted in only a slight improvement over zinc bismuthate, likely due to interactions between the two materials, where one might be diminishing the effect of the other, leading to a moderate overall performance. High-resolution XPS spectra further confirmed that the introduction of Bi disrupted the spinel structure, with Fe(III) occupying both ‘Td’ and ‘Oh’ sites along with Bi(III), converting the normal spinel structure into a mixed spinel. As demonstrated in earlier studies in chapter 3, the type of spinel structure plays a crucial role in

electrochemical sensing performance due to its impact on conductive mechanisms and cation occupancies in different leading to different reactions at the interface.

5.4 Type of Electron Transfer at the Electrochemical Interface

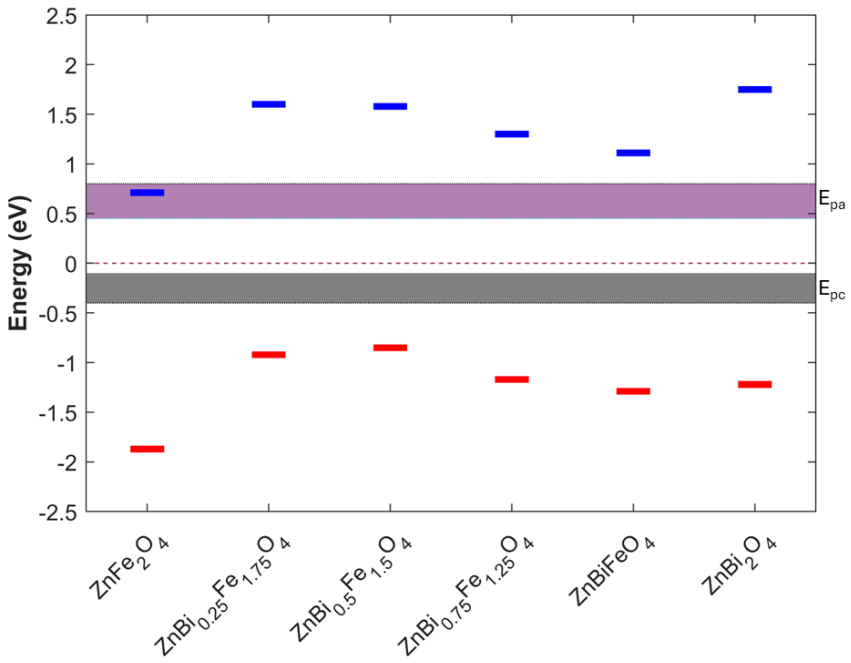

Fig. 5.13 Conduction (E_C) band minimum (blue) and valence (E_V) (red) band maximum of $ZnBi_xFe_{2-x}O_4$ nanomaterials constructed by using E_g (the energy gap between E_C and E_V). Electron transfer prediction from/to paracetamol to/from the surface of the WE by mapping the E_C of the WE with the experimental E_{pa} and E_{pc} of paracetamol. The black dotted lines represent the fermi energy level 'E_f' at '0' eV.

Similarly as in chapters 3 and 4, we utilized the band energy levels of the nanomaterials to predict the type of electron transfer. The estimated conduction band minimum (E_C) and valence band maximum (E_V) are mapped to the experimental redox potentials of paracetamol, as shown in Figure 5.13. Since these materials have two distinct material phases, it is difficult to differentiate the effect of individual phases in electron transfer hence, this analysis is based on an average effect of two distinct phases. It is found that only the E_C of $ZnFe_2O_4$ overlaps with the redox

potential of paracetamol, suggesting a direct electron transfer at the ECI between the nanomaterial and paracetamol as seen before.

For the other sensors containing bismuth, no overlap between E_C and the redox potential of paracetamol is observed. This could be due to two distinct phases of the material affecting the overall energy band gap, conduction, and valence band positions. Despite this, there is a noticeable improvement in electrochemical sensitivity and the rate constant compared to the bare carbon sensor. In these cases, it is likely that electron transfer occurs indirectly via surface states or defects in the nanomaterials. XRD confirmed the presence of ZnO and Fe_2O_3, and Raman spectroscopy indicated the presence of cubic Bi_2O_3, supporting the possibility of surface-state-mediated electron transfer. This mechanism likely explains why zinc ferrite exhibited the highest sensitivity and faster reaction rates at the electrochemical interface, while the other sensors, involving surface states and multiple electron transfer rates, showed lower sensitivity and slower reaction kinetics.

Furthermore, it is observed that the incorporation of Bi(III) into $ZnFe_2O_4$ significantly reduced the sensitivity and kinetic rate constant compared to the performance of Cr(III) in $ZnFe_2O_4$. However, a direct comparison is challenging due to substantial differences in particle size, morphology, and crystal phases between the materials.

5.5 Original Contribution III

This work investigates the effect of larger ionic size trivalent cations of Bi^{3+} in the crystal structure of $ZnFe_2O_4$ in electrochemical sensing of paracetamol. Sensitivity and rate constant of sensors are presented and discussed with respect to the amount of Bi^{3+} ions in $ZnBi_xFe_{2-x}O_4$. The type of electron transfer at the electrochemical interface is predicted using the nanomaterials energy bands and redox potential of paracetamol.

A part of this work has been presented as a poster at the 1st IEEE Biosensors conference in London, UK, in July 2023. The paper can be found with title "$ZnM_xFe_{2-x}O_4$ (M = Cr, Bi) Nanoparticles-modified electrochemical sensors: Effect on sensitivity and first-order kinetic rate constant" at the url:

https://ieeexplore.ieee.org/abstract/document/10280910

A full manuscript of the work has been successfully published in "Applied Surface Science" journal of Elsevier publications as "Unveiling the effect of Bi in $ZnFe_2O_4$ nanoparticles in electrochemical sensors". The paper can be found at the following url:
https://www.sciencedirect.com/science/article/pii/S0169433224015836

Chapter 6

Applications of Spinel Nanomaterials

This chapter explores the potential applications of normal spinel nanomaterials, as demonstrated in previous chapters, where normal spinel nanomaterials exhibited superior electrochemical sensing performance than inverse spinel nanomaterials. The chapter is divided into two parts, with the first part conducted during a research period abroad at KU Leuven in Belgium. During this time, I investigated the potential applications of $ZnFe_2O_4$ nanomaterials, both individually and in combination with ZnO, aiming to fine-tune the band gap of $ZnFe_2O_4$ through the introduction of a double interface.

In the second part, an investigation is conducted into the use of normal spinel $ZnFe_2O_4$ and $ZnCr_2O_4$ nanomaterials for electrochemical sensing of anti-cancer drugs, specifically 5-Fluorouracil and Etoposide, during the research period at EPFL in Switzerland.

6.1 Potential Applications : Part I

Dissolved oxygen is the molecular oxygen present in water, fluctuations in Do level can change the quality of water. The amount of DO plays a crucial role in water quality [179]. DO levels are also critical in bioreactor systems, in fermentation , medical detection [180, 181], therefore it is important to quantify DO levels. As per our knowledge, electrochemical sensing of DO using spinel nanomaterials is not reported in the literature. Therefore in this work, electrochemical sensing capability of $ZnFe_2O_4$, ZnO, and ZnO/$ZnFe_2O_4$ towards dissolved oxygen (DO) is studied.

As another application, ZnO and $ZnFe_2O_4$ performance as electrochemical pH sensors is studied since no work presented based on spinel ferrites as pH sensors. pH monitoring is very important because pH is crucial in soil, microbial activity, biological functions, and behaviour of chemicals [182, 183].

6.1.1 Material Characterization

ZnO and ZnO/$ZnFe_2O_4$ materials are synthesized similarly as $ZnFe_2O_4$ using the autocombustion method as described in section 2.2.2. Figure 6.1 shows the SEM images of ZnO and ZnO/$ZnFe_2O_4$ materials. It is observed that the ZnO particles have micrometer size with pyramid shaped morphology while the ZnO/$ZnFe_2O_4$ particles with nanometer dimensions with morphological features similar to $ZnFe_2O_4$. A certain degree of aggregation of particles is also observed in both the materials as observed previously with the other materials. We hypothesize that the presence of Fe in the synthesis process is controlling the growth of the particles in the case of ZnO/$ZnFe_2O_4$ or $ZnFe_2O_4$ compared to the synthesis of ZnO alone.

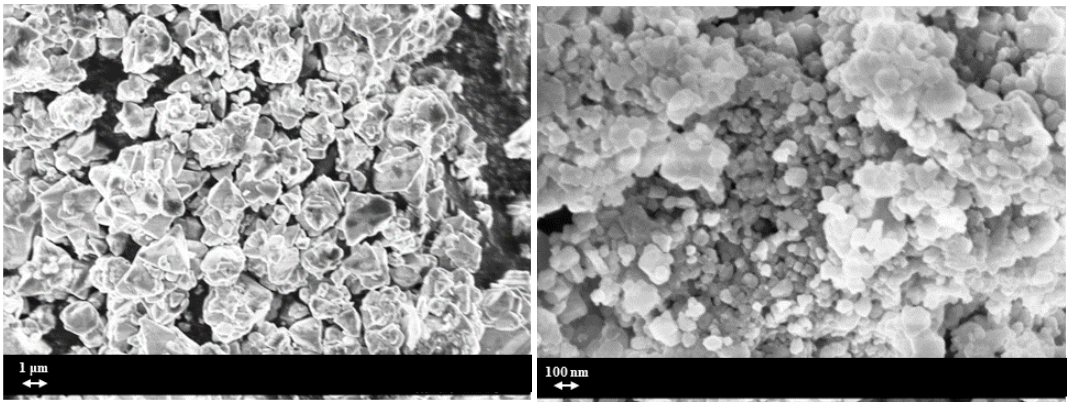

(a) ZnO (b) ZnO/$ZnFe_2O_4$

Fig. 6.1 FESEM images of ZnO and ZnO/$ZnFe_2O_4$ materials.

The XRD patterns of ZnO, $ZnFe_2O_4$, and ZnO/$ZnFe_2O_4$ materials are presented in Figure 6.2. XRD pattern for ZnO matches perfectly with the zinc oxide powder diffraction pattern (ZnO, reference code. 01-080-0075). The low intense peak between 25 and 30^o (2θ) related to graphite, which is possibly due to the use of graphite reactor in the synthesis. ZnO/$ZnFe_2O_4$ XRD pattern matches very well with

the peaks of ZnO and $ZnFe_2O_4$ as expected with a low intense peak of Fe_2O_3 around 33 degree (2θ) confirming the synthesis of ZnO in combination with $ZnFe_2O_4$.

Average crystallite size of the particles is calculated Using Scherrer's method [3] and the average crystallite size of the particles is reported in Table 6.1. ZnO has an average crystallite size of 45.7 ± 1.3 but the particles might be formed by the combination of many crystallites since the particle size is in the micrometres range while the crystallite size of ZnO/$ZnFe_2O_4$ is reported separately for ZnO and $ZnFe_2O_4$.

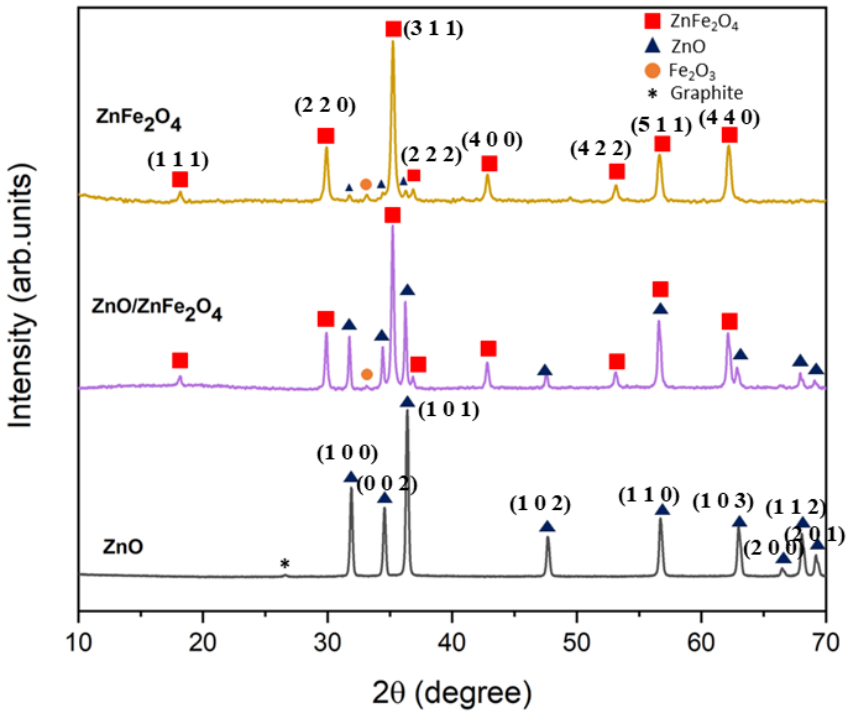

Fig. 6.2 XRD patterns of ZnO, $ZnFe_2O_4$, and ZnO/$ZnFe_2O_4$ materials showing different crystalline phases.

Table 6.1 The average crystallite size of $ZnBi_xFe_{2-x}O_4$ materials

Material	Average crystallite size (nm)
$ZnFe_2O_4$	36.2 ± 1.4
ZnO	45.7 ± 1.3
ZnO/$ZnFe_2O_4$	83 ± 18 (ZnO) 46.6 ± 3.6 ($ZnFe_2O_4$)

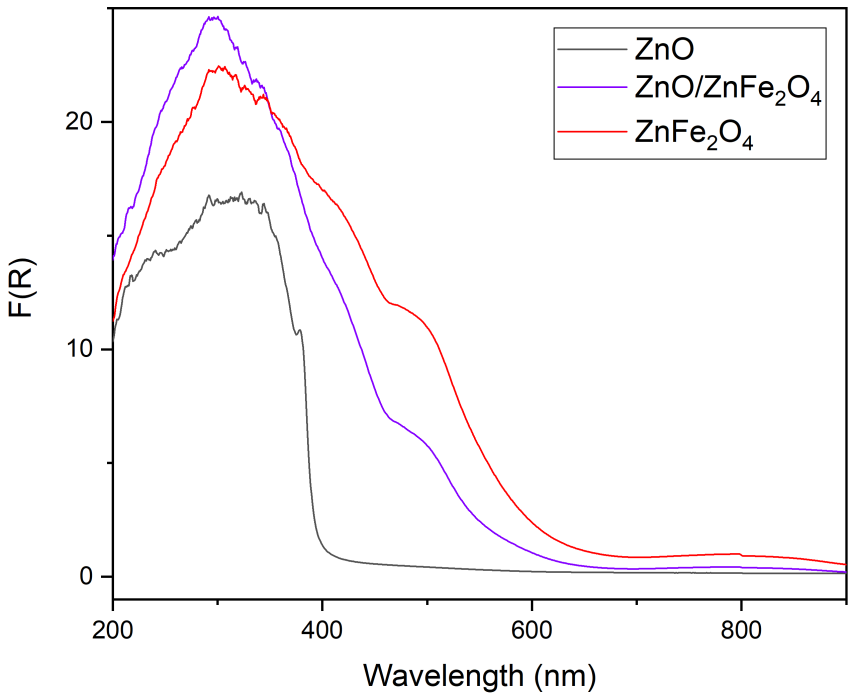

Fig. 6.3 Diffuse reflectance (DR) UV-vis spectra of ZnO, $ZnFe_2O_4$, and $ZnO/ZnFe_2O_4$ materials.

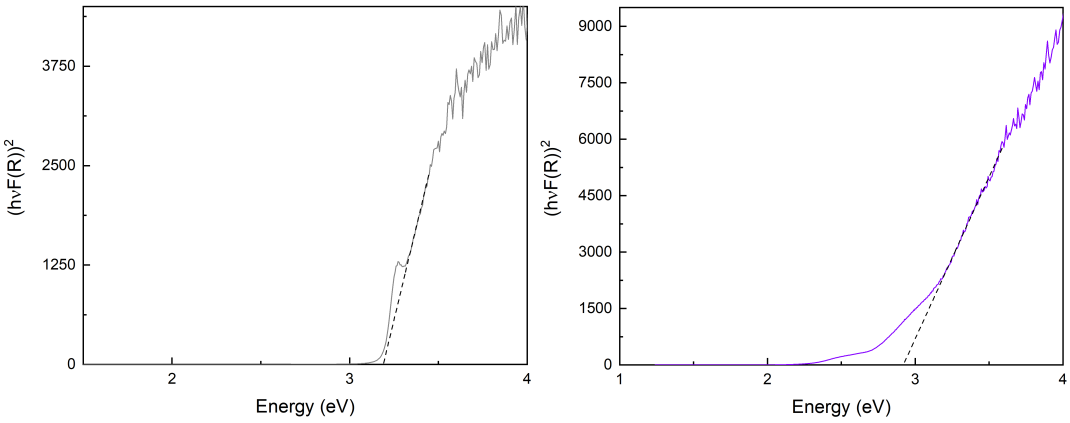

(a) ZnO (b) $ZnO/ZnFe_2O_4$

Fig. 6.4 Tauc's plot method to determine the energy gap (E_g) of ZnO, $ZnFe_2O_4$, and $ZnO/ZnFe_2O_4$ materials.

Diffuse reflectance (DR) UV-vis spectra of the materials are shown in Figure 6.3 and the respective Tauc plots for ZnO and $ZnO/ZnFe_2O_4$ are reported in Figure 6.4. The estimated energy band gap for ZnO is 3.2 ± 0.1 eV matching the band gap

reported in the literature for ZnO [73, 74]. While ZnO/$ZnFe_2O_4$ has an energy band gap of 2.92 ± 0.06 eV which is close to the average band gap of ZnO and $ZnFe_2O_4$ proving that the energy band gap has been tuned with the combination of ZnO and $ZnFe_2O_4$ as expected.

6.1.2 Electrochemical Sensing of Dissolved Oxygen

To evaluate the electrochemical sensing performance of the sensors for dissolved oxygen (DO) detection, cyclic voltammetry is initially carried out using a screen-printed carbon electrode as the counter electrode.Based on the cyclic voltammograms obtained for different sensors in a 10 mM PBS solution at pH 7.4 with a saturated DO level of 88%, as shown in Figure 6.5, a potential of -0.5 V is selected for chronoamperometric measurements, since the onset of the oxygen reduction process begins around that value.

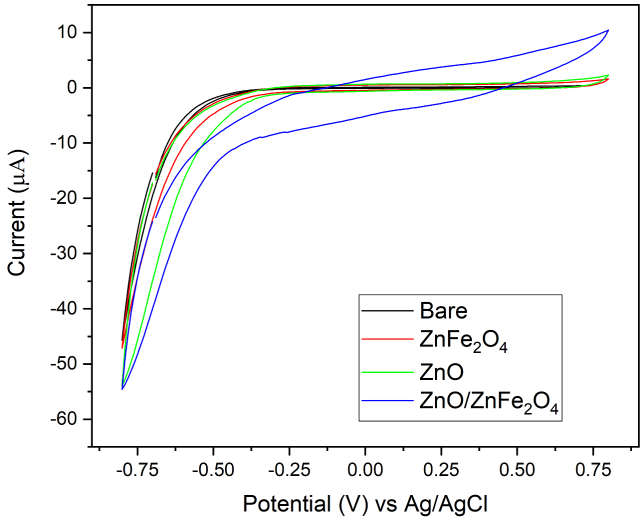

Fig. 6.5 Cyclic voltammograms of different sensors in 10 mM PBS solution at pH 7.4 at a scan rate of 100 mV/s

Figures 6.6 and 6.7 show the chronoamperometric response (current response vs time) at different saturated DO levels between 7 and 25% for bare, $ZnFe_2O_4$, ZnO, and ZnO/$ZnFe_2O_4$ sensors with screen-printed carbon as a counter electrode. The amperometric response showed that the reduction current increased with each increase in the saturated DO level rapidly reaching a steady state. The current starts to stabilize after 50s of the response and the sensors are calibrated by taking the

average response for 60s in a stable region after 50s of the response. The sensitivity of the sensors taken as the slope of the calibration from Figures 6.6 and 6.7 are reported in Table 6.2.

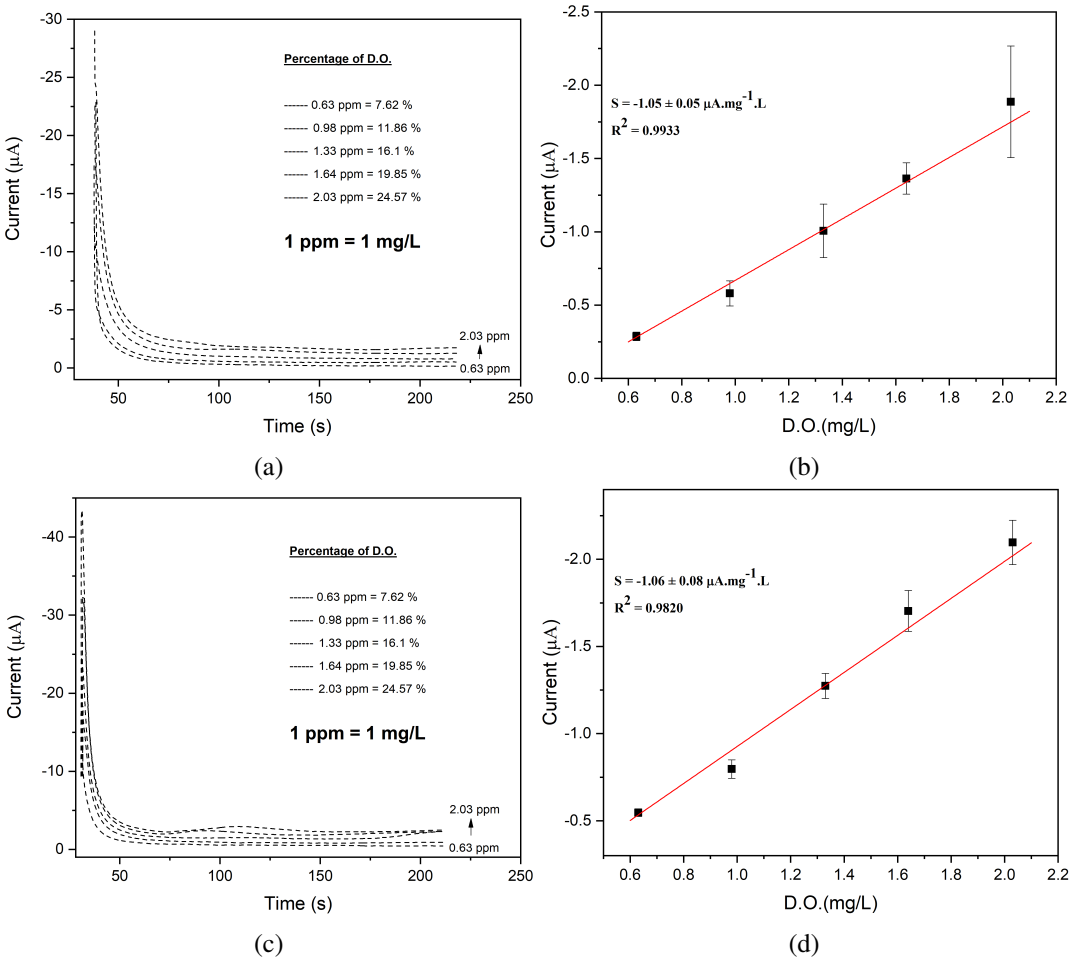

Fig. 6.6 Chronoamperometric dissolved oxygen sensing with a) bare and c) $ZnFe_2O_4$ sensors and calibration of b) bare and d) $ZnFe_2O_4$ sensors with carbon as counter electrode.

The bare sensor has a sensitivity of -1.05 ± 0.05 μA.mg^{-1}.L while the other modified sensors showed a similar electrochemical catalytic activity towards dissolved oxygen with very similar sensitivity. There is no significant enhancement in electrochemical activity using ZnO, $ZnFe_2O_4$ or ZnO/$ZnFe_2O_4$ nanomaterials compared to the bare carbon sensor in electrochemical sensing of DO.

Since it is found that all the sensors are producing the similar response in electrochemical sensing of DO, there might be the possibility of current limitation due to

the area of the counter electrode. Therefore to validate this hypothesis, instead of the screen-printed carbon electrode, platinum (Pt) wire with higher surface ares is used as a counter electrode and the measurements are repeated. The amperometric responses of the all the four different sensors are shown in Figures 6.8 and 6.9. The response has significantly enhanced compared to the previous case where screen-printed carbon was used as a CE validating the possibility of current limitation with lesser surface area of the counter electrode.

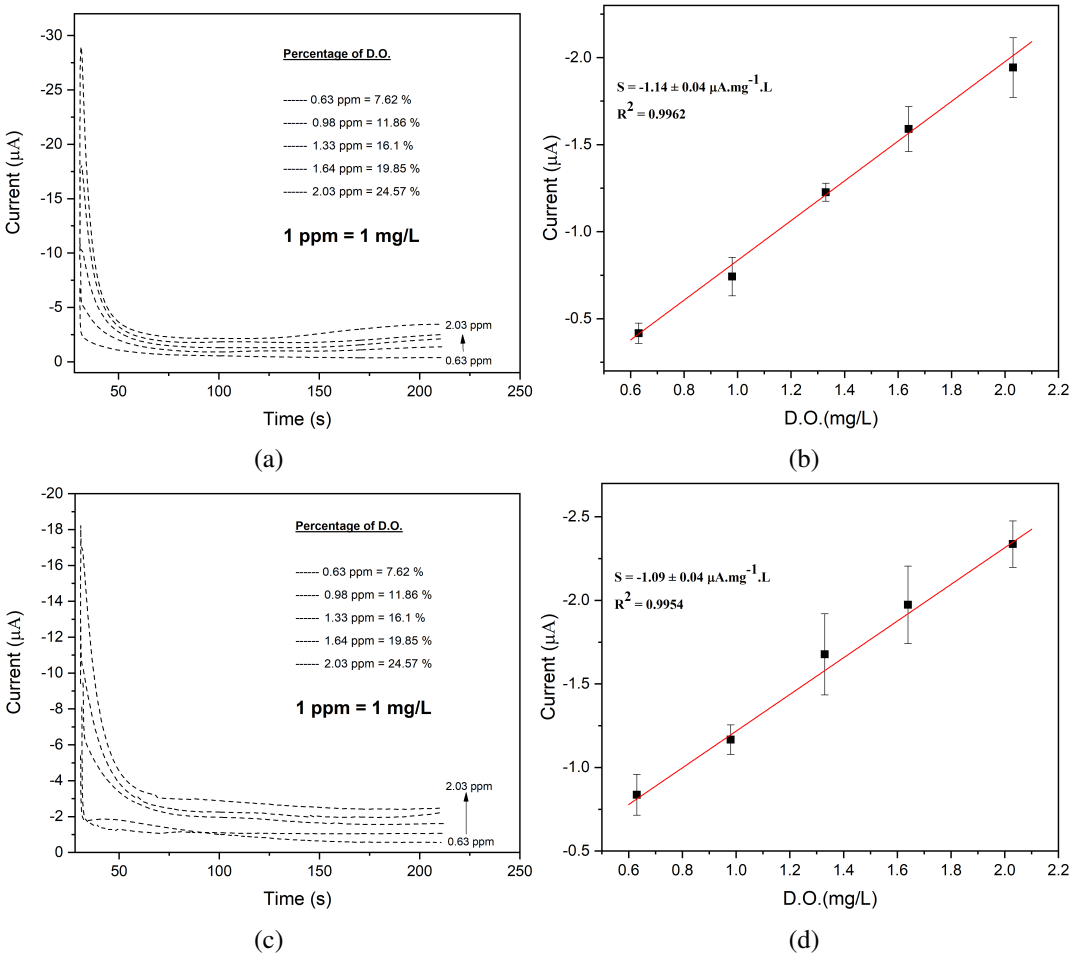

Fig. 6.7 Chronoamperometric dissolved oxygen sensing with a) ZnO and c) $ZnO/ZnFe_2O_4$ sensors and calibration of b) ZnO and d) $ZnO/ZnFe_2O_4$ sensors with carbon as counter a electrode.

The sensitivities of the sensors with Pt wire as a CE are reported in Table 6.2. The sensitivities are reported with a negative sign since the current is due to oxygen reduction process. Bare sensor now has a sensitivity of -1.19 ± 0.05

μA.mg^{-1}.L, 13% higher than the sensitivity with screen-printed carbon as a CE. The sensitivity of the other sensors also enhanced with $ZnFe_2O_4$ showing the high electrochemical catalytic activity with a sensitivity of -2.7 ± 0.2 μA.mg^{-1}.L which is 127% higher than the sensitivity of the bare sensor with Pt wire as a counter electrode. While the ZnO and ZnO/$ZnFe_2O_4$ sensors have an increment of 85% and 14% in sensitivities, respectively compared to the bare carbon sensor with Pt wire as a CE. The enhanced sensitivity is attributed to the nanostructurization of the screen-printed carbon working electrodes surface providing more surface area and also higher surface area of the counter electrode avoiding the current limitation.

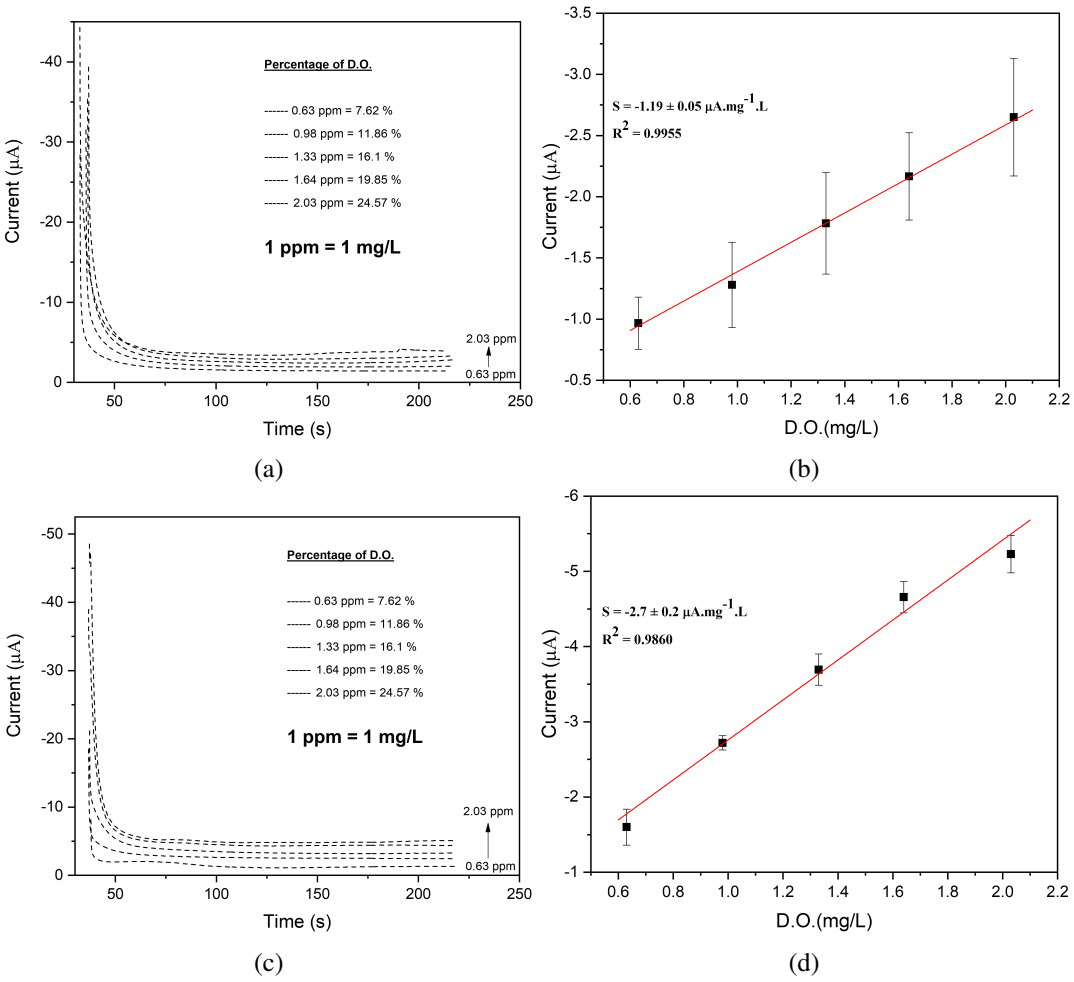

Fig. 6.8 Chronoamperometric dissolved oxygen sensing with a) bare and c) $ZnFe_2O_4$ sensors and calibration of b) bare and d) $ZnFe_2O_4$ sensors with platinum (Pt) wire as a counter electrode.

Table 6.2 Sensitivity of different sensors in DO sensing with carbon or Pt wire as CE.

Sensor	Sensitivity (μA.mg^{-1}.L) with Carbon as CE	Sensitivity (μA.mg^{-1}.L) with Pt wire as CE
Bare	-1.05 ± 0.05	-1.19 ± 0.05
$ZnFe_2O_4$	-1.06 ± 0.08	-2.7 ± 0.2
ZnO	-1.14 ± 0.04	-2.2 ± 0.1
$ZnO/ZnFe_2O_4$	-1.09 ± 0.04	-1.36 ± 0.04

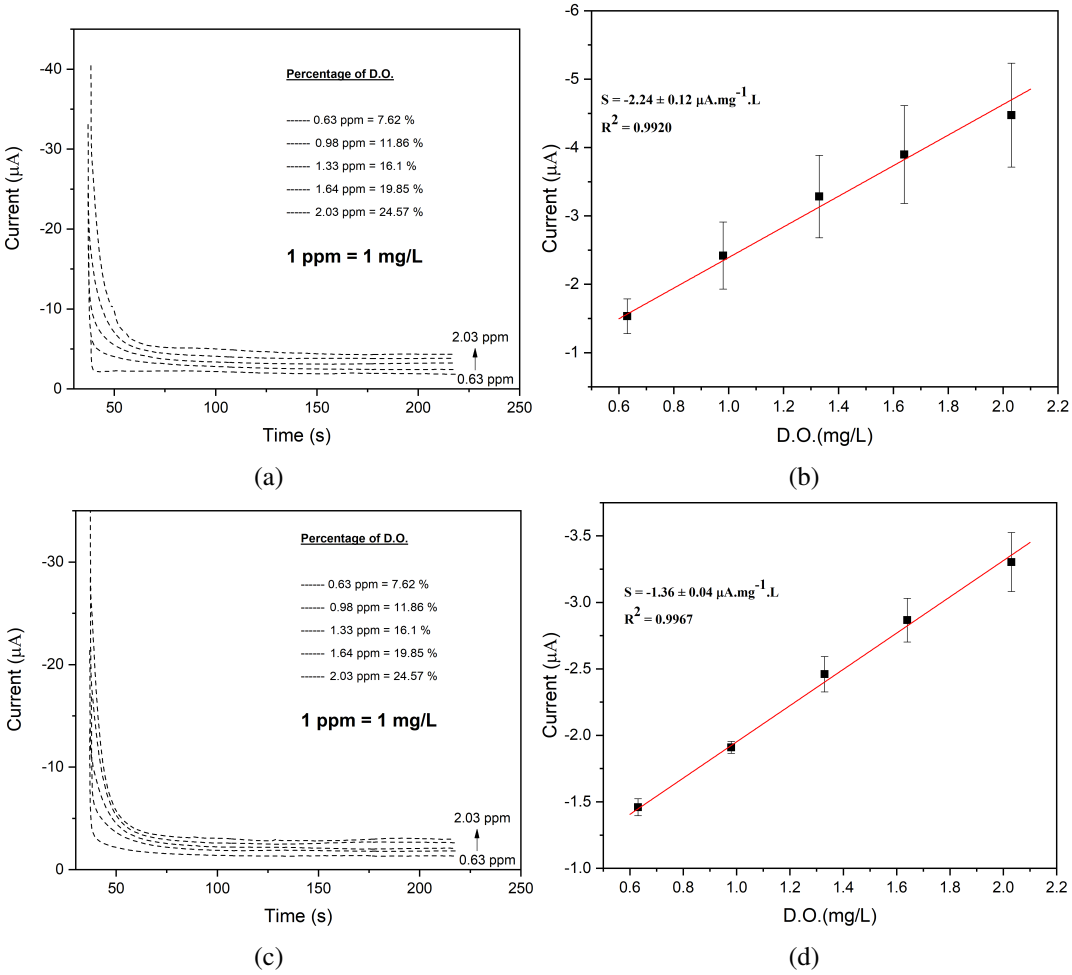

Fig. 6.9 Chronoamperometric dissolved oxygen sensing with a) ZnO and c) $ZnO/ZnFe_2O_4$ sensors and calibration of b) ZnO and d) $ZnO/ZnFe_2O_4$ sensors with platinum (Pt) wire as counter a electrode.

6.1.3 Electrochemical pH Sensing

ZnO and $ZnFe_2O_4$ materials are used as sensing materials in pH sensing of UBS solution. Figure 6.10 shows the potentiometric (OCP vs time) response of bare, ZnO, and $ZnFe_2O_4$ sensors in the pH loop of 2-12-2, the black and red down arrows indicate the addition of 1mL of 1M KOH solution to increase the pH and 1mL of 1M HNO_3 to decrease the pH of the solution, respectively. The response is recorded for two minutes at each pH value of the solution.

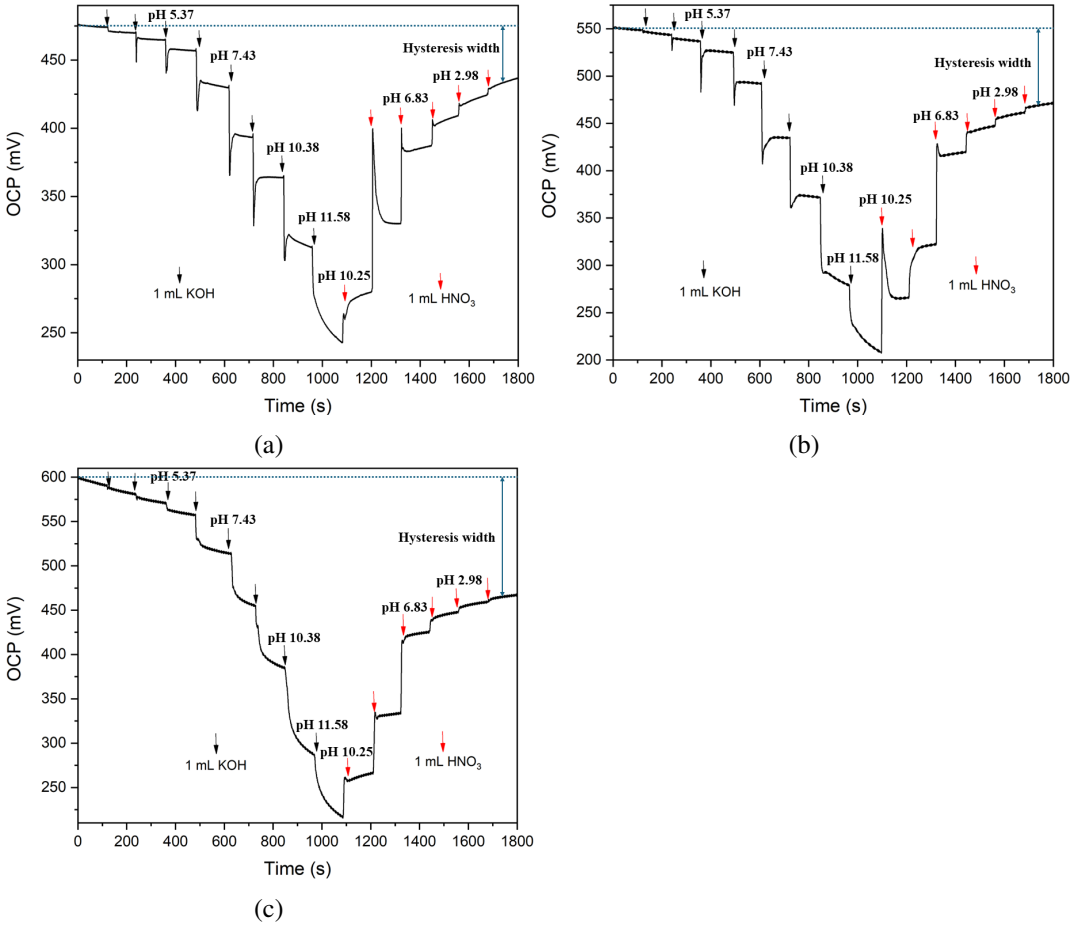

Fig. 6.10 Chronopotentiametric pH sensing with a) bare, b) $ZnFe_2O_4$, and c) ZnO with pH varying between 2 and 12.

All three sensors showed hysteresis behavior which is one of the phenomenons observed while characterizing metal oxide-based pH sensors [184]. The bare sensor showed a hysteresis width (the potential difference between the starting potential and the end potential by the end of the pH measurement loop) of 39 mV while the

$ZnFe_2O_4$ and ZnO sensors have a hysteresis width of 81 and 133 mV. respectively. The hysteresis width has increased due to the presence of $ZnFe_2O_4$ and further increased with ZnO sensor compared to the bare carbon sensor. Since, the hysteresis behaviour can be influenced by the surface area and crystalline properties of the materials [184], this is expected as $ZnFe_2O_4$ nanoparticles have a spinel crystalline structure with spherical shape while ZnO microparticles have a hexagonal crystalline structure with a pyramide shape. Hysteresis width also depends on the loop time, higher loop time leading to higher hysteresis width [185].

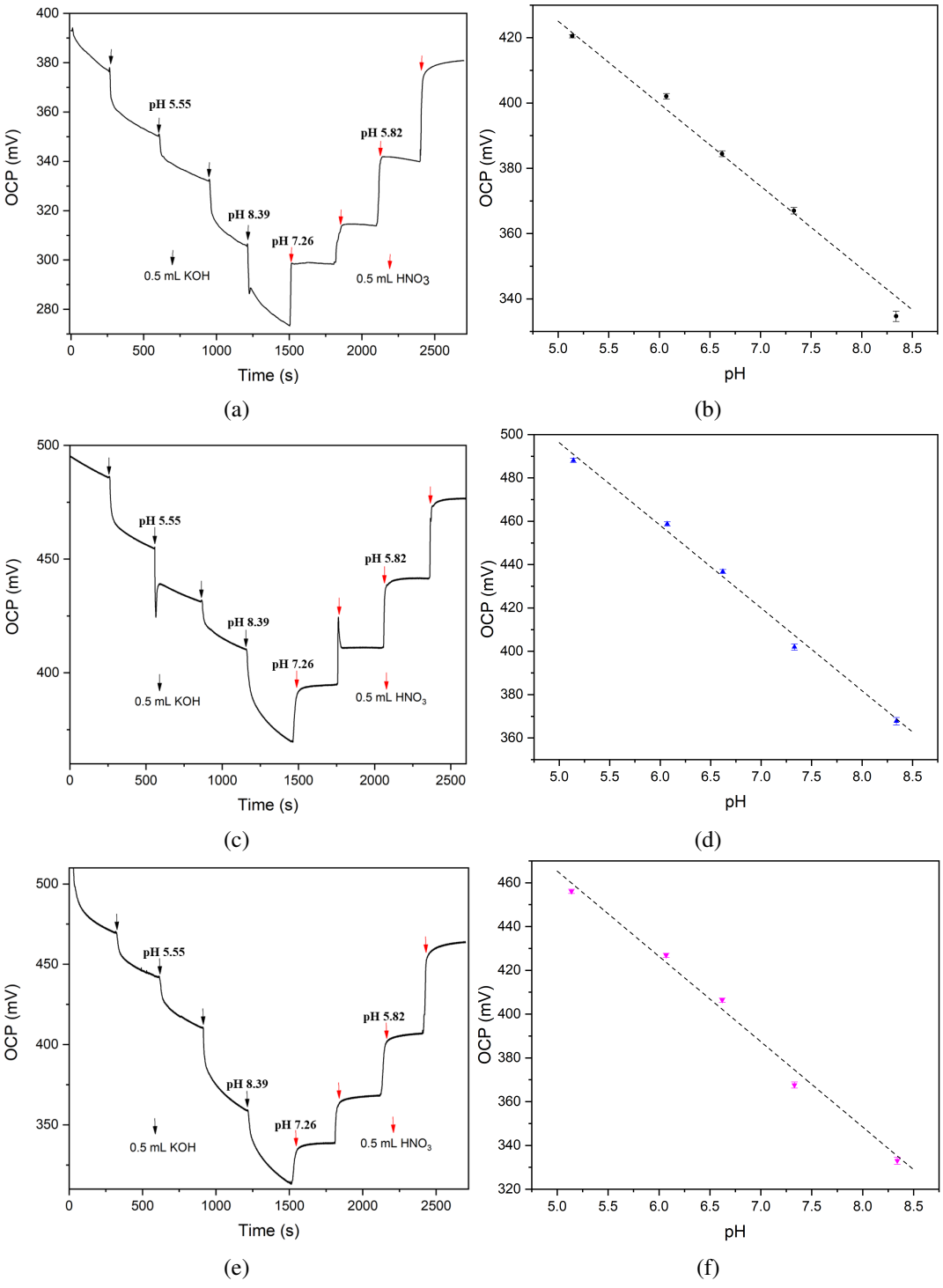

Fig. 6.11 Chronopotentiametric pH sensing with a) bare, c) $ZnFe_2O_4$, and e) ZnO sensors with pH varying between 4 and 8.5. pH calibration of b) bare, d) $ZnFe_2O_4$, and f) ZnO sensors, respectively.

As our interest is in the pharmaceutical pH range of 4 to 8.5, potentiometric measurements are repeated in this pH range by adding 0.5 mL of 1M KOH (black down arrow) and 0.5 mL of 1M HNO_3 (red down arrow) to control the pH and the response is recorded for 5 minutes at each pH of the solution as shown in Figure 6.11. The response now show that the hysteresis of the sensors is negligible or reduced significantly compared to the previous case with higher loop time, proving the point that the loop time shows significant effect on hysteresis behaviour of pH sensors apart from the other electrode properties. The sensors are calibrated by averaging the response over the last 60 seconds of measurement for each sensor type. The results are averaged across three sensors of each type, and the calibration results are presented in Figure 6.11 for all three sensor types. The bare sensor has a pH sensitivity of 23.9 ± 1.4 mV/pH, $ZnFe_2O_4$ and ZnO sensors have a sensitivity of 37.2 ± 1.1 and 38.1 ± 1.3 mV/pH, respectively. The presence of metal oxide nano/micro particles have enhanced the pH sensing capability of the screen-printed carbon sensor providing around 60% increase (% increment= (sensitivity of modified sensor/sensitivity of bare sensor $\times$ 100)-100) in sensitivity.

The achieved sensitivity of the surface-modified sensors with metal oxides in the current study is not comparable to Nernstian but the bare sensor performance is improved showing the potential to be used as pH sensing materials with further optimization of the material properties and the sensing procedure.

Another factor about pH sensors is the stability of the response. As we observe the response in Figure 6.11 for each addition of 0.5 mL of 1M KOH, the potential keeps changing without reaching a steady state response but immediately after the addition of 0.5 mL of 1M HNO_3 the potential is reaching a steady state value. To check whether it is taking more time to get stabilized, the response is measured for longer times (10 minutes and 20 minutes) with each addition of 0.5 mL of 1M KOH solution as shown in Figure 6.12 using $ZnFe_2O_4$ sensor since our main interest is the use of spinel nanomaterials in electrochemical sensors. Usually when the electrode is immersed into the solution, the electrode surface gets covered by hydroxide groups due to water dissociative adsorption leading to a potential difference between the WE and RE. This external addition of KOH solution leads to hydroxide rich electrode surface with always a potential difference between the WE and RE, hence the potential response keeps changing with time without reaching a steady state, whereas the addition of acid immediately balances these hydroxide rich surface since the diffusion of H^+ ions is faster than the diffusion of hydroxide ions. To avoid this

problem of hydroxide ions and improve the stability of the sensors, it will be wise to choose other alkaline solutions without hydroxide ions such as $NaHCO_3$ or $KHCO_3$.

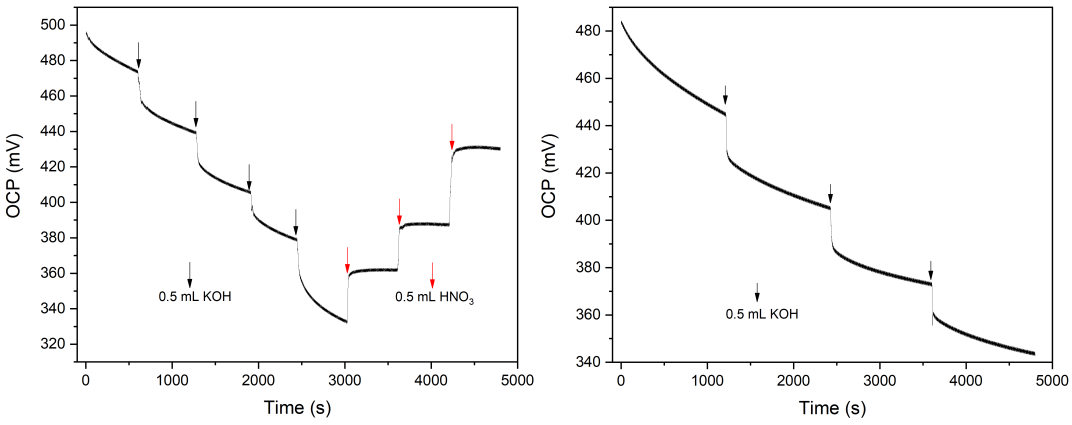

Fig. 6.12 Stability tests of $ZnFe_2O_4$ pH sensor. Measurement is performed for a) 10 minutes and b) 20 minutes at each pH value.

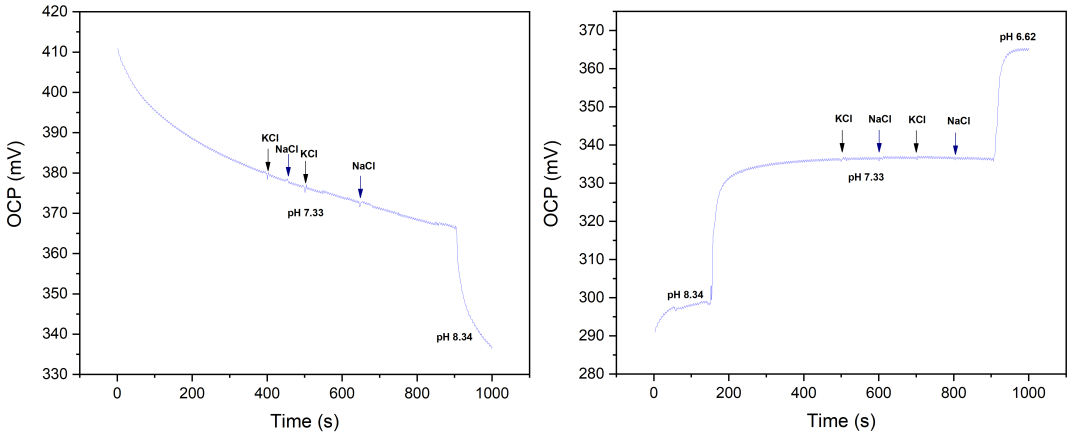

Fig. 6.13 Interference tests of $ZnFe_2O_4$ pH sensor using 30 mM KCl and 5 mM NaCl. a) adding KOH to increase the pH and b) using HNO_3 to decrease the pH.

Interference effect on $ZnFe_2O_4$ pH sensor is studied by adding KCL and NaCl while performing the pH sensing measurements. The measurement is started with a certain pH of the solution and then the pH is changed by adding KOH solution to reach a pH value around 7. While the measurement is in progress 1mL of 30 mM KCl and 1 mL of 5 mM NaCl solutions are added one after the other and the

response is recorded as shown in Figure 6.13a. Similarly the measurement is done by adding also the HNO_3 solution decreasing the pH of the solution around 7. In both cases, the interference effect is not observed showing excellent pH sensing ability of the $ZnFe_2O_4$ sensor.

6.2 Potential Applications : Part II

5-Fluorouracil (5-FU) is a widely used chemotherapy drug, primarily for the treatment of colorectal cancer. It belongs to the class of antimetabolites, which interfere with DNA and RNA synthesis, preventing cancer cell proliferation. 5-FU is a pyrimidine analog, structurally similar to uracil and thymine. Cancer cells can develop resistance due to mutations in thymidylate synthase or changes in drug metabolism. Common side effects include nausea, diarrhea, myelosuppression, hand-foot syndrome, and neurotoxicity [186]. Therefore, it is highly important to monitor the dosage levels of 5-FU in cancer treatment. Some work on electrochemical sensing of 5-FU based on metal oxide nanoparticles is reported in the literature [187, 188]. Etoposide is a semisynthetic derivative of podophyllotoxin, primarily used as a chemotherapeutic agent for treating various cancers. It is classified as a topoisomerase II inhibitor, which disrupts DNA replication and induces apoptosis in cancer cells. Common side effects include myelosuppression (neutropenia, thrombocytopenia), nausea, alopecia, and secondary malignancies (e.g., therapy-related leukemia). Etoposide has variable bioavailability, requiring careful dosing adjustments [189–191]. Electrochemical sensors are developed in sensing Etoposide based on carbon nanotubes [192], carbon quantum dots [193], and graphene nanoribbons [194]. There is no work reported using only spinel nanomaterials for electrochemical sensing of Etoposide. This part of the work reports the comparison of zinc ferrite and zinc chromite in electrochemical sensing of 5-FU and Etoposide interms of sensitivity and limit of detection.

6.2.1 Electrochemical sensing of 5-Fluorouracil

5-FU acts as a weak acid and high possibility of deprotonation of the drug at physiological or intracellular pH hence the electrochemical sensing experiments are performed around pH 7. Figure 6.14 shows the cyclic voltammograms of different

sensors with 500 μM 5-FU in 0.1M PB at pH 7. There is an increment of oxidation current around 2 μA and a decrease in potential around 80 mV using Zinc ferrite and zinc chromite modified-sensors compared to the bare carbon sensor proving the effect of nanostructured surface in the electrochemical sensing of 5-FU. The possible oxidation of the 5-FU drug involves the protonation of the drug and the possible oxidation scheme of the drug is presented in the literature [187].

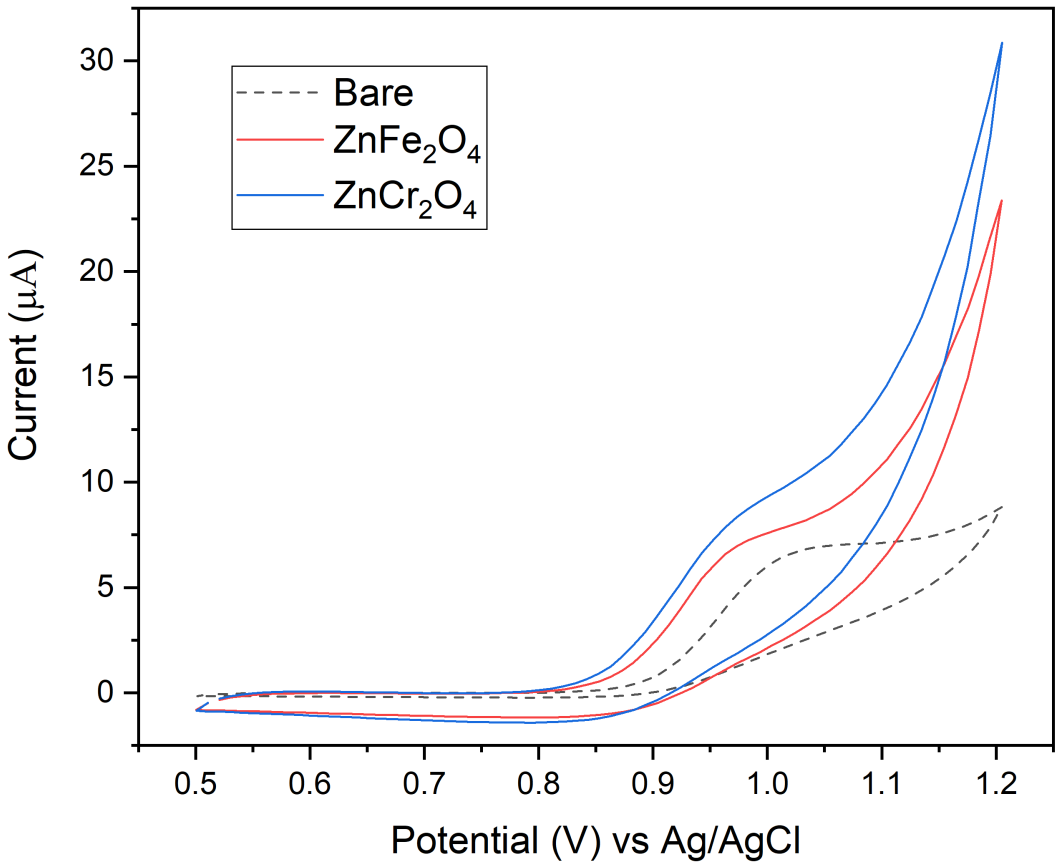

Fig. 6.14 Cyclic voltammograms of Bare, $ZnFe_2O_4$, and $ZnCr_2O_4$ sensors with 500 μM 5-Fu in 0.1 M PB at pH 7 at a scan rate of 100 mV/s.

Since the pharmaceutical dosage of the drug is at low concentrations (< 100 μM) it is very difficult to detect 5-FU using cyclic voltammetry due to the potential at which the oxidation of the drug occurs. Differential pulse voltammetry (DPV) is employed to electrochemically sense 5-FU at low concentration range from 10 to 200 μM range. DPV parameters were optimized before the final measurements, the modulation amplitude, modulation time, and interval time are set at 100 mV, 25 ms, and 100 ms, respectively. Figures 6.15 shows the differential pulse voltammograms

after baseline correction at different concentrations of 5-Fu in 0.1M PB at pH 7 for bare (fig. 6.15a), $ZnFe_2O_4$ (fig. 6.15b), and $ZnCr_2O_4$ (fig.6.15c) sensors. For all sensors, as the concentration of 5-FU increases the oxidation current increases.

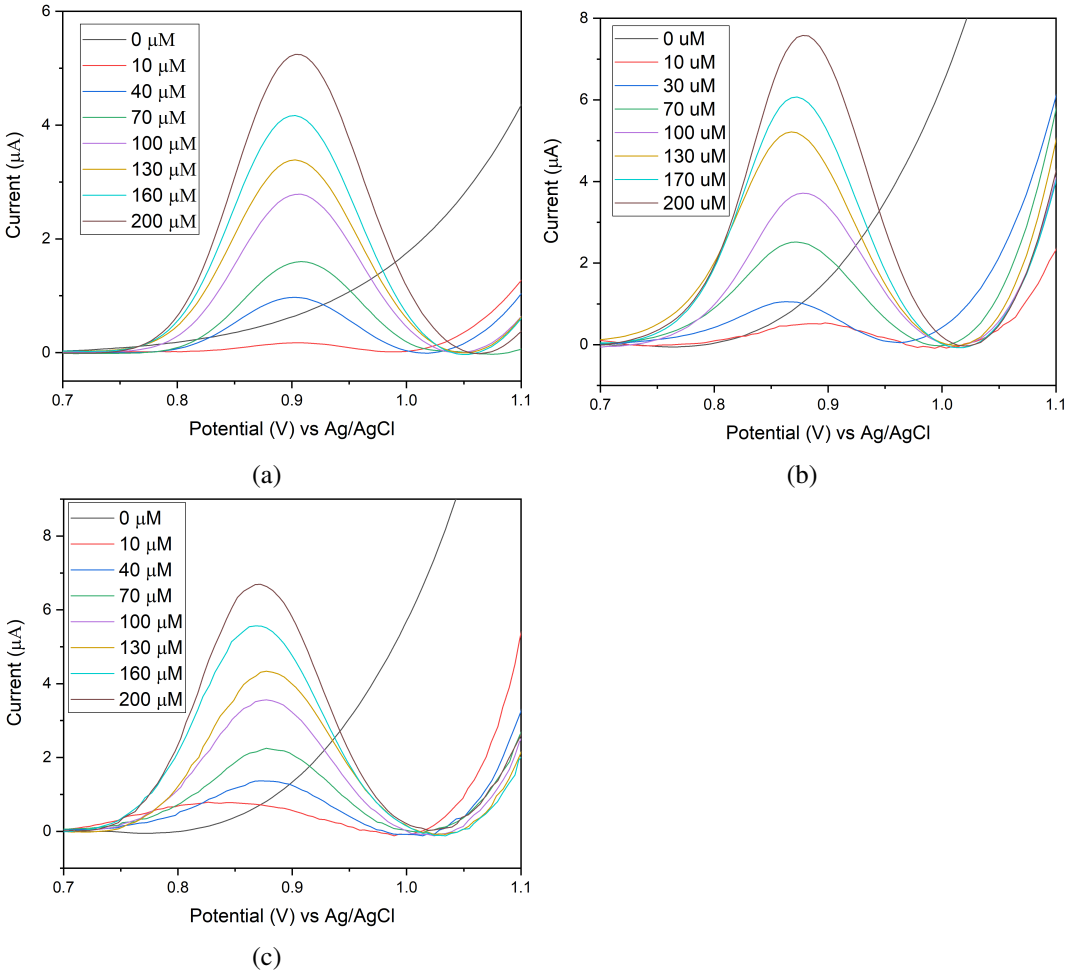

Fig. 6.15 Differential pulse voltammograms of a) bare, b) $ZnFe_2O_4$, and c) $ZnCr_2O_4$ sensors with the concentration 5-FU varying from 10 to 200 μM.

The sensors are calibrated by taking the average of oxidation peak current of three sensors of each type and the calibration of bare, $ZnFe_2O_4$, $ZnCr_2O_4$ sensors is shown in Figure 6.16. The sensitivities of the three sensors are reported in Table 6.3. It is found that $ZnFe_2O_4$, $ZnCr_2O_4$ sensors have sensitivity of 39.1 ± 0.2, 33.8 ± 2.1 nA/μM while the bare sensor has a sensitivity of 25.7 ± 0.6 nA/μM. The $ZnFe_2O_4$, $ZnCr_2O_4$ sensors have increased the sensitivity of bare carbon sensor by 52% and 32%, respectively, which is a very significant enhancement in electrochemical detec-

tion of 5-FU at this concentration level. LOD of the sensors is calculated as reported in Table 6.3 found that Bare, $ZnFe_2O_4$, $ZnCr_2O_4$ sensors have a LOD of 4.87 ± 0.65, 7.67 ± 0.02, and 9.88 ± 0.35 μM, respectively.

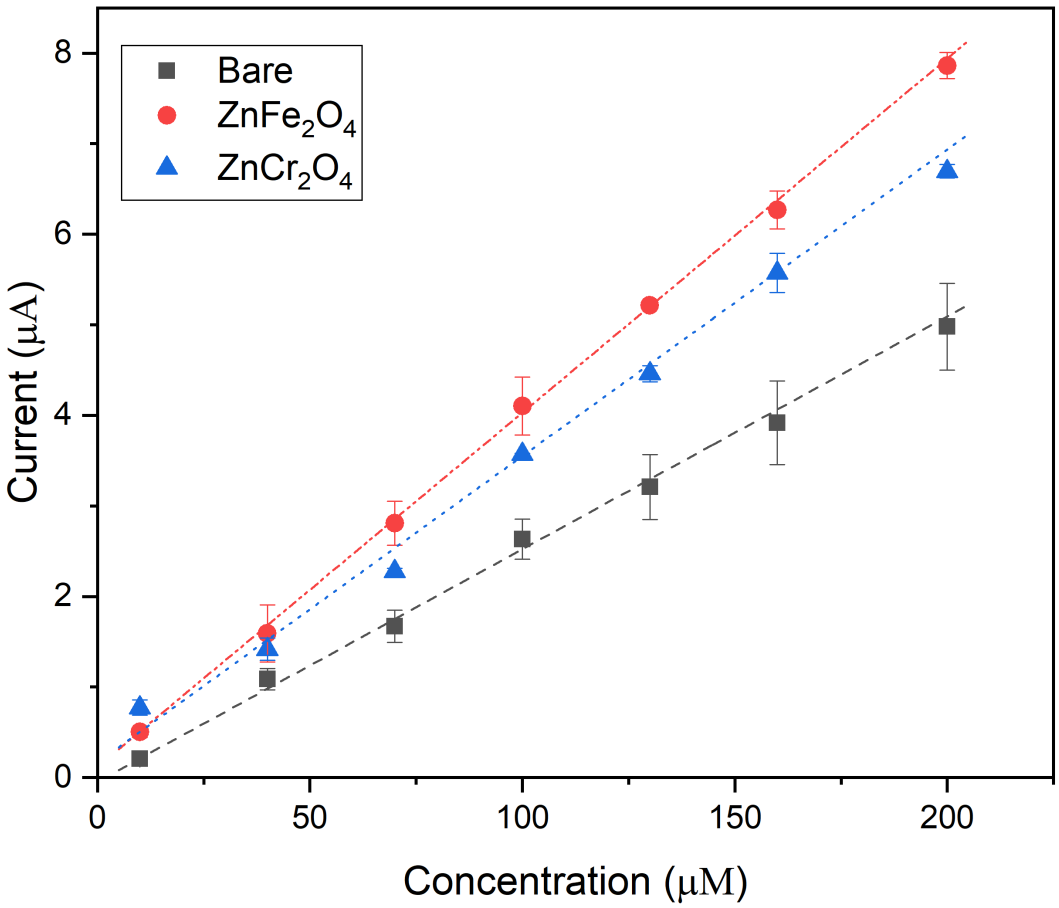

Fig. 6.16 Calibration of Bare, $ZnFe_2O_4$, and $ZnCr_2O_4$ sensors at different concentrations of 5-FU in 0.1 M PB at pH 7.

6.2.2 Electrochemical sensing of Etoposide

Electrochemical sensing of the anti-cancer drug etoposide is performed by using zinc ferrite and zinc chromite-based sensors. Figure 6.17 presents the cyclic voltammograms of bare, $ZnFe_2O_4$, and $ZnCr_2O_4$ sensors with etoposide concentration of 100 μM in 0.1M PB solution around pH 7. The drug etoposide undergoes multiple oxidations marked as 1, 2, and 3 representing the first, second, and third oxidation. We observe three oxidation peaks of etoposide for all the three sensors with first

and second oxidation occuring with two reduction peaks as a quasi-reversible one electron process while the third oxidation peak is the result of the product oxidation formed by the previous oxidation processess. To understand the electrochemical performance of the sensors usually the first oxidation peak is analysed [192]. It is observed that the bare sensor has the first oxidation peak around 161 ± 9 mV with an oxidation peak current of 0.21 ± 0.02 μA. $ZnFe_2O_4$, $ZnCr_2O_4$ sensors produced the oxidation peaks around 103 ± 1, 104 ± 2 mV with an oxidation current of 0.29 ± 0.02, 0.43 ± 0.04 μA, respectively. The oxidation potential is reduced about 55 mV and the current is increased by 38% and 105% with $ZnFe_2O_4$ and $ZnCr_2O_4$ sensors.

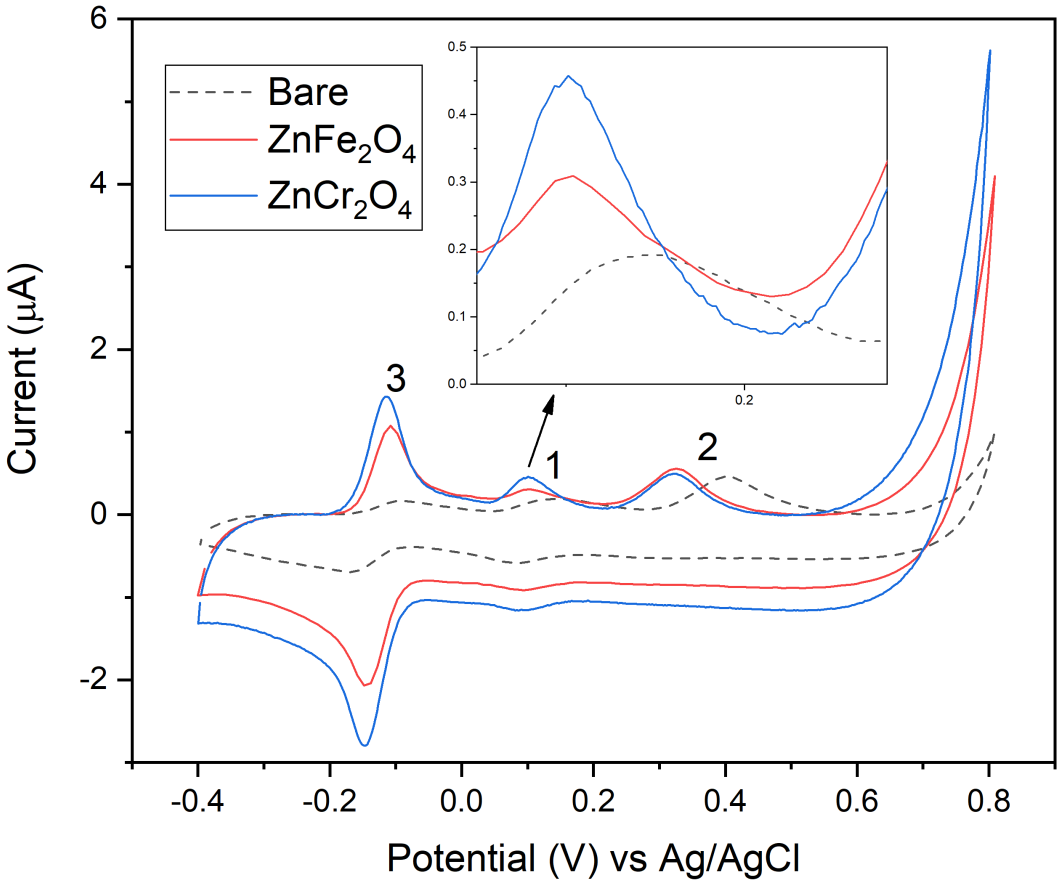

Fig. 6.17 Cyclic voltammograms for Bare, $ZnFe_2O_4$, and $ZnFe_2O_4$ sensors with 100 μM Etoposide in 0.1 M PB at pH 7.

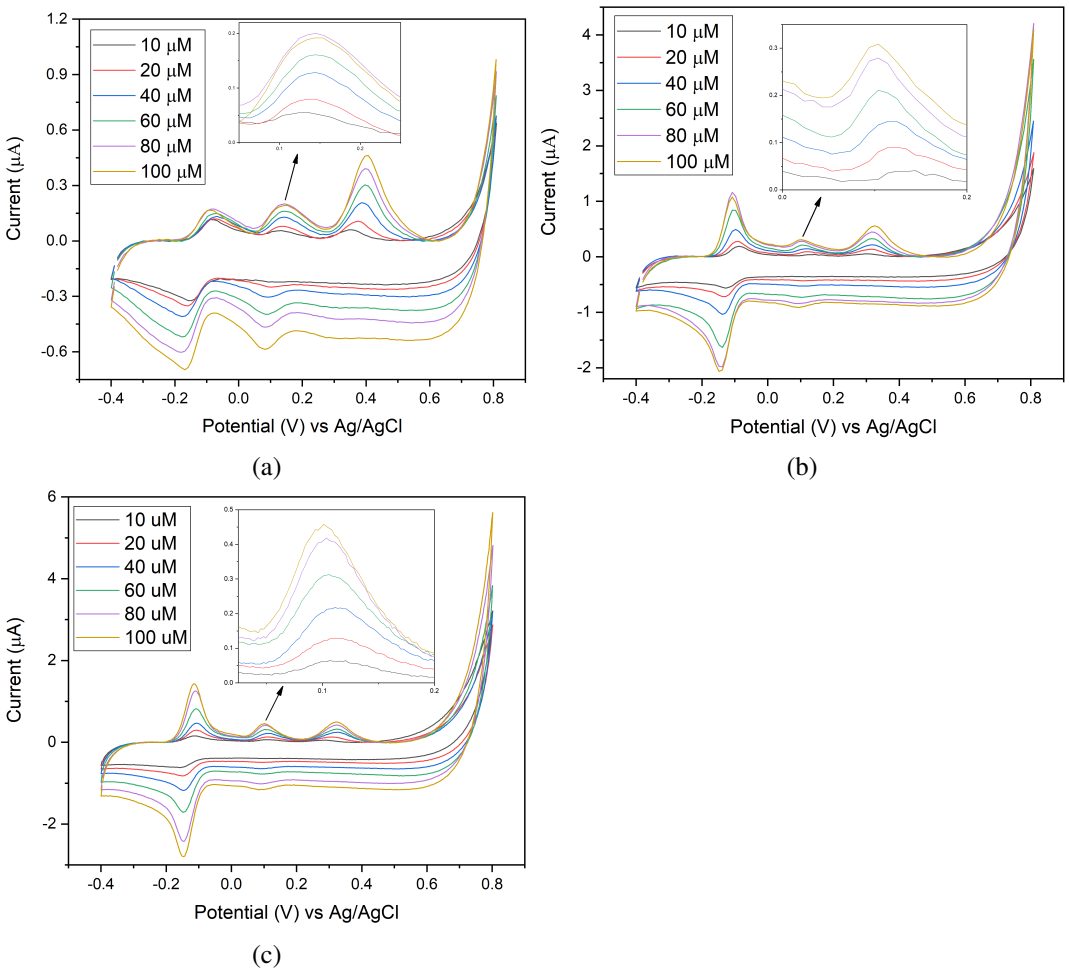

Fig. 6.18 Cyclic voltammograms of a) bare, b) $ZnFe_2O_4$, and c) $ZnCr_2O_4$ sensors at different concentrations of Etoposide in 0.1 M PB at pH 7.

The sensors are calibrated by conducting CV at different etoposide concentrations of 10, 20, 40, 60, 80, and 100 μM, the cyclic voltammograms are reported in Figure 6.18. The oxidation peak current is increased as the concentration of the drug increased as expected. The sensors are calibrated similarly as before with an average oxidation current of three sensors of each type and the calibration of bare, $ZnFe_2O_4$, and $ZnCr_2O_4$ sensors are displayed in Figure 6.19. The sensitivities of the three sensors are reported in Table 6.3. The sensitivity of the bare sensor is increased by 37% and 117% using $ZnFe_2O_4$, and $ZnCr_2O_4$ sensors, respectively. The calculated LOD of the three sensors characterized is higher than 10 μM which is higher than the concentration of Etoposide successfully detected in the current work, therefore the calculation of the LOD doesn't hold well in this case. To improve the

limit of detection of the sensors the sensitivity of the sensors should be improved further meaning the level of oxidation peak compared to the baseline or the standard deviation of the blank measurements should be reduced with less instrumental or background noise.

Table 6.3 Sensitivity and LOD of different sensors in 5-FU and Etoposide sensing.

Sensor	Sensitivity (nA/μM) Drug : 5-FU	Sensitivity (nA/μM) Drug : Etoposide
Bare	25.7 ± 0.6	2.08 ± 0.15
$ZnFe_2O_4$	39.1 ± 0.2	2.84 ± 0.14
$ZnCr_2O_4$	33.8 ± 2.1	4.51 ± 0.28

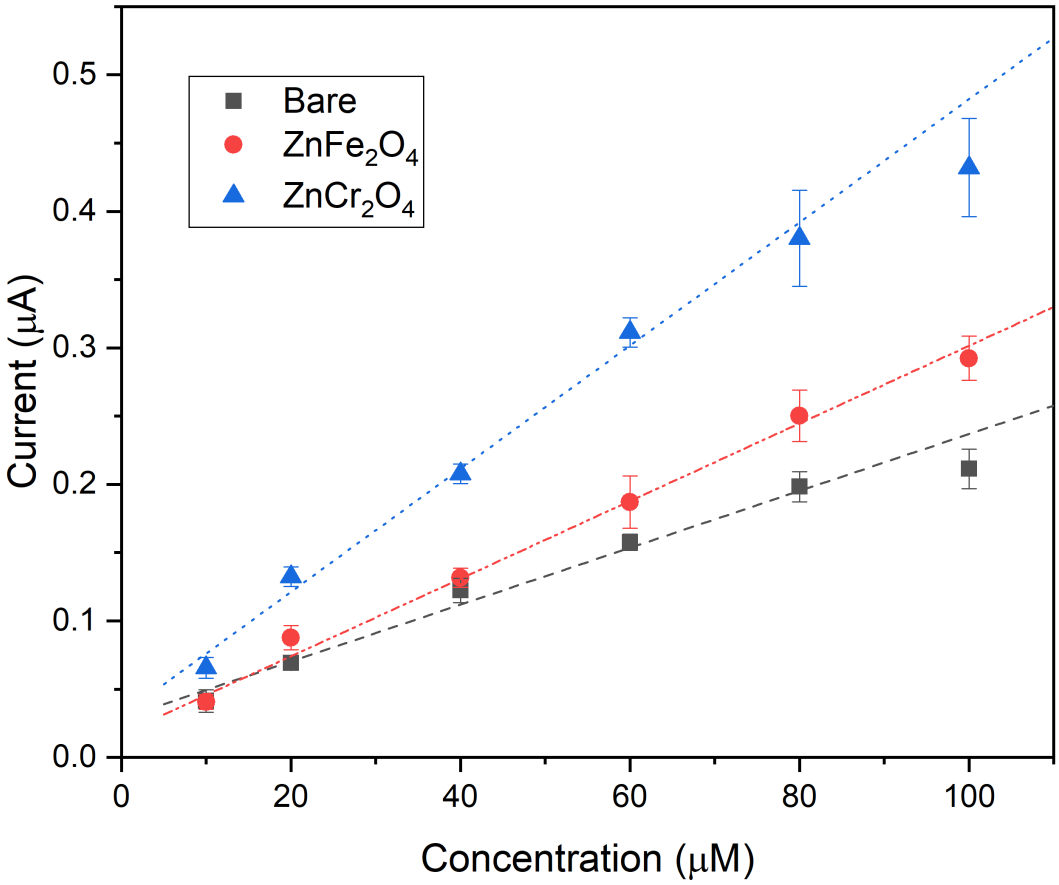

Fig. 6.19 Calibration of Bare, $ZnFe_2O_4$, and $ZnCr_2O_4$ sensors with different concentrations of Etoposide in 0.1 M PB at pH 7.

6.3 Original Contributions IV

This work focused on the potential applications of normal spinel $ZnFe_2O_4$ and $ZnCr_2O_4$. Zinc ferrite as a potential sensing material for dissolved oxygen and pH is studied by chronoamperometric and potentiometric techniques. Different aspects of the electrochemical sensors such as the role of counter electrode in DO sensing and stability issues of pH sensors are criticized. Application of normal spinel zinc ferrite and zinc chromite nanomaterials in electrohcemical sensing of anti cancer drugs such as 5-FU and etoposide is investigated by presenting the sensitivity and limit of detection.

The first part of the work in this chapter was successfully presented at the 245th Electrochemical Society (ECS) Meetings in San Francisco, California, USA. The abstract is published in ECS Meeting Abstracts by IOP publishing with title "Enhancing Electrochemical Sensor Performance: Studies of Electrodes Tailored with ZnO/$ZnFe_2O_4$ Nanoparticles". The abstract can be found at the following url:

https://iopscience.iop.org/article/10.1149/MA2024-01472627mtgabs/meta

From the first part of the work a manuscript titled "Comparative study of ZnO and $ZnFe_2O_4$ micro and nanoparticle-based screen-printed electrodes in pH sensing" has been accepted for publication in IEEE Sensors Journal.

A manuscript based on the second part of the work on anti-cancer drugs sensing is in progress and it will be submitted to a journal for publication in the near future.

Chapter 7

Conclusions

In this project I investigated the different aspects of nanomaterials that can influence the electrochemical sensing performance such as crystal structure, particle size, shape, composition, and ionic size. Spinel crystal structure was selected since it is easy to produce a uniform spherical shaped nanoparticles so that orientation of the particles would not play role in electrochemical reactions. Spinel crystal structural composition is easy to be manipulated without effecting the overall crystal structure by partially or fully substituting the cations present in the system.

In this study, a simple and cost-effective auto combustion synthesis (dry-technique) is employed to synthesize different sets of spinel nanomaterials. Four sets of materials were synthesized in order to study the effect of crystal structure, composition, trivalent cation, ionic size, and double interface (tuing also the band gap) in electrochemical sensing. The first set is with $ZnFe_2O_4$ (zinc ferrite), $NiFe_2O_4$(nickel ferrite) and combination of both ($Zn_xNi_{1-x}Fe_2O_4$). In total six materials ($Zn_xNi_{1-x}Fe_2O_4$) (x = 0, 0.2, 0.4, 0.6, 0.8, 1) are synthesized. In the second set, Fe(III) is partially and full substituted by Cr(III) to produce $ZnCr_xFe_{2-x}O_4$ (x = 0, 0.25, 0.5, 0.75, 1, 2) materials. Third set is zinc ferrite in which Fe(III) was partially and fully substituted with higher ionic sized cation of Bi(III) to synthesize $ZnBi_xFe_{2-x}O_4$ (x = 0, 0.25, 0.5, 0.75, 1, 2) materials. In the last set, $ZnFe_2O_4$, ZnO, and ZnO/$ZnFe_2O_4$ materials were investigated. The four sets of materials to understand the effect of crystal structure, trivalent cation with similar ionic size, higher ionic size on electron transfer at the electrochemical interface, and to study some applications of zinc ferrite along with ZnO, respectively.

The materials are characterized by FESEM technique to study the morphological features and confirmed that all the synthesized materials have close to a spherical shape except the materials where Fe(III) is replaced by Bi(III) and ZnO. The former set of materials have shown to be in two different shapes while the latter has shown pyramided shaped particles. The synthesis is successful in producing nanomaterials (particle size < 100 nm) in all sets except the materials with Bi(III) and ZnO which have sub-micrometer and micrometer sized particles, respectively. XRD patterns of the materials confirmed the spinel phase along with secondary phases of ZnO, Fe_2O_3, and graphite for the first, second, and fourth sets of materials, which are possibly due to the reactants and the use of a graphite reactor in the synthesis. The XRD patterns of the third set of materials have shown two separate spinel phases of $ZnFe_2O_4$ and $ZnBi_2O_4$ which is unexpected because the goal was to produce a single spinel phase with Bi(III) replacing Fe(III) in the crystal structure of $ZnFe_2O_4$. This might be due to the mismatch in the ionic sizes of Fe and Bi, or adopted synthesis method is not so suitable to produce this set of materials due to the drawbacks of the synthesis such as weak control over the growth kinetics of the particles.

Raman spectroscopy showed the expected Raman bands for all materials, all possible Raman bands were assigned for different bands and thoroughly discussed. XPS full survey measurements confirmed the presence of no contamination elements in the composition of materials except the adventitious carbon. High resolution spectra of the different elements in each material verified the valence state of the elements and their occupancy is in either tetrahedral or octahedral crystal sites. All elements have their respective stable oxidation (valence) states of either '+2' or '+3' with oxygen being '-2'. XPS valence band spectra was used to estimate the maximum of the valence band (E_V) edge for all materials. DR UV-vis spectra is interpreted by Tauc plot method to estimate the energy gap (E_g) of all the materials. Using the valence band edge maximum, E_V and energy gap, E_g values the position of the conduction band edge minimum E_C (= E_g+E_V) is computed. It is found that the energy gap has been significantly affected by the size, composition, and even minor changes in ionic radius significantly altered the energy bandgap.

Throughout this study, commercially available screen-printed electrodes, consisting of a carbon working electrode, a carbon counter electrode, and an Ag/AgCl reference electrode, were used as reference electrochemical sensors. The carbon working electrode surface is modified by using the spinel nanomaterials solution in butanol with drop-casting technique. The sensors are initially characterized by

cyclic voltammetry in 1 mM paracetamol in 0.1 M PB solution at pH 7. Spinel-based sensors exhibited approximately double sensitivity, lower peak-to-peak potential, and higher rate constants with respect to the bare carbon sensor. $ZnFe_2O_4$ demonstrated the highest sensitivity and kinetic rate constant for paracetamol detection, with normal spinel structures (zinc ferrite, zinc chromite, and combination of both) outperforming inverse spinels and mixed spinel variants in all electrochemical parameters due to higher electrical conductivity. Conduction occurs via electron hopping in normal spinel, whereas hole hopping dominates in inverse spinel structures. Despite this, all spinel-based sensors (zinc ferrite, nickel ferrite, zinc chromite, and mixed spinels) showed higher sensitivity and rate constant values, performing significantly better than the bare carbon sensor. In the third part, all $ZnBi_xFe_{2-x}O_4$ spinel-based sensors exhibited improved sensitivity compared to bare sensor, with lower ΔE_p and higher kinetic rate constants. However, direct comparisons are challenging due to variations in morphology and particle size across materials, ranging from nano to sub-micrometer scale.

The electron transfer process is further elucidated at the electrochemical interface by matching the band edges of the multi-metal oxide semiconductors with the redox potentials of paracetamol, emphasizing the importance of bandgap in electron transfer. Only zinc ferrite has proved to be involved in the direct electron transfer at the interface. Additionally, the critical role of surface energy levels in the electron transfer process is discussed, showing a strong correlation between predicted electron transfer via conduction band edge (E_C) and key electrochemical sensing metrics.

Some potential applications of normal spinel oxides are explored as the final part of the project. $ZnFe_2O_4$ has shown a very good sensitivity in dissolved oxygen sensing compared to the bare carbon sensor with Pt wire as a counter electrode. As a pH sensor, $ZnFe_2O_4$ has performed much better by improving the sensitivity of the carbon sensor taking towards Nernstian behaviour in the physiological pH range from 4 to 8.5. $ZnFe_2O_4$ and $ZnCr_2O_4$ are also used as sensing materials in electrochemical detection of anti-cancer drugs, namely 5-FU and etoposide. $ZnFe_2O_4$ has the higher sensitivity in the detection of 5-FU while $ZnCr_2O_4$ has shown better sensitivity for etoposide compared to the carbon sensor. It is possible due to the differences in the drugs composition, aromatic ring structure, and the possible oxidation states of Zn and Cr.

Electrochemical sensing performance is influenced by numerous nanomaterial parameters, including size, crystallinity, specific surface area, active electrode area, amount of deposition, dissolution behavior, nanoparticle orientation, semiconductor band gap, and surface coating. Achieving uniformity across these parameters to allow direct comparison between sensors is a challenging task. To further enhance the performance of these materials, alternative synthesis methods such as sol-gel, hydrothermal with surfactants could reduce particle aggregation and improve size control. Surface coatings may stabilize the nanoparticles and reduce agglomeration while achieving size control through bottom-up approaches. It will be interesting to study further the materials chemical and physical properties by employing more advanced characterization techniques and usage of high energy synchrotron radiation facilities. In-operando electrochemical sensing will help much better in understanding the interface between the metal oxide nanomaterials and the analyte of interest. Some electrochemical in-operando techniques are available but the techniques usually monitor the changes in the analyte while it will be very interesting to study the changes on the electrode surface by monitoring the changes in the sensing materials and their transitional states to understand the reactivity of the metal oxides. Developing such techniques to understand the solid/liquid interface is a cumbersome task.

Rather than these challenges, this research work can provide ways for rational design of electrochemical sensors for drug sensing in biomedical applications using mutli-metal oxide nanomaterials. It will be very interesting to revisit the Marcus theory to also include the structural and morphological parameters of electrode material in heterogeneous electron transfer to generalize the equation of kinetic rate constant through theoretical modelling and experimental verification.

7.1 List of Publications

7.1.1 Journal Papers

1. **Mallikarjun Madagalam**, Francesca Rodino, Mattia Bartoli, Alberto Tagliaferro, and Sandro Carrara. "*$ZnFe_2O_4$, $ZnCr_2O_4$, and $CuFe_2O_4$ Nanoparticle-based Screen-printed Electrodes for Electrochemical Sensing of Anti-Cancer Drugs: 5-Fluorouracil and Etoposide*". Manuscript in progress.

2. **Mallikarjun Madagalam**, Filippo Franceschini, Catarina Fernandes, Michele Rosito, Elisa Padovano, Sandro Carrara, Alberto Tagliaferro, Mattia Bartoli, and Irene Taurino. "*Comparative study of ZnO and $ZnFe_2O_4$ micro and nanoparticle-based screen-printed electrodes in pH sensing*". IEEE Sensors Journal, DOI : 10.1109/JSEN.2025.3543243.

3. **Mallikarjun Madagalam**, Michele Rosito, Nicola Blangetti, Marco Etzi, Elisa Padovano, Barbara Bonelli, Sandro Carrara, Alberto Tagliaferro, and Mattia Bartoli. "*Effect of Cr substitution in $ZnFe_2O_4$ nanoparticles on the electron transfer at electrochemical interfaces*". Materials Research Bulletin, Volume 183, March 2025, 113191.

4. **Mallikarjun Madagalam**, Mattia Bartoli, and Alberto Tagliaferro. "*A Short Overview on Graphene and Graphene-Related Materials for Electrochemical Gas Sensing*". Materials 17 (2), 303, 2024.

5. **Mallikarjun Madagalam**, Michele Rosito, Nicola Blangetti, Marco Etzi, Elisa Padovano, Barbara Bonelli, Sandro Carrara, Alberto Tagliaferro, and Mattia Bartoli. "*Unveiling the effect of Bi in $ZnFe_2O_4$ nanoparticles in electrochemical sensors*". Applied Surface Science, page 160870, 2024.

6. **Mallikarjun Madagalam**, Mattia Bartoli, Michele Rosito, Nicola Blangetti, Marco Etzi Coller Pascuzzi, Elisa Padovano, Barbara Bonelli, Sandro Carrara, and Alberto Tagliaferro. "*Unraveling the Effect of the Chemical and Structural Composition of $Zn_xNi_{1-x}Fe_2O_4$ on the Electron Transfer at the Electrochemical Interface*". Small Structures, 4(12):2300163, 2023.

7.1.2 Conference Proceedings

1. **Mallikarjun Madagalam**, Mattia Bartoli, Catarina Fernandes, Michele Rosito, Elisa Padovano, Irene Taurino, Sandro Carrara, and Alberto Tagliaferro. "*Enhancing Electrochemical Sensor Performance: Studies of Electrodes Tailored with ZnO/$ZnFe_2O_4$ Nanoparticles*". Electrochemical Society Meeting Abstracts 245, 2627-2627, CA, USA, 2024.

2. **Mallikarjun Madagalam**, Mattia Bartoli, Sandro Carrara, and Alberto Tagliaferro. "*$ZnCr_{2-x}Fe_xO_4$ Nanoparticles-Modified Electrochemical Sensors: A*

Comparative Study". In 2023 IEEE SENSORS, pages 01–04, Vienna, Austria, 2023.

3. **Mallikarjun Madagalam**, Mattia Bartoli, Sandro Carrara, and Alberto Tagliaferro. "*$ZnM_xFe_{2-x}O_4$ (M = Cr, Bi) Nanoparticles-modified electrochemical sensors: Effect on sensitivity and first-order kinetic rate constant*". In 2023 IEEE BIOSENSORS, pages 01–04, London, UK, 2023.

4. **Mallikarjun Madagalam**, Michele Rosito, Mattia Bartoli, Elisa Padovano, Sandro Carrara, and Alberto Tagliaferro. "*Ferrite-based Nanoparticles: Synthesis, Characterization, and Non-enzymatic Electrochemical Sensing Applications*". In 2022 Nanoinnovation, Rome, Italy, 2022.

References

[1] A.J Bard and L.R Faulkner. *Electrochemical Methods Fundamentals and Applications*. Wiley, Newyork, NY, USA, 2001.

[2] Joseph Wang, Jianmin Lu, Samo B. Hocevar, Percio A. M. Farias, and Bozidar Ogorevc. Bismuth-Coated Carbon Electrodes for Anodic Stripping Voltammetry. *Analytical Chemistry*, 72(14):3218–3222, July 2000. doi: 10.1021/ac000108x.

[3] Mallikarjun Madagalam, Mattia Bartoli, Michele Rosito, Nicola Blangetti, Marco Etzi Coller Pascuzzi, Elisa Padovano, Barbara Bonelli, Sandro Carrara, and Alberto Tagliaferro. Unraveling the Effect of the Chemical and Structural Composition of Zn x Ni1-x Fe2O4 on the Electron Transfer at the Electrochemical Interface. *Small Structures*, 4(12):2300163, 2023.

[4] Mallikarjun Madagalam, Mattia Bartoli, Alberto Tagliaferro, and Sandro Carrara. Bismuth-Nanocomposites Modified SPCEs for Non-Enzymatic Electrochemical Sensors. *IEEE Sensors Journal*, 21(9):11155–11162, 2021.

[5] Mallikarjun Madagalam, Michele Rosito, Nicola Blangetti, Marco Etzi, Elisa Padovano, Barbara Bonelli, Sandro Carrara, Alberto Tagliaferro, and Mattia Bartoli. Unveiling the effect of Bi in ZnFe2O4 nanoparticles in electrochemical sensors. *Applied Surface Science*, page 160870, 2024.

[6] Carrara Sandro. *Bio/CMOS Interfaces and Co-Design*. Springer, New York, NY, USA, 2013.

[7] Stephen Fletcher. The theory of electron transfer. *Journal of Solid State Electrochemistry*, 14(5):705–739, May 2010.

[8] Christopher C. Page, Christopher C. Moser, Xiaoxi Chen, and P. Leslie Dutton. Natural engineering principles of electron tunnelling in biological oxidation–reduction. *Nature*, 402(6757):47–52, November 1999.

[9] Brian O'Regan and Michael Grätzel. A low-cost, high-efficiency solar cell based on dye-sensitized colloidal TiO2 films. *Nature*, 353(6346):737–740, October 1991.

[10] Henry Taube. Electron transfer between metal complexes: Retrospective. *Science*, 226(4678):1028–1036, 1984.

[11] W. B. Lewis, C. D. Coryell, and J. W. Irvine. S 81. The electron transfer (exchange) between cobaltous and cobaltic amine complexes. *Journal of The Chemical Society*, (0):S386–S392, 1949.

[12] R. A. Marcus. On the theory of oxidation-reduction reactions involving electron transfer. I. *The Journal of Chemical Physics*, 24(5):966–978, May 1956.

[13] R. A. Marcus. On the theory of oxidation-reduction reactions involving electron transfer. II. Applications to data on the rates of isotopic exchange reactions. *The Journal of Chemical Physics*, 26(4):867–871, April 1957.

[14] Christopher C. Moser, Tammer A. Farid, Sarah E. Chobot, and P. Leslie Dutton. Electron tunneling chains of mitochondria. *Biochimica et Biophysica Acta (BBA) - Bioenergetics*, 1757(9):1096–1109, 2006. Mitochondria: from Molecular Insight to Physiology and Pathology.

[15] Christian Joachim and Mark A. Ratner. Molecular electronics: Some views on transport junctions and beyond. *Proceedings of the National Academy of Sciences*, 102(25):8801–8808, 2005.

[16] Jochen Blumberger. Recent Advances in the Theory and Molecular Simulation of Biological Electron Transfer Reactions. *Chemical Reviews*, 115(20):11191–11238, October 2015. doi: 10.1021/acs.chemrev.5b00298.

[17] Harry B. Gray and Jay R. Winkler. Electron flow through metalloproteins. *Biochimica et Biophysica Acta (BBA) - Bioenergetics*, 1797(9):1563–1572, 2010.

[18] Henry Taube, Howard Myers, and Ronald L Rich. Observations on the mechanism of electron transfer in Solution1. *Journal of the American Chemical Society*, 75(16):4118–4119, 1953.

[19] Henry Taube and Howard Myers. Evidence for a bridged activated complex for electron transfer reactions. *Journal of the American Chemical Society*, 76(8):2103–2111, 1954.

[20] John Edward Brough Randles. Kinetics of rapid electrode reactions. *Discussions of the faraday society*, 1:11–19, 1947.

[21] J. E. B. Randles. Kinetics of rapid electrode reactions. Part 2.—Rate constants and activation energies of electrode reactions. *Transactions of the Faraday Society*, 48(0):828–832, 1952.

[22] MG Evans. Thermodynamical treatment of transition state. *Transactions of the Faraday Society*, 34:49–57, 1938.

[23] Stephen Fletcher. A non-Marcus model for electrostatic fluctuations in long range electron transfer. *Journal of Solid State Electrochemistry*, 11:965–969, 2007.

[24] Rudolph A Marcus. Electron transfer reactions in chemistry. Theory and experiment. In *Protein Electron Transfer*, pages 249–272. Garland Science, 2020.

[25] RA Marcus. Free energy of nonequilibrium polarization systems. 4. A formalism based on the nonequilibrium dielectric displacement. *The Journal of Physical Chemistry*, 98(29):7170–7174, 1994.

[26] M Tachiya and S Murata. New explanation for the lack of the inverted region in charge separation reactions. *The Journal of Physical Chemistry*, 96(21):8441–8444, 1992.

[27] M Tachiya. Generalization of the Marcus equation for the electron-transfer rate. *The Journal of Physical Chemistry*, 97(22):5911–5916, 1993.

[28] M Tachiya and Maria Hilczer. Solvent effect on the electron transfer rate and the energy gap law. In *AIP Conference Proceedings*, volume 298, pages 447–459. American Institute of Physics, 1994.

[29] Noémie Elgrishi, Kelley J. Rountree, Brian D. McCarthy, Eric S. Rountree, Thomas T. Eisenhart, and Jillian L. Dempsey. A Practical Beginner's Guide to Cyclic Voltammetry. *Journal of Chemical Education*, 95(2):197–206, February 2018. doi: 10.1021/acs.jchemed.7b00361.

[30] David C Grahame. The electrical double layer and the theory of electrocapillarity. *Chemical reviews*, 41(3):441–501, 1947.

[31] David Leonard Chapman. Li. a contribution to the theory of electrocapillarity. *The London, Edinburgh, and Dublin philosophical magazine and journal of science*, 25(148):475–481, 1913.

[32] Joseph Wang. Electrochemical biosensors: towards point-of-care cancer diagnostics. *Biosensors and Bioelectronics*, 21(10):1887–1892, 2006.

[33] Adolph Fick. V. on liquid diffusion. *The London, Edinburgh, and Dublin Philosophical Magazine and Journal of Science*, 10(63):30–39, 1855.

[34] Walther Nernst. Zur kinetik der in lösung befindlichen körper. *Zeitschrift für physikalische Chemie*, 2(1):613–637, 1888.

[35] Max Planck. Ueber die erregung von electricität und wärme in electrolyten. *Annalen der Physik*, 275(2):161–186, 1890.

[36] Veniamin Grigorevich Levich and Charles W Tobias. Physicochemical hydrodynamics. *Journal of The Electrochemical Society*, 110(11):251C, 1963.

[37] John Newman and Nitash P Balsara. *Electrochemical systems*. John Wiley & Sons, 2021.

[38] E. Laviron. General expression of the linear potential sweep voltammogram in the case of diffusionless electrochemical systems. *Journal of Electroanalytical Chemistry and Interfacial Electrochemistry*, 101(1):19–28, 1979.

[39] Joseph Wang, Joseph Wang, and Kim Rogers. *Electrochemical sensors for environmental monitoring: a review of recent technology*. US Environmental Protection Agency, Office of Research and Development . . . , 1995.

[40] Yan Zeng, Zhihong Zhu, Dan Du, and Yuehe Lin. Nanomaterial-based electrochemical biosensors for food safety. *Journal of Electroanalytical Chemistry*, 781:147–154, 2016.

[41] Venkatesh S Manikandan, BalRam Adhikari, and Aicheng Chen. Nanomaterial based electrochemical sensors for the safety and quality control of food and beverages. *Analyst*, 143(19):4537–4554, 2018.

[42] Jitendra N Tiwari, Varun Vij, K Christian Kemp, and Kwang S Kim. Engineered carbon-nanomaterial-based electrochemical sensors for biomolecules. *ACS nano*, 10(1):46–80, 2016.

[43] Rodrigo Segura, Jaime Pizarro, Karina Díaz, Alan Placencio, Fernando Godoy, Eduardo Pino, and Francisco Recio. Development of electrochemical sensors for the determination of selenium using gold nanoparticles modified electrodes. *Sensors and Actuators B: Chemical*, 220:263–269, 2015.

[44] Devi D Liana, Burkhard Raguse, Lech Wieczorek, Geoff R Baxter, Kyloon Chuah, J Justin Gooding, and Edith Chow. Sintered gold nanoparticles as an electrode material for paper-based electrochemical sensors. *RSC advances*, 3(23):8683–8691, 2013.

[45] Stelian Lupu, Cecilia Lete, Mariana Marin, Nicolae Totir, and Paul Catalin Balaure. Electrochemical sensors based on platinum electrodes modified with hybrid inorganic–organic coatings for determination of 4-nitrophenol and dopamine. *Electrochimica Acta*, 54(7):1932–1938, 2009.

[46] Gabriela C Mauruto de Oliveira, Jefferson Henrique de Souza Carvalho, Laís Canniatti Brazaca, Nirton Cristi Silva Vieira, and Bruno Campos Janegitz. Flexible platinum electrodes as electrochemical sensor and immunosensor for parkinson's disease biomarkers. *Biosensors and Bioelectronics*, 152:112016, 2020.

[47] Moustafa Zahran, Ziad Khalifa, Magdy A-H Zahran, and Magdi Abdel Azzem. Recent advances in silver nanoparticle-based electrochemical sensors for determining organic pollutants in water: A review. *Materials Advances*, 2(22):7350–7365, 2021.

[48] Siriwan Nantaphol, Orawon Chailapakul, and Weena Siangproh. Sensitive and selective electrochemical sensor using silver nanoparticles modified glassy carbon electrode for determination of cholesterol in bovine serum. *Sensors and Actuators B: Chemical*, 207:193–198, 2015.

[49] Xuanyu Yang, Pengpeng Qiu, Jianping Yang, Yuchi Fan, Lianjun Wang, Wan Jiang, Xiaowei Cheng, Yonghui Deng, and Wei Luo. Mesoporous materials–based electrochemical biosensors from enzymatic to nonenzymatic. *Small*, 17(9):1904022, 2021.

[50] Chandran Karunakaran, Thangamuthu Madasamy, and Niroj Kumar Sethy. Enzymatic biosensors. In *Biosensors and bioelectronics*, pages 133–204. Elsevier, 2015.

[51] Howard D Goldberg, Richard B Brown, Dong P Liu, and Mark E Meyerhoff. Screen printing: a technology for the batch fabrication of integrated chemical-sensor arrays. *Sensors and Actuators B: Chemical*, 21(3):171–183, 1994.

[52] Dino A Pardo, Ghassan E Jabbour, and Nasser Peyghambarian. Application of screen printing in the fabrication of organic light-emitting devices. *Advanced Materials*, 12(17):1249–1252, 2000.

[53] Mallikarjun Madagalam, Paolo La Torraca, Mukhtar Ahmed, Ali Douaki, Ignacio Merino SanchezFayos, Nitzan Cohen, Luisa Petti, and Paolo Lugli. Screen-Printed Flexible Circular and Rectangular Silver Spirals for Planar Electrodynamic Loudspeakers: A Comparative Study of Pressure Frequency Response. In *2022 6th IEEE Electron Devices Technology & Manufacturing Conference (EDTM)*, pages 104–106, 2022.

[54] Jerónimo Agrisuelas, María-Isabel González-Sánchez, and Edelmira Valero. Hydrogen peroxide sensor based on in situ grown pt nanoparticles from waste screen-printed electrodes. *Sensors and Actuators B: Chemical*, 249:499–505, 2017.

[55] Paolo Bollella, Giovanni Fusco, Daniela Stevar, Lo Gorton, Roland Ludwig, Su Ma, Harry Boer, Anu Koivula, Cristina Tortolini, Gabriele Favero, et al. A glucose/oxygen enzymatic fuel cell based on gold nanoparticles modified graphene screen-printed electrode. proof-of-concept in human saliva. *Sensors and Actuators B: Chemical*, 256:921–930, 2018.

[56] Somayeh Tajik, Hadi Beitollahi, Mohammad Reza Aflatoonian, Bita Mohtat, Behnaz Aflatoonian, Iran Sheikh Shoaie, Mohammad A Khalilzadeh, Marzieh Ziasistani, Kaiqiang Zhang, Ho Won Jang, et al. Fabrication of magnetic iron oxide-supported copper oxide nanoparticles (fe 3 o 4/cuo): Modified screen-printed electrode for electrochemical studies and detection of desipramine. *RSC advances*, 10(26):15171–15178, 2020.

[57] Óscar A Loaiza, Elena Jubete, Estibalitz Ochoteco, German Cabañero, Hans Grande, and Javier Rodríguez. Gold coated ferric oxide nanoparticles based disposable magnetic genosensors for the detection of dna hybridization processes. *Biosensors and Bioelectronics*, 26(5):2194–2200, 2011.

[58] Richard S Nicholson. Theory and application of cyclic voltammetry for measurement of electrode reaction kinetics. *Analytical chemistry*, 37(11):1351–1355, 1965.

[59] Eric Bakker and Ernö Pretsch. Potentiometric sensors for trace-level analysis. *TrAC Trends in Analytical Chemistry*, 24(3):199–207, 2005.

[60] Tanji Yin and Wei Qin. Applications of nanomaterials in potentiometric sensors. *TrAC Trends in Analytical Chemistry*, 51:79–86, 2013.

[61] Libu Manjakkal, Saoirse Dervin, and Ravinder Dahiya. Flexible potentiometric ph sensors for wearable systems. *RSC advances*, 10(15):8594–8617, 2020.

[62] Martín Lucas Zamora, Juan Martín Domínguez, Ricardo Matias Trujillo, Carla Belen Goy, Maria Alejandra Sanchez, and Rossana Elena Madrid. Potentiometric textile-based ph sensor. *Sensors and Actuators B: Chemical*, 260:601–608, 2018.

[63] Mark-Jan Spijkman, Jakob J Brondijk, Tom CT Geuns, Edsger CP Smits, Tobias Cramer, Francesco Zerbetto, Pablo Stoliar, Fabio Biscarini, Paul WM Blom, and Dago M de Leeuw. Dual-gate organic field-effect transistors as potentiometric sensors in aqueous solution. *Advanced Functional Materials*, 20(6):898–905, 2010.

[64] Jiri Janata. Potentiometric microsensors. *Chemical Reviews*, 90(5):691–703, 1990.

[65] Shengli Cao, Peng Sun, Gang Xiao, Qiang Tang, Xinyue Sun, Hongyu Zhao, Shuang Zhao, Huibin Lu, and Zhao Yue. Isfet-based sensors for (bio) chemical applications: A review. *Electrochemical Science Advances*, 3(4):e2100207, 2023.

[66] Haiyuan Zhang, Zhaoxia Ji, Tian Xia, Huan Meng, Cecile Low-Kam, Rong Liu, Suman Pokhrel, Sijie Lin, Xiang Wang, Yu-Pei Liao, Meiying Wang, Linjiang Li, Robert Rallo, Robert Damoiseaux, Donatello Telesca, Lutz Mädler, Yoram Cohen, Jeffrey I. Zink, and Andre E. Nel. Use of Metal Oxide Nanoparticle Band Gap To Develop a Predictive Paradigm for Oxidative Stress and Acute Pulmonary Inflammation. *ACS Nano*, 6(5):4349–4368, May 2012. doi: 10.1021/nn3010087.

[67] Changzhou Yuan, Hao Bin Wu, Yi Xie, and Xiong Wen (David) Lou. Mixed Transition-Metal Oxides: Design, Synthesis, and Energy-Related Applications. *Angewandte Chemie International Edition*, 53(6):1488–1504, 2014.

[68] Jiheon Kim, Wonjae Ko, Ji Mun Yoo, Vinod K. Paidi, Ho Yeon Jang, Michael Shepit, Jongmin Lee, Hogeun Chang, Hyeon Seok Lee, Jinwoung Jo, Byung Hyo Kim, Sung-Pyo Cho, Johan van Lierop, Dokyoon Kim, Kug-Seung Lee, Seoin Back, Yung-Eun Sung, and Taeghwan Hyeon. Structural Insights into Multi-Metal Spinel Oxide Nanoparticles for Boosting Oxygen Reduction Electrocatalysis. *Advanced Materials*, 34(8):2107868, 2022.

[69] Haegyeom Kim, Dong-Hwa Seo, Hyungsub Kim, Inchul Park, Jihyun Hong, Kyu-Young Park, and Kisuk Kang. Multicomponent Effects on the Crystal Structures and Electrochemical Properties of Spinel-Structured M3O4 (M = Fe, Mn, Co) Anodes in Lithium Rechargeable Batteries. *Chemistry of Materials*, 24(4):720–725, February 2012. doi: 10.1021/cm2036794.

[70] Kyureon Lee, Daniel A. Ruddy, Gordana Dukovic, and Nathan R. Neale. Synthesis, optical, and photocatalytic properties of cobalt mixed-metal spinel oxides Co(Al1-xGax)2O4. *J. Mater. Chem. A*, 3(15):8115–8122, 2015.

[71] Mallikarjun Madagalam, Mattia Bartoli, Michele Rosito, Nicola Blangetti, Marco Etzi, Elisa Padovano, Barbara Bonelli, Sandro Carrara, and Alberto Tagliaferro. Effect of cr substitution in znfe2o4 nanoparticles on the electron transfer at electrochemical interfaces. *Materials Research Bulletin*, 183:113191, 2025.

[72] Kebede Keterew Kefeni and Bhekie B. Mamba. Photocatalytic application of spinel ferrite nanoparticles and nanocomposites in wastewater treatment: Review. *Sustainable Materials and Technologies*, 23:e00140, 2020.

[73] Roshidah Rusdi, Azilah Abd Rahman, Nor Sabirin Mohamed, Norashikin Kamarudin, and Norlida Kamarulzaman. Preparation and band gap energies of zno nanotubes, nanorods and spherical nanostructures. *Powder Technology*, 210(1):18–22, 2011.

[74] Sarunya Klubnuan, Sumetha Suwanboon, and Pongsaton Amornpitoksuk. Effects of optical band gap energy, band tail energy and particle shape on photocatalytic activities of different zno nanostructures prepared by a hydrothermal method. *Optical Materials*, 53:134–141, 2016.

[75] Anand Kumar Tripathi, Manish Kumar Singh, Mohan Chandra Mathpal, Sheo Kumar Mishra, and Arvind Agarwal. Study of structural transformation in tio2 nanoparticles and its optical properties. *Journal of Alloys and Compounds*, 549:114–120, 2013.

[76] K Madhusudan Reddy, Sunkara V Manorama, and A Ramachandra Reddy. Bandgap studies on anatase titanium dioxide nanoparticles. *Materials Chemistry and Physics*, 78(1):239–245, 2003.

[77] Rekha Dom, A Sadananda Chary, Raghavan Subasri, Neha Y Hebalkar, and Pramod H Borse. Solar hydrogen generation from spinel znfe2o4 photocatalyst: effect of synthesis methods. *International Journal of Energy Research*, 39(10):1378–1390, 2015.

[78] Sheetal Sharma, Vishal Dutta, Pankaj Raizada, Ahmad Hosseini-Bandegharaei, Vijay Thakur, Van-Huy Nguyen, Quyet VanLe, Pardeep Singh, et al. An overview of heterojunctioned znfe2o4 photocatalyst for enhanced oxidative water purification. *Journal of Environmental Chemical Engineering*, 9(5):105812, 2021.

[79] M Benlembarek, N Salhi, R Benrabaa, A Boulahouache, and M Trari. Enhanced photocatalytic performance of nife2o4 nanoparticle spinel for hydrogen production. *International Journal of Hydrogen Energy*, 48(24):8932–8942, 2023.

[80] JT Adeleke, T Theivasanthi, M Thiruppathi, M Swaminathan, T Akomolafe, and AB Alabi. Photocatalytic degradation of methylene blue by zno/nife2o4 nanoparticles. *Applied surface science*, 455:195–200, 2018.

[81] Te-Yu Wei, Chun-Hung Chen, Hsing-Chi Chien, Shih-Yuan Lu, and Chi-Chang Hu. A cost-effective supercapacitor material of ultrahigh specific capacitances: spinel nickel cobaltite aerogels from an epoxide-driven sol–gel process. *Advanced materials*, 3(22):347–351, 2010.

[82] Linfeng Hu, Limin Wu, Meiyong Liao, Xinhua Hu, and Xiaosheng Fang. Electrical transport properties of large, individual nico2o4 nanoplates. *Advanced Functional Materials*, 22(5):998–1004, 2012.

[83] Josué M. Gonçalves, Lucas V. de Faria, Amanda B. Nascimento, Rafael L. Germscheidt, Santanu Patra, Lucas P. Hernández-Saravia, Juliano A. Bonacin, Rodrigo A. A. Munoz, and Lúcio Angnes. Sensing performances of spinel ferrites MFe2O4 (M = Mg, Ni, Co, Mn, Cu and Zn) based electrochemical sensors: A review. *Analytica Chimica Acta*, 1233:340362, 2022.

[84] MRNS Hamdani, RN Singh, and PJIJES Chartier. Co3o4 and co-based spinel oxides bifunctional oxygen electrodes. *International journal of electrochemical science*, 5(4):556–577, 2010.

[85] Tian Xia, Michael Kovochich, Monty Liong, Lutz Mädler, Benjamin Gilbert, Haibin Shi, Joanne I. Yeh, Jeffrey I. Zink, and Andre E. Nel. Comparison of the Mechanism of Toxicity of Zinc Oxide and Cerium Oxide Nanoparticles Based on Dissolution and Oxidative Stress Properties. *ACS Nano*, 2(10):2121–2134, October 2008. doi: 10.1021/nn800511k.

[86] Kasper Wenderich, Johannes Noack, Anne Kärgel, Annette Trunschke, and Guido Mul. Effect of temperature and ph on phase transformations in citric acid mediated hydrothermal growth of tungsten oxide. *European Journal of Inorganic Chemistry*, 2018(7):917–923, 2018.

[87] MA Camacho-López, E Haro-Poniatowski, Luis Lartundo-Rojas, J Livage, and CM Julien. Amorphous–crystalline transition studied in hydrated moo3. *Materials Science and Engineering: B*, 135(2):88–94, 2006.

[88] Ala Manohar, V. Vijayakanth, S. V. Prabhakar Vattikuti, and Ki Hyeon Kim. A mini-review on AFe2O4 (A = Zn, Mg, Mn, Co, Cu, and Ni) nanoparticles: Photocatalytic, magnetic hyperthermia and cytotoxicity study. *Materials Chemistry and Physics*, 286:126117, 2022.

[89] Mallikarjun Madagalam, Mattia Bartoli, Sandro Carrara, and Alberto Tagliaferro. ZnCr2-xFexO4 Nanoparticles-Modified Electrochemical Sensors: A Comparative Study. In *2023 IEEE SENSORS*, pages 01–04, 2023.

[90] Shiyin Li, Xuyan Zhou, Gang Fang, Guoqiang Xie, Xingjun Liu, Xi Lin, and Hua-Jun Qiu. Multicomponent Spinel Metal Oxide Nanocomposites as High-Performance Bifunctional Catalysts in Zn–Air Batteries. *ACS Applied Energy Materials*, 3(8):7710–7718, August 2020. doi: 10.1021/acsaem.0c01121.

[91] Xia Yang, Hongtao Xue, Qingdan Yang, Ruo Yuan, Wenpei Kang, and Chun-Sing Lee. Preparation of porous ZnO/ZnFe2O4 composite from metal organic frameworks and its applications for lithium ion batteries. *Chemical Engineering Journal*, 308:340–346, 2017.

[92] Xun Zhao, Lei Mao, Qihui Cheng, Jie Li, Fangfang Liao, Guiyuan Yang, Li Xie, Chenglan Zhao, and Lingyun Chen. Two-dimensional Spinel Structured Co-based Materials for High Performance Supercapacitors: A Critical Review. *Chemical Engineering Journal*, 387:124081, 2020.

[93] Dawei Chu, Fengbo Li, Xiumei Song, Huiyuan Ma, Lichao Tan, Haijun Pang, Xinming Wang, Dongxuan Guo, and Boxin Xiao. A novel dual-tasking hollow cube NiFe2O4-NiCo-LDH@rGO hierarchical material for high preformance supercapacitor and glucose sensor. *Journal of Colloid and Interface Science*, 568:130–138, 2020.

[94] Fulan Zhong, Zhiyu Li, Yu Luo, Chongqi Chen, Chen Zhou, Li Lin, Guohui Cai, Chaktong Au, and Lilong Jiang. Geometric structure distribution and oxidation state demand of cations in spinel NixFe1-xCo2O4 composite cathodes for solid oxide fuel cells. *Chemical Engineering Journal*, 425:131822, 2021.

[95] A. C. F. M. Costa, E. Tortella, M. R. Morelli, M. Kaufman, and R. H. G. A. Kiminami. Effect of heating conditions during combustion synthesis on the characteristics of Ni0.5Zn0.5Fe2O4 nanopowders. *Journal of Materials Science*, 37(17):3569–3572, September 2002.

[96] F Albert Cotton, Geoffrey Wilkinson, Carlos A Murillo, and Manfred Bochmann. *Advanced inorganic chemistry*. John Wiley & Sons, 1999.

[97] Jeremy K Burdett, Geoffrey D Price, and Sarah L Price. Role of the crystal-field theory in determining the structures of spinels. *Journal of the american chemical society*, 104(1):92–95, 1982.

[98] Ashwini Kumar, Poorva Sharma, and Dinesh Varshney. Structural, vibrational and dielectric study of Ni doped spinel Co ferrites: Co1-xNixFe2O4 (x=0.0, 0.5, 1.0). *Ceramics International*, 40(8, Part B):12855–12860, 2014.

[99] Andris Šutka and Kārlis A. Gross. Spinel ferrite oxide semiconductor gas sensors. *Sensors and Actuators B: Chemical*, 222:95–105, 2016.

[100] K. N. Nithyayini, M. N. K. Harish, and K. L. Nagashree. Electrochemical detection of nitrite at NiFe2O4 nanoparticles synthesised by solvent deficient method. *Electrochimica Acta*, 317:701–710, 2019.

[101] Kogularasu Sakthivel, Govindasamy Mani, Shen-Ming Chen, Shih-Hao Lin, Akilarasan Muthumariappan, and Veerappan Mani. A novel synthesis of non-aggregated spinel nickel ferrite nanosheets for developing non-enzymatic reactive oxygen species sensor in biological samples. *Journal of Electroanalytical Chemistry*, 820:161–167, 2018.

[102] Ganesh Kesavan, Nandini Nataraj, Shen-Ming Chen, and Li-Heng Lin. Hydrothermal synthesis of nife 2 o 4 nanoparticles as an efficient electrocatalyst for the electrochemical detection of bisphenol a. *New Journal of Chemistry*, 44(19):7698–7707, 2020.

[103] Shohreh Jahani. Evaluation of the usefulness of an electrochemical sensor in detecting ascorbic acid using a graphite screen-printed electrode modified with nife2o4 nanoparticles. *Anal. Bioanal. Electrochem*, 10(6):739–750, 2018.

[104] Mohadeseh Safaei, Hadi Beitollahi, and Masoud Reza Shishehbore. Modified screen printed electrode for selective determination of folic acid. *Acta Chim. Slov*, 66:777–783, 2019.

[105] Hadi Beitollahi, Somayeh Tajik, Mohammad Reza Aflatoonian, and Asghar Makarem. Nife2o4 nanoparticles modified screen printed electrode for simultaneous determination of serotonin and norepinephrine. *Anal. Bioanal. Electrochem*, 10:1399, 2018.

[106] Maedeh Nouri, Mostafa Rahimnejad, Ghasem Najafpour, and Ali Akbar Moghadamnia. Simultaneous voltammetric determination of rizatriptan and acetaminophen using a carbon paste electrode modified with nife 2 o 4 nanoparticles. *Microchimica Acta*, 187:1–9, 2020.

[107] Nguyen Thi Vuong Hoan, Nguyen Ngoc Minh, Nguyen Thi Lieu, Nguyen Van Thang, Vo Thang Nguyen, Nguyen Thi Thanh Tu, Tran Thanh Tam Toan, Nguyen Hoang Tuan, Duong Quang Nhan, Ho Van Minh Hai, et al. Nickel ferrite: synthesis and application for voltammetric determination of uric acid. *Journal of Nanoparticle Research*, 23:1–14, 2021.

[108] A. Sutka, J. Zavickis, G. Mezinskis, D. Jakovlevs, and J. Barloti. Ethanol monitoring by ZnFe2O4 thin film obtained by spray pyrolysis. *Sensors and Actuators B: Chemical*, 176:330–334, 2013.

[109] Yarong Huang, Ying Tang, Shichong Xu, Ming Feng, Yongsheng Yu, Weiwei Yang, and Haibo Li. A highly sensitive sensor based on ordered mesoporous ZnFe2O4 for electrochemical detection of dopamine. *Analytica Chimica Acta*, 1096:26–33, 2020.

[110] Changchun Fan, Long Chen, Rong Jiang, Jiahui Ye, Haoquan Li, Yulin Shi, Yun Luo, Gang Wang, Juan Hou, and Xuhong Guo. ZnFe2O4 Nanoparticles for Electrochemical Determination of Trace Hg(II), Pb(II), Cu(II), and Glucose. *ACS Applied Nano Materials*, 4(4):4026–4036, April 2021. doi: 10.1021/acsanm.1c00379.

[111] Somayeh Tajik, Mohadeseh Safaei, and Hadi Beitollahi. A sensitive voltammetric sertraline nanosensor based on znfe2o4 nanoparticles modified screen printed electrode. *Measurement*, 143:51–57, 2019.

[112] Hadi Beitollahi, Mohadeseh Safaei, and Somayeh Tajik. Screen-printed electrode modified with znfe2o4 nanoparticles for detection of acetylcholine. *Electroanalysis*, 31(6):1135–1140, 2019.

[113] Nguyen Tuan Anh, Nguyen Van Quy, Ong Van Hoang, Ngo Xuan Dinh, Anh-Tuan Le, et al. An on-site and portable electrochemical sensing platform based on spinel zinc ferrite nanoparticles for the quality control of paracetamol in pharmaceutical samples. *Nanoscale Advances*, 6(1):256–267, 2024.

[114] Somayeh Tajik, Hadi Beitollahi, Fariba Garkani Nejad, Mohadeseh Safaei, and Peyman Mohammadzadeh Jahani. Electrochemical sensing of sudan i using the modified graphite screen-printed electrode. *International Journal of Environmental Analytical Chemistry*, 102(7):1477–1490, 2022.

[115] Salih Zeki Bas, Nese Yuncu, Keziban Atacan, and Mustafa Ozmen. A comparison study of mfe2o4 (m: Ni, cu, zn)-reduced graphene oxide nanocomposite for electrochemical detection of bisphenol a. *Electrochimica Acta*, 386:138519, 2021.

[116] Karim Asadpour-Zeynali and Fariba Mollarasouli. Novel electrochemical biosensor based on pvp capped cofe2o4@ cdse core-shell nanoparticles modified electrode for ultra-trace level determination of rifampicin by square wave adsorptive stripping voltammetry. *Biosensors and Bioelectronics*, 92:509–516, 2017.

[117] Juan Liu, Jian Shen, Mian Li, and Li-Ping Guo. A high-efficient amperometric hydrazine sensor based on novel electrospun cofe2o4 spinel nanofibers. *Chinese Chemical Letters*, 26(12):1478–1484, 2015.

[118] Weiwei Yang, Yongsheng Yu, Ying Tang, Keyun Li, Zheng Zhao, Menggang Li, Geping Yin, Haibo Li, and Shouheng Sun. Enhancing electrochemical detection of dopamine via dumbbell-like fept–fe 3 o 4 nanoparticles. *Nanoscale*, 9(3):1022–1027, 2017.

[119] XiuBo Xie, Baolei Wang, Yukun Wang, Cui Ni, Xueqin Sun, and Wei Du. Spinel structured mfe2o4 (m= fe, co, ni, mn, zn) and their composites for microwave absorption: A review. *Chemical Engineering Journal*, 428:131160, 2022.

[120] S-H Feng and G-H Li. Hydrothermal and solvothermal syntheses. In *Modern inorganic synthetic chemistry*, pages 73–104. Elsevier, 2017.

[121] Farzana Majid, Javeria Rauf, Sadia Ata, Ismat Bibi, Abdul Malik, Sobhy M Ibrahim, Adnan Ali, and Munawar Iqbal. Synthesis and characterization of nife2o4 ferrite: Sol–gel and hydrothermal synthesis routes effect on magnetic, structural and dielectric characteristics. *Materials Chemistry and Physics*, 258:123888, 2021.

[122] Morassa Hassannezhad, Morteza Hosseini, Mohammad Reza Ganjali, and Majid Arvand. Electrochemical sensor based on carbon nanotubes decorated with znfe2o4 nanoparticles incorporated carbon paste electrode for determination of metoclopramide and indomethacin. *ChemistrySelect*, 4(25):7616–7626, 2019.

[123] Ekjot Singh, Manpreet Kaur, and Sucheta Sharma. Structural tuning of ctab@ mgfe2o4 nanocomposite as peroxidase mimic for h2o2 and glucose sensing. *Materials Chemistry and Physics*, 271:124851, 2021.

[124] Mian Li, Yueping Xiong, Xiaotian Liu, Xiangjie Bo, Yufan Zhang, Ce Han, and Liping Guo. Facile synthesis of electrospun mfe 2 o 4 (m= co, ni, cu, mn) spinel nanofibers with excellent electrocatalytic properties for oxygen evolution and hydrogen peroxide reduction. *Nanoscale*, 7(19):8920–8930, 2015.

[125] George P Sutton and Oscar Biblarz. *Rocket propulsion elements*. John Wiley & Sons, 2011.

[126] Kenneth K Kuo and Martin J Chiaverini. *Fundamentals of hybrid rocket combustion and propulsion*. American Institute of Aeronautics and Astronautics, 2007.

[127] Stephen R Turns et al. *Introduction to combustion*, volume 287. McGraw-Hill Companies New York, NY, USA, 1996.

[128] Irvin Glassman, Richard A Yetter, and Nick G Glumac. *Combustion*. Academic press, 2014.

[129] KC Patil. Advanced ceramics: combustion synthesis and properties. *Bulletin of Materials Science*, 16:533–541, 1993.

[130] JJ Kingsley and KC Patil. A novel combustion process for the synthesis of fine particle α-alumina and related oxide materials. *Materials letters*, 6(11-12):427–432, 1988.

[131] Zeynep Karcıoğlu Karakaş, Recep Boncukcuoğlu, İbrahim Hakkı Karakaş, and Mehmet Ertuğrul. The effects of heat treatment on the synthesis of nickel ferrite (NiFe2O4) nanoparticles using the microwave assisted combustion method. *Journal of Magnetism and Magnetic Materials*, 374:298–306, 2015.

[132] Anju Ahlawat and V. G. Sathe. Raman study of NiFe2O4 nanoparticles, bulk and films: Effect of laser power. *Journal of Raman Spectroscopy*, 42(5):1087–1094, 2011.

[133] Fran Nekvapil, Alexander Bunge, Teodora Radu, Simona Cinta Pinzaru, and Rodica Turcu. Raman spectra tell us so much more: Raman features and saturation magnetization for efficient analysis of manganese zinc ferrite nanoparticles. *Journal of Raman Spectroscopy*, 51(6):959–968, 2020.

[134] Olga N. Shebanova and Peter Lazor. Raman study of magnetite (Fe3O4): Laser-induced thermal effects and oxidation. *Journal of Raman Spectroscopy*, 34(11):845–852, 2003.

[135] María Rivero, Adolfo del Campo, Álvaro Mayoral, Eva Mazario, Jorge Sánchez-Marcos, and Alexandra Muñoz-Bonilla. Synthesis and structural characterization of ZnxFe3-xO4 ferrite nanoparticles obtained by an electrochemical method. *RSC Adv.*, 6(46):40067–40076, 2016.

[136] Jitendra Pal Singh, R. C. Srivastava, H. M. Agrawal, and Ravi Kumar. Micro-Raman investigation of nanosized zinc ferrite: Effect of crystallite size and fluence of irradiation. *Journal of Raman Spectroscopy*, 42(7):1510–1517, 2011.

[137] M. Šćepanović, M. Grujić-Brojčin, K. Vojisavljević, S. Bernik, and T. Srećković. Raman study of structural disorder in ZnO nanopowders. *Journal of Raman Spectroscopy*, 41(9):914–921, 2010.

[138] M. A. Shilpa Amulya, H. P. Nagaswarupa, M. R. Anil Kumar, C. R. Ravikumar, S. C. Prashantha, and K. B. Kusuma. Sonochemical synthesis of NiFe2O4 nanoparticles: Characterization and their photocatalytic and electrochemical applications. *Applied Surface Science Advances*, 1:100023, 2020.

[139] K. Dileep, B. Loukya, N. Pachauri, A. Gupta, and R. Datta. Probing optical band gaps at the nanoscale in NiFe2O4 and CoFe2O4 epitaxial films by high resolution electron energy loss spectroscopy. *Journal of Applied Physics*, 116(10):103505, September 2014.

[140] Manish Srivastava, Animesh K. Ojha, S. Chaubey, and A. Materny. Synthesis and optical characterization of nanocrystalline NiFe2O4 structures. *Journal of Alloys and Compounds*, 481(1):515–519, 2009.

[141] M. Sultan and R. Singh. Structural and optical properties of RF-sputtered ZnFe2O4 thin films. *Journal of Physics D: Applied Physics*, 42(11):115306, May 2009.

[142] B. Delley and E. F. Steigmeier. Size dependence of band gaps in silicon nanostructures. *Applied Physics Letters*, 67(16):2370–2372, October 1995.

[143] Kuo-Feng Lin, Hsin-Ming Cheng, Hsu-Cheng Hsu, Li-Jiaun Lin, and Wen-Feng Hsieh. Band gap variation of size-controlled ZnO quantum dots synthesized by sol–gel method. *Chemical Physics Letters*, 409(4):208–211, 2005.

[144] Sarunya Klubnuan, Sumetha Suwanboon, and Pongsaton Amornpitoksuk. Effects of optical band gap energy, band tail energy and particle shape on photocatalytic activities of different ZnO nanostructures prepared by a hydrothermal method. *Optical Materials*, 53:134–141, 2016.

[145] Kalpana Panwar, Shailja Tiwari, Komal Bapna, N. L. Heda, R. J. Choudhary, D. M. Phase, and B. L. Ahuja. The effect of Cr substitution on the structural, electronic and magnetic properties of pulsed laser deposited NiFe2O4 thin films. *Journal of Magnetism and Magnetic Materials*, 421:25–30, 2017.

[146] NS McIntyre and MG Cook. X-ray photoelectron studies on some oxides and hydroxides of cobalt, nickel, and copper. *Analytical chemistry*, 47(13):2208–2213, 1975.

[147] Marco Etzi Coller Pascuzzi, Alex J. W. Man, Andrey Goryachev, Jan P. Hofmann, and Emiel J. M. Hensen. Investigation of the stability of NiFe-(oxy)hydroxide anodes in alkaline water electrolysis under industrially relevant conditions. *Catal. Sci. Technol.*, 10(16):5593–5601, 2020.

[148] Chaker Fares, Marko J. Tadjer, Jeffrey Woodward, Neeraj Nepal, Michael A. Mastro, Charles R. Eddy, Fan Ren, and Stephen J. Pearton. Valence and Conduction Band Offsets for InN and III-Nitride Ternary Alloys on (-201) Bulk β-Ga2O3. *ECS Journal of Solid State Science and Technology*, 8(7):Q3154, March 2019.

[149] Trevor J. Davies, Craig E. Banks, and Richard G. Compton. Voltammetry at spatially heterogeneous electrodes. *Journal of Solid State Electrochemistry*, 9(12):797–808, December 2005.

[150] Ian Streeter, Gregory G. Wildgoose, Lidong Shao, and Richard G. Compton. Cyclic voltammetry on electrode surfaces covered with porous layers: An analysis of electron transfer kinetics at single-walled carbon nanotube modified electrodes. *Sensors and Actuators B: Chemical*, 133(2):462–466, 2008.

[151] J.M Savéant. *Elements of Molecular and Biomolecular Electrochemistry*. John Wiley & Sons, Hoboken, NJ, 2006.

[152] Sang Jun Yoon, Seung Hun Lee, Keu Hong Kim, and Kyung Soo Ahn. Electrical and magnetic properties of spinel ZnCr2-xFexO4 ($0 \leq x \leq 1.0$). *Materials Chemistry and Physics*, 73(2):330–334, 2002.

[153] N. Ponpandian, P. Balaya, and A. Narayanasamy. Electrical conductivity and dielectric behaviour of nanocrystalline NiFe2O4 spinel. *Journal of Physics: Condensed Matter*, 14(12):3221, March 2002.

[154] D. R. Patil and B. K. Chougule. Effect of copper substitution on electrical and magnetic properties of NiFe2O4 ferrite. *Materials Chemistry and Physics*, 117(1):35–40, 2009.

[155] Cecilia Solís, Simona Somacescu, Elena Palafox, María Balaguer, and José M. Serra. Particular Transport Properties of NiFe2O4 Thin Films at High Temperatures. *The Journal of Physical Chemistry C*, 118(42):24266–24273, October 2014. doi: 10.1021/jp506938k.

[156] Liufang Yang, Yongan Xie, Heyun Zhao, Xinghui Wu, and Yude Wang. Preparation and gas-sensing properties of NiFe2O4 semiconductor materials. *Solid-State Electronics*, 49(6):1029–1033, 2005.

[157] Asif Ali Tahir and K. G. Upul Wijayantha. Photoelectrochemical water splitting at nanostructured ZnFe2O4 electrodes. *Journal of Photochemistry and Photobiology A: Chemistry*, 216(2):119–125, 2010. 3rd International Conference on Semiconductor Photochemistry, SP-3, April, 2010, Glasgow UK.

[158] Enrico Burello and Andrew P. Worth. QSAR modeling of nanomaterials. *WIREs Nanomedicine and Nanobiotechnology*, 3(3):298–306, 2011.

[159] Enrico Burello and Andrew P. Worth. A theoretical framework for predicting the oxidative stress potential of oxide nanoparticles. *Nanotoxicology*, 5(2):228–235, June 2011. doi: 10.3109/17435390.2010.502980.

[160] L. Gomathi Devi and B. Narasimha Murthy. Characterization of Mo Doped TiO2 and its Enhanced Photo Catalytic Activity Under Visible Light. *Catalysis Letters*, 125(3):320–330, October 2008.

[161] Serena Esposito, Nicoletta Ditaranto, Gianfranco Dell'Agli, Roberto Nasi, Paola Rivolo, and Barbara Bonelli. Effective Inclusion of Sizable Amounts of Mo within TiO2 Nanoparticles Can Be Obtained by Reverse Micelle Sol–Gel Synthesis. *ACS Omega*, 6(8):5379–5388, March 2021. doi: 10.1021/acsomega.0c05552.

[162] Mélanie Auffan, Jérôme Rose, Mark R. Wiesner, and Jean-Yves Bottero. Chemical stability of metallic nanoparticles: A parameter controlling their potential cellular toxicity in vitro. *Environmental Pollution*, 157(4):1127–1133, 2009. The Behaviour and Effects of Nanoparticles in the Environment.

[163] Tian Xia, Yan Zhao, Tina Sager, Saji George, Suman Pokhrel, Ning Li, David Schoenfeld, Huan Meng, Sijie Lin, Xiang Wang, Meiying Wang, Zhaoxia Ji, Jeffrey I. Zink, Lutz Mädler, Vincent Castranova, Shuo Lin, and Andre E. Nel. Decreased Dissolution of ZnO by Iron Doping Yields Nanoparticles with Reduced Toxicity in the Rodent Lung and Zebrafish Embryos. *ACS Nano*, 5(2):1223–1235, February 2011. doi: 10.1021/nn1028482.

[164] K Kugimiya and H Steinfink. Influence of crystal radii and electronegativities on the crystallization of AB2X4 stoichiometries. *Inorganic Chemistry*, 7(9):1762–1770, 1968.

[165] Christian Suchomski, Christian Reitz, Kirstin Brezesinski, Célia Tavares de Sousa, Marcus Rohnke, Ken-ichi Iimura, Joao Pedro Esteves de Araujo, and Torsten Brezesinski. Structural, Optical, and Magnetic Properties of Highly Ordered Mesoporous MCr2O4 and MCr2–xFexO4 (M = Co, Zn) Spinel Thin Films with Uniform 15 nm Diameter Pores and Tunable Nanocrystalline Domain Sizes. *Chemistry of Materials*, 24(1):155–165, January 2012. doi: 10.1021/cm2026043.

[166] L. H. Ahrens. The use of ionization potentials Part 1. Ionic radii of the elements. *Geochimica et Cosmochimica Acta*, 2(3):155–169, 1952.

[167] Wei Huang, Weiwei Zha, Donglin Zhao, and Shaojie Feng. The effect of active oxygen species in nano-ZnCr2O4 spinel oxides for methane catalytic combustion. *Solid State Sciences*, 87:49–52, 2019.

[168] Jianfeng Xu, W. Ji, X. B. Wang, H. Shu, Z. X. Shen, and S. H. Tang. Temperature dependence of the raman scattering spectra of Zn/ZnO nanoparticles. *Journal of Raman Spectroscopy*, 29(7):613–615, 1998.

[169] Jing (Jeanne) Yang, Wayde N. Martens, and Ray L. Frost. Transition of chromium oxyhydroxide nanomaterials to chromium oxide: A hot-stage Raman spectroscopic study. *Journal of Raman Spectroscopy*, 42(5):1142–1146, 2011.

[170] Mark C. Biesinger, Brad P. Payne, Andrew P. Grosvenor, Leo W. M. Lau, Andrea R. Gerson, and Roger St C. Smart. Resolving surface chemical states in XPS analysis of first row transition metals, oxides and hydroxides: Cr, Mn, Fe, Co and Ni. *Applied Surface Science*, 257(7):2717–2730, 2011.

[171] O. M. Hemeda and M. M. Barakat. Effect of hopping rate and jump length of hopping electrons on the conductivity and dielectric properties of Co–Cd ferrite. *Journal of Magnetism and Magnetic Materials*, 223(2):127–132, 2001.

[172] Ch Kant, J. Deisenhofer, V. Tsurkan, and A. Loidl. Magnetic susceptibility of the frustrated spinels ZnCr2O4, MgCr2O4 and CdCr2O4. *Journal of Physics: Conference Series*, 200(3):032032, January 2010.

[173] S. Ayyappan, S. Philip Raja, C. Venkateswaran, John Philip, and Baldev Raj. Room temperature ferromagnetism in vacuum annealed ZnFe2O4 nanoparticles. *Applied Physics Letters*, 96(14):143106, April 2010.

[174] Osmary Depablos-Rivera, Ana Martínez, and Sandra E. Rodil. Interpretation of the Raman spectra of bismuth oxide thin films presenting different crystallographic phases. *Journal of Alloys and Compounds*, 853:157245, 2021.

[175] Ameerah N. Alqarni, Emre Cevik, M. A. Almessiere, A. Baykal, M. A. Gondal, M. Hassan, Ayhan Bozkurt, Arfa Iqbal, Sarah M. Asiri, and Y. Slimani. Fabrication of Bismuth-doped Co–Ni spinel ferrite electrodes for

enhanced cyclic performance in asymmetric supercapacitors. *Journal of Physics and Chemistry of Solids*, 177:111288, 2023.

[176] Kun Xu, Luo Zhang, Andy Godfrey, Dongsheng Song, Wenlong Si, Yawen Zhao, Yi Liu, Yiheng Rao, Huaiwu Zhang, Heng-An Zhou, Wanjun Jiang, Wenbin Wang, Zhiying Cheng, and Jing Zhu. Atomic-scale insights into quantum-order parameters in bismuth-doped iron garnet. *Proceedings of the National Academy of Sciences*, 118(20):e2101106118, 2021.

[177] Marco Etzi Coller Pascuzzi, Matthijs van Velzen, Jan P. Hofmann, and Emiel J. M. Hensen. On the Stability of Co3O4 Oxygen Evolution Electrocatalysts in Acid. *ChemCatChem*, 13(1):459–467, 2021.

[178] Nguyen Thi Mai Tho, Dang Nguyen Nha Khanh, Nguyen Quoc Thang, Yong-Ill Lee, and Nguyen Thi Kim Phuong. Novel reduced graphene oxide/ZnBi2O4 hybrid photocatalyst for visible light degradation of 2,4-dichlorophenoxyacetic acid. *Environmental Science and Pollution Research*, 27(10):11127–11137, April 2020.

[179] Syahidah Nurani Zulkifli, Herlina Abdul Rahim, and Woei-Jye Lau. Detection of contaminants in water supply: A review on state-of-the-art monitoring technologies and their applications. *Sensors and Actuators B: Chemical*, 255:2657–2689, 2018.

[180] Imanol Tubia, Karthik Prasad, Eva Pérez-Lorenzo, Cristina Abadín, Miren Zumárraga, Iñigo Oyanguren, Francisca Barbero, Jacobo Paredes, and Sergio Arana. Beverage spoilage yeast detection methods and control technologies: A review of brettanomyces. *International journal of food microbiology*, 283:65–76, 2018.

[181] Shaoqi Zhang, Tao Liu, Zhenyu Chu, and Wanqin Jin. Recent progress on nanomaterial-based electrochemical dissolved oxygen sensors. *Chinese Journal of Chemical Engineering*, 2024.

[182] Dora Neina. The role of soil ph in plant nutrition and soil remediation. *Applied and environmental soil science*, 2019(1):5794869, 2019.

[183] S Andersson and S Ingvar Nilsson. Influence of ph and temperature on microbial activity, substrate availability of soil-solution bacteria and leaching of dissolved organic carbon in a mor humus. *Soil Biology and Biochemistry*, 33(9):1181–1191, 2001.

[184] Libu Manjakkal, Dorota Szwagierczak, and Ravinder Dahiya. Metal oxides based electrochemical ph sensors: Current progress and future perspectives. *Progress in Materials Science*, 109:100635, 2020.

[185] C-N Tsai, Jung-Chuan Chou, Tai-Ping Sun, and Shen-Kan Hsiung. Study on the time-dependent slow response of the tin oxide ph electrode. *IEEE Sensors Journal*, 6(5):1243–1249, 2006.

[186] Daniel B Longley, D Paul Harkin, and Patrick G Johnston. 5-fluorouracil: mechanisms of action and clinical strategies. *Nature reviews cancer*, 3(5):330–338, 2003.

[187] Abdollah Fallah Shojaei, Khalil Tabatabaeian, Shahryar Shakeri, and Fatemeh Karimi. A novel 5-fluorouracile anticancer drug sensor based on znfe2o4 magnetic nanoparticles ionic liquids carbon paste electrode. *Sensors and Actuators B: Chemical*, 230:607–614, 2016.

[188] Nehal Salahuddin, Salem Awad, and Mona Elfiky. Vanillin-crosslinked chitosan/zno nanocomposites as a drug delivery system for 5-fluorouracil: study on the release behavior via mesoporous zro 2–co 3 o 4 nanoparticles modified sensor and antitumor activity. *RSC advances*, 12(33):21422–21439, 2022.

[189] Alessandra Montecucco and Giuseppe Biamonti. Cellular response to etoposide treatment. *Cancer letters*, 252(1):9–18, 2007.

[190] Maurice L Slevin. The clinical pharmacology of etoposide. *Cancer*, 67(S1):319–329, 1991.

[191] EL Baldwin and N Osheroff. Etoposide, topoisomerase ii and cancer. *Current Medicinal Chemistry-Anti-Cancer Agents*, 5(4):363–372, 2005.

[192] Francesca Rodino, Mattia Bartoli, and Sandro Carrara. Simultaneous and selective detection of etoposide and methotrexate with single electrochemical sensors for therapeutic drug monitoring. *IEEE Sensors Letters*, 2023.

[193] Hoai Viet Nguyen, Lukas Richtera, Amitava Moulick, Kledi Xhaxhiu, Jiri Kudr, Natalia Cernei, Hana Polanska, Zbynek Heger, Michal Masarik, Pavel Kopel, et al. Electrochemical sensing of etoposide using carbon quantum dot modified glassy carbon electrode. *Analyst*, 141(9):2665–2675, 2016.

[194] Weimin Zhang, Rongguo Lu, Xinglong Fan, and Yuan Weng. An electrochemical sensor based on graphene nanoribbon nano-catalyst for determination of etoposide as an approved drug in lung cancer. *Alexandria Engineering Journal*, 77:247–254, 2023.